

Dissertation zur Erlangung des Doktorgrades
der Fakultät für Chemie und Pharmazie
der Ludwig-Maximilians-Universität München

Mesoporous Transparent Conducting Films of Antimony Doped Tin Oxide as Nanostructured Electrodes

von

Vesna Müller (geb. Ličina)

aus

Zagreb, Croatia

2013

Erklärung

Diese Dissertation wurde im Sinne von § 7 der Promotionsordnung vom 28. November 2011 von Herrn Professor Dr. Thomas Bein betreut.

Eidesstattliche Versicherung

Diese Dissertation wurde eigenständig und ohne unerlaubte Hilfe erarbeitet.

München, am 20. März 2013

.....
(Unterschrift des Autors)

Dissertation eingereicht am: 21.03.2013

1. Gutacher: Prof. Dr. Thomas Bein

2. Gutachter: Prof. Dr. Christina Scheu

Mündliche Prüfung am: 10.06.2013

Acknowledgment

Behind the work presented in this thesis there is lots of hard lab work and sweating, crying and laughing, many wasted tears but most of all lots of joy. Therefore I would like to thank many people who supported me and who were together with me during this period.

First of all I would like to express my thankfulness to Dr. Dina Fattakhova-Rohlfing for being my supervisor and for giving me all the help and support. I would like to thank Prof. Dr. Thomas Bein for all the nice discussions and advices. To both of them I am very much grateful for all the positive stimulation which they gave to me during this work and the possibility to broaden my knowledge. Working for you completely changed my life and a view on science. Thank you!

I would like especially to thank Prof. Dr. Christina Scheu for the nice collaboration during my work on this thesis and for being my second reviewer.

Special thanks go as well to Prof. Dr. Sebastian Günther, Dr. Jiri Rathousky (J. Heyrovsky' Institute of Physical Chemistry, Prague), Dr. Goran Štefanić (Ruđer Bošković Institute, Zagreb), Dr. Diemo Ködderitzsch, Dr. Jan Minar, and Sebastian Wimmer for all the nice work we did together. It was an absolute pleasure to collaborate with you!

I am also very grateful to Regina Huber for all the administrative assistance at LMU.

To Tina Reuther and to Dr. Steffen Schmidt I even do not know how to express my thankfulness for all the great measurements they have made. Moreover, I would like to use this opportunity to apologize to them for all my lousy samples which they also had to measure. I have to say that without this I would not have been able to know which sample preparation procedure works ☺. Thank you deeply from the heart!

My colleagues Askhat, Yujing, Yan, Karin, Miha, Alex, Christian, Benni, Norma, Florian, Hans, Stefan, Fabian, Johann, Axel, Mirjam, Jörg, Andreas, Alesja, Basti, Kun, Flo HiHo, Dana and Stefan Wuttke I would like to say thank you for all the nice time we had together.

Two persons, beside my gratefulness for all the support they gave me during writing this thesis, I owe tons of printing paper, several cartridges for the printer and probably a new printer as well considering that I do not know how much longer their printer will live because of my thesis. Thank you Barbara and Wolfgang!

There are also persons to whom there are no words for saying thank you. Because of them I am what I am and for them I can say:

Vi ste proljetni osmijeh na mome lice,

ljetni povjetarac u mojoj kosi

i dok me držite za ruke kada koračam prema jesenima koje dolaze

moje srce nikada neće osjetiti zimu.

I tako svakog dana života moga...

Mojem Jensu, mami, tati, Lidiji, Sanji, Filipu, Mladenu, Chiari, Wolfangu, Barbari, Davoru i Siniši.

Abstract

Nanostructured electrodes based on transparent conducting oxides (TCOs) have attracted significant interest during recent years. Such 3D electrode architectures with a high surface area are suitable as conductive hosts for the incorporation of electroactive functional species. The huge surface area offers the possibility to increase the amount of immobilized species which results in higher electron efficiency leading to the increased efficiency of these hybrid devices.

One of the transparent conducting oxides that recently drew significant attention is antimony doped tin oxide (ATO). The combination of the good transparency and high electrical conductivity of ATO and a three-dimensional mesoporous network offers the possibility to use this material as an electrode system which involves immobilized functional species. However, the preparation of three-dimensional mesoporous transparent electrodes of ATO remains a non-trivial task.

In order to achieve the main property, i.e. the high conductivity, the ATO mesoporous network has to be crystalline. All reported methods for the preparation of these transparent and conductive ATO electrodes are based on self-assembly of sol-gel-derived metal oxide precursors assisted by amphiphilic structure-directed agents. As the inorganic framework formed by this method is amorphous, it must be transformed into a crystalline state, which is essential for the electrical conductivity. This transfer from an amorphous into the crystalline phase is achieved by treating the sample at elevated temperatures. However, without concomitant mesostructural collapse this phase transformation was only achieved for the ATO films where special amphiphilic block co-polymers of the type poly(ethylene-co-butylene)-block-poly(ethylene oxide) (KLE) were used. However these types of polymers, used as a template for the mesostructure, are not commercially available. In case of the commercially available polymers from the Pluronic family, the formation of a crystalline mesoporous

structure requires a special post-synthetic treatment which is rather elaborate and time consuming.

Within this thesis a novel strategy for the preparation of transparent conducting ATO electrodes was developed. The amorphous metal oxide precursor was replaced by crystalline ATO nanoparticles, serving as building blocks for these three dimensional mesostructures. The nanoparticles that can be used for the assembly into such structures must be monodispersed with a well-known composition.

The method which was used for the preparation of the ATO nanoparticles is known as non-aqueous sol-gel synthesis where the benzyl alcohol serves both as a solvent and as an oxide source. The ATO nanoparticles synthesized by this method were investigated in detail with respect to their size, composition and doping level in relation to their electrical conductivity. The structural and microstructural characterization of these nanoparticles was performed in collaboration with Prof. Dr. Christina Scheu (LMU, Munich), Prof. Dr. Sebastian Günther (LMU, Munich) and Dr. Goran Štefanić (Ruđer Bošković Institute, Zagreb). The highest conductivities were obtained for those compositions that contained small amounts of antimony. None of the methods used for the characterization of these nanoparticles was able to detect any phase separation induced by the incorporation of antimony into the tin oxide matrix. Moreover, it was shown that the cassiterite SnO_2 lattice can accommodate up to 38 mol % of Sb. The first phase separation appears at an antimony fraction of about 40 mol%.

The nanoparticles which contained up to 30 mol % of antimony were used for the assembly of mesostructured films. The porosity of the films was investigated in collaboration with Dr. Jiri Rathousky (J. Heyrovsky Institute of Physical Chemistry, Prague). All films possess a high optical transparency (above 90 %) and a large surface area. The conductivity of the films is dependent on the composition of the used nanoparticles and the annealing temperature used

for the removal of the template and the sintering of the nanoparticles into an inorganic mesoporous framework.

The potential applications of these electrodes were investigated by cyclic voltammetry measurements where a significant increase in current collection was obtained in comparison to the flat ITO electrodes. The various small redox species, such as hexaaminoruthenium(II), hexacyanoferrate(II), ferrocenecarboxylic acid, dye ruthenizer 470, proteins cytochrome c, that were investigated for the incorporation in this porous network by adsorption indicated a strong negative charge of the ATO walls. However, the leaching of the adsorbed electroactive species requires the introduction of a stabilization method which bonds the electroactive molecules to the surface of mesoporous ATO. Therefore a covalent attachment was investigated.

For these purposes two types of surface functionalization were studied, where the introduced functional groups can serve as potential linkers to the functional electroactive molecules. In the first type the direct attachment of the organic species by Grignard reactions was investigated. Secondly, the surface functionalization through the attachment of organosilane compounds was performed. Both methods provide a high surface coverage with organic groups.

The covalent attachment of the electroactive molecules to the surface-modified ATO electrode was studied on ferrocene serving as a model redox moiety. The ferrocene moieties were bonded to the terminal group of an aminosilane via the formation of an amide bond with the carboxylic groups of ferrocenecarboxylic acid. The attached molecules were electroactive and stable toward leaching indicating that such bonding could offer a fruitful basis for the incorporation of other types of electro-active molecules, such as luminescence dyes and small redox proteins. The incorporation of such electroactive species would provide a design of the model of optoelectronic device in which the functionalized surface of the transparent

electrode would give an optical signal in interaction with selective species from the surrounding.

For the investigation of the incorporation of small redox proteins cytochrome c was chosen. Considering that cytochrome c has a strongly positive charge at pH 7, this offered the possibility for the incorporation of the protein by adsorption due to electrostatic forces between the negatively charged ATO electrode and the positively charged cytochrome c. However, the disadvantage of this attachment was found in leaching of the protein in the presence of strong electrolytes. A more stable incorporation of cytochrome c was obtained by covalent attachment of the protein.

The obtained results indicate that the mesoporous ATO network can be used as a three dimensional electrode architecture serving as a suitable matrix for the incorporation of various electroactive species.

Table of Contents

1	Introduction	1
1.1	Transparent Conducting Oxides (TCOs).....	1
1.1.1	Correlation Between the Optical and Electrical Properties in TCOs.....	3
1.1.2	Classification of the TCOs	5
1.1.3	Applications of TCOs.....	6
1.2	TCOs Based on Tin Dioxides.....	7
1.2.1	Antimony Doped Tin Oxide (ATO).....	8
1.3	Nanostructured Electrodes.....	10
1.3.1	Conducting Electrodes.....	11
1.3.2	Metal Oxide Electrodes	16
1.3.3	Transparent Conducting Oxide Electrodes.....	19
1.4	Mesoporous Films	21
1.4.1	Evaporation Induced Self Assembly	23
1.4.2	Nanobuilding Blocks (NBBs) for EISA Process	27
1.5	Synthesis of Metal Oxide Nanoparticles as NBBs	28
1.5.1	Sol-Gel Synthesis of Metal Oxide Particles	29
1.5.2	Non Aqueous Sol-Gel Synthesis of Metal Oxide Nanoparticles.....	30
1.6	Incorporation of Electro-Active Molecules into Mesoporous Oxide Frameworks	31
1.6.1	Surface Functionalization with Organotrialkoxysilanes.....	33
1.6.2	Surface Functionalization with Grignard Reagents.....	34
1.6.3	Attachment of Electroactive Moieties	36
1.6.4	Incorporation of the Metalloprotein Cytochrome C	37
1.7	References	40
2	Characterization Methods.....	51
2.1	X-Ray Diffraction.....	51
2.2	Infrared Spectroscopy.....	53
2.3	Raman Spectroscopy	54
2.4	UV-Vis Spectroscopy.....	55
2.5	Thermogravimetric Analysis and Differential Scanning Calorimetry.....	58
2.6	Electron Microscopy	59
2.6.1	Transmission Electron Microscopy.....	60
2.6.2	Energy Dispersive X-Ray Spectroscopy (EDX)	63
2.6.3	Electron Energy Loss Spectroscopy (EELS).....	64
2.6.4	Scanning Electron Microscopy.....	66

2.7	X-ray Photoelectron Spectroscopy	68
2.8	Dynamic Light Scattering.....	69
2.9	Zeta Potential Measurements	73
2.10	Gas Sorption	75
2.11	Potential Sweep Voltammetry.....	79
2.11.1	Faradaic and non-Faradaic Processes	80
2.11.2	Linear Sweep Voltammetry.....	82
2.11.3	Cyclic Voltammetry	83
2.11.4	Kinetics of Electrode Reactions	87
2.11.5	Evaluation of the Cyclic Voltammetry Data	89
2.12	Electrical Conductivity Measurements.....	90
2.13	Conductivity Measurement Through Van der Pauw Method.....	91
2.14	Hall Effect Measurement.....	93
2.15	References	97
3	Antimony Doped Tin Oxide (ATO) Nanoparticles	99
3.1	Introduction	99
3.2	Experimental Section	101
3.2.1	Chemicals	101
3.2.2	Synthesis of ATO Nanoparticles	101
3.2.3	Characterization Techniques	102
3.3	Results and Discussion.....	105
3.3.1	Morphology and Size of ATO Nanoparticles.....	107
3.3.2	Solubility of ATO Nanoparticles.....	109
3.3.3	Structure of ATO Nanoparticles (XRD, Raman)	110
3.3.4	Composition of ATO Nanoparticles.....	114
3.3.5	Characterization of Nanoparticles by Spatially Resolved Techniques.....	116
3.3.6	Electrical Conductivity (Hall Effect Measurements)	120
3.4	Conclusions	123
3.5	Appendix	124
3.6	References	129
4	Assembly of ATO Nanoparticles into Mesoporous Films	133
4.1	Introduction	133
4.2	Experimental Section	135
4.2.1	Chemicals	135
4.2.2	Preparation of Mesoporous Films	136
4.2.3	Functionalization of Mesoporous Films	137

4.2.4	Preparation of the Phosphate Buffer.....	138
4.2.5	Characterization Techniques	138
4.3	Results and Discussion	140
4.3.1	Morphology of the Mesoporous Films	143
4.3.2	Structure of ATO Films.....	146
4.3.3	Porosity of Mesostructured ATO Films	147
4.3.4	Conductivity of ATO Films.....	149
4.3.5	Applicability of the Mesoporous ATO Films as Nanostructured Electrodes	151
4.3.6	Incorporation of Ruthenium Dye.....	154
4.3.7	Cyclic Voltammetry of Ruthenium Dye.....	157
4.4	Conclusions	160
4.5	Appendix	162
4.6	References	165
5	Surface Functionalization of Mesoporous Antimony Doped Tin Oxide.....	169
5.1	Introduction	169
5.2	Experimental Section	171
5.2.1	Chemicals	171
5.2.2	Synthesis of ATO Nanoparticles and Mesoporous Powders.....	171
5.2.3	Surface Functionalization of Mesoporous ATO with APTES	172
5.2.4	Surface Functionalization of Mesoporous ATO with Grignard Reagents.....	172
5.2.5	Characterization Techniques	173
5.2.6	Calculation Methods.....	174
5.3	Results and Discussion	175
5.3.1	Mesoporous ATO Powders	175
5.3.2	Surface Functionalization with APTES.....	176
5.3.3	Surface Coverage with APTES Molecules.....	179
5.3.4	Surface Functionalization with Grignard Reagents.....	180
5.3.5	Surface Coverage Obtained by Metalorganic Reactions	184
5.3.6	Confirmation of the Presence of Organic Groups by Vibrational Spectroscopy Measurements.....	186
5.4	Conclusions	187
5.5	Appendix	189
5.6	References	191
6	Incorporation of Cytochrome C in Transparent Conducting Electrode Networks	193
6.1	Introduction	193
6.2	Experimental Part	195

6.2.1	Chemicals	195
6.2.2	Synthesis of ATO Nanoparticles	195
6.2.3	Preparation of Solutions for Mesoporous Films and Mesoporous Powders.....	196
6.2.4	Incorporation of Cytochrome C in Mesoporous ATO.....	196
6.2.5	Preparation of the Phosphate Buffer.....	198
6.2.6	Characterization Techniques	198
6.2.7	Calculation Methods.....	199
6.2.8	Leaching Stability.....	200
6.3	Results and Discussion.....	200
6.3.1	Influence of the Incorporation of Cytochrome C on the ATO Mesostructure.....	202
6.3.2	Influence of the Incorporation of Cytochrome C on Pore Size of ATO.....	203
6.3.3	Amount of Incorporated Cytochrome C	205
6.3.4	Spectroscopic Characterization of Incorporated Cytochrome C	206
6.3.5	Electrochemical Activity of Incorporated Cytochrome C	208
6.3.6	Surface Coverage with Cytochrome C	209
6.3.7	Leaching of Cytochrome C	212
6.3.8	Electrocatalytic Activity of Cytochrome C	215
6.4	Conclusions	217
6.5	Appendix	219
6.6	References	223
7	General Conclusions.....	227
8	Curriculum vitae.....	231
9	Publications and Presentations	232
9.1	Publications	232
9.2	Poster Presentations.....	233
9.3	Oral Presentations.....	234

1 Introduction

The main part of the research in this thesis is devoted to the development of mesoporous antimony doped tin oxide (ATO) films and their use as nanostructured electrodes. The ATO belongs to transparent conducting oxides (TCOs) which found their application as flat electrodes in optoelectronic devices. Therefore, in the following chapter a literature overview of the transparent conducting oxides is given. Various three dimensional electrode architectures are presented together with their benefits for the applications which require anchored species. Furthermore, the most common methods for the surface functionalization and anchorage of the electro-active species are reviewed.

1.1 Transparent Conducting Oxides (TCOs)

Transparent conducting oxides (TCOs) are a class of oxides which combine high electrical conductivity and high optical transparency.^{1, 2} Compared to the other materials, metals are conductive but not transparent for visible light. Whereas, other transparent materials like glasses are often not conductive.³

The main prerequisite for the TCO materials is that the one property, the electrical conductivity is strongly coupled with the second (optical) property, the refractive index or the extinction coefficient. Generally they can have very low resistivities of $10^{-3} \Omega \text{ cm}$ and a high transparency in the visible range of above 80 %. These two characteristics are correlated with the presence of a high concentration of charge carriers of the order of 10^{20} cm^{-3} and a wide band gap of above 3 eV. Although all known TCO materials possess high charge carrier concentrations, slight variations in the electrical conductivity between various TCO systems were observed. This behavior was ascribed to the variation in the charge carrier mobility which can be between about 20 and $100 \text{ cm}^2 (\text{V s})^{-1}$.^{2, 3}

Transparent conducting oxides can be *n*- or *p*-type conductors and the conductivity can be a result either of a nonstoichiometry of the oxide or a presence of impurities. In the *n*-type of conductivity free electrons (free carriers obtained either by oxygen deficiency or from impurity dopant) are associated to the metal defect energy level. This level is close in energy to the bottom of the conduction band of oxides. These charge-compensating electrons can be thermally promoted from defect energy levels to the conduction band, thus contributing to the conductivity. The *p*-type of conductivity in TCO was observed in the systems where the defect energy level is close to the valence band of the metal oxide. In this case, the electron promotion to the defect energy level creates a hole in the valence band which promotes the conductivity. Generally good optical transparency for both types of conductivity can be obtained. However, the obtained value of the *p*-type of conductivity is considerably lower than the value of the *n*-type, as a result of the restricted hole mobility in the valence band of solids.^{3, 4}

Conductivity in TCO materials can be either native or induced by doping with an appropriate dopant.^{1-3, 5-7}

In the native transparent conducting oxides the high conductivity is a result of the presence of oxygen vacancies and/or interstitial metal atoms incorporated into their crystalline structures. Native oxides can show *n*-type conductivity with very high charge carrier concentrations of the order of 10^{20} cm^{-3} . However, it was shown that the substoichiometric oxygen content is difficult to control. Therefore, the native oxide films are unstable when they are used at elevated temperatures and they did not find practical applications as transparent conducting electrodes.²

In order to obtain higher conductivities different types of the doped TCOs have been developed. There are three main requirements in order to observe doping.⁵

1. The dopant must be soluble in the matrix of the host.
2. The doping levels must be shallow.

3. The doping must not be compensated by native defects of the opposite charge.

In the doping mechanism, the shallow dopant states are located either close to the host conduction band (*n*-type) or close to the valence band (*p*-type). In the *n*-type systems the donor electrons undergo promotion to the conduction band. Upon further doping a degenerated gas of current-carrying electrons is formed. This gives an increase in the infrared absorption and high electrical conductivity. In the *p*-type systems the shallow donor band is located close to the valence band of the host. Due to the thermal excitation the electrons from the valence band of the host are promoted into the shallow dopant energy levels leaving the holes in the valence band. In both cases, the band gap of the host remains unchanged thus ensuring that the electrically conducting material retains the optically transparency in the visible range.⁵⁻⁷

Most of the research performed on TCOs was made on *n*-type semiconductors and these types of materials found their commercial applications as flat electrodes in various touch panel displays or dye sensitized solar cells.² In 1993 the *p*-type doping of TCO thin films was for the first time reported.⁸ However, up to now there has been no report on the preparation of the *p*-type TCOs with a direct commercial application. Detailed classification of the TCOs according to the types of the oxide and the dopants is presented and discussed in the part 1.1.3; classification of the TCOs Materials.

1.1.1 Correlation Between the Optical and Electrical Properties in TCOs

One of the accepted theories describing the electrical and optical properties of TCOs is based on the description of the charge transport in metals which is coupled with the optical properties of these materials.³ The concept combines all important parameters which are used for the description of the performance of TCO such as: conductivity (σ), sheet resistance (R_S), carrier mobility (μ), carrier density (N), optical absorption coefficient (α) and extinction

coefficient (κ). The optical absorption coefficient and extinction coefficient are correlated according to equation:

$$\alpha = 4\pi\kappa/\lambda \quad (\text{eq. 1.1.1})$$

where λ is the wavelength of light.

The equation which describes the performance of TCOs and gives the correlation of conductivity to wavelength is written as a ratio of the electrical conductivity, σ , and the optical absorption coefficient, α , as:

$$\sigma/\alpha = 1/[R_s \ln(T + R)] \quad (\text{eq. 1.1.2})$$

where T is the total transmittance, R the reflectance of the material and R_s the sheet resistance.⁹

This equation gives a qualitative estimation of the performance of the different TCO materials with a similar microstructure. The factors which are included in the equation 1.1.2 are dependent on the processing conditions. Therefore, the TCOs which are highly polycrystalline will behave as optically scattering materials and will have a higher resistivity due to the decreased charge carrier mobility at grain boundaries.

The specular reflectivity, R , of the TCO material is defined as:³

$$R = \left| \varepsilon^{1/2} - 1 \right| / \left| \varepsilon^{1/2} + 1 \right| \quad (\text{eq. 1.1.3})$$

where ε is the dielectric constant.

This equation correlates the optical properties of TCOs to their dielectric (and electric) properties. Both equations (eq. 1.1.2 and 1.1.3) can be used as a guidance to design a desired transparent conducting oxide film.³

1.1.2 Classification of the TCOs

The most known TCOs are based on indium oxide, tin oxide, zinc oxide and cadmium oxide; by nature they are semiconductors.^{1, 2, 10, 11} As described above, a common way to increase their conductivities and to retain a good transparency is by doping them with appropriate dopants. Therefore various binary TCO materials have been developed up to now. In Table 1.1.1. the most common TCOs and their respective dopants are enlisted.

Table 1.1.1. Classification of the TCO semiconductors for transparent electrodes.

	TCO materials			
host	In ₂ O ₃	SnO ₂	ZnO	CdO
dopant	Sn, Ge, Mo, F, Ti, Zr, Hf, Nb, Ta, W, Te	Sb, F, As, Nb, Ta	Al, Ga, B, In, Y, Sc, F, V, Si, Ge, Ti, Zr, Hf	In, Sn

To obtain the TCO films for use in specialized applications several new multicomponent oxides such as ternary or quaternary oxide phases have been developed.^{2, 11} The advantage of these ternary and quaternary TCOs is the possibility of controlling the electrical, optical, chemical and physical properties by alternating their chemical composition. Some of these ternary and quaternary oxides are presented in the schematic phase diagram in Figure 1.1.1.

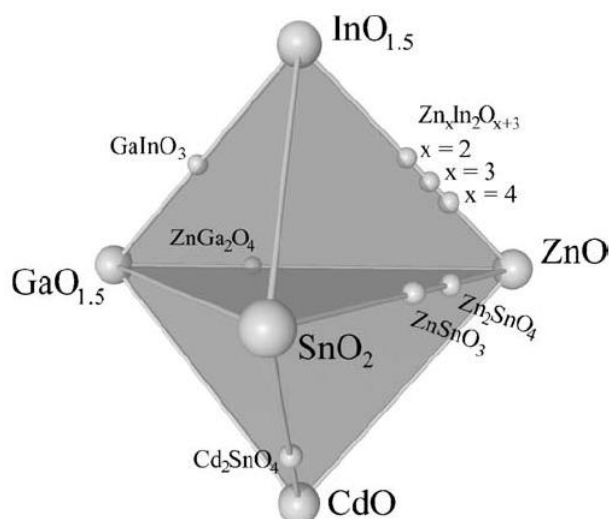


Figure 1.1.1. Phase diagram of the multicomponent TCOs. Adopted from reference [11].

The binary compounds show an advantage in practical use over ternary or multicomponent compounds. The reason for this is a relatively simple control of the stoichiometry which is highly advantageous for their processing in the form of thin films.²

1.1.3 Applications of TCOs

One of the most known TCO materials is tin doped indium oxide (commonly called indium-tin-oxide or ITO) which already found its commercial application as a flat transparent electrode in various optoelectronic devices in touch panel displays,¹² non-silicon solar cells¹³,¹⁴ or organic light-emitting diodes (OLEDs).¹⁵

Aluminium doped zinc oxide (AZO) is another promising TCO material. However, the main drawback of AZO films is their relatively low conductivity in comparison to the ITO or fluorine doped tin oxide (FTO) compounds.

Cadmium containing TCO films exhibit a low resistivity. However, due to the high toxicity of cadmium they did not find practical use up to now.

One of the more recently extensively studied TCO materials is tin oxide.¹⁶⁻¹⁹ Fluorine doped tin oxide (FTO) is already commercially available as flat film and it is widely used in non-

silicon solar cells due to its much thermal stability compared to ITO. However, the drawback of FTO films is a certain lack of transparency in comparison to the films based on ITO.²⁰ Antimony doped tin oxide (ATO) belongs to the group of oxides being a promising substitute of ITO. In the light of this, in the last years significant research has been performed on this system.^{1, 2, 21-24}

1.2 TCOs Based on Tin Dioxides

Due to the rather high availability of tin, tin dioxide (SnO_2) is one of the most extensively studied transparent conducting materials.^{16-19, 25, 26} Prepared in the form of dense films, it is polycrystalline with a rutile (cassiterite) type of structure in the space group $P4_{2/mnm}$.^{16, 27, 28} As all other TCOs, SnO_2 is transparent for the visible part of the electromagnetic radiation. However, it is highly reflective for infrared radiation. Due to this property, SnO_2 is nowadays dominantly used as an energy conserving material. SnO_2 -coated windows are used to transmit the light (as a result of the transparency of SnO_2) and to keep the heat out or inside of buildings depending on the climate regime.^{12, 16}

SnO_2 exhibits a band gap of 3.6 eV.^{1, 2, 16} Undoped SnO_2 is an n-type semiconductor, which is a result of the non-stoichiometry, or in particular due to the oxygen deficiency. Moreover, the conductivity of SnO_2 depends on the preparation procedure. For instance, the films prepared from tin chlorides incorporate chlorine ions into the structure, thus contributing to the conductivity. Similar to the other TCOs the SnO_2 has high a charge carrier concentration at the order of 10^{19} up to 10^{20} cm^{-3} and a charge carrier mobility of the order of $5\text{-}30 \text{ cm}^2 \text{ V}^{-1} \text{ s}^{-1}$, as reported by various authors.^{1, 2, 11, 16} Various values for the electrical conductivity of the SnO_2 were reported as well, but they are all in the range of 10^{-3} to $10^{-2} \text{ S cm}^{-1}$.^{1, 2, 11, 16}

In order to increase the conductivity of the SnO_2 , various doped SnO_2 materials have been prepared up to now.^{1, 2, 10, 11, 16, 20, 21, 23, 24}

The highest conductivities obtained for the fluorine doped tin oxide (FTO) are in the order of 10^4 S cm^{-1} .¹ As mentioned above, FTO is quite broadly used in non-silicon solar cells however, it shows a slight drawback in comparison to the more expensive tin doped indium oxide (ITO) and that is its lower transparency.

1.2.1 Antimony Doped Tin Oxide (ATO)

In antimony doped tin oxide (ATO) the conductivity of SnO_2 is increased by substituting the tin (Sn^{4+}) with antimony ions in a higher valence state than tin, namely Sb^{5+} .^{1, 2} The so formed doped tin oxide can be presented as $\text{Sn}^{4+}_{(1-x)}\text{Sb}^{5+}_x\text{O}_{2-x}$, or as Kröger-Vink notation as $\text{Sn}^{\bullet\bullet\bullet\bullet}_{\text{Sn}} + \text{Sb}^{\bullet\bullet\bullet\bullet}_{\text{Sn}} + \text{O}''_{\text{O}} + e'$. From the notation it can be seen that the dopant atoms, Sb, sit on the Sn sites in the lattice and bring one electron more into the host lattice being placed into the conduction band. Thus the donation of this electron into the conduction band upon replacement of tin with antimony induces an increase in conductivity.^{4, 16}

This doping of tin oxide with antimony modifies the band structure giving rise to a conduction band of 35 meV.¹ The modification of the conduction band leads to a shift in the optical adsorption edges to higher energies with increasing charge carrier concentration. This type of behavior is known as the Burstein-Moss effect. This effect is a result of the increase of energy required to promote an electron from the valence band into an empty state of the conduction band.¹⁶

Typically the ATO films have a charge carrier concentrations at the order of 10^{20} cm^{-3} , the mobility of the charge carriers at the order of $15\text{-}30 \text{ cm}^2 \text{ V}^{-1} \text{ s}^{-1}$ and values of conductivity of $10^{-3} \text{ S cm}^{-1}$. Beside this, the films can possess high optical transparency of 80 % - 90 % and IR reflectivity of 75 % - 85 %.¹

The influence of the amount of incorporated antimony on the structural and electrical properties of the ATO was intensively studied by several authors.^{21, 23, 24, 29-31} The highest

conductivity was obtained for dense ATO films of the order of 1×10^3 S/cm and the films contained 7 mol % of antimony.¹ Small ATO nanoparticles typically show significantly lower conductivity values than dense films due to the presence of the high amount of grain boundaries which act as electron scatter centers.^{11, 31, 24, 31-33} Nutz et al.²⁴ obtained a conductivity value of 5×10^{-7} S/cm for the ATO particles 4-6 nm in size pressed in pellets while, Goebbert et al. reported a conductivity of the order of 10^{-8} S/cm for the ATO nanoparticles ca. 4 nm in size. Beside the conductivity, a maximal amount of the incorporated antimony in SnO₂ matrix remained an issue. Terrier et al.³⁴ showed that a maximal doping level reaches 20 mol % of antimony as a result of a difficulty in introduction of further antimony atoms into cassiterite lattice. Although such high amount of antimony can be introduced into the SnO₂ lattice, it was found that the conductivity does not increase by doping higher than 10 %, but rather decreases. The highest conductivity values were obtained for the doping levels between 4 and 8 mol %.^{1, 24, 31, 32}

The incorporation of antimony into the SnO₂ matrix causes a change in color from white (SnO₂) to brownish-grayish-blue (ATO).^{23, 24, 31} This bluish coloration is attributed to the coexistence of Sb³⁺ and Sb⁵⁺.¹¹ Although this intense absorption in the region of red light and near IR has been assigned to the electronic transfer between two oxidation states,³⁴ it has also been argued that it appears due to a free charge carrier absorption in the material.^{11, 23}

Terrier et al. intensively studied the ATO system through X-ray photoelectron spectroscopy in order to evaluate the amount of antimony in different oxidation states.^{34, 35} Their results indicated that although the Sb⁵⁺ is an effective donor, the antimony exhibits always a mixture of two oxidation states namely Sb⁵⁺ and Sb³⁺.^{29, 31, 35} In contrast to Sb⁵⁺, which acts as an electron donor, the Sb³⁺ produces a hole which acts as an electron trap. Because of this reason, only the excess of Sb⁵⁺ provides the positive doping effect.

Even though ATO has been intensively studied over the last years it did not find yet an industrial application as transparent electrode. One of the reasons for this is its low

conductivity in comparison to ITO. Moreover, its characteristics have not been sufficiently explored up to now.³⁶

1.3 Nanostructured Electrodes

Although TCO films found their application as flat electrodes in various optoelectronic devices, there are other types of devices that require rather three dimensional electrode morphologies rather than flat electrodes. These types of electrode architectures are beneficial in devices which are based on monolayers of the electro-active species on the electrode surface, particularly in bio-optoelectronic devices. The porous morphology of such electrodes with a large interface area acts as a conductive matrix for the incorporation of electro-active moieties at high loadings. As a consequence, a great number of electrons can be collected from a smaller geometric electrode area, leading directly to an increased efficiency of such optoelectronic devices.

In recent years significant research was carried out on the development of advanced electrodes with improved architectures for various applications.^{33, 37-40} There are several important areas which require an improved design of 3-dimensional electrode structures, namely photo-electrochemical solar cells, photohydrolysis, photoelectrocatalytic devices, Li-ion batteries, supercapacitors, fuel cells or biosensors.⁴¹

Up to now various nanostructures and materials were studied as advanced electrode layers with 3-dimensional structure.^{33, 37-40, 42-46} There are several possible ways of how these electrode layers can be classified.

The first criterion can be described as the ability of the electrode material to conduct the electric current. Therefore, such electrode layers can be divided into conducting electrodes, semiconducting electrodes and insulating electrodes.

In the second criterion the nanostructured electrode layers can be classified from the point of view of the periodicity of their morphologies. The electrode architectures which are not periodically structured are usually prepared by deposition of various nanomaterials such as nanoparticles, nanorods, nanosheets etc. on the substrates and used as high surface electrodes. The second type of the nanostructured electrode architectures is classified as ordered porous materials. In this respect different ordered porous materials can be classified into three categories according to IUPAC nomenclature depending on their pore diameters (d):⁴⁷

- microporous ($d < 2$ nm)
- mesoporous (2 nm $< d < 50$ nm)
- macroporous ($d > 50$ nm)

The suitable pore size of porous electrodes is dictated by the size of electro-active guest molecules. Therefore, a significant part of the research is devoted to the use of macroporous and mesoporous systems which can incorporate bulkier redox guests without restriction of the electrolyte diffusion in the pores.⁴⁸⁻⁵¹ Although microporous systems possess high surface areas, the small pore size limits their application as a host matrix for large molecules. In the following part a short overview on the most common porous electrode materials and their periodic nanostructured morphologies will be presented.

1.3.1 Conducting Electrodes

Electrode materials that show good electrical conductivity are carbon-based materials (such as graphitic materials, graphene or carbon nanotubes), metals and transparent conducting oxides.

Metallic Electrodes

Porous metallic electrodes are mostly prepared by four main approaches: 1. nanoparticle-based approach, 2. template-based approach, 3. dealloying and 4. decoration approach.⁵²

In the nanoparticle-based approach pre-synthesized metal nanoparticles are deposited on a conducting electrode.⁵² One of the most common way of the synthesis of metal nanoparticles is a reduction of metal precursor in solution by reducing agent in the presence of stabilizing agents (polymer or inorganic additives). Some less common approaches for the synthesis of metal nanoparticles are based on photochemistry, sonochemistry, sonoelectrochemistry or thermal decomposition. Example of nanostructured electrode prepared in this way is porous platinum electrode assembled from platinum nanoparticles which are deposited on carbon support. However, the structural stability of nanoparticles limits the long-term stability of such electrodes.⁵²

The templated-based approach is based on electrodeposition, electroless deposition, galvanic replacement, thermal deposition or chemical vapor deposition of metal over a template which is placed on the top of the conductive surface of the electrode.⁵²⁻⁵⁶ In the second step the template is removed leaving a three-dimensional network of deposited metal. Depending on the template, which can be either hard or soft template, different metallic electrode structures can be prepared varying from nanotubes up to mesostructured metallic electrodes or hierarchically structured electrodes. For instance, hollow platinum nanotubes can be prepared by electrodeposition of platinum over an anodized aluminium oxide membrane which is subsequently removed.⁵² Other hard templates for the electrodeposition of metal are self assembled colloidal microspheres of silica or polystyrene which give macroporous structures⁵³⁻⁵⁶ while mesoporous silica as a template gives a mesoporous structure.^{52, 57} By using a combination of templates such as colloidal silica particles and mesoporous silica it is possible to obtain a hierarchical structure. Example of such material is hierarchical structure of platinum nanowire,⁵⁷ Figure 1.3.1.

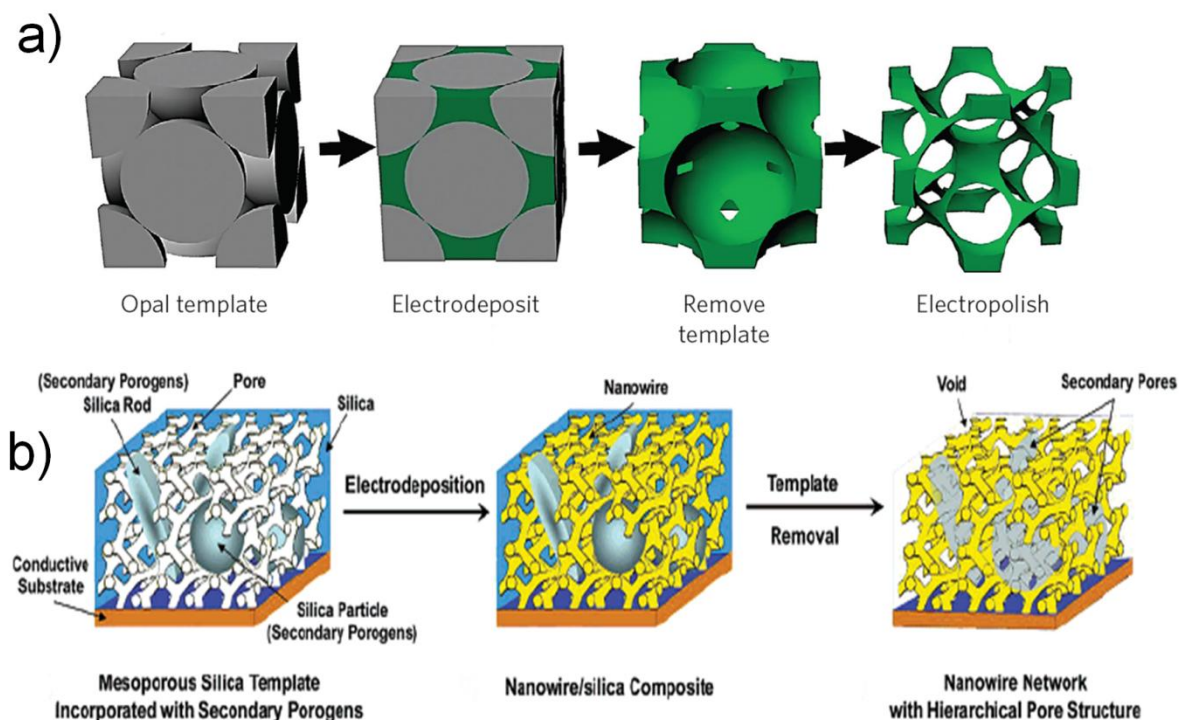


Figure 1.3.1. Illustration of the preparation of a) macroporous metallic electrodes by using opal template, and b) hierarchical structure by using combination of silica beads and mesoporous silica material. Figure a) is adapted from the reference [53] and figure b) is adapted from the reference [57].

The dealloying is based on the etching of less noble component of alloy which is selectively dissolved leaving behind a nanoporous structure of noble component from the alloy.

The decoration approach is based on decoration of already porous electrode with metal. This can be performed through various methods such as sputtering, electrodeposition, galvanic replacement, etc.

Also, a combination of techniques for the preparation of metallic electrodes can be used if there is a demand for the electrode of particular porous structure.⁵⁸⁻⁶⁰ Example for this is porous gold electrode prepared by electrodeposition of gold and silver, whereas silver was subsequently removed leaving the porous gold structure, Figure 1.3.2.

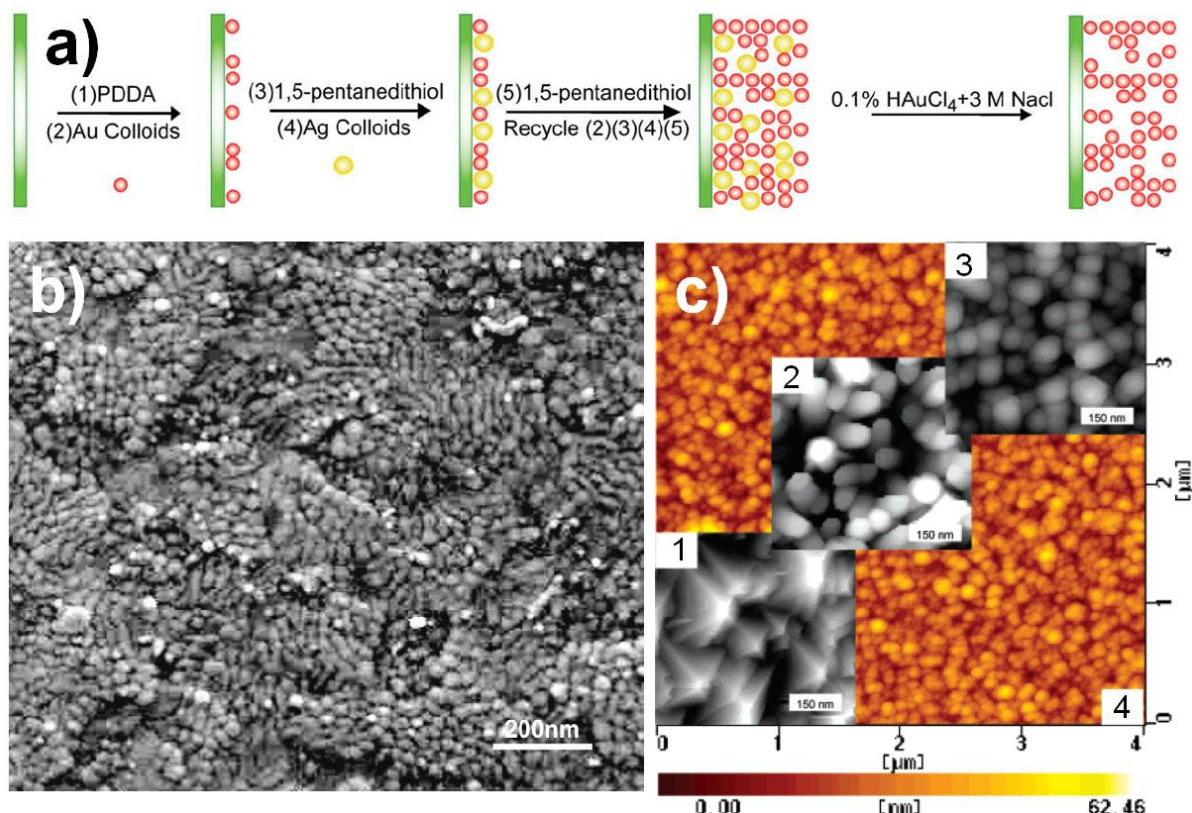


Figure 1.3.2. a) The process of preparation of nanostructured gold electrodes and the obtained electrode morphology if b) colloidal gold nanoparticles were used or c) various gold nanoparticles were electrodeposited: 1-pyramidal gold nanoparticles, 2-rod-like gold nanoparticles and 3-spherical gold nanoparticles. Images a) and b are adapted from reference [60] whereas image c is adapted from reference [58].

Carbon Electrodes

Due to their good conductivity, carbons are commonly used as the electrode materials. Several types of carbon materials such as carbon nanotubes, graphene, carbon paste or structured mesoporous and macroporous carbons were investigated as nanostructured electrodes^{49, 61-63}.

In the case of non-periodically structured carbon electrodes, carbon pastes, nanotubes or nanosheets are the most investigated materials. The carbon paste electrodes are prepared by mixing together different types of carbon powders with the electro-active components and some binder. Carbon nanotubes and nanosheets are usually cast on conductive substrates resulting in non structured porous layers. Another approach to prepare carbon nanotubes is a direct growth of carbon nanotubes (nanotube forest) on the conducting substrates.⁶⁴⁻⁶⁷

There is also a significant amount of research on the fabrication of periodic porous carbon electrodes, which can be made with various porous morphologies and pore sizes ranging from microporous to macroporous materials. The ordered mesoporous carbons (OMC) are very attractive as nanostructured electrodes due to their high surface area.⁶¹ Usually these materials are prepared through self-assembly of organic precursors and template molecules followed by a subsequent condensation of the carbon framework and the template removal. Another common strategy for fabrication of mesoporous carbonaceous materials is hard-templating, which typically involves pyrolysis of organic precursors (for example sucrose) filled into the pores of a mesoporous silica template. A basic approach to prepare macroporous carbon electrodes involves hard templating using silica based opals as the template.⁴⁹ The carbon precursor can be either mixed together with the template or impregnated over previously deposited template and followed by subsequent carbonization of the carbon precursor and the extraction of the silica template. Both mesoporous and macroporous carbon materials proved to be a good conducting hosts with the pores large enough for incorporation of various electroactive guests.

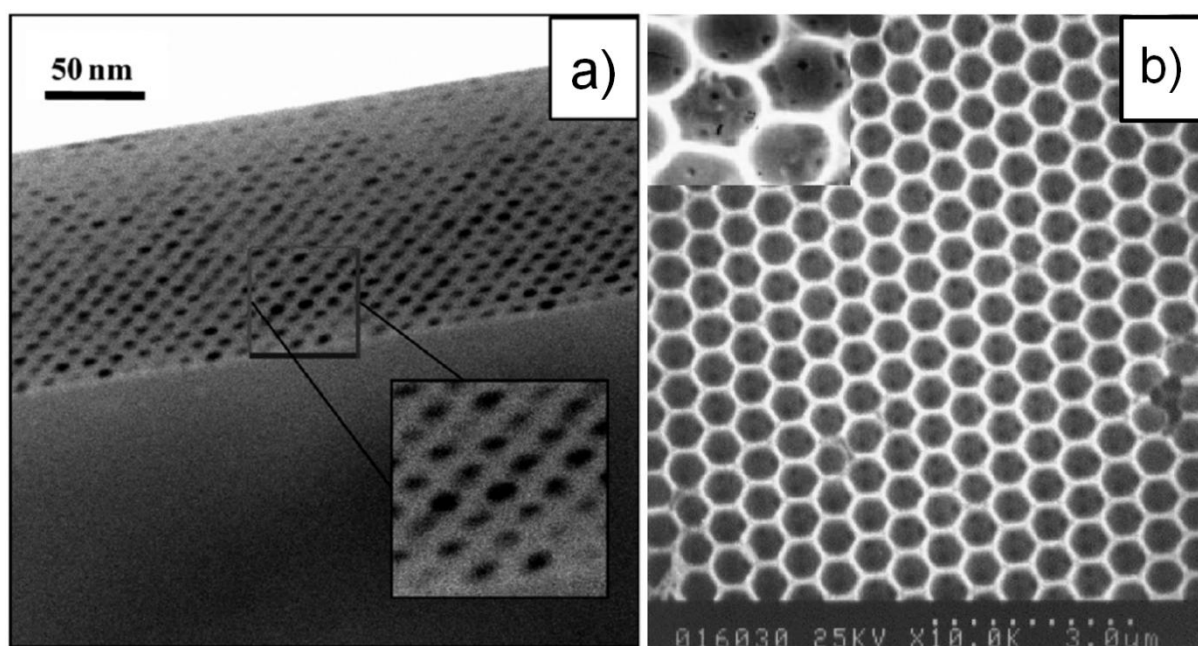


Figure 1.3.3. a) Morphology of OMC films and b) macroporous carbon. Image a) is adapted from reference [61] and b) from reference [62].

1.3.2 Metal Oxide Electrodes

One of the most investigated oxide scaffolds for nanostructured electrodes is silica. Silica can be easily prepared with a large variety of microporous, mesoporous,⁶⁸⁻⁷¹ macroporous⁷² and hierarchical⁷³⁻⁷⁵ structures and a broad range of pore sizes, which can be tuned by selection of the templating agents (Figure 1.3.4). Moreover, it can possess a very high surface area up to 1000 m²/g,⁷⁶ so that very high loadings of the anchored species can be obtained.^{76, 77}

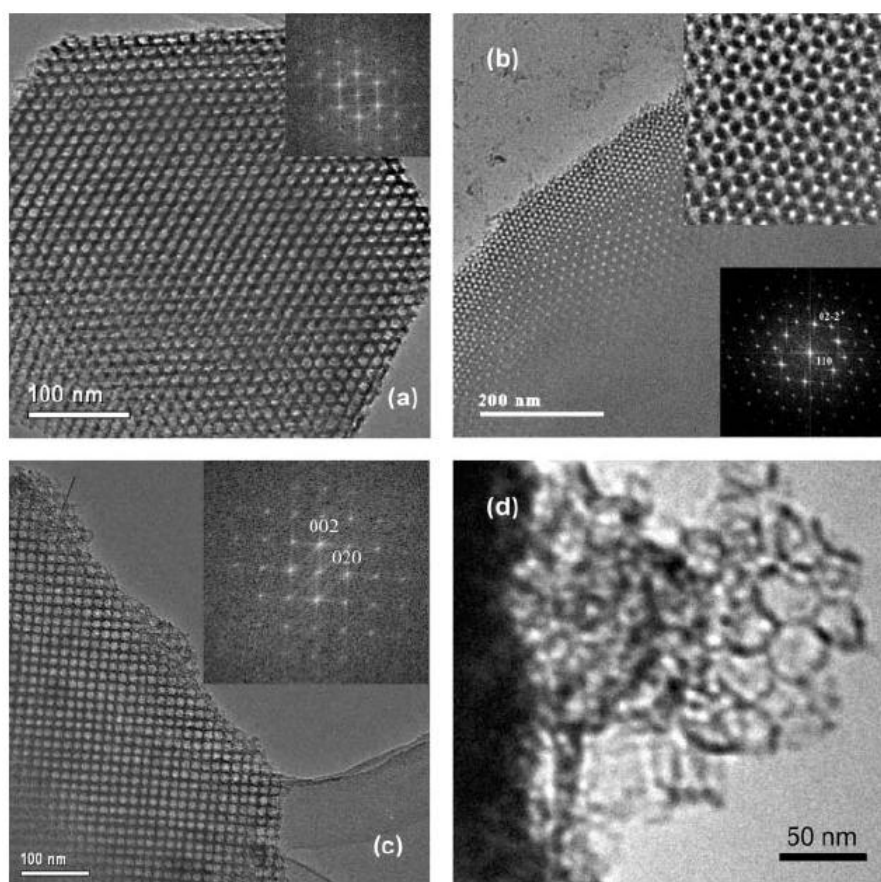


Figure 1.3.4. TEM images of the mesoporous silica materials with different pore sizes: **a)** SBA-15, **b)** FDU-5, **c)** FDU-12, **d)** MCF. Adopted from reference [76].

Due to the above mentioned reasons, the mesoporous silica materials were studied for the incorporation of guest molecules by adsorption and covalent anchorage.^{50, 70, 71, 76} The first use of mesoporous silica films as nanostructured electrodes was reported in 2005 by Fattakhova-Rohlfing et al.⁷¹ Further, the mesoporous silica was used as a support for the incorporation of

proteins such as cytochrome c, myoglobin or hemoglobin, whose activity was electrochemically investigated.^{50, 76, 78}

However, although easily accessible pores and high surface areas for the silica materials can be obtained, the most common disadvantage of the silica as host electrode is its low electrical conductivity. Due to this a charge transport between the redox molecules is possible only via hopping mechanism.⁷¹

Various semiconducting oxides are studied as nanostructured electrodes, including zinc oxide, tin oxide, indium oxide, titanium dioxide, etc.^{44, 79-82} Varieties of methods are established for the preparation of such electrodes and they mostly depend on the final application of the electrode and the chemistry of the starting material.³³

The non-structured porous oxide electrodes can be simply obtained by deposition of the respective oxide nanoparticles, nanorods or nanosheets on the desired substrate. Structured oxide electrodes have been in the focus of extensive research activities in the last decade, and nowadays they can be prepared with a broad variety of morphologies such as nanotubes and mesoporous or macroporous materials.

Oxide nanotube arrays can be obtained by the anodization of metals.^{44, 81} Through this procedure various nanotubes can be obtained. The size of the opening of the tubes is controlled by the anodization potential and electrolyte composition whereas the length of the tubes is controlled by the anodization time. Figure 1.3.5. illustrates the possible morphologies of the nanostructured electrodes obtained by anodization.

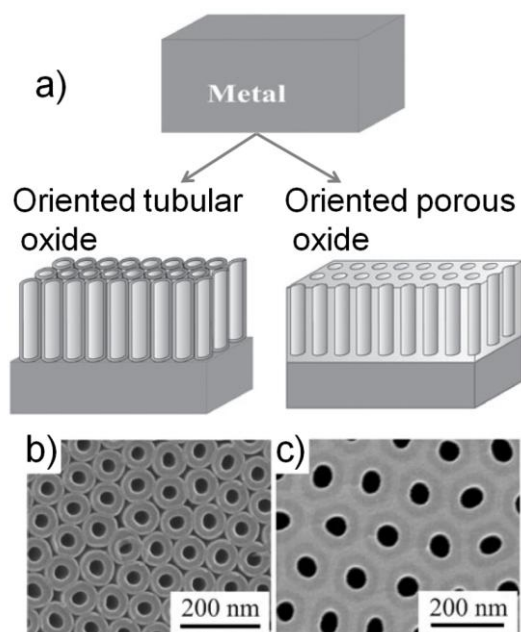


Figure 1.3.5. a) Illustration of the possible morphologies obtained by anodization, compared to the actual morphologies of TiO_2 in b) and c). Figure is adapted from reference [81].

Periodic macroporous electrodes can be obtained by using colloidal crystal templating, Figure 1.3.6.⁸³ The template is infiltrated or mixed with corresponding solutions of metal oxide precursors. Subsequent condensation of sols of metal oxide precursors and removal of template is performed through calcination procedures. The obtained macroporous oxide has an inverse opal like structure.

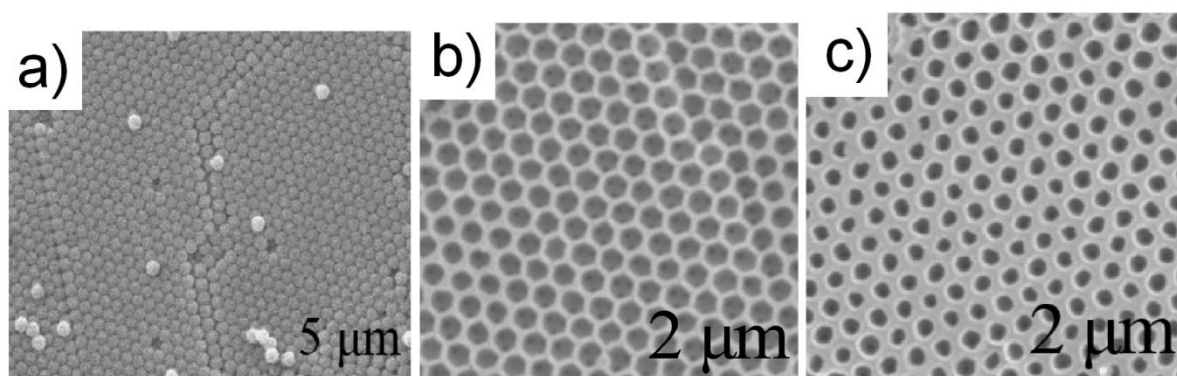


Figure 1.3.6. a) Opal structure of the polystyrene template and b) morphology of the SiO_2 and c) morphology of the TiO_2 macroporous oxides. Adapted from reference [83].

The macroporous layers and ordered nanotube arrays are very periodically organized, but the surface areas of the obtained electrodes are usually not large enough to provide high loadings

of electroactive guest molecules. Much higher surface areas can be obtained for mesoporous electrodes. Such electrode morphologies possess sufficiently high surface area and still a large enough pore size enabling incorporation of electroactive guests up to 10 nm in size,^{51, 71} which makes mesoporous electrodes promising host electrode materials.

1.3.3 Transparent Conducting Oxide Electrodes

In contrast to the other oxide electrodes the TCOs electrodes possess high electrical conductivity approaching that of metals, which makes them very popular electrodes in optoelectronic devices. Recent research demonstrates that the microscopic architectures of TCO electrodes can significantly influence and improve the properties of such devices.⁸⁴⁻⁹³ Patterning is one of the strategies to obtain a more complex morphology of the TCO electrodes. Electrodes can be patterned in several ways including etching, photon-, ion- and electron-beam lithography and nano-imprinting.^{33, 94} Kong et al. prepared patterned FTO electrodes by lithography and inductively coupled plasma etching. Such types of electrodes improved the efficiency of the dye sensitized solar cells by ca. 1 % compared to dye sensitized solar cells without patterned electrodes.⁸⁷

In addition to the patterned electrodes, fabrication of three-dimensional TCO architectures was a subject of intense research activity in the last years. In particular, significant efforts were made towards the fabrication of mesoporous films due to their large conducting interface area and due to their practical interest in a large variety of electrochemical, spectro-electrochemical and photo-electrochemical applications.^{48, 51, 93, 95, 96}

In 2006 Fattakhova-Rohlfing et al. demonstrated the potential of mesoporous ITO films as an efficient electrode system suitable for obtaining high loadings of the electro-active moieties inside of the electrode matrix, Figure 1.3.7.⁹⁵

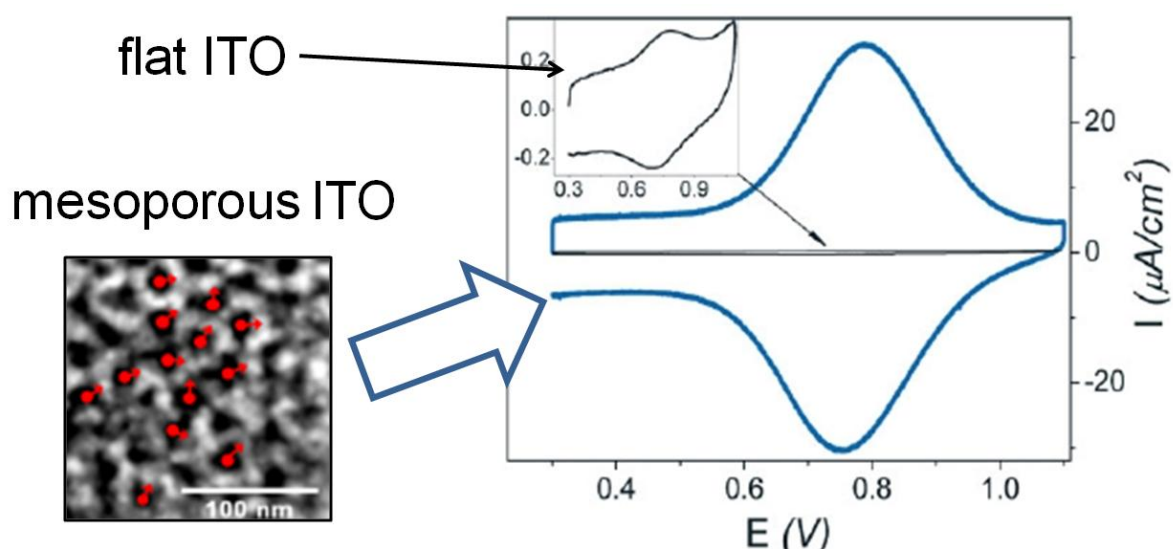


Figure 1.3.7. On the left: the morphology of mesoporous structured ITO film with illustration of incorporated electroactive molecules in the pores of ITO. On the right is shown the comparison of cyclic voltammetry data for flat ITO and mesoporous ITO. The significant increase in current for mesoporous ITO films is a result of high loadings of electro-active molecules on the high surface area. Adapted from reference [95].

Later on Fraska and Aksu showed the potential of the mesoporous ITO network as a platform for the incorporation of small biomolecules.^{51, 93}

In 2010 Hoertz et. Al. showed a simple preparation method of ITO films from ITO nanoparticles. The obtained films combine high surface area, optical transparency and good electrical conductivity.⁹⁷

Other TCO mesoporous systems with good conductivity were investigated for the application as nanostructured electrodes.^{48, 96} Hou and Wang reported on mesoporous antimony doped tin oxide films.^{22, 96} The potential of mesoporous ATO electrodes was demonstrated regarding their use as efficient electroluminescence biosensors.

Recently Yu et al. showed the influence of the three dimensional TCO electrode architecture on the efficiency in organic solar cells. The three dimensional electrode network, made from ITO branches, offers a large surface area which provides a higher electron collection and leads to an increased efficiency of the organic solar cells.⁸⁶

1.4 Mesoporous Films

Due to the favorable combination of sufficiently large pores together with a high surface area, mesoporous films provide a good host platform for the incorporation of a wide variety of molecules for nanostructured electrode applications.^{48, 95}

The method for preparation of mesostructured materials by self assembly of the organic surfactant and the inorganic species was first introduced by the studies of Mobile for mesoporous silica.⁹⁸ Later on this concept was extended for the fabrication of mesoporous films of various metal oxide systems.⁹⁹⁻¹⁰⁶

By definition the self assembly process is a spontaneous organization of materials through non covalent interactions such as electrostatic forces, hydrogen bonding or van der Waals forces.^{104, 107, 108} The self assembly usually employs asymmetric molecules, most commonly amphiphilic surfactant molecules or block co-polymers which contain hydrophobic and hydrophilic parts. In polar solvents such as aqueous solutions, the surfactants assemble into micelles, which form spherical or cylindrical structures in order to keep the hydrophilic parts in contact with the polar solvent. At the same time the surfactant shields the hydrophobic part inside of the micellar interior from the contact with water. By decreasing the amount of solvent the concentration of the surfactant increases, leading to the self-organization of the micelles into periodic hexagonal, cubic or lamellar mesophases, Figure 1.4.1

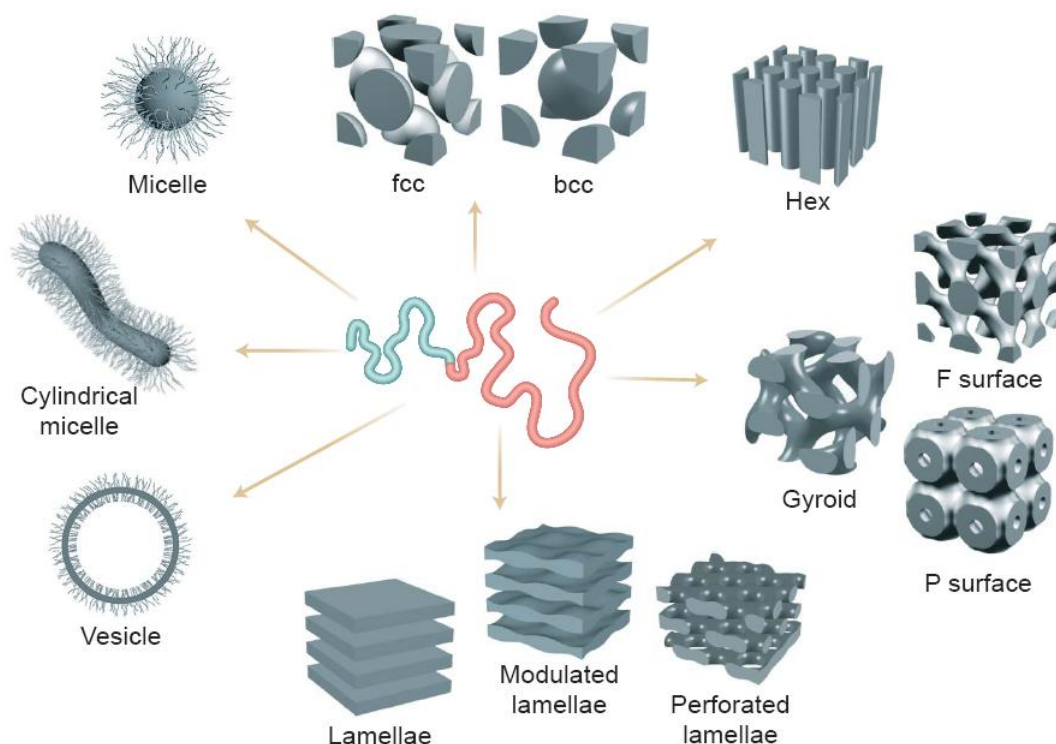


Figure 1.4.1. Various mesophases of block co-polymers. Adopted from reference [108].

The formed mesostructured material usually requires a condensation of the inorganic network while the template removal creates a periodic mesoporous solid.

The size of pores is defined by the size of the micelles and consequently by the size of the surfactant, i.e. template.^{104, 107} The first applied templates were low molecular weight surfactants in which the hydrophobic part consists of long chain alkanes while the hydrophilic head group can be either ionic or non-ionic. Considering that the pore size is mainly defined by the length of the hydrophobic chain, the pore size in the surfactant template materials is usually restricted to 2-5 nm as a result of the length of their chains. Larger pore sizes are obtainable with the use of block co-polymers as template molecules. The hydrophilic part of these amphiphilic polymers usually consists of poly(ethylene oxide) (PE), while the hydrophobic part can be either poly(propylene oxide) (PP), poly(ethylene-co-butylene) (KL), polystyrene (PS) or polybutadiene (PB).

The easiest way for the preparation of mesoporous films is through evaporation induced self assembly (EISA) of sol-gel metal oxide precursors assisted with amphiphilic structure

directing agents. Although this procedure was intensively studied and applied for various systems, the preparation of 3D structured electrodes through the EISA process for some types of oxides still remains a nontrivial task.⁴⁸ In the following chapter the evaporation induced self assembly process, as a method for the preparation of mesoporous thin films is presented.

1.4.1 Evaporation Induced Self Assembly

The preparation of the mesoporous films by evaporation induced self assembly (EISA) has its origin in Mobil's work on surfactant-templated materials.^{98, 105, 109} Different to the process described above, the concentration of the amphiphilic molecules in the EISA process is below the critical micelle concentration so that no micelles are initially present. The micelle formation and their self organization into a periodic structure is triggered by evaporation of the solvent which results in the increase of the concentration of the surfactant.¹⁰⁹ The advantage of this process is that the viscosity of the initial solutions is low, which enables solution deposition of thin homogeneous films using techniques for the solution deposition such as dip-, spin- and meniscus-coating. The EISA combines the surfactant assisted self assembly of either sol-gel precursors or pre-synthesized well defined nanobuilding blocks (NBBs), Figure 1.4.2.^{110, 111}

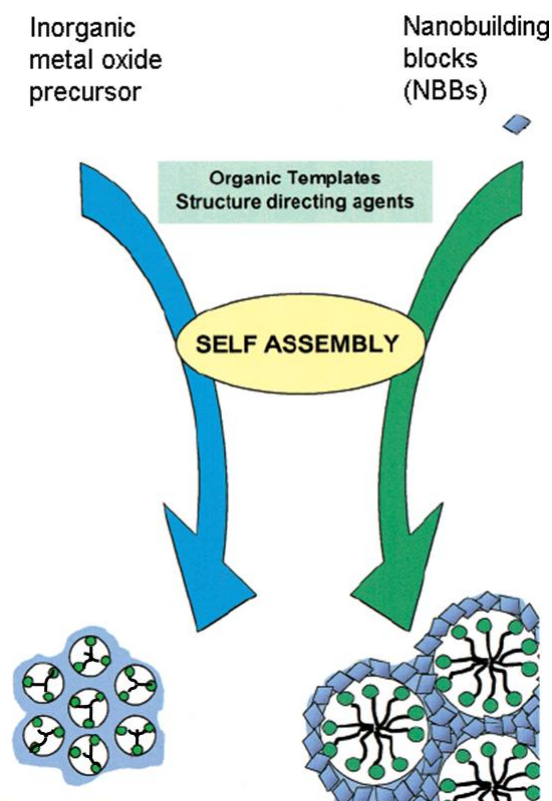


Figure 1.4.2. Illustration of two pathways for obtaining the mesoporous metal oxide structures. Adapted from reference [111].

The steps of the assembly process into periodically organized mesoporous materials (POMMs) were intensively studied by Grosso and Sanchez.¹⁰⁹⁻¹¹¹

For the formation of the micelle structure by organization of precursor/ NBBs together with the surfactant two main processes have been proposed. In the first mechanism, so called liquid crystal templating (LCT), the inorganic phase condenses around a stabilized surfactant phase. In the second mechanism, the cooperative self assembly (CSA), the surfactant molecules and the inorganic species first combine to form hybrid intermediate species which then behave as independent surfactant species, i.e. the building blocks of the mesostructure. However, in reality it is most likely that both mechanisms happen simultaneously considering that they depend on both chemical and processing parameters for a given system.^{109, 111} A schematic representation of the mesostructuring during the dip coating procedure is given in the Figure 1.4.3.

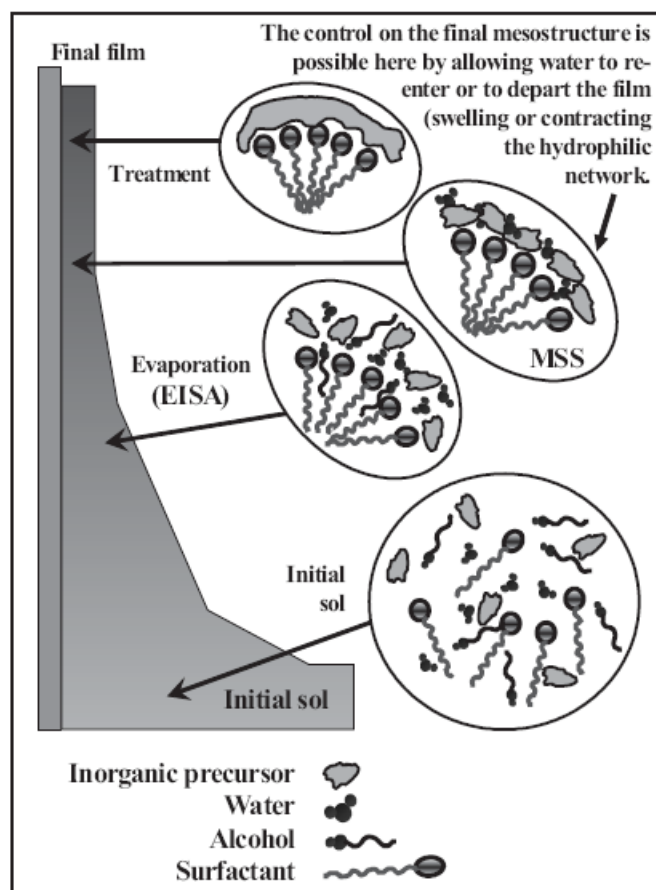


Figure 1.4.3. Illustration of the mesostructuring during the dip-coating procedure in ethanol solution inorganic precursor, surfactant (template) and some amount of water. The process of mesostructuring can be divided into four parts. The first part presents the initial solution where critical micelle concentration is not yet achieved due to the high concentration of solvent. The second part presents evaporation of solvent during the deposition procedure of the films. In this step assembly of template is happening due to the reached critical micelle concentration through evaporation of solvent. The third step occurs after the solvent is mostly evaporated and involves further equilibration of the mesostructure in the presence of some remaining water molecules. The fourth step involves the condensation of the inorganic network. Adapted from reference [109].

For the preparation of reproducible mesoporous organized thin films three main parameters are important: 1) the nature and chemistry associated with the coating solution, 2) the process of the layer deposition, 3) the final post synthetic treatment of the film with the purpose to eliminate the organic phase and to sinter the oxide network. A more detailed consideration of those parameters is given below.^{105, 109, 112}

1 The Nature and Chemistry of the Coating Solution

The initial solution used for deposition must be homogeneous in concentration. It is essential that the solution perfectly wets the substrate during the deposition. It is desirable that the solution contains a solvent (typically ethanol) which is more volatile than water. Usually these

are controlled sol-gel solutions in which hydrolysis and condensation steps of the inorganic precursors are adjusted by selecting appropriate components and their relative quantities. Typically those are solutions of metal oxide precursors, such as metal alkoxides or metal halides, and templates which can be surfactants or block co-polymers in volatile solvents such as ethanol or tetrahydrofuran. Addition of a small amount of volatile acids, such as HCl can catalyse the hydrolysis or control the dispersibility of the nanoparticles. In order to obtain the periodic mesostructure, the amount of the organic template and the inorganic precursor or nano building blocks must be in the appropriate ratio. This applies also to the other components such as water content, pH, dilution, etc. The template concentration in such solutions is below the critical micelle concentration (CMC) and the self organization does not occur in this step.

2 The Deposition Process

This step is related to the processing conditions and the self assembly process. The driving force in this step is the phase segregation, the self assembly and the condensation of the metal oxide precursor which is in total a result of the evaporation of the solvent. During the deposition of the initial layer, for example through dip coating, the evaporation of the volatile components takes place at the air-film interface. The evaporation leads to a rapid enrichment of the films with metal oxide precursors and template molecules. At the point when the surfactant reaches the critical micelle concentration of the system, the micelles start to form by hydrophobic segregation of their alkyl chains. This state is critical for the formation of the mesostructure and can be tuned by varying the relative humidity (e.g. 20-70 %) inside the dipping chamber. This specific humidity (water) at the air/film interface influences the final organization which can lead to the formation of different mesophases (from one-dimensional up to three-dimensional) for the same surfactant depending on the applied parameters.

3 The Post-Deposition Treatment

The aim of this step is to stabilize the inorganic framework through a post deposition treatment, either by further condensation or by sintering of the inorganic network to eliminate the template in order to form the porous sample. This is usually performed by thermal treatment of the sample which leads to the decomposition of the organic phase accompanied by contraction of the porous domains perpendicular to the surface plane of the film. In this step it is possible to combine a mild temperature treatment with the other techniques for template removal such as degradation of organic material by plasma decomposition, solvent extraction or treatment with base.

1.4.2 Nanobuilding Blocks (NBBs) for EISA Process

One of the limitations of the EISA process is the difficulty to control the crystallinity of the obtained mesoporous framework. In some cases where the crystallinity of the framework is not the issue, especially in the case of silica, the EISA process using the standard sol-gel procedure is applicable. On the other hand, in the case of many oxides the crystallinity of the three dimensional mesoporous framework is required. This transformation of the mesostructured framework from amorphous into crystalline is usually performed at elevated temperatures which can lead to the collapse of the mesostructure. Some modifications of the EISA process are usually required to obtain crystalline mesoporous films.^{109, 110} Some of the strategies which use a direct assembly of pre-synthesized well-defined nanobuilding blocks (NBBs) that preserve their integrity during the assembly instead of molecular or amorphous precursors. The prerequisite for these NBBs is that they should be at least four times smaller than the micelles in order to be able to adopt the curvature (2-30 nm in size) of the organic template interface.^{107, 111} The variety of possible NBBs offers a wide range for the creation of numerous different architectures. Small clusters (metallic oxoclusters, Zintl phase, etc.),

inorganic nanoparticles (metal oxides, metals, chalcogenides, etc.) and core-shells nanoparticles can be used as NBBs. The advantages in using NBBs for building the mesostructure are as follows:

- Through this method is possible to define precisely the inorganic component and to minimize the collapse problems which might occur with the removal of the template and crystallization of the framework.
- NBBs possess a lower hydrolytic reactivity than molecular precursors. Due to that, the chemistry, self assembly and processing parameters can be decoupled.

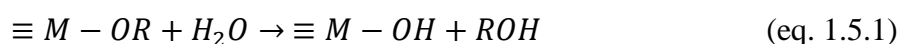
1.5 Synthesis of Metal Oxide Nanoparticles as NBBs

The elaboration of metal oxide nanoparticles was studied very intensively due to their practical and fundamental importance, and a vast number of approaches based on physical as well as chemical methods does already exist.^{4, 33, 113} In this chapter, only the approaches enabling the fabrication of non-agglomerated dispersible nanoparticles will be shortly described.

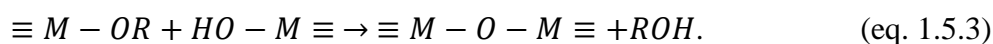
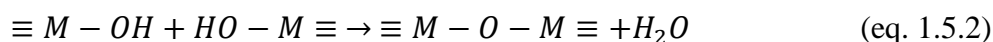
The physical methods, such as pyrolysis or ball milling, are mostly not suitable for the preparation of this kind of nanoparticles, as they do not offer the control over size and morphology. On the other hand, the synthesis of monodispersed nanoparticles can be challenging. From this point of view, soft chemistry routes are usually more suitable for the preparation of the monodispersed colloidal solution of nanoparticles. This is due to the better control of the reaction course and offers the possibility for the better stabilization of the nanoparticles in the solution.¹¹⁴⁻¹¹⁷ Besides, they also offer products of high purity with a good homogeneity at low processing temperatures. One of long known and traditionally successful methods for the preparation of bulk metal oxides is sol-gel chemistry^{118, 119} which was more recently adapted for the preparation of nanoscale metal oxides.

1.5.1 Sol-Gel Synthesis of Metal Oxide Particles

The sol-gel process can be described as the conversion of a molecular metal precursor into metal oxide by chemical reactions.¹¹⁸⁻¹²⁰ Usually the metal oxide precursors are inorganic metal salts such as acetates, chlorides, nitrates, sulphates, or organic species like metal alkoxides. The latter are commonly used in aqueous sol-gel synthesis. The processes which occur during the formation of metal oxide particles in sol-gel synthesis can be described as follows. In the first step of the synthesis the metal alkoxide is transferred into a sol, which can be presented as a dispersion of colloidal particles in a liquid. This sol is transferred into a gel through condensation, forming an interconnected porous inorganic framework filled with the liquid phase. This process consists of two reaction parts: hydrolysis and condensation.^{119, 120} Hydrolysis can be described as:



whereas the condensation can be presented as:



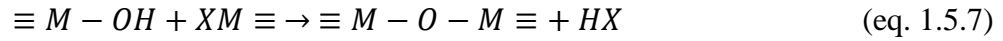
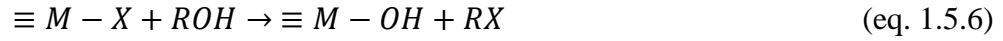
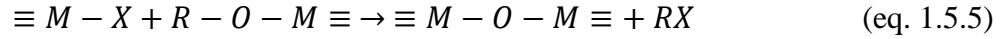
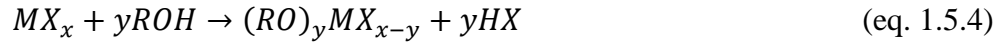
In the hydrolysis reaction the metal alkoxide groups ($-OR$) change into hydroxide groups ($-OH$) through a nucleophilic attack of the hydroxide ions water with a simultaneous release of alcohol. In condensation reactions the formation of the $M - O - M$ bond is achieved either by condensation of two hydroxylated metal species together with the release of water or through reaction of the metal alkoxide and the metal hydroxide under release of alcohol. Considering that these two reactions happen simultaneously, they lead to a wide variety of different species. Therefore this reaction is not fully controllable. However, the advantage of the aqueous sol-gel process is the fact that the sol or gel can be transferred into desired forms, such as fibers, films or powders or even ceramic materials by subsequent heating.¹²⁰ Still, a

better control of the particle size, doping level, and particle dispersibility in different solvents remains an issue.

1.5.2 Non Aqueous Sol-Gel Synthesis of Metal Oxide Nanoparticles

The major problem of the aqueous sol-gel synthesis lies in the hydrolysis and condensation steps which are very fast for most of the metal oxide precursors and thus result in a loss of morphological and structural control over the final oxide material. This problem can be avoided through nonhydrolytic or nonaqueous sol-gel chemistry. In such reactions the oxygen is provided from organic molecules such as ethers, alcohols or alkoxides. This leads as a result to a completely changed chemistry due to the different reactivity of the oxygen-carbon bond.^{120, 121} Intensive studies on non aqueous sol-gel synthesis of metal oxide nanoparticles were performed in the group of Prof. Niederberger.^{114, 120, 122-125} In comparison to the aqueous sol-gel synthesis, where even smallest changes in experimental conditions can result in a large variety of products, the reaction in non aqueous solvents is rate-limiting and is usually much slower than that with water. This type of synthesis can be performed with various metal oxide precursors and organic solvents.¹²⁶⁻¹³² One of the most promising solvents in this type of synthesis is benzyl alcohol due to its non-toxicity, high boiling point and special reactivity caused by the stabilization of the intermediate states by the aromatic ring.¹¹⁴ Benzyl alcohol plays a special role in the non-aqueous sol-gel synthesis due to the fact that it can react with many metal oxide precursors such as metal alkoxides, halides, acetylacetonates or acetates providing a wide variety of metal oxide nanoparticles and oxide based nanostructures.^{123, 133-135} The benzyl alcohol serves both as a solvent and as an oxide source and the reaction can be performed at mild temperatures between 40 °C and 200 °C. The size of the obtained metal oxide nanoparticles can vary from 2 to 10 nm depending on the applied temperature. Due to the low cost and broad availability the first systematic investigation of the nonaqueous

synthesis was performed on metal halides with benzyl alcohol. The steps of the reactions can be presented as:¹²⁰



The steps of the metal oxide synthesis involve the formation of metal alkoxides through alcoholysis (eq. 1.4.4) and condensation between metal alkoxide and metal halide (eq. 1.4.5) under release of an alkyl halide. The second type of reaction which is happening simultaneously is the elimination of alkyl halides through the reaction of metal halides with benzyl alcohol (eq. 1.4.6) accompanied by subsequent condensation of hydroxylated species according to the equation 1.4.7.

This type of reaction provides highly crystalline and pure metal oxide nanoparticles. It was found that these nanoparticles are useful NBBs for the preparation of mesostructured films through the modified EISA procedure.^{48, 125}

1.6 Incorporation of Electro-Active Molecules into Mesoporous Oxide Frameworks

The 3D porous electrode architectures offer a good host platform for the incorporation of electro-active molecules. One of the main advantages of such system is a large conductivity interface, which provides a direct communication with the electrode and at the same time a high loading of the electro-active molecules. Additionally, the surface modification of the pore interior enables one to tune the chemical surrounding of the incorporated molecules changing their stability and reactivity, or to covalently bind the electro-active molecules to prevent their leaching and desorption from the electrode surface.

The pore size of the mesoporous framework puts certain limitations on the size of electro-active molecules. Typically, mesoporous materials are suitable for incorporation of simple molecules up to smaller proteins with a size of ca. 5 nm.

The choice of the electro-active species and the way of their immobilization are determined by final application of the electrodes. A variety of devices such as electroluminescence- or, bio-sensors require a stable incorporation of either expensive or sensitive electro-active moieties. There are several ways to incorporate the electro-active molecules. One of the simplest ways for the incorporation is adsorption of electro-active guests on the surface of the porous framework. This type of anchorage can be governed by the electrostatic interactions between the electro-active molecules and the oppositely charged mesoporous oxide surface. Usually this type of interaction can be achieved if the electro-active molecules are either acid- or aminogroup-bearing compounds carrying negative or positive charge, respectively, depending on the pH.

When the affinity between the electrode surface and guest species is too weak or the specifically substituted electro-active molecules are not available, the surface of the mesoporous electrodes can be functionalized with molecules which later on serve as covalent linkers to the electroactive species. This type of attachment provides a good and a stable connection of the guest molecules preventing their leaching. There are several types of such grafting approaches which can be used for the covalent attachment of the molecules such as click chemistry, maleimide reaction or the commonly used amide bonding. In the present work two types of surface functionalization were investigated namely surface functionalization with organotrialkoxysilanes and with Grignard reagents. The surface functionalized with organotrialkoxysilanes was further used for the anchorage of the various molecules via amide bond formation. Therefore, in the following chapters these two types of surface functionalization and possible ways of incorporation of electroactive molecules are presented.

1.6.1 Surface Functionalization with Organotrialkoxysilanes

For the covalent attachment of the electro-active species the first step of the grafting i.e. surface functionalization with the linker molecules is an important task for obtaining the high surface coverage.^{77, 136}

Organotrialkoxysilanes are one of the most common binding linkers for the guest species used in the first step of the surface functionalization. Most of the surface functionalization reactions with organotrialkoxysilanes were studied on mesoporous silica materials and later implemented for the other types of oxides.^{48, 77, 96, 137-139}

Reaction with the organotrialkoxysilanes requires the presence of free hydroxylic groups on the surface of the oxide. These groups interact with alkoxysilanes via condensation under formation of an oxo bridge. The organotrialkoxysilanes usually bear some functional groups that can be used in the second step of the grafting of desired molecules. The most common functional groups in organotrialkoxysilanes are chlorides, mercapto groups or amines.¹³⁸ For example, surface functionalization can be achieved with organotrialkoxysilanes such as γ -aminopropyltriethoxysilane (APTES). The reason for this is the free terminal amino group which offers an anchoring site for the covalent attachment via peptide bond formation with molecules bearing carboxylic groups. The surface modification with APTES is based on a three step reaction of the free hydroxylic groups from the surface with APTES molecules according to the Figure 1.6.1.

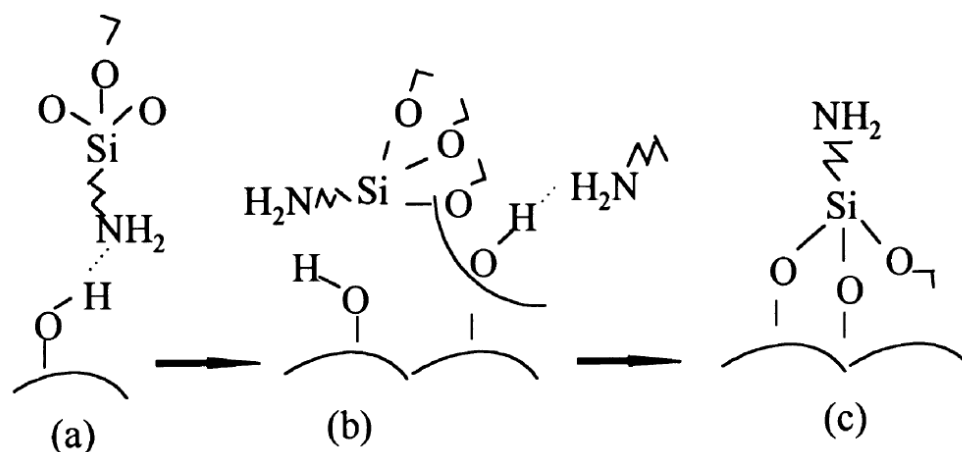


Figure 1.6.1. The proposed flip mechanism of the APTES reaction with surface hydroxylic groups in dry conditions, **a)** physisorption, **b)** condensation, **c)** obtained structure. Adapted from reference [138].

In the reaction mechanism proposed by Impens,¹³⁸ the amine group from APTES forms a hydrogen bond with a surface hydroxyl group. This hydrogen bonded molecule self-catalyses the condensation of the second APTES molecule with the surface, resulting in a covalent siloxane bond. The terminal amino group can be further on used for the next step of the attachment of various small molecules and proteins.^{76, 77, 95}

1.6.2 Surface Functionalization with Grignard Reagents

Another possible way which results in surface functionalization can be performed through the direct attachment of carbon atoms from an organic compound to the metal atom on the surface of metal oxide via metal organic modification through Grignard reactions. Such type of bonding is of special interest for applications involving charge transfer between the metal atom and the attached group. Attachment of various functional or conjugated groups to the surface of nanostructured electrode provides the possibility to use these groups both as covalent linker (in the second step of the anchorage of electroactive molecules) and as a conductive chain between the oxide surface and functional electroactive moieties. The use of Grignard reactions can provide an advantage over surface functionalization with organotrialkoxysilanes because this type of reaction excludes the pore blocking by condensed

oligomeric silane species. Additionally, various Grignard reagents can be either purchased or easily prepared in the laboratory from the respective halogenic compounds. The surface functionalization with Grignard reagents was studied separately by Yamamoto and our group.¹⁴⁰⁻¹⁴⁴ Surface functionalization via Grignard reactions was up to now performed on various materials, such as mesoporous silica,¹⁴⁰⁻¹⁴² on Au and Ge nanoparticles,^{145, 146} amorphous carbon substrates,¹⁴⁷ or semiconductor surfaces.^{148, 149}

The reaction mechanism of the Grignard reaction with silica can be explained by the scheme proposed by Lim.¹⁵⁰ The formation of the Si-C bond is obtained by direct attachment of the nucleophile to the silicon atom from the mesoporous silica according to the Figure 1.6.2.

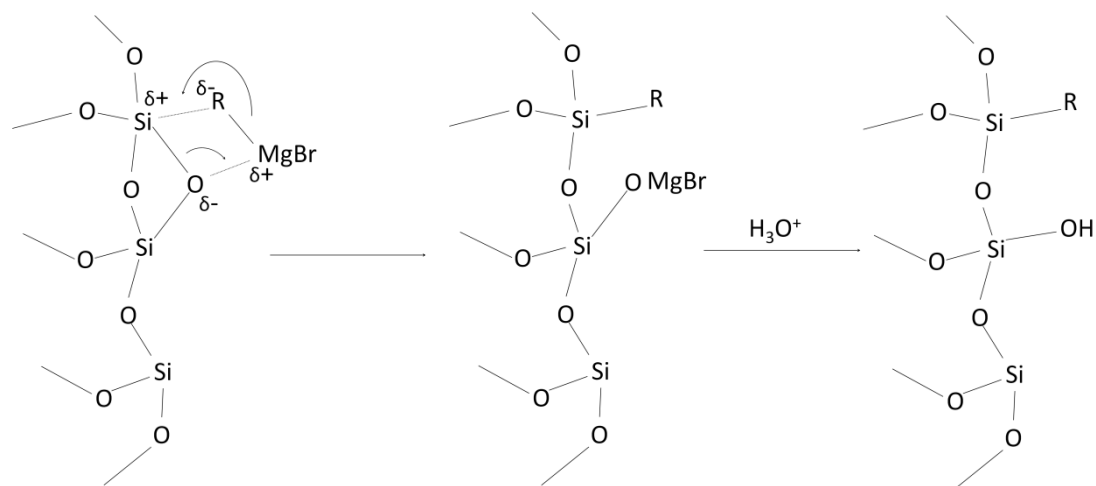


Figure 1.6.2. Proposed reaction mechanism of the Grignard reagent with silica.

During the reaction of the Grignard reagents, typically presented as R-MgBr (or R-MgX), with the surface of silica, the magnesium atoms form a complex with the bridging oxygen from the SiO₂ surface and increases the electrophilicity of the silicon atom on the surface. Simultaneously, the organic part of the Grignard reagent (R) acts as a nucleophile. An addition of the nucleophile (organic part of the Grignard reagent) to the silicon atom builds a starting product of the Grignard reaction. Hydrolysis of the Mg-O bond gives a final product, i.e. hydroxyl group, while the organic part R is attached to the neighboring silicon atom.

1.6.3 Attachment of Electroactive Moieties

Various electrochemical devices such as biosensors or redox protein based arrays require incorporation of electro-active species into the electrode. The incorporation of electro-active molecules into structured materials can be performed either by adsorption or by covalent binding to the inner surface of the porous electrodes. Covalent attachment usually provides better binding stability of guest molecules and decreases the vulnerability to the influence of the environment.

In the present work the incorporation of electro-active groups into the mesoporous network was studied through both methods, i.e. adsorption and covalent attachment through amide bond formation with the APTES functionalized surface. For the later, the guest molecules have to possess a carboxylic group. The carboxylic group reacts with the amino group from APTES using N-(3-Dimethylaminopropyl)-N'-ethylcarbodiimide (EDC) or N,N'-dicyclohexylcarbodiimide (DCC) as activating agents for the formation of the amide bond, Fig. 1.6.3.

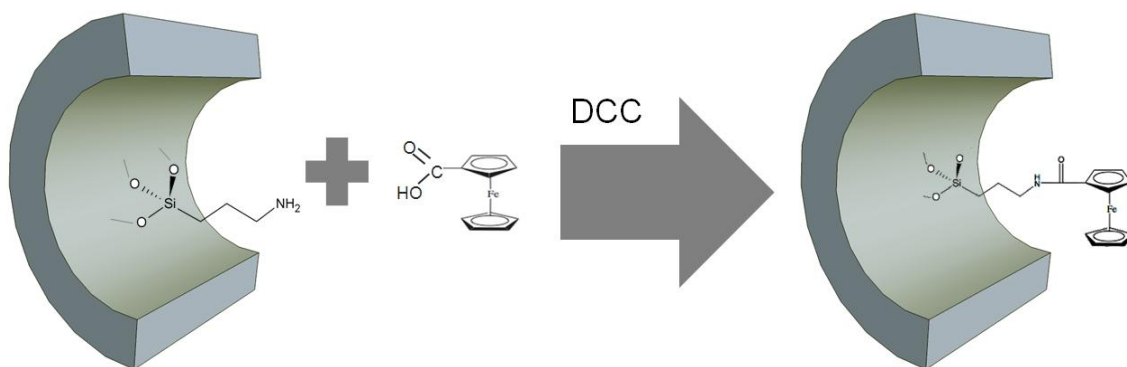


Figure 1.6.3. Illustration of the attachment of ferrocene molecule onto the surface of the pore through amide bond formation.

Based on the same principle, the other types of molecules, such as ruthenium dyes were covalently attached into the mesoporous structure.⁹⁶

1.6.4 Incorporation of the Metalloprotein Cytochrome C

In comparison to small molecules, the stable incorporation of proteins into a mesoporous network does not necessarily need to be performed through covalent attachment, although it was shown to be beneficial for the prevention of leaching. The incorporation of small proteins into the mesoporous network can be performed through adsorption of proteins due to electrostatic interaction.

One of the most studied metalloproteins for these purposes is cytochrome c. Cytochrome c is a small, nearly spherical, heme protein with the size of $2.6 \times 3.2 \times 3.0 \text{ nm}^3$ and has a molecular weight of 12,400 Da.⁵⁰ Cytochrome c consists of a single polypeptide chain containing 104 amino acids covalently attached to the heme group, Figure 1.6.4.^{151, 152}

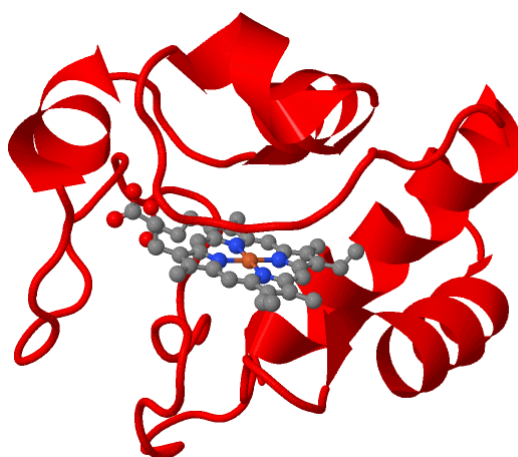


Figure 1.6.4. The structure of the cytochrome c. The picture is adopted from the Protein Data Bank according to the solved crystallographic structure according to reference [152].

The active centre of cytochrome c is the heme which has a porphyrin ring, where four pyrrole nitrogen atoms are coordinated to a central Fe atom forming a square planar complex. The iron in the heme centre can switch between the ferric (Fe^{3+}) and the ferrous (Fe^{2+}) state and as a consequence acts as an electron carrier. The heme centre is tightly packed inside of the hydrophobic side chains of the polypeptide chain framework, whereas hydrophilic side groups

are positioned on the outer surface of the protein. The axial ligands of the iron in the heme centre are histidine 18 and methionine 80 from the polypeptide chain.¹⁵³ One edge of the central heme is exposed to the surface. The lysine residues which contain cationic side chains are positioned at the surface of the molecule, whereas some of them surround the opening of the heme.

At neutral pH cytochrome c is positively charged as a result of the fact that its isoelectric point (IEP) is settled at pH 10. This means that the amino groups of lysine's amino acids, which surround the redox centre and thus play an important role in the electron transfer, are positively charged at neutral pH.

Cytochrome c is a very stable and robust protein and due to this fact it was chosen as a model molecule for the numerous studies of the incorporation of proteins in various systems.

It was shown that the incorporation of cytochrome c into porous networks can be performed by adsorption and by covalent attachment, Figure 1.6.5. The adsorption of the cytochrome c on the negatively charged oxide surfaces is governed by Coulomb interactions. Topoglidis and Willit showed that the surface of various oxides is negatively charged and cytochrome c can be adsorbed on it.^{90, 154-156}

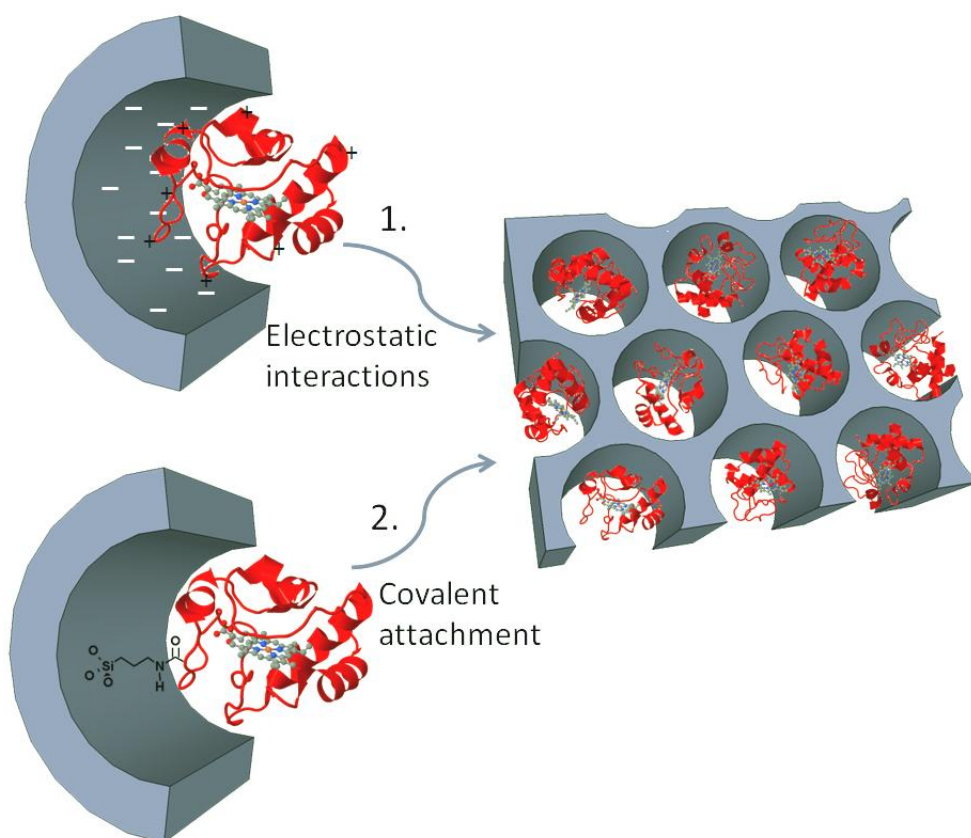


Figure 1.6.5. Possible ways of incorporation of cytochrome c into mesoporous oxides. The pathway 1. presents the incorporation through electrostatic interactions between the positively charged protein and negatively charged oxide surface, whereas the pathway 2 presents covalent immobilization.

Although this type of immobilization was shown to be easy and efficient, it cannot prevent the leaching of protein molecules in the presence of high ionic strength solutions. For example, it was shown before that the adsorption and desorption of the cytochrome c can be influenced by the ionic strength of solutions.^{59, 157, 158}

The electrochemistry of cytochrome c was studied on various types of electrodes such as carbon,^{49, 67} zeolites,^{157, 159} tin oxide,^{90, 156} mesoporous silica,⁷⁸ titanium dioxide^{154, 160} or gold electrodes.¹⁶¹ The obtained results show that the direct electron transfer between the electrode and cytochrome c can be demonstrated. This offers the possibility to use this protein in the bio-sensor applications.^{51, 93}

1.7 References

1. Chopra, K. L.; Major, S.; Pandya, D. K., *Thin Solid Films* **1983**, 102, 1.
2. Minami, T., *Semicond. Sci. Technol.* **2005**, 20, S35.
3. Exarhos, G. J.; Zhou, X.-D., *Thin Solid Films* **2007**, 515, 7025.
4. West, A. R., *Solid State Chemistry and its Applications*. John Wiley & Sons: Chichester, 1998.
5. Robertson, J., *Thin Solid Films* **2008**, 516, 1419.
6. Zunger, A., *Appl. Phys. Lett.* **2003**, 83, 57.
7. Edwards, P. P.; Porch, A.; Jones, M. O.; Morgan, D. V.; Perks, R. M., *Dalton Trans.* **2004**, 2995.
8. Sato, H.; Minami, T.; Takata, S.; Yamada, T., *Thin Solid Films* **1993**, 236, 27.
9. Gordon, R. G., *MRS Bull.* **2000**, 25, 52.
10. Minami, T., *Thin Solid Films* **2008**, 516, 1314.
11. Kurz, A.; Brakecha, K.; Puetz, J.; Aegerter, M. A., *Thin Solid Films* **2006**, 502, 212.
12. Granqvist, C. G., *Sol. Energy Mater. Sol. Cells* **2007**, 91, 1529.
13. Bach, U.; Lupo, D.; Comte, P.; Moser, J. E.; Weissortel, F.; Salbeck, J.; Spreitzer, H.; Gratzel, M., *Nature* **1998**, 395, 583.
14. Grätzel, M., *J. Photochem. Photobiol. C: Photochem. Rev.* **2003**, 4, 145.
15. Gather, M. C.; Köhnen, A.; Meerholz, K., *Adv. Mater.* **2011**, 23, 233.
16. Batzill, M.; Diebold, U., *Progr. Surf. Sci.* **2005**, 79, 47.
17. Popescu, D. A.; Herrmann, J.-M.; Ensueque, A.; Bozon-Verduraz, F., *Phys. Chem. Chem. Phys.* **2001**, 3, 2522.
18. Fang, Z.; Assaaoudi, H.; Lin, H.; Wang, X.; Butler, I.; Kozinski, J., *J. Nanoparticle Res.* **2007**, 9, 683.

19. Pan, J. H.; Chai, S. Y.; Lee, C.; Park, S.-E.; Lee, W. I., *J. Phys. Chem. C* **2007**, 111, 5582.
20. Tseng, S.-F.; Hsiao, W.-T.; Chiang, D.; Huang, K.-C.; Chou, C.-P., *App. Surf. Sci.* **2011**, 257, 7204.
21. Guglielmi, M.; Menegazzo, E.; Paolizzi, M.; Gasparro, G.; Ganz, D.; Pütz, J.; Aegerter, M. A.; Hubert-Pfalzgraf, L.; Pascual, C.; Durán, A.; Willems, H. X.; Van Bommel, M.; Büttgenbach, L.; Costa, L., *J. Sol-Gel Sci. Technol.* **1998**, 13, 679.
22. Wang, Y.; Brezesinski, T.; Antonietti, M.; Smarsly, B., *ACS Nano* **2009**, 3, 1373.
23. Nutz, T.; Haase, M., *J. Phys. Chem. B* **2000**, 104, 8430.
24. Nutz, T.; zum Felde, U.; Haase, M., *J. Chem. Phys.* **1999**, 110, 12142.
25. Zhou, J. X.; Zhang, M. S.; Hong, J. M.; Yin, Z., *Solid State Commun.* **2006**, 138, 242.
26. Rumyantseva, M. N.; Gaskov, A. M.; Rosman, N.; Pagnier, T.; Morante, J. R., *Chem. Mater.* **2005**, 17, 893.
27. Abello, L.; Bochu, B.; Gaskov, A.; Koudryavtseva, S.; Lucazeau, G.; Roumyantseva, M., *J. Solid State Chem.* **1998**, 135, 78.
28. Acciarri, M.; Canevali, C.; Mari, C. M.; Mattoni, M.; Ruffo, R.; Scotti, R.; Morazzoni, F.; Barreca, D.; Armelao, L.; Tondello, E.; Bontempi, E.; Depero, L. E., *Chem. Mater.* **2003**, 15, 2646.
29. Geraldo, V.; Scalvi, L. V. A.; Lisboa-Filho, P. N.; Morilla-Santos, C., *J. Phys. Chem. Solids* **2006**, 67, 1410.
30. Grzeta, B.; Tkalcec, E.; Goebbert, C.; Takeda, M.; Takahashi, M.; Nomura, K.; Jaksic, M., *J. Phys. Chem. Solids* **2002**, 63, 765.
31. Müller, V.; Rasp, M.; Štefanić, G.; Ba, J.; Günther, S.; Rathousky, J.; Niederberger, M.; Fattakhova-Rohlfing, D., *Chem. Mater.* **2009**, 21, 5229.
32. Goebbert, C.; Aegerter, M. A.; Burgard, D.; Nass, R.; Schmidt, H., *J. Mater. Chem.* **1999**, 9, 253.

33. Cao, G., *Nanostructures & Nanomaterials; Synthesis, Properties & Applications*. Imperial College Press, London: London, 2004.
34. Terrier, C.; Chatelon, J. P.; Berjoan, R.; Roger, J. A., *Thin Solid Films* **1995**, 263, 37.
35. Terrier, C.; Chatelon, J. P.; Roger, J. A.; Berjoan, R.; Dubois, C., *J. Sol-Gel Sci. Technol.* **1997**, 10, 75.
36. Jeon, H. J.; Jeon, M. K.; Kang, M.; Lee, S. G.; Lee, Y. L.; Hong, Y. K.; Choi, B. H., *Mater. Lett.* **2005**, 59, 1801.
37. Jiang, S. P., *Mater. Sci. and Eng. A* **2006**, 418, 199.
38. Guldi, D. M.; Prato, M., *Chem. Commun.* **2004**, 40, 2517.
39. Wallace, G. G.; Chen, J.; Mozer, A. J.; Forsyth, M.; MacFarlane, D. R.; Wang, C., *Materials Today* **2009**, 12, 20.
40. Liu, D.; Cao, G., *Energy Environ. Sci.* **2010**, 3, 1218.
41. Centi, G.; Perathoner, S., *Catal. Today* **2010**, 150, 151.
42. Bruce, P. G.; Scrosati, B.; Tarascon, J.-M., *Angew. Chem. Int. Ed.* **2008**, 47, 2930.
43. Brezesinski, T.; Wang, J.; Tolbert, S. H.; Dunn, B., *Nature Materials* **2010**, 9, 146.
44. Roy, P.; Berger, S.; Schmuki, P., *Angew. Chem. Int. Ed.* **2011**, 50, 2904.
45. Paramasivam, I.; Nah, Y.-C.; Das, C.; Shrestha, N. K.; Schmuki, P., *Chem. A Eur. J.* **2010**, 16, 8993.
46. Lang, X.; Hirata, A.; Fujita, T.; Chen, M., *Nature Nanotech.* **2011**, 6, 232.
47. Sing, K. S. W.; Everett, D. H.; Haul, R. A. W.; Moscou, L.; Pierotti, R. A.; Rouquerol, J.; Siemieniewska, T., *Pure and Applied Chemistry* **1985**, 57, 603.
48. Müller, V.; Rasp, M.; Rathouský, J.; Schütz, B.; Niederberger, M.; Fattakhova-Rohlfing, D., *Small* **2010**, 6, 633.
49. Zhang, L., *Biosens. Bioelectr.* **2008**, 23, 1610.
50. Hartmann, M., *Chem. Mater.* **2005**, 17, 4577.

51. Aksu, Y.; Frasca, S.; Wollenberger, U.; Driess, M.; Thomas, A., *Chem. Mater.* **2011**, 23, 1798.
52. Kloke, A.; von Stetten, F.; Zengerle, R.; Kerzenmacher, S., *Adv. Mater.* **2011**, 23, 4976.
53. Zhang, H.; Yu, X.; Braun, P. V., *Nature Nanotech.* **2011**, 6, 277.
54. Yu, X.; Lee, Y. J.; Furstenberg, R.; White, J. O.; Braun, P. V., *Adv. Mater.* **2007**, 19, 1689.
55. Szamocki, R.; Reculosa, S.; Ravaine, S.; Bartlett, P. N.; Kuhn, A.; Hempelmann, R., *Angew. Chem. Int. Ed.* **2006**, 45, 1317.
56. Szamocki, R.; Masse, P.; Ravaine, S.; Ravaine, V.; Hempelmann, R.; Kuhn, A., *J. Mater. Chem.* **2009**, 19, 409.
57. Wang, D.; Jakobson, H. P.; Kou, R.; Tang, J.; Fineman, R. Z.; Yu, D.; Lu, Y., *Chem. Mater.* **2006**, 18, 4231.
58. Liu, H.; Tian, Y.; Deng, Z., *Langmuir* **2007**, 23, 9487.
59. Avila, A.; Gregory, B. W.; Niki, K.; Cotton, T. M., *J. Phys. Chem. B* **2000**, 104, 2759.
60. Zhu, A.; Tian, Y.; Liu, H.; Luo, Y., *Biomater.* **2009**, 30, 3183.
61. Schuster, J. r.; Köhn, R.; Keilbach, A.; Döblinger, M.; Amenitsch, H.; Bein, T., *Chem. Mater.* **2009**, 21, 5754.
62. Lei, Z.; Zhang, Y.; Wang, H.; Ke, Y.; Li, J.; Li, F.; Xing, J., *J. Mater. Chem.* **2001**, 11, 1975.
63. Liang, C.; Li, Z.; Dai, S., *Angew. Chem. Int. Ed.* **2008**, 47, 3696.
64. Alwarappan, S.; Joshi, R. K.; Ram, M. K.; Kumar, A., *App. Phys. Lett.* **2010**, 96, 263702.
65. Ju, H.; Liu, S.; Ge, B.; Lisdat, F.; Scheller, F. W., *Electroanal.* **2002**, 14, 141.
66. Wang, J.; Li, M.; Shi, Z.; Li, N.; Gu, Z., *Anal. Chem.* **2002**, 74, 1993.

67. Yin, Y.; Wu, P.; Lü, Y.; Du, P.; Shi, Y.; Cai, C., *J. Solid State Electrochem.* **2007**, 11, 390.
68. Keilbach, A.; Döblinger, M.; Köhn, R.; Amenitsch, H.; Bein, T., *Chem. A Eur. J.* **2009**, 15, 6645.
69. Chae, W.-S.; Braun, P. V., *Chem. Mater.* **2007**, 19, 5593.
70. Walcarius, A.; Kuhn, A., *TrAC Trends Anal. Chem.* **2008**, 27, 593.
71. Fattakhova Rohlffing, D.; Rathouský, J.; Rohlffing, Y.; Bartels, O.; Wark, M., *Langmuir* **2005**, 21, 11320.
72. Cademartiri, R.; Brook, M. A.; Pelton, R.; Brennan, J. D., *J. Mater. Chem.* **2009**, 19, 1583.
73. Newalkar, B. L.; Komarneni, S., *Chem. Mater.* **2001**, 13, 4573.
74. Guo, L.; Fan, Y.; Arafune, H.; Teramae, N., *Micro. Meso. Mater.* **2012**, 162, 122.
75. Mascotto, S.; Wallacher, D.; Brandt, A.; Hauss, T.; Thommes, M.; Zickler, G. A.; Funari, S. r. S.; Timmann, A.; Smarsly, B. M., *Langmuir* **2009**, 25, 12670.
76. Yiu, H. H. P.; Wright, P. A., *J. Mater. Chem.* **2005**, 15, 3690.
77. Hartmann, M.; Jung, D., *J. Mater. Chem.* **2010**, 20, 844.
78. Vinu, A.; Murugesan, V.; Tangermann, O.; Hartmann, M., *Chem. Mater.* **2004**, 16, 3056.
79. Szeifert, J. M.; Fattakhova-Rohlffing, D.; Georgiadou, D.; Kalousek, V.; Rathousky, J.; Kuang, D.; Wenger, S.; Zakeeruddin, S. M.; Graetzel, M.; Bein, T., *Chem. Mater.* **2009**, 21, 1260.
80. Wu, Q.; Rankin, S. E., *J. Phys. Chem. C* **2011**, 115, 11925.
81. Ghicov, A.; Schmuki, P., *Chem. Commun.* **2009**, 2791.
82. Liu, Y.; Szeifert, J. M.; Feckl, J. M.; Mandlmeier, B.; Rathousky, J.; Hayden, O.; Fattakhova-Rohlffing, D.; Bein, T., *ACS Nano* **2010**, 4, 5373.
83. Li, S.; Zheng, J.; Yang, W.; Zhao, Y., *Chem. Lett.* **2007**, 36, 542.

84. Smoukov, S. K.; Grzybowski, B. A., *Chem. Mater.* **2006**, 18, 4722.
85. Vaufrey, D.; Ben Khalifa, M.; Besland, M. P.; Sandu, C.; Blanchin, M. G.; Teodorescu, V.; Roger, J. A.; Tardy, J., *Synthetic Metals* **2002**, 127, 207.
86. Yu, H. K.; Dong, W. J.; Jung, G. H.; Lee, J.-L., *ACS Nano* **2011**, 5, 8026.
87. Kong, S. M.; Xiao, Y.; Kim, K. H.; In Lee, W.; Chung, C. W., *Thin Solid Films* **2011**, 519, 3173.
88. Franke, M. E.; Koplin, T. J.; Simon, U., *Small* **2006**, 2, 36.
89. Briseno, A. L.; Yang, P., *Nat. Mater.* **2009**, 8, 7.
90. Topoglidis, E.; Astuti, Y.; Duriaux, F.; Grätzel, M.; Durrant, J. R., *Langmuir* **2003**, 19, 6894.
91. Vargo, M. L.; Gulka, C. P.; Gerig, J. K.; Manieri, C. M.; Dattelbaum, J. D.; Marks, C. B.; Lawrence, N. T.; Trawick, M. L.; Leopold, M. C., *Langmuir* **2010**, 26, 560.
92. Astuti, Y.; Topoglidis, E.; Briscoe, P. B.; Fantuzzi, A.; Gilardi, G.; Durrant, J. R., *J. Am. Chem. Soc.* **2004**, 126, 8001.
93. Frasca, S.; von Graberg, T.; Feng, J.-J.; Thomas, A.; Smarsly, B. M.; Weidinger, I. M.; Scheller, F. W.; Hildebrandt, P.; Wollenberger, U., *ChemCatChem* **2010**, 2, 839.
94. Rosamond, M. C.; Gallant, A. J.; Petty, M. C.; Kolosov, O.; Zeze, D. A., *Adv. Mater.* **2011**, 23, 5039.
95. Fattakhova-Rohlfing, D.; Brezesinski, T.; Rathouský, J.; Feldhoff, A.; Oekermann, T.; Wark, M.; Smarsly, B. M., *Adv. Mater.* **2006**, 18, 2980.
96. Hou, K.; Puzzo, D.; Helander, M. G.; Lo, S. S.; Bonifacio, L. D.; Wang, W.; Lu, Z. H.; Scholes, G. D.; Ozin, G. A., *Adv. Mater.* **2009**, 21, 2492.
97. Hoertz, P. G.; Chen, Z.; Kent, C. A.; Meyer, T. J., *Inorg. Chem.* **2010**, 49, 8179.
98. Kresge, C. T.; Leonowicz, M. E.; Roth, W. J.; Vartuli, J. C.; Beck, J. S., *Nature* **1992**, 359, 710.
99. Yang, H.; Coombs, N.; Sokolov, I.; Ozin, G. A., *Nature* **1996**, 381, 589.

100. Yang, H.; Kuperman, A.; Coombs, N.; Mamiche-Afara, S.; Ozin, G. A., *Nature* **1996**, 379, 703.
101. Brinker, C. J.; Lu, Y.; Sellinger, A.; Fan, H., *Adv. Mater.* **1999**, 11, 579.
102. Lu, Y.; Fan, H.; Stump, A.; Ward, T. L.; Rieker, T.; Brinker, C. J., *Nature* **1999**, 398, 223.
103. Schüth, F., *Chem. Mater.* **2001**, 13, 3184.
104. Boettcher, S. W.; Fan, J.; Tsung, C.-K.; Shi, Q.; Stucky, G. D., *Acc. Chem. Res.* **2007**, 40, 784.
105. Grosso, D.; Boissière, C.; Nicole, L.; Sanchez, C., *J. Sol-Gel Sci. Technol.* **2006**, 40, 141.
106. Pan, J. H.; Zhao, X. S.; Lee, W. I., *Chem. Eng. J.* **2011**, 170, 363.
107. Sanchez, C.; Boissiere, C.; Grosso, D.; Laberty, C.; Nicole, L., *Chem. Mater.* **2008**, 20, 682.
108. Bucknall, D. G.; Anderson, H. L., *Science* **2003**, 302, 1904.
109. Grosso, D.; Cagnol, F.; Soler-Illia, G.; Crepaldi, E.; Amenitsch, H.; Brunet-Bruneau, A.; Bourgeois, A.; Sanchez, C., *Adv. Funct. Mater.* **2004**, 14, 309.
110. Sanchez, C.; Boissière, C.; Grosso, D.; Laberty, C.; Nicole, L., *Chem. Mater.* **2008**, 20, 682.
111. Sanchez, C.; Soler-Illia, G. J. d. A. A.; Ribot, F.; Lalot, T.; Mayer, C. R.; Cabuil, V., *Chem. Mater.* **2001**, 13, 3061.
112. Soler-Illia, G. J. d. A. A.; Sanchez, C.; Lebeau, B.; Patarin, J., *Chemical Reviews* **2002**, 102, 4093.
113. Niederberger, M.; Pinna, N., *Metal oxide nanoparticles in organic solvents*. Springer-Verlag: London, 2009.
114. Garnweitner, G.; Niederberger, M., *J. Am. Ceram. Soc.* **2006**, 89, 1801.
115. Schwartz, R. W.; Schneller, T.; Waser, R., *Comptes Rendus Chimie* **2004**, 7, 433.

116. Segal, D., *J. Mater. Chem.* **1997**, 7, 1297.
117. Cushing, B. L.; Kolesnichenko, V. L.; O'Connor, C. J., *Chem. Rev.* **2004**, 104, 3893.
118. Hench, L. L.; West, J. K., *Chem. Rev.* **1990**, 90, 33.
119. Livage, J.; Ganguli, D., *Sol. Eng. Mater. Sol. Cells* **2001**, 68, 365.
120. Niederberger, M.; Garnweitner, G., *Chem.-Eur. J.* **2006**, 12, 7282.
121. Corriu, R.; Leclercq, D., *Angewandte Chemie* **1996**, 108, 1524.
122. Pinna, N.; Niederberger, M., *Angew. Chem., Int. Ed.* **2008**, 47, 5292.
123. Niederberger, M.; Garnweitner, G.; Buha, J.; Polleux, J.; Ba, J.; Pinna, N., *J. Sol-Gel Sci. Technol.* **2006**, 40, 259.
124. Niederberger, M.; Bartl, M. H.; Stucky, G. D., *J. Am. Chem. Soc.* **2002**, 124, 13642.
125. Ba, J.; Polleux, J.; Antonietti, M.; Niederberger, M., *Adv. Mater.* **2005**, 17, 2509.
126. Gotić, M.; Musić, S., *Eur. J. Inorg. Chem.* **2008**, 2008, 966.
127. Praserttham, P.; Silveston, P. L.; Mekasuwandumrong, O.; Pavarajarn, V.; Phungphadung, J.; Somrang, P., *Crystal Growth & Design* **2003**, 4, 39.
128. Djerdj, I.; Arčon, D.; Jagličić, Z.; Niederberger, M., *J. Phys. Chem. C* **2007**, 111, 3614.
129. Niederberger, M.; Bartl, M. H.; Stucky, G. D., *Chem. Mater.* **2002**, 14, 4364.
130. Wang, J.; Polleux, J.; Lim, J.; Dunn, B., *J. Phys. Chem. C* **2007**, 111, 14925.
131. Zhu, J.; Yang, J.; Bian, Z.-F.; Ren, J.; Liu, Y.-M.; Cao, Y.; Li, H.-X.; He, H.-Y.; Fan, K.-N., *App. Catal. B: Environ.* **2007**, 76, 82.
132. Ye, Y.; Yuan, F.; Li, S., *Mater. Lett.* **2006**, 60, 3175.
133. Bilecka, I.; Djerdj, I.; Niederberger, M., *Chem. Commun.* **2008**, 2008, 886.
134. Pinna, N.; Neri, G.; Antonietti, M.; Niederberger, M., *Angew. Chem. Int. Ed.* **2004**, 43, 4345.
135. Pinna, N.; Neri, G.; Antonietti, M.; Niederberger, M., *Angew. Chem.* **2004**, 116, 4445.

136. Vilaça, G.; Jousseume, B.; Mahieux, C.; Belin, C.; Cachet, H.; Bernard, M. C.; Vivier, V.; Toupance, T., *Adv. Mater.* **2006**, 18, 1073.
137. Subramanian, A.; Kennel, S. J.; Oden, P. I.; Jacobson, K. B.; Woodward, J.; Doktycz, M. J., *Enz. Microbial Technol.* **1999**, 24, 26.
138. Impens, N. R. E. N.; van der Voort, P.; Vansant, E. F., *Microporous and Mesoporous Mater.* **1999**, 28, 217.
139. Bruhwiler, D., *Nanoscale* **2010**, 2, 887.
140. Yamamoto, K.; Tatsumi, T., *Microporous and Mesoporous Mater.* **2001**, 44-45, 459.
141. Angloher, S.; Bein, T., *J. Mater. Chem.* **2006**, 16, 3629.
142. Angloher, S.; Kecht, J.; Bein, T., *Chem. Mater.* **2007**, 19, 5797.
143. Angloher, S.; Kecht, J.; Bein, T., *Chem. Mater.* **2007**, 19, 3568.
144. Angloher, S. Organische Modifizierung von mesoporösen Silicaten unter der Verwendung metallorganischer Reagenzien. LMU, Munich, 2006.
145. Thode, C. J.; Williams, M. E., *Langmuir* **2008**, 24, 5988.
146. Wang, D.; Chang, Y.-L.; Liu, Z.; Dai, H., *J. Amer. Chem. Soc.* **2005**, 127, 11871.
147. Lockett, M. R.; Smith, L. M., *Langmuir* **2009**, 25, 3340.
148. Mukherjee, J.; Peczonczyk, S.; Maldonado, S., *Langmuir* **2010**, 26, 10890.
149. Bansal, A.; Li, X.; Yi, S. I.; Weinberg, W. H.; Lewis, N. S., *J. Phys. Chem. B* **2001**, 105, 10266.
150. Lim, J. E.; Shim, C. B.; Kim, J. M.; Lee, B. Y.; Yie, J. E., *Angew. Chem. Int. Ed.* **2004**, 43, 3839.
151. Nakashima, T.; Higa, H.; Matsubara, H.; Benson, A. M.; Yasunobu, K. T., *J. Biol. Chem.* **1966**, 241, 1166.
152. Protein Data Bank. <http://www.rcsb.org/pdb/home/home.do> (12.03.2011),
153. Mirkin, N.; Jaconic, J.; Stojanoff, V.; Moreno, A., *Proteins* **2008**, 70, 83.

154. Topoglidis, E.; Campbell, C. J.; Cass, A. E. G.; Durrant, J. R., *Langmuir* **2001**, 17, 7899.
155. Willit, J. L.; Bowden, E. F., *J. Electroanal. Chem. Interf. Electrochem.* **1987**, 221, 265.
156. Willit, J. L.; Bowden, E. F., *J. Phys. Chem.* **1990**, 94, 8241.
157. Guo, K.; Hu, Y.; Zhang, Y.; Liu, B.; Magner, E., *Langmuir* **2010**, 26, 9076.
158. McKenzie, K. J.; Marken, F., *Langmuir* **2003**, 19, 4327.
159. Dai, Z.; Liu, S.; Ju, H., *Electrochim. Acta* **2004**, 49, 2139.
160. Renault, C.; Balland, V.; Martinez-Ferrero, E.; Nicole, L.; Sanchez, C.; Limoges, B., *Chem. Comm.* **2009**, 7494.
161. Bonanni, B.; Andolfi, L.; Bizzarri, A. R.; Cannistraro, S., *J. Phys. Chem. B* **2007**, 111, 5062.

2 Characterization Methods

In this chapter the methods used for the characterization of the materials investigated in this thesis, i.e. antimony doped tin oxide (ATO) nanoparticles and mesoporous ATO films are discussed. The fundamental understanding and potential applications of these materials require the ability and instrumentation to observe and measure the individual nanomaterials and nanostructures. This chapter provides a description of the essential principles of the applied characterization techniques. A detailed description of experimental conditions used for the characterization of the specific materials is given in the chapters 3.2, 4.2, 5.2, and 6.2.

2.1 X-Ray Diffraction

X-ray diffraction is a characterization technique which gathers information about structural properties of crystalline solid materials from elastically scattered X-rays.^{1, 2}

X-rays are a form of electromagnetic radiation having a wavelength between 0.01 and 10 nm. In X-ray diffractometers, X-rays are generated when accelerated electrons collide with a cooled target (anode). Due to the collision process, electrons are decelerating and losing energy. This energy is converted into electromagnetic radiation which is known as X-ray ‘white radiation’, Fig. 2.1.1.

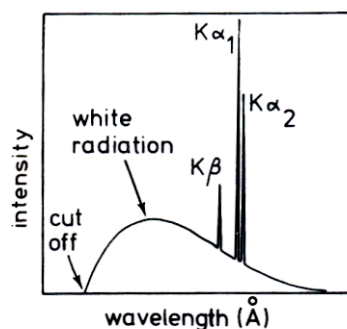


Figure 2.1.1. X-ray emission spectrum of a metal. Adapted from reference [1].

Additionally to this, narrow lines appear in the emitted spectrum, which are characteristic for the material of the anode. These lines are formed as follows: accelerated electrons eject a core electron from the inner shell of the atoms of the anode. In the relaxation step electrons from the upper shell fill the gap. During this process, a specific wavelength X-ray quantum is emitted. This process generates these lines in the spectrum. These monochromatic X-rays, which are then used in X-ray diffraction, are assigned by the relaxation process (K_α , K_β , etc). By using filters, which isolate only one of these single narrow lines a monochromatic X-ray source is generated. For example, if the anode material consists of copper, the copper K_α line is used as monochromatic X-ray source.

For obtaining information about the structure of materials, samples are illuminated with these monochromatic X-rays. Considering that the wavelength of this radiation is similar to atomic distances in solid materials, the structure information is obtained by interpretation of constructive and destructive interferences of the scattered X-rays. This scattering of X-rays on a crystal lattice is explained through Bragg's law and is schematically illustrated in Fig. 2.1.2.

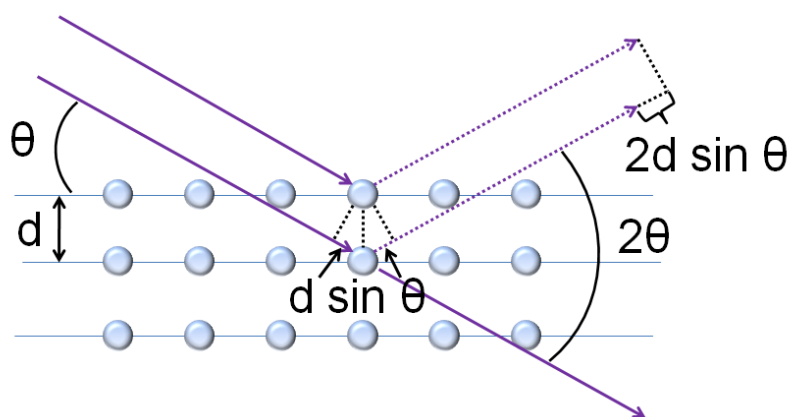


Figure 2.1.2. Illustration of Bragg's law for X-ray diffraction.

Bragg's law describes the conditions of coherent and incoherent interference of scattered X-rays on a crystal lattice:

$$n\lambda = 2d\sin\theta \quad (\text{eq. 2.1.1})$$

where n is the order of interference, λ is the wavelength of X-ray radiation (normally 1.5418 Å for Cu K $_{\alpha}$ radiation), d is the lattice spacing and θ is the angle of incidence.

When constructive interference occurs, at a specific angle, the reflection peaks in XRD patterns are obtained. The width of the reflection peaks is dependent on the size of the crystalline domains which give the constructive interference whereas; the intensity of the reflex is dependent on the amount of crystallites, among other factors. From the broadening of the peaks in the XRD patterns, it is possible to calculate the size of crystalline domains using Scherrer's equation:¹

$$D = \frac{0.9\lambda}{\beta \cos\theta_{\beta}} \quad (\text{eq. 2.1.2})$$

where D is the calculated size of the crystalline domain, λ is the wavelength of used X-rays, β is the full width at half maximum in $^{\circ}2\theta$ and θ_{β} is the angle of incidence (reflex peak in XRD pattern).

At small angles of incidence (ca. 0.5-10 $^{\circ}2\theta$) it is possible to obtain constructive interference, i.e. reflection of X-rays, which does not come from the ordered crystal structure, but rather from ordering at the nanometer scale. This technique which is known as small-angle X-ray scattering (SAXS), delivers information about characteristic distances of ordered and partially ordered porous materials where ordered mesopores define the lattice planes (d-spacing).

2.2 Infrared Spectroscopy

Infrared spectroscopy^{2, 3} is a spectroscopic technique that is used for the characterization of chemical bonding in materials through excitation of vibrational modes with the infrared part of the electromagnetic radiation. The characteristic vibrational modes of functional groups are used for the identification of chemical bonds in materials. The most common part of the infrared spectrum used for this measurement is known as middle infrared (mid-IR) and covers the spectrum in the range of 200 to 4000 cm^{-1} . The intensity of the infrared beam is measured

after the interaction with the sample. The absorbed part of the spectrum is often characteristic for the vibrations of functional groups in the material. The absorption of mid-IR can be a result of induced transitions between molecular or collective vibrational energy levels. In order to cause absorption, the molecules must show a change in dipole moment during the vibration caused by the IR irradiation. This means that the molecule does not need to have a permanent dipole moment, but the dipole moment can be induced during vibration.

2.3 Raman Spectroscopy

Raman spectroscopy is a spectroscopic technique which is complementary to IR spectroscopy. In this technique, the information about the interaction of the electromagnetic radiation with the material is obtained through the collection of the inelastically scattered photons upon irradiation with monochromatic light.^{2, 3} The selection rules in Raman spectroscopy are different from IR spectroscopy. The selection rule in Raman spectroscopy is that the polarizability of the bond during the vibration must change (and not the dipole moment like in IR spectroscopy). The change in polarizability is a result of the deformation of the electron cloud. This occurs when a photon from the monochromatic light beam excites the system from a given vibrational state into a virtual energy state. After this, the system relaxes by re-emitting (scattering) the photons in all directions (Fig. 2.3.1).

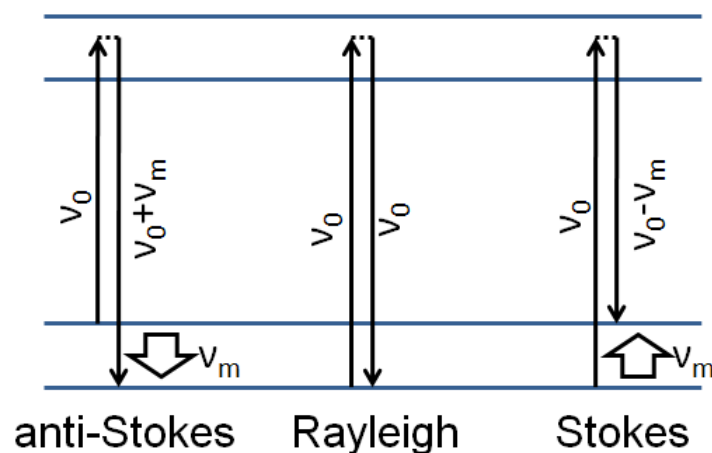


Figure. 2.3.1. Illustration of the principle of Rayleigh-, Stokes- and anti-Stokes scattering in Raman spectroscopy.

However, these re-emitted photons can differ in energy from the incident light. Most of this scattered light is scattered elastically, i.e. the system relaxes into the same ground state, and scattered light has the same frequency as an incident light beam. This type of scattering is known as Rayleigh scattering. If the system does not relax back into the ground state but into some higher vibrational state, the energy (thus the frequency) of the scattered light is lower than from the incident beam. This type of scattering is known as Stokes scattering and generates weak side bands in the spectrum at lower frequencies. In the case that the system relaxes into an energy level being lower than the ground state, the resulting scattered photons possess a higher energy and therefore a higher frequency than the incident light beam. This type of scattering is called anti-Stokes scattering. For Raman measurements Stokes scattering is mainly used due to a higher intensity and lower temperature sensitivity compared to anti-Stokes scattering.

2.4 UV-Vis Spectroscopy

Ultraviolet and visible light (UV-Vis) spectroscopy is an absorption spectroscopy technique which is widely used for the identification and determination of various inorganic and organic

species.³ The absorption of visible or ultraviolet radiation is a result of the excitation of bonding electrons in the absorbing species. These transitions of electrons between outermost energy levels are correlated with energy changes in the range of 10^4 to 10^5 cm^{-1} , which covers near infrared (NIR), visible light (Vis) and ultraviolet (UV) electromagnetic radiation. Due to this they are associated with the color of the examined species.

Organic compounds are able to absorb in the UV-Vis region because they all contain valence electrons that can be excited to higher energy levels. Mostly, the absorption spectroscopy of organic compounds is based on the transition of nonbonding n or π bonding electrons to the π^* excited states. Both types of transition require the existence of an unsaturated functional group which can provide the π orbitals. Molecules which contain such functional groups, thus absorbing in the UV-Vis region, are sometimes called chromophores.

The absorption of solid inorganic species (extended lattice) can be explained according to the Figure 2.4.1.

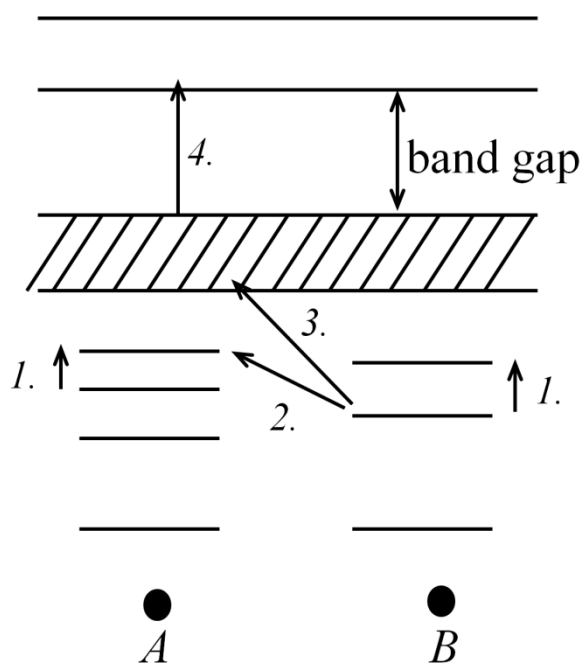


Figure 2.4.1. Illustration of the possible electronic transitions in solid material during UV-Vis absorption.

In Figure 2.4.1 A and B present two neighboring atoms. The inner electron shells are localized on each atom, whereas the outermost shell may overlap and form delocalized bands.

The processes which can occur during absorption are presented in Figure 2.4.1 as:

1. Promotion of an electron, on the same atom, from a localized orbital to a higher energy localized orbital. The spectroscopic absorption band which corresponds to this transition is known as excitation band. These types of absorption involve transitions between filled and unfilled *d*- and *f*-orbitals in some metal ions and complexes.
2. Promotion of an electron from a localized orbital of one atom to a higher energy localized orbital of the neighboring atom. The corresponding absorption bands are known as charge transfer bands. This type of absorption can also be found in charge transfer complexes which consist of an electron donor group bonded to an electron acceptor.
3. Promotion of an electron from a localized orbital to the delocalized energy band which is characteristic for the entire solid, i.e. the conduction band. Materials which show this type of absorption are photoconductive.
4. Promotion of an electron from one energy band to another higher energy band. This type of transition can occur for instance between valence band and conduction band. As a result, the magnitude of the band gap of some materials can be measured spectroscopically.

The UV-Vis spectroscopy measurement can be used for quantification of the analyzed species by measuring a transmittance or an absorbance of solutions or films in a transparent cell having a defined path length.³ The concentration of the absorbing species is linearly related to the absorbance according to the Lambert's-Beer's law:

$$A = -\log T = \log \frac{P_0}{P} = \epsilon bc \quad (\text{eq. 2.4.1})$$

where A is the absorbance, T is the transmittance, P_0 is the intensity of the incident beam, P is the intensity of the transmitted beam, ϵ is the molar absorption coefficient of the analyte, b is the path length (in centimeters) and c is the concentration of the analyte.

2.5 Thermogravimetric Analysis and Differential Scanning Calorimetry

Thermogravimetric analysis (TGA) is a method through which the behavior and mass losses of the sample during a thermal treatment are determined. The TGA is a quantitative and powerful technique, but gives no direct chemical information. The essential component of the TGA is the thermo-balance, which consists of a recording balance, the furnace, a temperature controller, a sample holder, a gas-delivery system for establishing the required atmosphere, and a data acquisition system.³

The analysis is performed by linearly increasing the temperature of the sample and simultaneously monitoring its weight loss in the desired gas atmosphere. Several processes can occur during the heat treatment of the sample and can lead to mass loss. The loss in the weight might be the result of evaporation or pyrolysis. Other possibilities, such as oxidation or reduction of the sample can be monitored by controlling the atmosphere to which the sample is exposed during heat treatment. The atmosphere can be either inert by using argon or nitrogen or oxidizing by using a synthetic air mixture, respectively. The applied gas passes the sample with laminar flow and removes the desorbed species from the heated sample.

Additionally, differential scanning calorimetry (DSC) measurements can be performed together with TGA measurements, also known as TGA-DSC. This technique measures the amount of heat required to increase the temperature of the sample and an empty reference crucible. By comparing the energy needed for the heating of the sample with the reference, the enthalpy and consequently the nature of the weight loss can be studied by this method.

Hence, information about the endothermic (evaporation) and exothermic (combustion) processes during the heat treatment of the sample are obtained.

2.6 Electron Microscopy

In 1924 Louis de Broglie postulated the wave-particle dualism. The direct implication of this theory is that accelerated electrons are not only acting as particles but also as waves. This characteristic peculiarity is used in electron microscopy where the source for illumination and imaging of specimens is an electron beam. The first electron microscope was built in 1931 by Ernst Ruska and Max Knoll. Because of this achievement and due to his fundamental work in electron optics Ernst Ruska received the Nobel Prize in 1986.⁴ Electron microscopes use electrons which have a wavelength 100,000 times shorter than visible light, and they can achieve a resolution 1,000× higher than ordinary light microscopes. However, the interaction of the electron beam with the specimen is different from the interaction of light with matter in light microscopes.

When a sample is irradiated with an electron beam, the interaction of the electron beam with the specimen induces several processes which can be used either for imaging of the sample or for chemical analysis (Fig. 2.6.1).

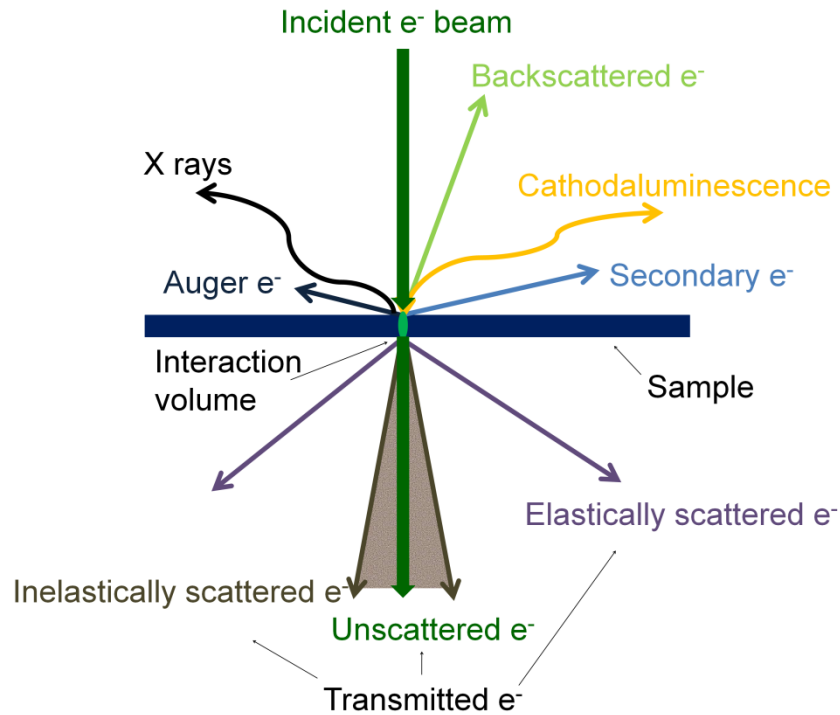


Figure. 2.6.1. Interaction of the electron beam with the specimen.

The most important interactions, which are used for imaging in scanning electron microscopes, are back-scattered and secondary electrons. Beside this, Auger-electrons and X-rays can be produced. The latter are discussed in more detail below. In transmission electron microscopes the electrons which are transmitted through the sample are used for imaging.

2.6.1 Transmission Electron Microscopy

The scheme of transmission electron microscopes is shown in Fig. 2.6.2.

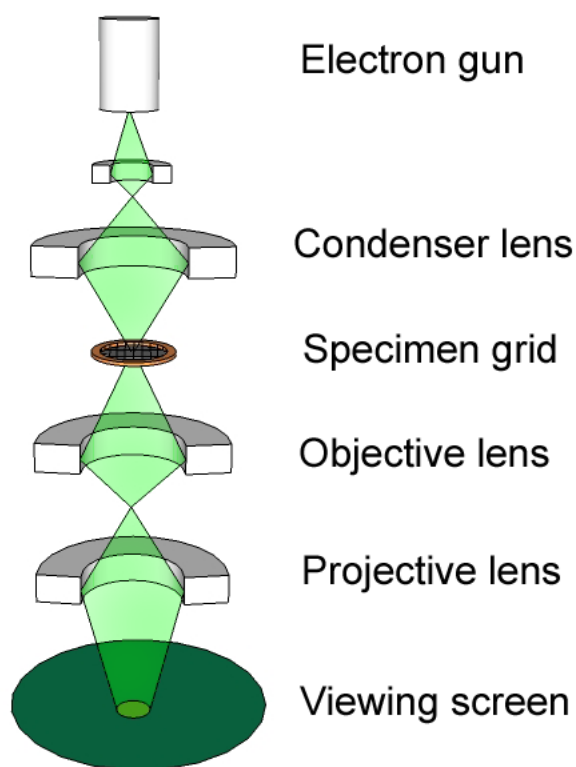


Figure 2.6.2. Scheme of a transmission electron microscope

The electron beam is generated in an electron gun which consists of a cathode and an anode; between them a voltage of typically 60-300 kV is applied. The emitter of electrons in the electron gun is the cathode which can be made either from (a) a tungsten filament or lanthanum hexaboride (LaB_6 crystal) or (b), in the case of a field emission gun (FEG), a special sharply pointed tip of tungsten crystal. The electron beam is then produced either by thermal emission (a) or field emission (b). In electron microscopes, a field emission gun is used to produce an electron beam with a small diameter, being more coherent and having an up to three orders of magnitude greater current density or brightness than can be achieved with thermal emitters. The electron beam is focused through a condenser system onto the sample (Fig. 2.6.2). The beam can be either focused to a small probe (the smallest being down to ca. 1 Å in diameter) or can be held parallel and illuminate a much larger area of the sample. After the interaction with the sample (Fig. 2.6.1) only electrons which are transmitted and elastically scattered through the sample are used for imaging in transmission electron

microscopes. After passing through the sample the electron beam carries the information about the internal structure of the sample. The first image of the sample is further magnified through the projective lenses to the imaging screen which can be a phosphorous screen (ZnS) or a CCD camera.

By changing the strength of the intermediate lenses it is possible to obtain either an image of the sample or diffraction patterns. Moreover, different imaging procedures are possible in the TEM which result in different types of information about the sample.^{4,5}

In conventional TEM imaging, the image is formed by illuminating the sample with a parallel electron beam and collecting forward scattered electrons. The contrast in the image is a result of electron scattering due to the mass-thickness or diffraction effect. Such images are also known as bright field images.⁵

In dark field imaging instead of collecting the direct beam, one of the diffracted beams is chosen for imaging. These electrons carry the information about a specific crystalline orientation of crystallites inside of the sample.⁵

In case of lattice imaging the image is formed by the interference of the diffracted beams with the direct beam. If the lattice resolution of the microscope is sufficiently high and a suitable crystalline sample is oriented along a zone axis, then high-resolution TEM (HRTEM) images can be obtained. In many cases, the atomic structure of a specimen can directly be investigated by HRTEM.⁵

In scanning transmission electron microscopes (STEM) the image is formed by using a focused (converged) beam instead of a parallel one and by scanning the sample with this beam. For the image formation transmitted electrons are usually collected on an annular detector. If only electrons are used which are scattered at large angles, contrast arises due to strong Coulomb interaction of the negatively charged electrons with the positive potential of the atomic nuclei of the atoms in the sample. Because of this electrons are scattered at high angles (designated as Rutherford scattering). This high angle scattering is employed in the

STEM mode imaging also known as Z-contrast or high angle annular dark field (HAADF) imaging method. Considering that heavier atoms possess more positively charged atomic nuclei they can scatter more strongly than light atoms. Therefore, heavier atoms are brighter in the image since the contrast is approximately proportional to the square of the atomic number (Z^2).⁵

2.6.2 Energy Dispersive X-Ray Spectroscopy (EDX)

Energy-dispersive X-ray spectroscopy (EDX) is an analytical technique used for the elemental analysis of a sample.⁶ The technique is based on analyzing X-rays emitted from the sample as a response of its inelastic interaction with the electron beam. If the electron beam interacts with the atom, it is possible that an electron from the inner shell, e.g. K-shell, is excited above the Fermi level and the atom becomes ionized (Fig. 2.6.3).

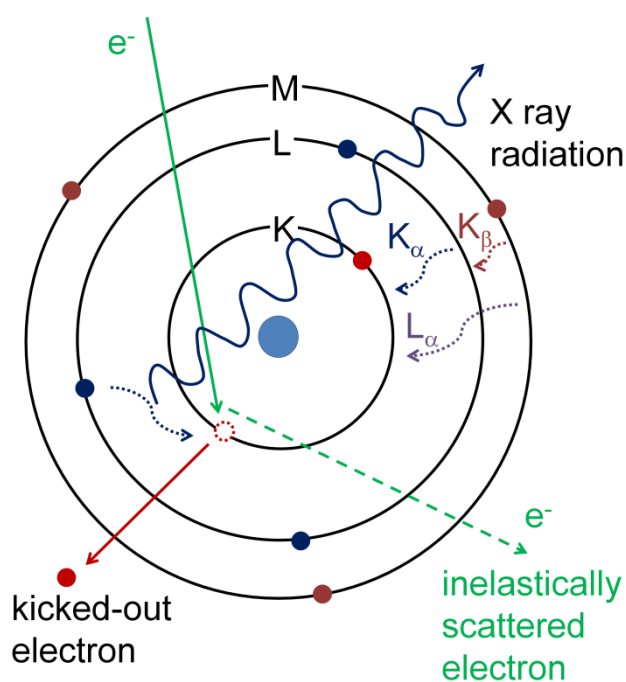


Figure 2.6.3. Interaction of the atom with an electron beam

The formed unoccupied state can be filled by an electron from an outer shell. During this transition the electron can emit radiation of a very short wave length; X-rays. Due to the

fundamental principle that each element has a unique atomic structure, the formed X-rays are a characteristic of an element and therefore the elements can be identified uniquely due to their specific energy of X-rays. This technique is used both for qualitative and quantitative elemental analysis.

EDX spectra are collected with EDX detectors which can be installed both on TEM and SEM instruments. The active part of an EDX detector is a Si(Li) semiconductor. The working principle of EDX detectors is based on the interaction of X-rays with a semiconductor, i.e. Si. The incoming X-rays induce a transfer of electrons from the valence into the conduction band thus creating an electron-hole pair in the semiconductor. The number of the created electrons or holes is directly proportional to the energy of the incoming X-rays. These electron-hole pairs are then separated through a voltage bias which is applied on the electrode contacts on the opposite sides of the semiconductor. The collected charges are further amplified and electronically identified.

2.6.3 Electron Energy Loss Spectroscopy (EELS)

Electron energy loss spectroscopy is often known as a complementary method to the EDX. EELS is in principle capable of measuring atomic composition and conduction band electronic properties. The technique is usually combined with transmission electron microscopy or more precisely STEM and it relies on the detection of inelastically transmitted scattered electrons (Fig. 2.6.3).⁶

In the basic principle of EELS, when the sample is illuminated with the electron beam, some electrons undergo inelastic scattering, causing them to lose energy and have their paths slightly deflected. This interaction, i.e. energy loss of the incident electron beam can be caused by phonon excitations, inter and intra band transitions, plasmon excitations, inner shell ionization, and Čerenkov radiation. The inner shell ionization, i.e. energy loss which is a

result of the transition of electrons from the inner shells to states above the Fermi level (Fig. 2.6.3) is of particular interest for elemental analysis.

The amount of electron energy loss in the transmitted beam can be detected through an electron spectrometer (Fig. 2.6.4), which is mounted below the viewing screen of transmission electron microscopes.

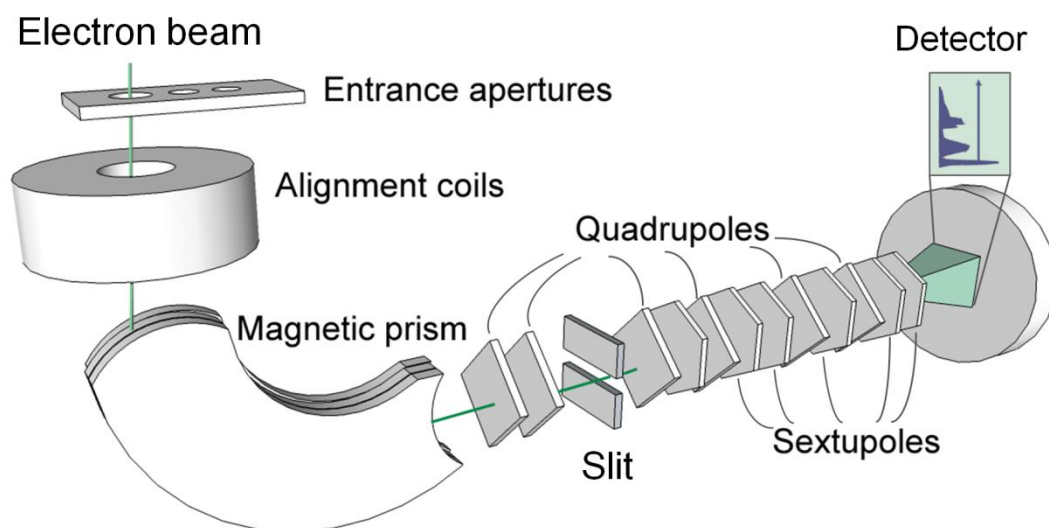


Figure 2.6.4. Schematic presentation of the EELS detector and formation of the EELS spectra.

The transmitted beam is first selected by the entrance aperture. The beam passing the aperture goes through the alignment coils into the magnetic prism. In the prism the electron beam becomes dispersed due to the Lorentz force as a result of the different energies (velocities) of electrons. The dispersed beam, which goes out of the prism, is further magnified by quadrupole and sextupole lenses and projected to a CCD camera and recorded. The obtained spectrum can be divided into different energy loss regions. One sharp peak occurs at zero eV, due to unscattered electrons. This peak is known as a zero loss peak. Next to it, in the region up to 30 eV, comes the so-called low loss region. This region is usually dominated by a broad peak that results from plasmon excitations and is in intensity several times lower than the zero loss peak. Core loss peaks, which are the result of the shell ionization of atoms, come at a

much higher energy and are approximately $1000\times$ lower in intensity than the zero loss peak. The obtained spectra are further interpreted in terms of the origin of the energy loss.

2.6.4 Scanning Electron Microscopy

The scanning electron microscope is a type of electron microscope that images the sample by scanning it with an electron beam which is focused into a small probe, Fig. 2.6.5.⁷

The beam is generated in an electron gun (same as in TEM) but has an energy ranging from 0.5 keV to 40 keV and is focused by one or two condenser lenses to a spot about 0.1 nm to 5 nm in diameter. The beam passes through pairs of scanning coils or pairs of deflector plates in the electron column, typically located in the final lens, which deflects the beam in the x - and y -axes so that it scans in a raster fashion over a rectangular area of the sample surface. When the primary electron beam interacts with the sample several processes can occur as shown in Fig. 2.6.1. The beam that is focused on the surface of the sample interacts with a volume of the sample which is called interaction volume. This volume has a teardrop shape and its depth has a size of 100 nm to 5 μm into the sample. For SEM imaging only backward scattered electrons or secondary electrons are used for image formation (Fig. 2.6.1).

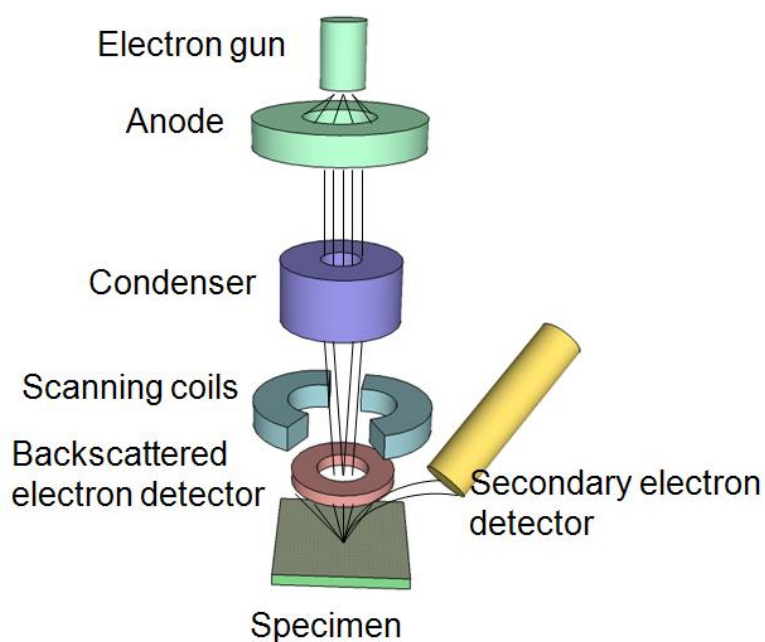


Figure 2.6.5. Scheme of SEM.

The energy of the backscattered electrons is similar to the energy of the incident electron beam, while secondary electrons possess an energy <50 eV, typically 5-10 eV.

Backscattered electrons (BSE) are electrons of the incident beam that are reflected from the sample by elastic scattering. This happens when electrons from the beam approach the nuclei of the atoms and due to the Coulomb forces nearby these electrons change their direction without changing the energy. Because the intensity of the BSE signal is strongly related to the atomic number (Z) of the specimen, BSE images can provide information about the distribution of different heavy and light elements in the sample.

On the other hand, when the electron interacts with the sample, secondary electrons can emerge from the atoms on the surface. Considering that the amount of secondary electrons depends on the surface and topology, these electrons carry information about the morphology of the sample. SEM micrographs can yield a characteristic three-dimensional appearance useful for understanding the surface structure of a sample.

Both types of electrons are collected with respective detectors where they are converted into electrical signals and further through a computer system transferred into an image.

2.7 X-ray Photoelectron Spectroscopy

X-ray photoelectron spectroscopy (XPS) is a quantitative (surface sensitive) spectroscopic technique which enables one to obtain information about the elemental composition, the empirical formula, and the chemical and oxidation state of elements within the material of investigation.^{1, 8, 9} Because of this, the method is also called electron spectroscopy for chemical analysis (ESCA) technique. The method is based on the photoelectric effect. If the matter is irradiated with a light of sufficiently small wavelength (i.e. high energy) it will emit electrons. The number of emitted electrons (photoelectrons) depends on the intensity and the energy of the photoelectrons corresponding to the wavelength of the applied X-rays.

The basic principle of this technique is the measurement of the kinetic energy of the electrons which are emitted from the sample as a consequence of irradiating it with X-rays. The process that takes place when the sample is exposed to X-ray radiation is the direct ionization of an electron from the inner shell (Fig. 2.7.1) of atoms.

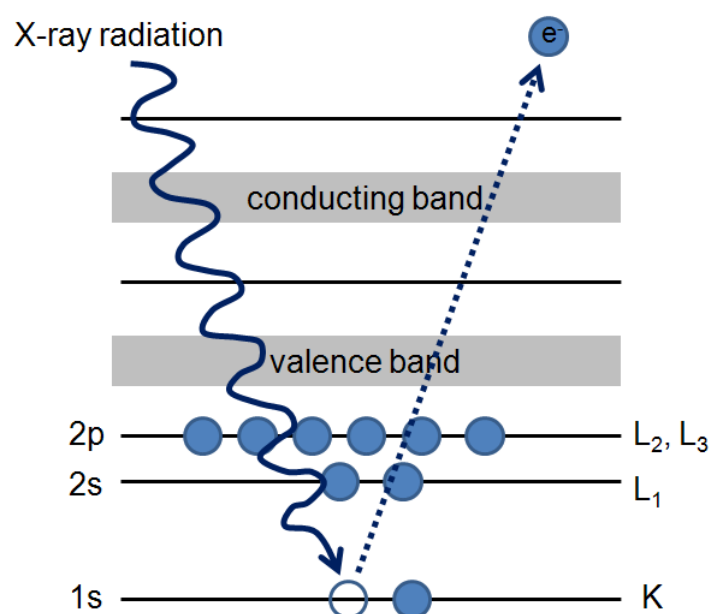


Figure 2.7.1. Interaction of an atom with X-ray radiation

The ionizing radiation which is used in XPS is a monochromatic X-ray radiation either from Mg K $_{\alpha}$ (1254 eV) or Al K $_{\alpha}$ (1487 eV). Because the energy of a particular X-ray wavelength is

known, the electron binding energy of each of the emitted electrons can be determined by using the equation:

$$E_{binding} = E_{photon} - (E_{kin} + \Phi) \quad (\text{eq. 2.7.1})$$

where $E_{binding}$ is the binding energy of the electron, E_{photon} is the energy of the used X-ray photons, $E_{kinetic}$ is the kinetic energy of the electron measured by the instrument and Φ is the work function of the spectrometer. The obtained XPS spectrum is a plot of the number of detected electrons versus the binding energy of the detected electrons. This spectrum contains the peaks at specific binding energies characteristic for each element present in the investigated material. These peaks in XPS spectra are directly related to the electronic configuration of the atoms of each element, i.e. $1s$, $2s$, $2p$, etc. Considering that the binding energy of electrons is characteristic for each element, measurements of $E_{binding}$ provide an identification of the atoms. However, the area below the peaks is proportional to the amount of the present material. Therefore, the XPS can be used for the quantitative analysis of samples. For this purpose, the area below the peak must be measured after the appropriate baseline subtraction and compared with suitable standard. The limitation of the XPS is the detection volume of the sample, which is limited to the region near the surface since the inelastic free path of electrons is limited. The detection in XPS is typically several nanometers in the depth of the sample.¹⁰

2.8 Dynamic Light Scattering

Dynamic light scattering is an analytical technique which enables one to obtain information about the size and the size distribution of colloidal nanoparticles by measuring the diffusion speed of the particles in solution. This non-invasive technique is based on the scattering of light on colloidal particles which undergo Brownian motion. Due to this motion the intensity of the scattered light fluctuates depending on the speed of particle movement. From the

measurements of these light fluctuations it is possible to obtain information about the size of the particles. However, the measured value represents the hydrodynamic diameter of the particle which does not have to be the same as the real size of the particle. This hydrodynamic diameter represents the sphere of the particle together with the solvent core which moves together with the particle in its Brownian motion.^{3, 11, 12}

In the experiment the colloidal solution is illuminated with monochromatic and coherent laser light and the light scatters from the moving colloidal particle. The laser light is randomly scattered and, due to the motion of the particles, the scattered light contains differences in the phase. As a result of the variation in the phase of the light, the light forms constructive or destructive interference on the detector in the form of speckle patterns. Considering that the particles are constantly moving, the speckle patterns are constantly changing. Thereby this motion results in time-dependent fluctuations of the intensity of the scattered light which are then recorded within a time scale. These fluctuations are subsequently quantified via the second order autocorrelation function which is given by:

$$g^2(q; \tau) = \frac{\langle I(t)I(t+\tau) \rangle}{\langle I(t)^2 \rangle} \quad (\text{eq. 2.8.1})$$

where $g^2(q; \tau)$ is the second order autocorrelation function at a particular q wave vector and the delayed time τ , whereas I is the intensity of the scattered light.

The first order autocorrelation function is related to the second order autocorrelation function via Siegert equation:

$$g^2(q; \tau) = 1 + \beta [g^1(q; \tau)]^2 \quad (\text{eq. 2.8.2})$$

Where $g^2(q; \tau)$ is the second whereas $g^1(q; \tau)$ is the first order autocorrelation function at a particular q wave vector and delayed time τ whereas β is a correction factor that depends on geometry and alignment of the laser beam in the light scattering setup.

This autocorrelation function is then used for the particle size determination by fitting it through mathematical models in order to obtain the diffusion coefficient of the particles. In

the case of monodispersed particles the autocorrelation function is treated with a single exponential function as:

$$g^1(q; \tau) = e^{-\Gamma \tau} \quad (\text{eq. 2.8.3})$$

where $g^1(q; \tau)$ is the first order autocorrelation function and Γ is the reciprocal of the characteristic decay time rate ($\tau = 1/\Gamma$). From the decay time rate the diffusion coefficient can be calculated according to:

$$\tau = q^2 D_t \quad (\text{eq. 2.8.4})$$

and q is presented as:

$$q = \frac{4n_0\pi}{\lambda} \sin\left(\frac{\theta}{2}\right) \quad (\text{eq. 2.8.5})$$

where D is the diffusion coefficient, Γ is the reciprocal of the characteristic decay time rate ($\tau = 1/\Gamma$), n_0 is the refractive index of the solution, λ is the wave length of the laser light and θ is the angle of the scattering experiment. A plot of Γ/q^2 vs. q^2 will result in a line with intercept D_t .

When the diffusion coefficient (D) is known the hydrodynamic diameter can be calculated by using the Stoke-Einstein equation:

$$d = \frac{kT}{3\pi\eta D} \quad (\text{eq. 2.8.6})$$

where d is the hydrodynamic diameter, k is the Boltzmann's constant, T is the temperature and η is the viscosity of the solvent.

However, most of the samples show some kind of size distribution and therefore the interpretation of the data obtained by scattering the light on monodispersed particles can be misleading.

In most of the cases, the particles present in the solution are polydispersed and autocorrelation function is a sum of the exponential decays of each particle in the population, eq. 2.8.7.

$$g^1(q; \tau) = \sum_{i=1}^n G_i(\Gamma_i) e^{-\Gamma_i \tau} = \int G(\Gamma) e^{-\Gamma \tau} d\Gamma \quad (\text{eq. 2.8.7})$$

$G(\Gamma)$ is proportional to the relative scattering from the each particle and contains information about the size distribution. In order to extract useful information from the autocorrelation function several methods have been developed, such as Cumulant method, Contin algorithm or Maximum entropy method.

The cumulant method is one of the most common methods and it is based on that the autocorrelation function can be expressed as:

$$g^1(q, \tau) = \left(1 + \frac{\mu_2}{2!} \tau^2 + \frac{\mu_3}{3!} \tau^3\right) e^{-\bar{\Gamma} \tau} \quad (\text{eq. 2.8.8})$$

where $\bar{\Gamma}$ is the average decay rate and $\mu_2/\bar{\Gamma}^2$ is second order polydispersity index. The z-averaged translation diffusion coefficient, D_z , can be derived as:

$$\bar{\Gamma} = q^2 D_z \quad (\text{eq. 2.8.9})$$

This method is valid for small τ and sufficiently narrow $G(\Gamma)$.

The CONTIN algorithm is based on inverse Laplace transform of the autocorrelation function and it is ideal for heterodispersed, polydispersed and multimodal systems.

The maximum entropy method is used for the quantification of sedimentation velocity from analytical ultracentrifugation and involves a number of iterative steps to minimize the deviation of the fitted data.

In the case of larger particles the Mie theory can be applied, which describes the scattering of light on particles, being similar or larger in size than the wavelength of the used laser beam. The scattering intensity from the particles in a beam of unpolarized light can be described by Rayleigh scattering:

$$I = I_0 \frac{1 + \cos^2 \theta}{2R^2} \left(\frac{2\pi}{\lambda}\right)^4 \left(\frac{n^2 - 1}{n^2 + 1}\right)^2 \left(\frac{d}{2}\right)^6 \quad (\text{eq. 2.8.10})$$

where I and I_0 are the intensities of the scattered light and the incident beam, respectively, θ is the scattering angle, R is the distance to the particle, λ is the wavelength of the incoming light, n is the refractive index of the particles and d the particle diameter.

Considering that the scattering intensity is proportional to d^6 , the obtained curves can be dominated by a small amount of the large particles or aggregates. Because of this it is of advantage to show volume-weighted or number-weighted distributions which are proportional to d^3 and d , respectively.

2.9 Zeta Potential Measurements

The zeta potential of particles describes an electric potential at the boundary of the electric double layer of the particle which is also known as hydrodynamic shear or slipping plane. The zeta potential is also known as the electrokinetic potential in colloid systems. Measurements of the zeta potential are used, for example, for determining the stability of colloidal suspensions by investigating the degree of electrostatic repulsion between the neighbouring and similarly charged particles in relation to the pH value of the aqueous solution.^{2, 13, 14}

When colloid particles are dispersed in an ion-containing solution, the charge of the surface of the particles will influence the distribution of the ions in the surrounding interfacial region of the solution. Consequently this will result in the formation of an electric double layer around the colloid particle. This electric double layer can be divided into an inner layer, also known as Stern layer, and an outer diffuse layer, Fig.2.9.1.

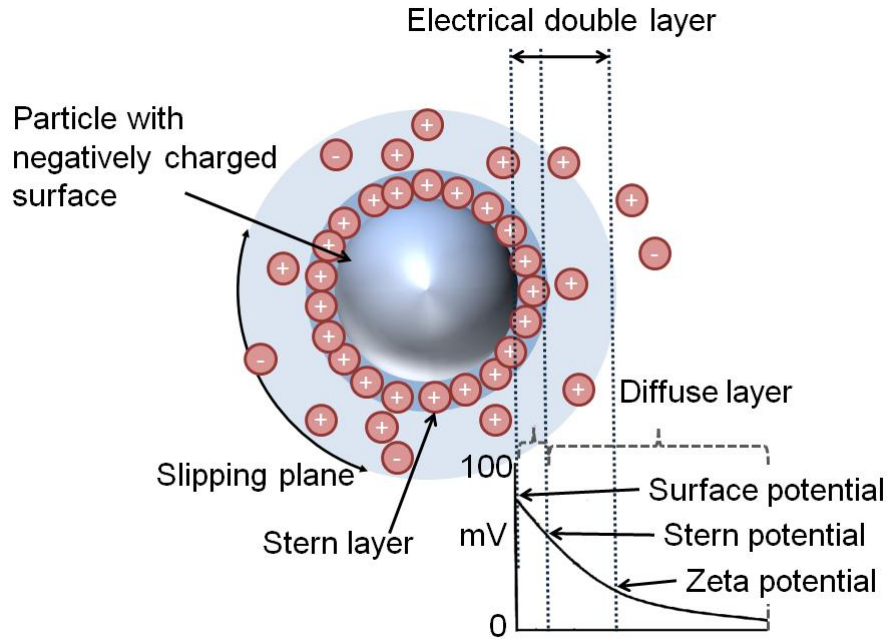


Figure 2.9.1. Scheme of the electric double layer around a negatively charged colloidal particles.

The inner or Stern layer consists of strongly bounded ions. The outer layer is formed of less strongly bonded ions. The zeta potential cannot be measured directly but can be calculated by measuring the electrophoretic mobility. The electrophoretic mobility of the colloidal solution is measured by applying an electric field across the dispersion. Because of their surface charge the particles will move toward the electrode with opposite charge with a velocity which is proportional to the magnitude of the zeta potential. The zeta potential is correlated to the electrophoretic velocity through the Henry equation:

$$U_E = \frac{2\varepsilon Z f(Ka)}{3\eta} \quad (\text{eq. 2.9.1})$$

where U_E is the electrophoretic mobility, ε is the dielectric constant, Z is the zeta potential, $f(Ka)$ is Henry's function and η is the viscosity. The electrophoretic mobility can be measured by using a Laser Doppler Velocimetry (LDV). The LVD technique is based on the Doppler Effect. The measurement is performed by passing the laser beam through the colloid solution. When the electric field is applied the particles start to move towards the corresponding electrodes. Their movement will cause a frequency shift of the incident laser beam, i.e. Doppler shift. As the Doppler shift is proportional to the velocity of the particles, the resulting

frequency difference forms a signal corresponding to the velocity of the particles between the electrodes in the measurement cell. According to the Smoluchowski approximation Henry's function is set to 1.5 and can be used if the thickness of the electric double layer in comparison to the size of the particles is very small. If the thickness of the double layer is large in comparison to the diameter of the particles the Hückel approximation, where $f(Ka)=1$, should be used.

2.10 Gas Sorption

Gas sorption is the most common technique for the characterization of porous materials. The principle of the measurement is based on physisorption of gas molecules on the surface of porous materials, which involves weak van der Waals interactions between gas molecules (the molecules which are accumulated) and the surface of porous materials. The porous material is usually referred to as 'adsorbent' while adsorbed gas molecules are referred to as 'adsorbate'. Various gases can be used as adsorbates. The most common adsorbates used for gas (physic)sorption measurements are nitrogen, argon and krypton. Most of the gas sorption measurements are performed with nitrogen as adsorbate due to its broad application range and availability. In the experiment the nitrogen is added to the sample at 77 K and simultaneously adsorbs at the surface of the porous solid. From the adsorption and desorption of nitrogen, measured at different pressures and constant temperature, the characteristic adsorption and desorption isotherms are obtained. The adsorption isotherm of the porous material can then be classified as one of the major six types of isotherms proposed by IUPAC,¹⁵ Fig. 2.10.1.

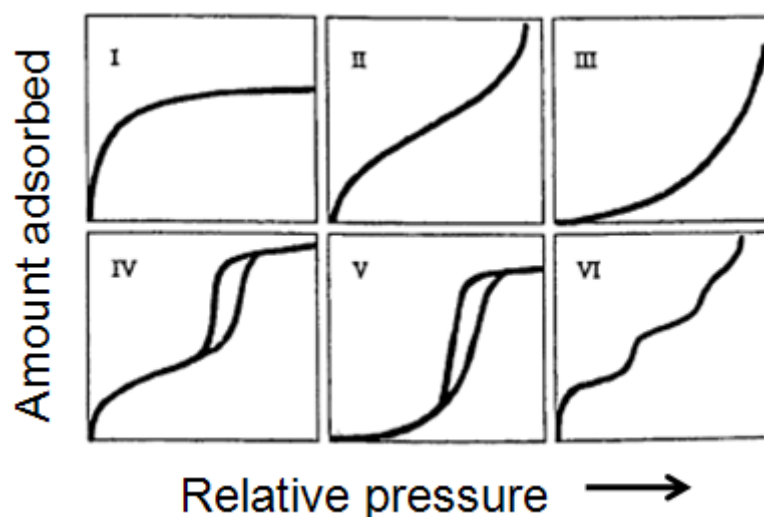


Figure 2.10.1. The six types of gas adsorption isotherms according IUPAC. Adopted from reference [14].

The six types of isotherms, proposed by IUPAC, are characteristic for different types of porous materials and can be described as follows:

- a) Isotherm type I, with a concave shape, can be obtained with microporous materials with relatively small external surfaces.
- b) Isotherm type II can be obtained in the case of non-porous or macroporous adsorbents.
- c) Isotherm type III can be obtained in non-porous and macroporous materials in the case when adsorbate-adsorbate interactions play an important role.
- d) Isotherm type IV, with hysteresis loop, can be obtained for mesoporous adsorbents and is correlated with capillary condensation of the adsorbate inside of the pores of the adsorbent.
- e) Isotherm type V is uncommon and can be obtained with certain porous materials where the adsorbent-adsorbate interaction is weak.
- f) Isotherm type VI presents a stepwise multilayer adsorption on a uniform non-porous surface.

The obtained isotherms can be further interpreted to obtain information about the characteristics of the porous system such as surface area and pore sizes. There are several

methods for the description of the obtained isotherms. However, the two methods which are common for studying porous materials are Brunauer-Emmett-Teller theory (BET) and density functional theory (DFT).¹⁶

The BET method has become one of the most widely used procedures for the evaluation of the surface area of porous materials. The theory is a generalization of Langmuir's theory, which is built on several simple approximations:

- The adsorption of the molecules leads to the formation of one monolayer of the adsorbate on the surface of the adsorbent
- The surface of the adsorbent is uniform and all binding sites are equal
- The ability of the adsorbate to bind specific sites on the surface of the adsorbent is independent of the occupancy of the neighbouring sites.

The BET theory extends the assumption about the formed monolayer, from Langmuir's theory, to a multilayer of the adsorbate where the initially formed monolayer serves as a substrate for further adsorption of the adsorbate. For low pressures ($p/p^0 < 0.3$) the BET equation can be expressed in linear form:

$$\frac{p/p^0}{n(1-p/p^0)} = \frac{1}{n_m C} + \frac{C-1}{n_m C} (p/p^0) \quad (\text{eq. 2.10.1})$$

where p/p^0 is the relative pressure, p^0 is the saturation pressure of the adsorptive, n is the amount of adsorbate, n_m is the monolayer capacity, and C is the BET constant. From this, the BET plot of $p/n(p^0-p)$ versus p/p^0 gives a linear plot with a slope $(C-1)/n_m C$ and an intercept $1/n_m C$. In this way it is possible to obtain n_m , which together with the average area a_m (molecular cross-section area) occupied with adsorbed molecules in the complete monolayer, is used for the calculation of the surface area A (BET) according the equation:

$$A(\text{BET}) = n_m \cdot L \cdot a_m \quad (\text{eq. 2.10.2})$$

where L is the Avogadro constant, n_m is the monolayer capacity (obtained from equation 2.10.1) and a_m is the average area occupied by a molecule of nitrogen. Usually, it is assumed

that the BET nitrogen monolayer is closed-packed and in which $a_m(\text{N}_2)$ results as 0.162 nm^2 at 77 K.

For the calculation of the pore diameter a model developed by Barrett, Joyner and Halenda (BJH) which is based on Kelvin's equation can be used. However, the obtained values for pore sizes in the range of a few nm are usually 1 nm smaller than the real values obtained through other methods. This behavior is a result of the assumption of a certain pore filling mechanism and a condensation phenomena that does not describe precisely the behavior in small pores.

The technique which yields a more realistic result about pore sizes uses a microscopic model, based on molecular simulations (Monte Carlo simulations) and density functional theory (DFT), which requires a specific knowledge about the structure and surface atoms of the investigated materials. Due to this, the technique cannot be applied to unknown systems and as a result the macroscopic approaches are still often employed.¹⁷

The DFT technique is based on assumptions about the site-wise attractions between the surface atoms and the adsorbate molecules, and the adsorbate-adsorbate attractions. In order to obtain a minimum in the free energy of the system the adsorbate molecules are adjusted by primarily changing the number density as a function of distance from the surface. One can distinguish local and non-local density functional theory (NLDF). The local density functional theory is based on the assumption that the fluid is structureless for the calculation of long-range interactions between adsorbate molecules. On the other hand, this assumption can not be used in the case of surface adsorption with strongly interacting boundaries. In this case the NLDF calculations become essential.

2.11 Potential Sweep Voltammetry

Voltammetry describes a group of electroanalytical methods in which the information about the sample is obtained by measuring the current as a function of the applied voltage.¹⁸

The voltammetry measurements are performed in an electrochemical cell connected to a potentiostat. The cell consists of three electrodes which are immersed in a solution containing an ionic conductor called supporting electrolyte according to the Figure 2.11.1.

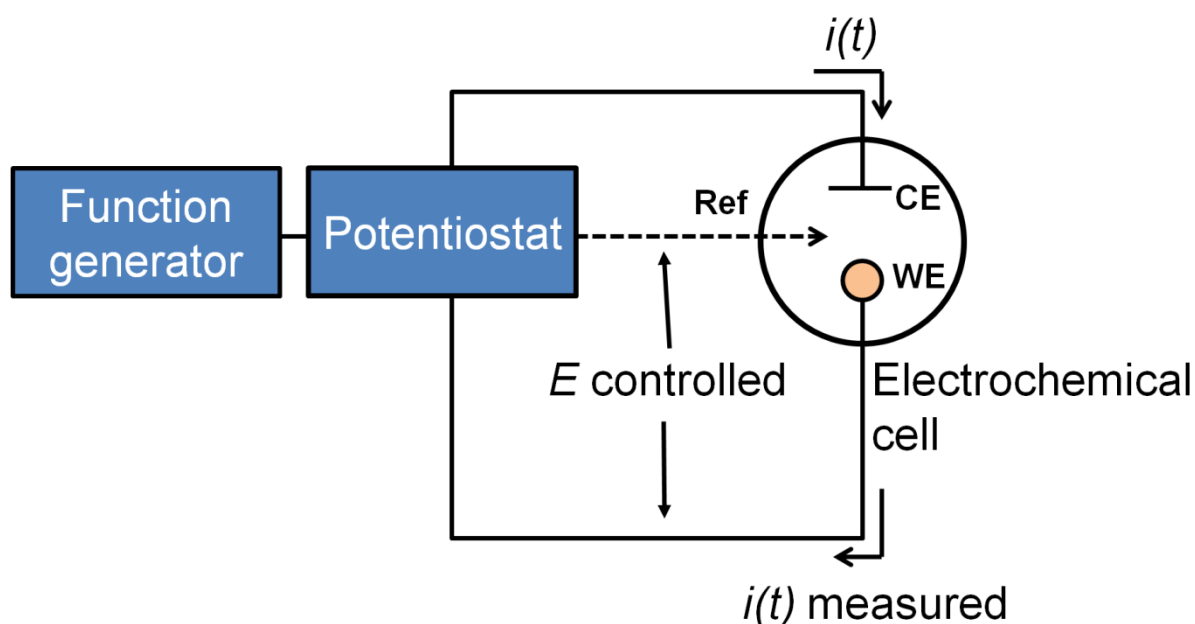


Figure 2.11.1. Scheme of the experimental arrangement for controlled-potential measurements. The experiment is controlled and run by function generator (commonly computer). Via the potentiostat a voltage is applied on the electrodes of the electrochemical cell. The electrochemical cell contains three electrodes: working electrode (WE), counter electrode (CE) and reference electrode (Ref).

The electrode at which the electro-active compound of interest is investigated is called the working electrode. The second electrode needed to complete the electrical circuit is called counter electrode. For analytical purposes it is usually made of platinum wire or a platinum mesh. The third electrode is a reference electrode whose potential remains constant during the experiment. Commonly reference electrodes are a saturated calomel electrode or, a silver-silver chloride electrode. The electrical resistance of the reference electrode measurement is so large that it withdraws practically no current. Due to this, the entire current from the

potentiostat is carried from the counter electrode to the working electrode. The control circuit in a potentiostat adjusts this current in the way that the difference in potential between the working electrode and the reference electrode is identical to the output voltage from the potentiostat. The resulting current is directly proportional to the difference in potential between the working electrode and the reference electrode and is converted to a voltage which is recorded as a function of time by the attached data acquisition system.

2.11.1 Faradaic and non-Faradaic Processes

There are two basic types of electrochemical processes that occur at the electrode surface namely Faradaic and non-Faradaic process. The Faradaic process involve charge transfer through the electrode-electrolyte interface leading to either oxidation or reduction of the electro-active on the electrode surface. Faradaic process take place at certain potential corresponding to the oxidation or reduction of the electro-active compound. The simplest case of a reversible electrochemical reaction of the electro-active species is described by the following scheme:



where O presents the oxidized form, R the reduced form of the electro-active compound and e^- the electrons. The applied potential at the working electrode controls the concentration of the redox species (C_O^0 and C_R^0) at the electrode surface and the rate of the reaction (k^0). This type of reactions is governed by Faraday's law which means that the amount of the chemical reaction caused by a flow of the current is proportional to the amount of the electricity which passed through the electrode. The current describes the transfer of the charge during the time according to:

$$i = \frac{dQ}{dt} \quad (\text{eq. 2.11.2})$$

where i is the current, Q is the charge and t is the time. The amount of the oxidized or reduced forms of the electro-active species can be presented according to:

$$N = \frac{Q}{nF} \quad (\text{eq. 2.11.3})$$

where N is the amount of the oxidized or reduced electro-active species (in moles), Q is the charge, n is the stoichiometric number of the transferred electrons involved in the reaction and F is the Faraday constant ($96485.4 \text{ C mol}^{-1}$). The Faradaic current is mainly limited by the rates of the processes that occur at the electrode surface and can be summarized as:

- a) mass transfer; the transfer of the electro-active species from the bulk of the solution onto the surface of the electrode
- b) charge transfer between the electro-active species and the surface of the electrode
- c) chemical reaction which follows the charge transfer; e.g. protonation
- d) other surface reactions, such as adsorption, desorption or crystallization.

The current in which electrons cross the surface from the electrode to the electro-active species is called cathodic current. The flow of electrons from electro-active species into the electrode is called anodic current.

Besides the Faradaic processes, processes related to the charging of the electrode-electrolyte interface but not involving the interfacial charge transfer take place at any electrode surface. These types of processes are known as non-Faradaic processes. Usually the observed current is called charging current and it is expressed as:

$$|i_c| = AC_d v \quad (\text{e.q. 2.11.4})$$

where i_c is the charging current, A is the electrode area, C_d is the capacitance of the double layer, and v is the scan rate. The Faradaic and non-Faradaic processes take place simultaneously and the observed current is a superposition of both types of current.

2.11.2 Linear Sweep Voltammetry

The simplest voltammetric technique is a linear sweep voltammetry (LSV). In linear sweep voltammetry the potential of the working electrode is changing linearly with the time, from the value E_1 to the value E_2 , with a proportionality constant called scan rate v (V/s) (Fig.2.11.2).

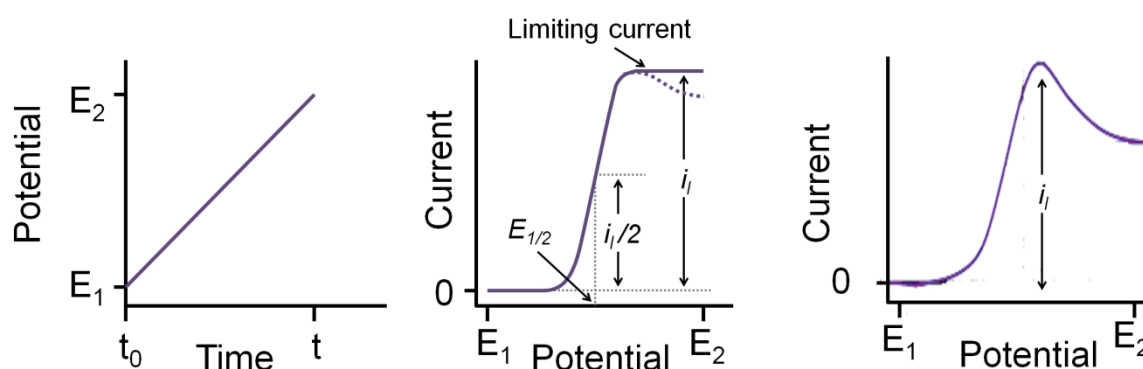


Figure 2.11.2. Illustration of the principle of linear sweep voltammetry: sweeping of the potential from the value E_1 to the value E_2 with time (left). In the middle is shown a linear sweep voltammogram for the reduction of the hypothetical oxidized electroactive species O to give the product R (according to the equation 2.11.1) for the stationary diffusion, spherical electrodes or microelectrodes. The limiting current is proportional to the concentration of the electroactive species. The half wave potential, $E_{1/2}$, is the applied potential at which half of the limiting current, $i_l/2$ is obtained. On the right is shown voltammogram for macroelectrode in non-stirred solution (non-stationary diffusion).

In the experiment, the scan or sweep rate typically can vary from 1 to 1000 mV/s (much lower or higher rates can also be used) whereas the current is recorded as a function of the potential. The shape of the linear scan current-potential curves for the electro-active compound present in solution depends on the diffusion conditions. The sigmoidal shape, also known as voltammetric waves presented in the Figure 2.11.2 (middle) is observed for the stationary diffusion, spherical electrodes or microelectrodes. The non-symmetric peak shape, on the right in the Figure 2.11.2, is observed for macroelectrodes in non-stirred solutions. The final constant current, i_l , is called limiting current and is proportional to the concentration of the electro-active compound. In the case of macroelectrodes in non-stirred solutions the

voltammograms have a non-symmetric peak shape. The characteristics of the obtained current-potential wave form depend on several factors such as the rate of the electron transfer, the chemical reactivity of the electro-active species and the applied scan rate. In the case of reversible (Nernstian) electrode process, i.e. fast electron transfer (fast electrode kinetics), the dependence between the electrode potential and the surface concentration of the redox species is described by Nernst equation:

$$E = E^{0'} + \frac{RT}{nF} \ln \frac{C_O(0,t)}{C_R(0,t)} \quad (\text{eg. 2.11.5})$$

where E is the potential, $E^{0'}$ is the standard potential, R is the molar gas constant, T is the temperature, n is the number of electrons involved in the electrode reaction, F is the Faraday constant, $C_O(0,t)$ is the surface concentration of the oxidized form and $C_R(0,t)$ is the surface concentration of the reduced form of the electroactive compound. For the totally irreversible electron transfer (slow electrode kinetic) the applied potential will not result in an increase of the concentration (and consequently in the current) at the electrode surface according to the Nernst equation (eq. 2.11.5). To observe the reaction on the electrode, the cathodic (reduction) process must be strongly activated by application of the cathodic overpotential, while the anodic (oxidation) process is inhibited.

For a quasireversible (quasi-Nernstian) electrode process, electrode processes are not always extremely slow or very fast. In such cases the net current includes appreciable activated components from the oxidation and the reduction processes.

2.11.3 Cyclic Voltammetry

Cyclic voltammetry (CV) is a modification of the linear voltammetry. In cyclic voltammetry the potential is linearly increased from the value E_1 to the value E_2 and reversed back to the value E_1 after the first scan, while the current is measured continuously, Figure 2.11.3.

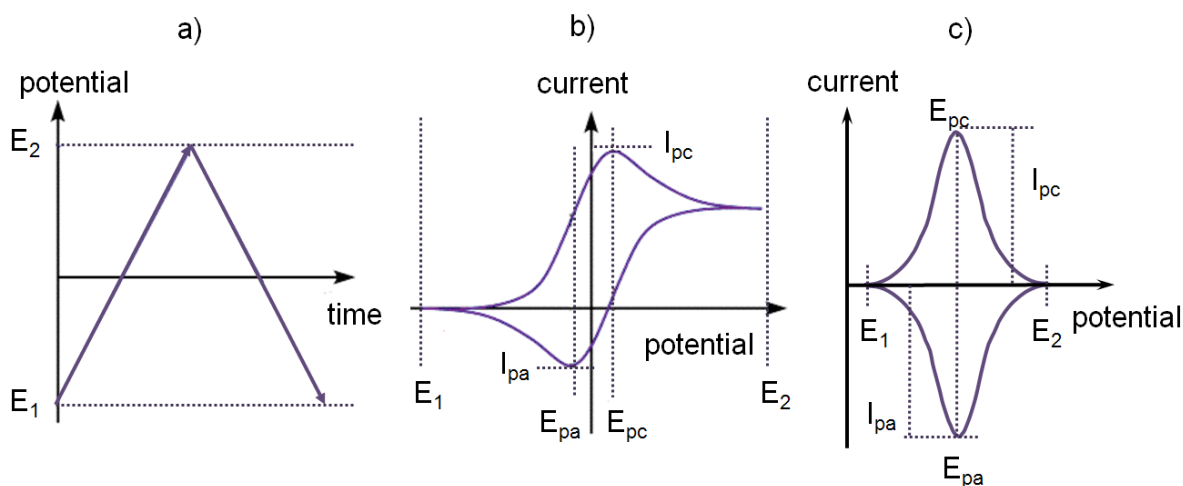


Figure 2.11.3. Illustration of the principle of cyclic voltammetry. **a)** Linear change of applied potential over time. **b)** Current voltage curve for the measured electro-active species present in the electrolyte solution. **c)** Current-voltage curve for measured electro-active species attached to the surface of the working electrode.

These cycles can be repeated numerous times for the investigation of the stability of the sample under specified conditions.

The shape of the cyclic voltammogram (CVA) is different for electroactive compounds present in the solution or attached to the electrode surface.

An example of the voltammogram of a reversible redox couple present in the electrolyte solution is given in Fig. 2.11.3-b. The reversible redox processes show both redox couples as cathodic (reduction) and anodic (oxidation) peaks while the irreversible redox processes show only one of the mentioned peaks. In general, there are several parameters which are characteristics of the current-potential plot and those are:

- a) peak current, i_p (i_{pa} -anodic peak current, i_{pc} -cathodic peak current)
- b) peak potential, E_p (E_{pa} -anodic peak potential, E_{pc} -cathodic peak potential)
- c) peak separation, ΔE_p ; it can be calculated according to:

$$\Delta E_p = |E_{pa} - E_{pc}|. \quad (\text{eq. 2.11.6})$$

These parameters are influenced by the kinetics of the charge transfer reaction (i.e. reversible (Nerstian), irreversible or quasireversible) and on the way of the mass transfer of the electroactive components to the electrode.

Consider the case when the electroactive compound is present in the electrolyte solution. The peak current, i_p , for such a process is limited by diffusion to the electrode. In the case of the reversible electrode reaction, the limiting reduction current is given by:

$$i_p = (2.69 \times 10^5) n^{3/2} A D_O^{1/2} C_O^* v^{1/2} \quad (\text{eq. 2.11.7})$$

where n is the number of the electrons involved in the electrochemical reaction, A is the electrode area, D_O is the diffusion coefficient of oxidized electroactive species, C_O^* is the concentration of the electro-active species and v is the scan rate.

The peak potential, E_p , is to the:

$$E_p = E^0 + \frac{28.5}{n} \text{ mV} \quad (\text{eq. 2.11.8})$$

where E^0 is the standard potention and n is the number of electrons involved in the electrode process.

The peak separation, ΔE_p , is expected to be:

$$\Delta E_p = |E_{pa} - E_{pc}| = \frac{59.2}{n} \text{ mV} \quad (\text{eq. 2.11.9})$$

where E_{pa} is the potential of the anodic peak, E_{pc} is the potential of the cathodic peak and n is the number of electrons involved in the electron transfer.

The ratio of the anodic peak current, i_{pa} , and anodic peak current, i_{pc} , for the reversible electrode process is equal to one,

$$\left| \frac{i_{pa}}{i_{pc}} \right| = 1 \quad (\text{eq. 2.11.10})$$

Deviation from this value is indicative of kinetic limitation or other complications in the electrode system.

In the case of the irreversible electrode process the peak current is given by:

$$i_p = (2.99 \times 10^5) \alpha^{1/2} A C_O^* D_O^{1/2} v^{1/2} \quad (\text{eq. 2.11.11})$$

where α is the transfer coefficient, A is the electrode area, D_O is the diffusion coefficient of electro-active species, C_O^* is the concentration of the electro-active species and v is the scan rate.

The peak potential, E_p , for the irreversible process can be expressed as:

$$E_p = E^{0'} - \frac{RT}{\alpha F} \left[0.78 + \ln \left(\frac{D_O^{1/2}}{k^0} \right) + \ln \left(\frac{\alpha F v}{RT} \right)^{1/2} \right] \quad (\text{eq. 2.11.12})$$

where $E^{0'}$ is the formal potential, R is the gas constant, T is the temperature, F is the Faraday constant, α is the transfer coefficient, D_O is the diffusion coefficient, k^0 standard rate constant, and v is the scan rate.

The peak separation, ΔE_p , in the case of irreversible processes is expressed as:

$$\Delta E_p = \frac{47.7}{\alpha} \text{ mV} \quad (\text{eq. 2.11.13})$$

For the quasireversible processes it was found that the peak and the various peak parameters are a function of the α and a parameter Λ , which is defined as:

$$\Lambda = \frac{k^0}{(D_O^{1-\alpha} D_R^\alpha f v)^{1/2}} \quad (\text{eq. 2.11.14})$$

Another typical case occurs when the electro-active species are immobilized on the electrode surface (for example via adsorption or covalent attachment). The current-voltage curves of the immobilized species have Gaussian shape, Figure 2.11.3-c.

For the reversible electrode process of the immobilized electro-active species, the peak current, i_p , is expressed as:

$$i_p = \frac{n^2 F^2}{4RT} v A \Gamma_O^* \quad (\text{eq. 2.11.15})$$

where n is the number of electrons involved in the reaction, F is the Faraday constant, R is the gas constant, T is the temperature, v is the scan rate, A is the surface area and Γ_O^* is the surface coverage.

The peak potential, E_p , can then be written as:

$$E_{pa} = E_{pc} = E^{0'} - \left(\frac{RT}{nF} \right) \ln \left(\frac{b_O}{b_R} \right) \quad (\text{eq. 2.11.16})$$

where $E^{0'}$ is the formal potential, R is the gas constant, T is the temperature, n is the number of electrons, b_O and b_R are moles of oxidized and reduced forms of the electro-active species present on 1 cm^2 of the electrode area.

In the case of irreversible processes for the immobilized electro-active species, the peak current is given as:

$$i_p = \frac{\alpha F^2 A \nu \Gamma_O^*}{2.718 RT} \quad (\text{eq. 2.11.17})$$

where α is the transfer coefficient, F is the Faraday constant, R is the gas constant, T is the temperature, ν is the scan rate, A is the surface area and Γ_O^* is the surface coverage.

The peak potential, E_p , for the irreversible process of the attached electro-active species is expressed as:

$$E_p = E^{0'} + \frac{RT}{\alpha F} \ln \left(\frac{RT}{\alpha F} \frac{k^0}{\nu} \right) \quad (\text{eq. 2.11.18})$$

where $E^{0'}$ is the formal potential, R is the gas constant, T is the temperature, α is the transfer coefficient, k^0 is the standard rate constant, F is Faraday constant and ν is the scan rate.

2.11.4 Kinetics of Electrode Reactions

Considering the simplest case of the electrode reaction:



where O is the oxidized form and R is the reduced form of the electroactive species, e are the electrons, n is the total number of the electrons involved in the reaction, k_f is the rate constant for the forward reaction and k_b is the rate constant for the backward reaction.

The equilibrium for such reaction is given by the Nernst equation:

$$E = E^{0'} + \frac{RT}{nF} \ln \frac{C_O^*}{C_R^*} \quad (\text{eq. 2.11.20})$$

where E is the electrode potential, $E^{0'}$ is the formal potential, C_O^* is the concentration of the oxidized species, C_R^* is the concentration of the reduced species, R is the gas constant, T is the temperature, n is the number of the electrons involved in the reaction and F is the Faraday constant.

This equation directly links the electrode potential to the bulk concentration of the reactants. The rate of the electrode reaction and both forward and backward rate constants (k_f and k_b) depend on the potential. The influence of the potential can be presented through the change of the standard free energy for this process.

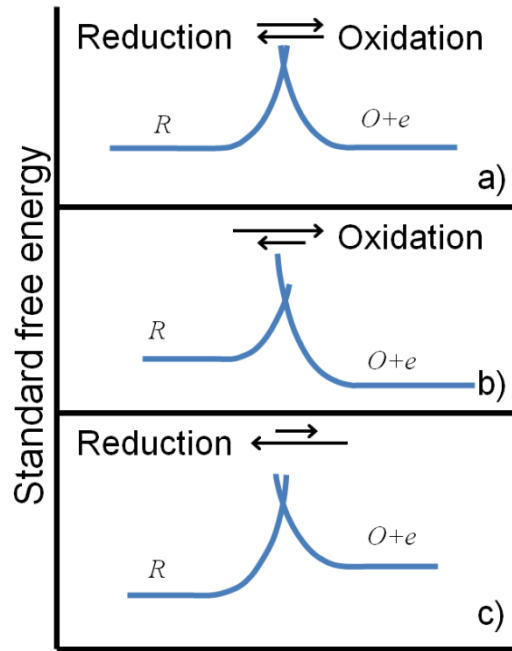


Figure 2.11.4. Scheme of standard free energy changes during a Faradaic process at various potentials. a) At potential corresponding to the equilibrium. b) At a more positive potential than the equilibrium. c) At a more negative potential than the equilibrium value.

In the case of equilibrium where $C_O^* = C_R^*$, the $E^{0'}$ is the potential where the forward and backward rate constants from the equation 2.11.19 have the same value; $k_f = k_b$. This value is called standard rate constant, k^0 . At some other potential, the rate constants are given as:

$$k_f = k^0 \exp[-\alpha f(E - E^{0'})] \quad (\text{eq. 2.11.21})$$

$$k_b = k^0 \exp[(1 - \alpha)f(E - E^{0'})] \quad (\text{eq. 2.11.22})$$

where E is the potential and $E^{0'}$ is the formal potential. The formal potential, $E^{0'}$, represents a measure of individual potential on the reversible electrode for the solutes of the effective concentration of 1 mol/dm³ and for the gasses at pressure of 1 atm, at 25 °C.

These relations lead to the complete current-potential characteristics that are given by the Butler-Volmer equation:

$$i = F A k^0 [C_O(0, t) e^{-\alpha f(E-E^{0'})} - C_R(0, t) e^{(1-\alpha)f(E-E^{0'})}] \quad (\text{eq. 2.11.23})$$

The transfer coefficient, α , is a measure of the symmetry of the energy barrier presented in the Figure 2.11.4.

2.11.5 Evaluation of the Cyclic Voltammetry Data

In order to evaluate the contribution of the Faradaic processes in cyclic voltammetry, it is necessary to subtract the charging current from the current-potential plot. The charging current is usually approximated as the baseline below the Faradaic peak. The total amount of charge is then equal to the area below the peak and the amount of the transferred charges can be obtained by integration of the peaks in the current-time plot of the voltammograms. It should be mentioned that current-time plots are equivalent to the current-potentials plots because in cyclic voltammetry the potential is linearly changing with the time.

The current, i , depends on the sweep rate, v , according to:

$$i = a v^b \quad (\text{eq. 2.11.24})$$

where a and b are adjustable parameters. The value b can be determined from the slope of the plot $\log i$ vs. $\log v$. As it was shown before, the value b can be 0.5 or 1. In the case when b is equal to 0.5 the current is proportional to the square root of the scan rate which is typical for diffusion controlled processes. In the case when the obtained value b is 1, the current is proportional to the scan rate, what is typical for the immobilized species. This implies that the electro-active compound is attached to the surface of the electrode.

The kinetics of the analyzed system can be evaluated from the plot of the peak potentials, E_p , vs. $\log v$. Such plots are also known as “trumpet” plots (due to their shape). From the slope of the plots the transfer coefficient can be evaluated and used further for the calculation of the rate constant.

2.12 Electrical Conductivity Measurements

Electrical conductivity is a measure of how good the electric current can flow through some material. The measurement is usually performed in the way that a potential, V , is applied on the sample while the resulting current, I , is measured. From these two values the resistance, R , of the sample can be calculated according to Ohm’s law:

$$R = \frac{V}{I} \quad (\text{eq.2.12.1})$$

The resistance, R , is in relation with conductance, G , according to the:

$$G = \frac{1}{R} \quad (\text{eq. 2.12.2})$$

Electric conductivity, σ , of the sample is then expressed as:

$$\sigma = \frac{1}{R} \frac{d}{A}$$

where R is the resistance, d is the thickness of the sample and A is the area of the electrode.

Two types of conductivity measurements can be performed. Direct current (*d.c.*) conductivity measurements are obtained when the applied potential is constant in the way that it does not change the polarity. Alternating current (*a.c.*) conductivity measurements are performed in the way that the polarity of the applied potential is alternating within time. The number of the alternations of the voltage per unit time is expressed as frequency. Therefore, in *a.c.* conductivity measurements the current is measured as a function of the frequency. *A.c.* conductivity measurements are also known as impedance spectroscopy.

For the simple evaluation of the conductivity of the sample, ordinary *d.c.* conductivity can be measured. In the simplest form, the measurement is performed by placing the sample between two electrodes which are connected to the electrometer according to the Figure 2.12.1

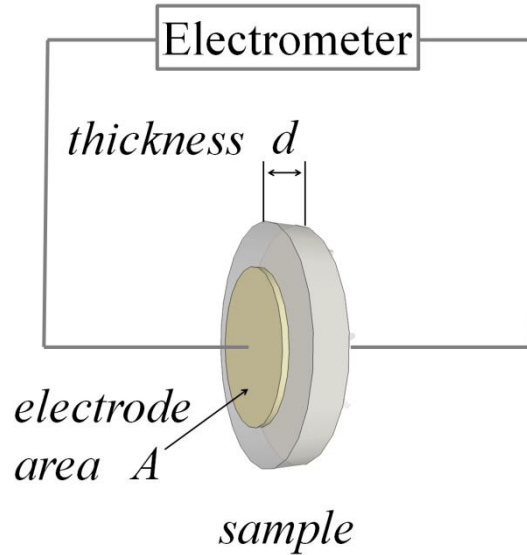


Figure 2.12.1. Scheme of the 2-point electrical conductivity measurement.

However, the main disadvantage of this method is the fact that the obtained result contains the effect of the electrode polarization which decreases the value of the conductivity.

2.13 Conductivity Measurement Through Van der Pauw Method

The most common technique used for measuring the sheet resistance of materials is called Van der Pauw method. The method was the first time proposed by Leo J. van der Pauw in 1958.^{19, 20} The method is based on a four point measurement and its advantage comes from the ability to measure precisely the resistivity of two-dimensional samples of an arbitrary shape. The approximation of two-dimensional samples can be achieved if the sample is much thinner than it is wide. In order to reduce the errors in calculations the sample needs to be symmetrical. For the measurement four contacts have to be placed on the sample as shown in Fig. 2.12.1.

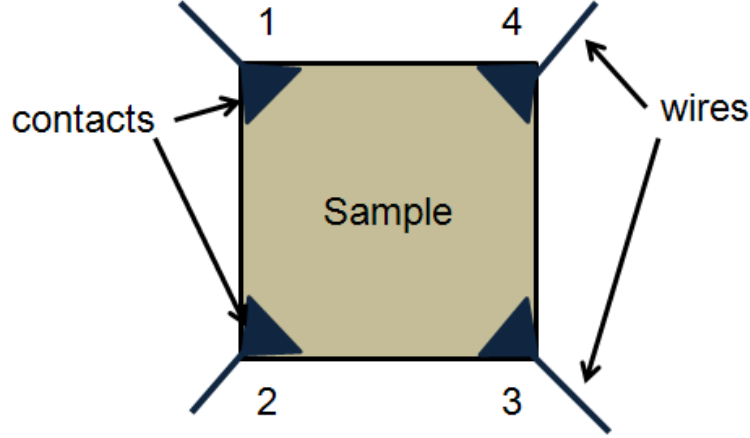


Figure 2.12.1. Illustration of the four contacts placed on the sample according to the van der Pauw method.

The contacts are placed at the boundary of the sample and must be as small as possible. The contacts are numbered counter-clockwise. In the measurement the DC current is applied between the contacts 1 and 2 (I_{12}) while the voltage is measured between contact 3 and 4 (V_{34}). According to Ohm's law, from these two values the resistance, $R_{12,34}$, can be calculated as:

$$R_{12,34} = \frac{V_{34}}{I_{12}} \quad (\text{eq. 2.12.1})$$

The sheet resistance, R_s , can be determined from the measurement of the resistance along the vertical ($R_{12,34}$) and horizontal ($R_{23,41}$) edge of the sample according to the van der Pauw equation:

$$e^{-\pi R_{12,34}/R_s} + e^{-\pi R_{23,41}/R_s} = 1 \quad (\text{eq. 2.12.2})$$

To obtain a better accuracy of the measurement, the repetition of the resistance measurement by switching the polarities of both current sources and voltage meter between all contacts is performed. From this the combination of the obtained resistivities can be presented as:

$$R_{vertical} = \frac{R_{12,34} + R_{34,12} + R_{21,43} + R_{43,21}}{4} \quad (\text{eq. 2.12.3})$$

and

$$R_{horizontal} = \frac{R_{23,41} + R_{41,23} + R_{32,14} + R_{14,32}}{4} \quad (\text{eq. 2.12.4})$$

From this the accurate sheet resistance can be calculated as:

$$e^{-\pi R_{vertical}/R_S} + e^{-\pi R_{horizontal}/R_S} = 1 \quad (\text{eq. 2.12.5})$$

In the case if $R_{vertical}=R_{horizontal}=R$ the sheet resistance, R_S , can be easily calculated as:

$$R_S = \frac{\pi R}{\ln 2} \quad (\text{eq. 2.12.6})$$

2.14 Hall Effect Measurement

The van der Pauw method is commonly applied in Hall effect measurements. The effect was discovered by Edwin Herbert Hall in 1879. Basically it describes a formation of voltage (Hall voltage) across a sample transverse to the applied electric current and an external magnetic field perpendicular to the current.^{1 21}

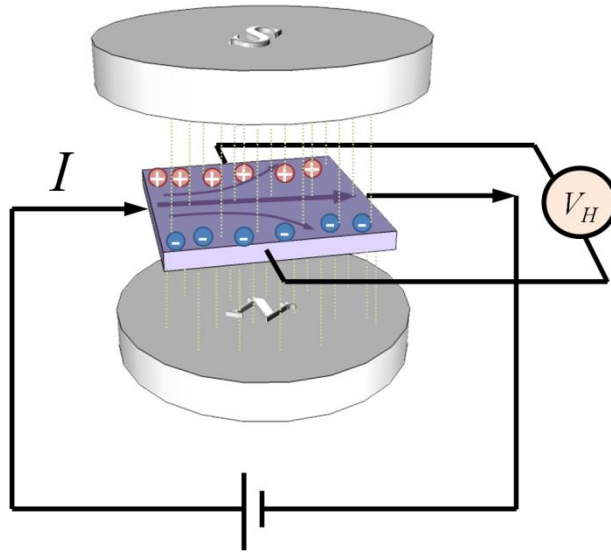


Figure 2.14.1. Illustration of the Hall effect measurement. The sample is placed into the magnetic field. The current is applied on the sample. Due to the magnetic field the charges are separating in the sample and cause the formation of a voltage perpendicular to the applied current.

The Hall effect can be used to measure the mobility and density of charge carriers. Moreover, one of the values obtained through this method is the Hall coefficient, R_H , which is a property of the material since its value depends on the number, type and properties of the charge carriers of the sample.

During the experiment, when a sample is placed in a magnetic field the charge carriers in the sample experience a Lorentz force which is proportional to the strength of the applied field and the velocity at which the charges are moving through it. If the direction of the motion of the charges is perpendicular to the applied field, the Lorentz force is the strongest and can be expressed as:

$$F_L = qvB \quad (\text{eq. 2.13.1})$$

where F_L is the Lorentz force, q is the charge of the charge carrier, v is the velocity and B is the strength of the magnetic field. If only a current is applied to the material the result is a flow of charge carriers through the material where the velocity of the flow of charge carriers is given by:

$$v = \frac{I}{nAq} \quad (\text{eq. 2.13.2})$$

where v is the velocity, I is the applied current, n is the density of charge carriers, A is the cross section area and q is the elementary charge. However, when an external magnetic field is additionally applied perpendicular to the current flow, then the Lorentz force will cause an asymmetric accumulation of charge carriers in the sample. This accumulation of charge carriers creates an electric field within the sample which leads to a potential difference across the material. This potential difference is known as Hall voltage or V_H . The Lorentz force, which the charge carriers experience under motion in the magnetic field, can be expressed as:

$$F_L = \frac{IB}{nA} \quad (\text{eq. 2.13.3})$$

where F_L is the Lorentz force, I is the current, B is the magnetic field, n is the density of charge carriers and A is the cross section area. The current continues to flow in the material as a result of the balance between the formed electric field and Lorentz force. The electric field ε induces a force F on the charge carrier q given by:

$$F = \varepsilon q \quad (\text{eq. 2.13.4})$$

From the equilibrium between the electric field and the Lorentz force, the electric field can be expressed as:

$$\varepsilon = \frac{IB}{qnA} \quad (\text{eq. 2.13.5})$$

where ε is the electric field, I is the current, B is the magnetic field, q is the charge, n is the charge carrier density and A is the cross section area. The Hall voltage is then defined as the electric field multiplied by the width of material. By combining this with the above equation the expression for the Hall voltage, V_H , can be written as:

$$V_H = \frac{IB}{qn_s} \quad (\text{eq. 2.13.6})$$

where I is the applied current, B is the magnetic field, q is the charge of charge carrier, and n_s is the density of charge carriers defined as a number of charge carriers multiplied by the depth of the sample. The polarity of the Hall voltage indicates the type of semiconductor (n- or p-type).

The measurement is performed according to the van der Pauw method. Two sets of measurements are performed; one with a magnetic field positive to the z direction and one with a magnetic field negative to the z direction. The voltage is measured by switching the polarity of the current source between two contacts and altering this between all four contacts on the sample. From this the Hall voltage, V_H , is given by:

$$V_H = \frac{V_{13}+V_{24}+V_{31}+V_{42}}{8} \quad (\text{eq. 2.13.7})$$

Where, V_{13} , V_{24} , V_{31} and V_{42} are the differences of the voltage for the positive and negative magnetic field between the respective contacts.

Considering that the Hall coefficient can have a positive or negative sign for the calculation of the charge carrier density (equation 2.13.6) the absolute value of the Hall coefficient should be taken. The mobility of the charge carriers, μ , can be calculated from the charge carrier density, n_s , and the sheet resistance, R_s , obtained through the van der Pauw method, according to the equation:

$$\mu = \frac{1}{qn_s R_s} \quad (\text{eq. 2.13.8})$$

2.15 References

1. West, A. R., *Solid State Chemistry and its Applications*. John Wiley & Sons: Chichester, 1998.
2. Cao, G., *Nanostructures & Nanomaterials; Synthesis, Properties & Applications*. Imperial College Press, London: London, 2004.
3. Skoog, D. A.; Holler, F. J.; Crouch, S. R., *Principles of Instrumental Analysis*. Thomson Brooks/Cole: 2007.
4. Williams, D. B.; Carter, C. B., *Transmission Electron Microscopy I Basics*. Plenum Press: 1996.
5. Williams, D. B.; Carter, C. B., *Transmission electron microscopy III Imaging*. Plenum Press: 1996.
6. Williams, D. B.; Carter, C. B., *Transmission electron microscopy IV Spectrometry*. Plenum Press: 1996.
7. Goldstein, J.; Newbury, D. E.; Joy, D. C.; Lyman, C. E.; Echlin, P.; Lifshin, E.; Sawyer, L.; Michael, J. R., *Scanning electron microscopy and X-ray microanalysis*. Plenum Press: 1981.
8. Adamson, A. W.; Gast, A. P., *Physical Chemistry of Surfaces*. John Wiley & Sons: 1997.
9. Turner, N. H.; Colton, R. J., *Anal. Chem.* **1982**, 54, (5), 293R.
10. Kolasinski, K. W., *Surface Science, Foundation of Catalysis and Nanoscience*. John Wiley & Sons: Chichester, 2009.
11. Santos, N. C.; Castanho, M. A., *Biophys. J.* **1996**, 71, (3), 1641.
12. El Haskouri, J.; Ortiz de Zárate, D.; Guillem, C.; Beltrán-Porter, A.; Caldés, M.; Marcos, M. D.; Beltrán-Porter, D.; Latorre, J.; Amorós, P., *Chem. Mater.* **2002**, 14, 4502.

13. Malvern Instruments, *Zetasizer Nano Series - User Manual*. 2003.
14. Hunter, J. R., *Introduction to modern colloid science*. Oxford University Press: Oxford, 1993.
15. Sing, K. S. W.; Everett, D. H.; Haul, R. A. W.; Moscou, L.; Pierotti, R. A.; Rouquerol, J.; Siemieniewska, T., *Pure and Applied Chemistry* **1985**, 57, 603.
16. Brunauer, S.; Emmett, P. H.; Teller, E., *J. Am. Chem. Soc.* **1938**, 60, (2), 309.
17. Sangwichien, C.; Aranovich, G. L.; Donohue, M. D., *Colloids and Surfaces A: Physicochemical and Engineering Aspects* **2002**, 206, 313.
18. Bard, A. J.; Faulkner, L. R., *Electrochemical Methods, Fundamentals and Applications*. Jonh Wiley & Sons, Inc.: New York, 2001.
19. van der Pauw, L. J., *Philips Research Report* **1958**, 13, (1), 1-9.
20. van der Pauw, L. J., *Philips Technical Review* **1958/59**, 20, (8), 220-224.
21. Ashcroft, N. W.; Mermin, N. D., *Solid State Physics*. Saunders College: Philadelphia, 1981.

3 Antimony Doped Tin Oxide (ATO) Nanoparticles

This chapter is based on the following publication:

Vesna Müller, Matthias Rasp, Goran Štefanić, Jianhua Ba, Sebastian Günther, Jiri Rathousky, Markus Niederberger, Dina Fattakhova-Rohlfing, “*Highly Conducting Nanosized Monodispersed Antimony Doped Tin Oxide Particles Synthesized via Nonaqueous Sol-Gel Procedure*” *Chemistry of Materials*, **2009**, 21, 5229-5236

3.1 Introduction

Because of the unique combination of transparency in the visible range and high electric conductivity, transparent conducting oxides (TCOs) such as doped indium, tin, or zinc oxides are widely used as electrodes in thin-layer transparent devices such as solar cells, flat-panel displays, smart windows or electronics, and chemical sensors. Very recently, the focus of scientific attention has shifted from thin films to crystalline TCO nanoparticles. Although the conductivity of nanocrystals cannot compete with that of the dense films, the use of nanocrystals opens the way to novel applications and novel systems unachievable by the traditional techniques. Thus, colloidal dispersions of nanocrystals make the deposition of conductive coatings by wet chemical methods possible under mild conditions, replacing expensive vacuum-based techniques and enabling coating temperature-sensitive plastic substrates.¹⁻³ Moreover, such colloidal dispersions are of great interest for inkjet printing technologies, enabling patterning of the surfaces and printing directly onto the desired electrode architectures. Finally, the nanocrystals are very attractive as primary building units for assembling nanostructured materials with defined porous architectures,⁴ which are promising as large-surface-area transparent electrodes for efficient optoelectronic devices.⁵⁻⁹ All these applications require monodispersed highly crystalline nanoparticles that are easy to

redisperse in various solvents to form stable colloidal solutions. Antimony-doped tin oxide (ATO) is a well-known transparent semiconductor with a large band gap (>3.6 eV), providing transparency in the visible range and high n-type electric conductivity, which makes it a valuable alternative to much more rare and expensive indium tin oxide (ITO).¹⁰

Consequently, the preparation of ATO nanoparticles with different shape, size, conductivity, and degree of agglomeration has been addressed by a large variety of techniques. Generally, chemical methods provide much better control over the particle size and their stabilization in solution than the physical methods.¹¹ The sol-gel,¹²⁻¹⁴ polymeric precursor,¹⁵⁻¹⁸ and coprecipitation^{19, 20} techniques mostly provide either large particles or nanoparticle agglomerates. Much better control over the growth of ATO particles was achieved by hydrothermal and solvothermal techniques.²¹⁻²⁶ Despite the variety of the existing preparation methods, better control of the particle size, doping level, and particle dispersibility in different solvents is still the objective. Recently Prof. Niederberger invented a general nonaqueous-solution route to metal-oxide nanoparticles, using benzyl alcohol as both the oxide source and the solvent.²⁷⁻²⁹ This method was successfully used for the preparation of dispersible crystalline SnO_2 nanoparticles, which were assembled into crystalline films with periodic mesoporous architecture and large surface area.⁶ Recently, da Silva et al. Prepared ATO nanoparticles with 18 mol% antimony via this route, which are redispersible in organic solvents using surface-modifying agents.³⁰ However, the authors did not characterize the structure and conductivity of the obtained nanoparticles. In the present study, the intention was to make the best use of the potential of this synthesis route to prepare ATO nanoparticles with very small particle size, a narrow size distribution, and especially high electric conductivity. Special emphasis was placed on their good self-assembling properties, because they are intended as suitable building blocks for the assembly of more complex nanoarchitectures. The good electric properties of conducting oxides require an optimum doping level, a uniform distribution of the doping atom within the host lattice without phase

separation and without any surface enrichment.³¹ Therefore, the ATO nanoparticles that contain antimony in a wide range of concentrations were prepared. The focusing of the research was placed on the effect of the nature and relative concentration of the metal oxide precursors and processing conditions on the structure, morphology, and conductivity properties of the obtained nanoparticles. This synthetic approach provides ATO nanoparticles with exceptional properties such as facile redispersibility in various solvents and high electric conductivity, making them superior to reported ATO particles prepared via other techniques.

3.2 Experimental Section

3.2.1 Chemicals

Tin(IV) chloride (99 %), antimony(V) chloride (1 M in CH₂Cl₂), antimony(III) chloride ($\geq 99.0\%$), antimony(III) acetate (99.99 %), antimony(III) ethoxide, anhydrous toluene ($\geq 99.7\%$; $<0.005\%$ water), anhydrous benzyl alcohol (99.8 %, $<0.003\%$ water), and tetrahydrofuran (THF) ($\geq 99.5\%$) were purchased from Aldrich and used without further purification.

3.2.2 Synthesis of ATO Nanoparticles

The ATO particles with different antimony contents are labeled as X% ATO, where $X = \text{Sb}/(\text{Sb} + \text{Sn})$ (mol %). In a typical synthesis of the 10% ATO particles, the tin tetrachloride (3.2 g, 12.3 mmol) and antimony compound (1.35 mmol) were dissolved in toluene (10 mL) and added to benzyl alcohol (30 mL, 291 mmol) under continuous stirring.³² The total amount of tin and antimony was constant, equaling 13.65 mmol (0.34 mol/L) for all antimony contents. The clear solution was placed in a closed glass vessel into a laboratory oven at the temperatures from 100 °C to 150 °C and was kept there until it turned turbid, then cooled

down to room temperature. The reaction time was dependent on the reaction temperature and the relative amount of the antimony precursor. While the reaction at 100 °C was completed within 20 h, the reaction at 150 °C was already completed within 2 h. The particles were separated by centrifugation at 50 000 rcf for 10 min, and then washed sequentially in toluene and three times in acetone. Each washing step included ultrasonication for 15 minutes and centrifugation. The residual organic content of the washed and air-dried particles is 15-20 wt %, according to thermogravimetric (TGA) analysis.

3.2.3 Characterization Techniques

The TGA analysis was performed on a Netzsch Model STA 4400 C TG/DSC (heating rate of 10 K/min in a stream of synthetic air of 25 mL/min).

High-resolution transmission electron microscopy (HRTEM) and scanning transmission electron microscopy in high-angle annular dark-field mode (STEM-HAADF) were performed using a FEI Titan 80-300 system that was equipped with a field-emission gun operated at 300 kV. The particulate samples were prepared by evaporating a drop of a diluted suspension of particles with small amounts of Pluronic F127 in THF on a Plano carbon-coated copper grid. EDX analysis of the ATO particles deposited on the silicon wafer was performed using a JEOL Model JSM-6500F SEM microscope that was equipped with a field-emission gun operated at 4 kV. Calculation of the amount of antimony and tin from EDX spectra was performed using INCA Analyzer 4.07 Microanalysis Suite software.

EELS spectra were recorded on GIF Tridiem 863 spectrometer. The samples were illuminated with parallel beam and the spectra were taken in diffraction mode with camera length 90 mm. Raman spectra were recorded with a LabRAM HR UV-vis (Horiba Jobin Yvon) Raman microscope (Olympus BX41) coupled with a Symphony CCD detection system, using a HeNe

laser at a wavelength of 632.8 nm. The recorded Raman spectra were deconvoluted using a symmetric Gaussian function.

X-ray diffraction (XRD) was performed in reflection mode, using a Bruker Model D8 Discover diffractometer with Ni-filtered Cu K α -radiation equipped with a Vantec-1 position-sensitive detector. XRD measurements used for precise determination of lattice parameters of cassiterite and cassiterite-type solid solutions were conducted in reflection mode using an ItalStructures diffractometer APD2000 with monochromatic Cu K α radiation (graphite monochromator). XRD patterns of the samples and lanthanum hexaboride (LaB₆, space group: $Pm\bar{3}m$, $a = 4.15690$ Å, JCPDS File Card No. 34-427), added as an internal standard, were collected over a 2θ range of 20°-100° with a step of 0.02° and fixed counting time of 30 s per step. To determine deviations of the estimated lattice parameters, the obtained XRD patterns were refined using two different approaches, namely, the Le Beil³³ method of whole-powder-pattern decomposition (program GSAS³⁴ with graphical user interface EXPGUI³⁵) and the Rietveld refinements³⁶ (program MAUD³⁷). In all cases, the R_{wp} indexes of the refined patterns were <5%.

The particle size d was estimated from (i) the broadening of the 110 reflection in the XRD pattern, using the Scherrer equation, $d = \frac{K\lambda}{B \cos\theta_B}$ where B is the full width at half-maximum (FWHM) of a diffraction peak, θ_B the diffraction angle, and K the Scherrer constant (~ 0.9), and (ii) from the HRTEM images. To eliminate contribution of the carbon film background and to calculate the particle size more precisely, a fast Fourier transform (FFT) filtering was performed in the following way. On the FFT image of the desired HRTEM image, reflections with the highest intensities were masked (in this case, 110) and an inverse Fourier transform of the masked area was performed. In this way, it is possible to obtain information only about the crystalline part of the desired reflection and the contribution of background carbon is decreased. The average particle size was determined from ca. 100 particles.

X-ray photoelectron spectroscopy (XPS) analysis of the particles on a silicon substrate was performed using a VSW Model HA 100 electron analyzer. The $K\alpha$ radiation was provided by a non monochromatized magnesium anode system ($MgK\alpha=1253.6$ eV). The recorded photoelectron spectra were fitted using Gaussian profiles, and the concentration of excited surface atoms was determined by measuring the integral intensity of the peaks under investigation after subtracting the background counts. The binding energy scale of the spectrometer has been calibrated by referring to the Ag $3d_{5/2}$ peak obtained from a clean silver metal foil (binding energy (BE) of 368.25 eV). The linearity of the energy scale was adjusted using the so-called auger parameter of metallic silver.³⁸ Because of the high conductivity of the investigated films, no charging of the samples was observed. The main XPS peaks for the O and Sb atoms, O 1s and Sb $3d_{5/2}$, respectively, are superposed at ~ 530 eV, which prevents direct evaluation of the incorporated antimony. Therefore, for quantification of the antimony content in the film, the Sb $3d_{3/2}$ peak was used. The photo-ionization cross sections listed by Yeh and Lindau³⁹ were used for quantitative analysis. Because of the almost-identical BE values of the core levels of interest (Sn 3d, Sb 3d, and O 1s), the electron analyzer transmittance is almost identical for the acquired photoelectrons and does not have to be taken explicitly into account. To determine the amount of oxygen in the film, photoelectron spectra at ~ 530 eV were acquired and deconvoluted to the O 1s and Sb $3d_{5/2}$ contribution. The spin-orbit splitting between the Sb $3d_{5/2}$ and Sb $3d_{3/2}$ peak was set to 9.4 eV. Evaluation of $Sb^{5+}/(Sb^{3+} + Sb^{5+})$ ratio by XPS calculation was performed according to the Sb $3d_{3/2}$ band, following the method developed by Terrier et al.⁴⁰ The $3d_{3/2}$ band can be split into two Gaussian lines, centered at 540.1 eV (Sb^{5+}) and 539.2 (Sb^{3+}), respectively.

Conductivity measurements on ATO nanoparticles were performed on pellets 15 mm in diameter. The pellets were prepared by pressing 300 mg of finely ground ATO in an evacuated KBr press under a pressure of 10 tons/cm². The cold-pressed pellets were directly used for the measurements without any additional thermal treatment. The pellets were

contacted between the gold-plated cylindrical electrodes (Bürklin, 4 mm in diameter) which acted both as voltage and current leads. Resistance across the pellet was measured by a digital multimeter (Keithley Instruments, Model 2000) in a four-probe mode to eliminate the undesired resistance of the measuring circuit. The specific conductivity (σ) was calculated from the measured resistance R as $\sigma = \frac{d}{R \cdot A}$ where A is the electrode area and d is the pellet thickness. The Hall mobility, the charge carrier density, and the respective conductivity/resistivity were measured using the Hall method (ECOPIA, Model HMS 3000), using a magnetic field of 0.55 T.

3.3 Results and Discussion

An anhydrous benzyl alcohol, which was used in the synthesis, served both as a solvent and as an oxygen source. Tin tetrachloride was used as tin precursor, whereas several antimony precursors were tested. The purpose for this was to test the influence of the nature of the antimony precursor on the doping efficiency and solubility of antimony in a tin oxide lattice. The used commercially available antimony compounds with different antimony valence states and various ligands were antimony(III) chloride, antimony(V) chloride, antimony(III) acetate, and antimony(III) ethoxide. In the synthesis, the precursors were first dissolved in a toluene and the obtained mixture was afterward added to the benzyl alcohol. The role of the toluene mixture is to dilute the solution of tin (IV) tetrachloride prior to mixing it with benzyl alcohol in order to prevent exothermic hydrolysis reaction of the tin precursor. The final obtained mixtures in benzyl alcohol were completely transparent independently on the composition, Fig. 3.3.1-a. The reaction mixtures in the closed glass bottles were put into laboratory oven at the temperatures from 100 °C to 150 °C and kept till they turned turbid, afterwards cooled down to room temperature.

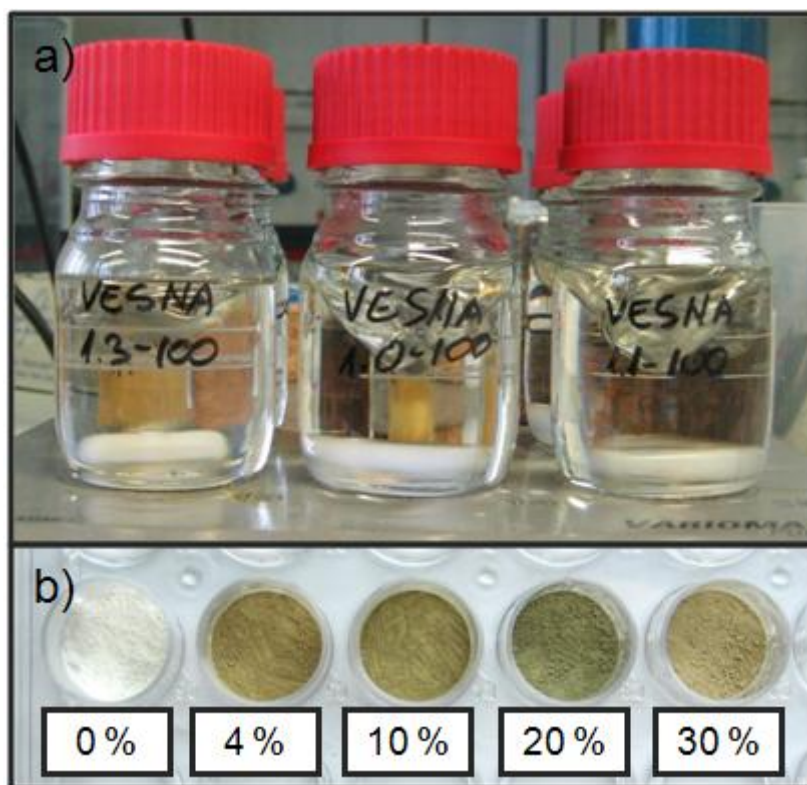


Figure 3.3.1. a) Synthesis mixtures in benzyl alcohol for elaboration of ATO nanoparticles with various Sb content prior to the transfer into the oven and **b)** ATO nanoparticles with different Sb content (indicated in labels) obtained after the solvothermal reaction. The particles were separated by centrifugation and dried without any additional thermal treatment.

The rate of the particle formation and the particle yield are greatly dependent on the reaction temperature. The reaction at 100 °C requires 20 h in order to be completed, while only 2 h are sufficient if the temperature is increased to 150 °C. In contrast, the nature of the antimony precursor influences only marginally the mean particle size and its distribution, and the degree of agglomeration (see Table 3.3.1).

Table 3.3.1. Influence of the Antimony Precursor and the Reaction Temperature on the Reaction Time, Yield, and Mean Size of 10% ATO Nanoparticles.

Synthesis temperature 100°C				Synthesis temperature 150°C		
Sb precursor	Reaction time, h	Yield (%)	Particle size ^a , nm (TEM/XRD)	Reaction time, h	Yield (%)	Particle size ^a , nm (TEM/XRD)
SbCl ₅	18.5	20	3.2 /3.1	1.5	75	4.0 /4.5
Sb(ac) ₃	21	30	2.9 /2.9	2	80	3.6 /4.1
SbCl ₃	19.5	15	3.0 /2.7	1.75	80	3.9 /4.2
Sb(OEt) ₃	23	30	3.1 /3.0	2.25	70	3.7 /4.3

^a Determined from HRTEM images and from the line broadening of the d₁₁₀ reflection in XRD patterns using the Scherrer formula.

Precipitates obtained from the synthesis, which were centrifuged and washed, differed in color, depending on the composition of the starting precursor's solution. The sample where no antimony precursors in the synthesis were added was white in color, typical for the tin oxide. However, an addition of a very small amount of antimony, namely 4 mol%, induced a change in color of the product from white to brownish. Further addition of antimony, namely 10 or 20 mol% of antimony precursors, leads to a brownish-green coloration of the obtained powder. The color in the doped samples is an indication of the presence of electrons in the conducting band due to impurity doping.²²

3.3.1 Morphology and Size of ATO Nanoparticles

For all used precursors, the TEM images show practically nonagglomerated or only loosely agglomerated highly crystalline nanoparticles, what can be seen as lattice fringes in HRTEM and STEM (see Table 3.3.1 and Figure 3.3.2).

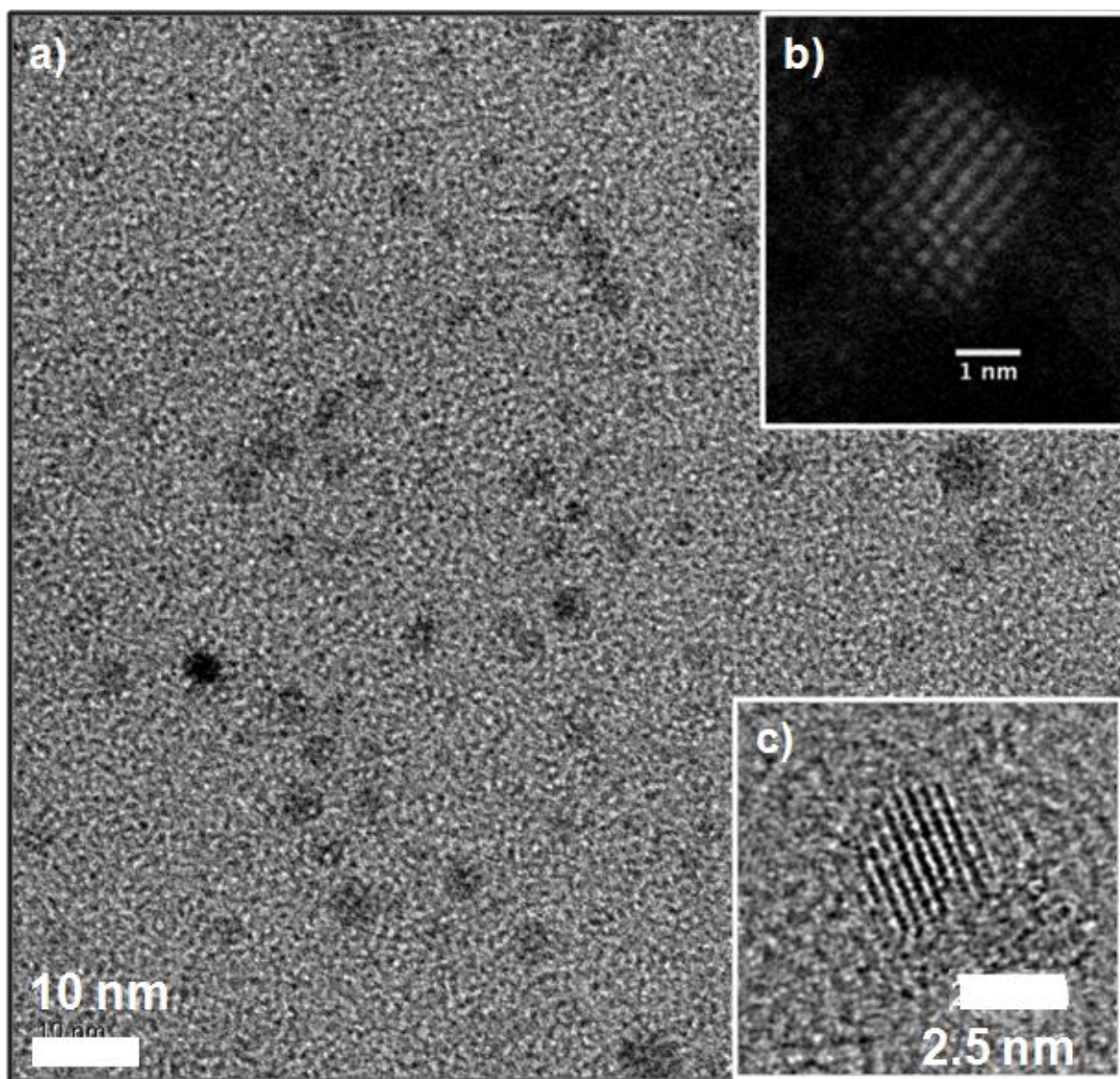


Figure 3.3.2. a) An overview TEM image of 10 % ATO nanoparticles prepared by using $\text{Sb}(\text{Ac})_3$ as antimony precursor and at reaction temperature of 150 °C. b) High-resolution STEM-HAADF image of a single nanoparticle. c) HR-TEM image of a single nanoparticle in the inset. All images demonstrate completely crystalline and practically non-agglomerated particles.

The average size of the particles is ~3 nm and ~4 nm when they were synthesized at 100 or 150 °C, respectively. Independently of the ligand nature, all the $\text{Sb}(\text{III})$ precursors provide similar nonagglomerated particles exhibiting a narrow particle size distribution. The use of precursors which are more reactive toward solvolysis, such as of SbCl_5 , leads to an acceleration of the particle formation reaction, a slight increase in the particle size, and an increase in the amount of agglomerated nanoparticles, Fig. 3.3.3.

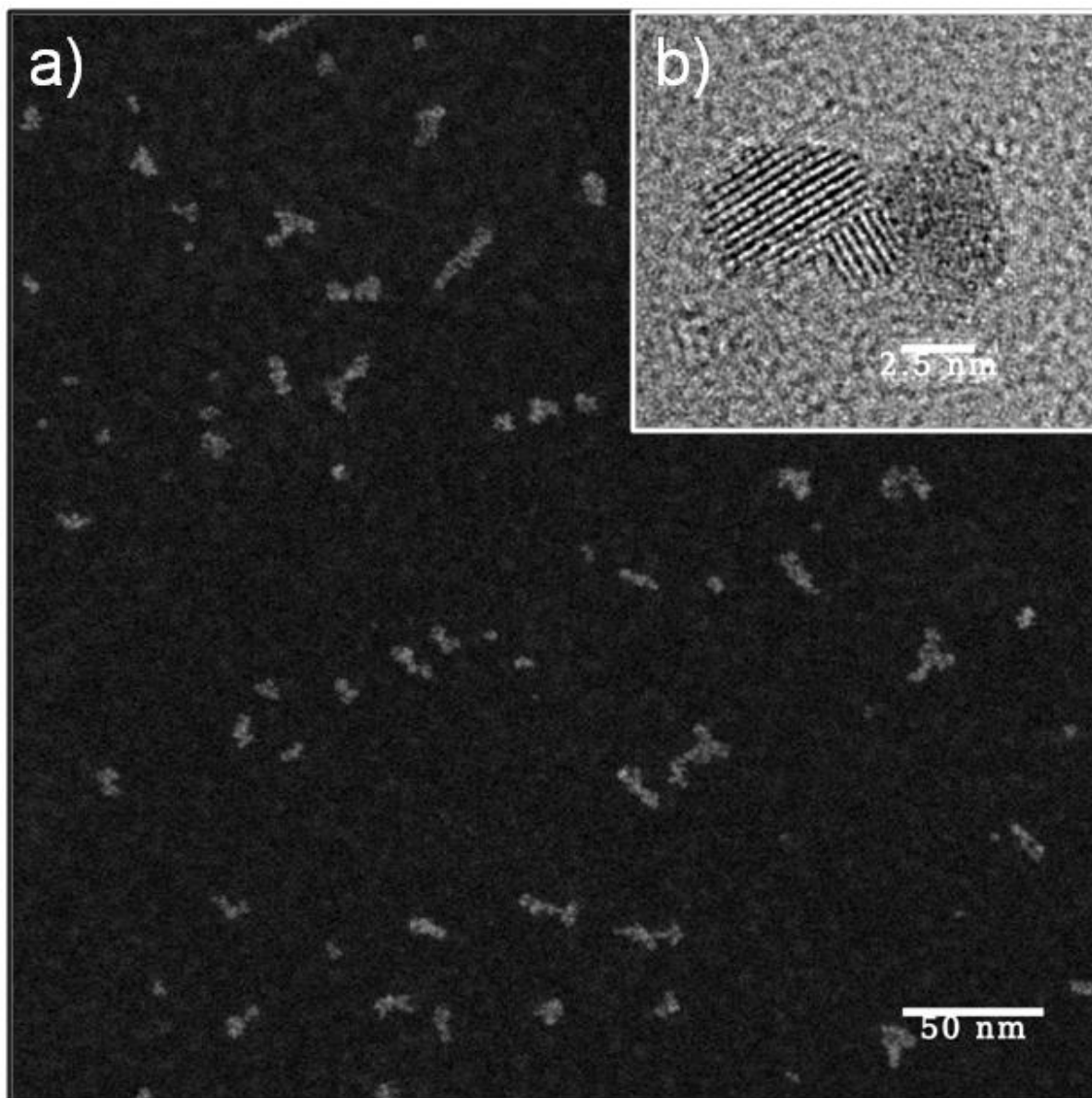


Figure 3.3.3. a) Overview STEM-HAADF image of the 10 % ATO nanoparticles prepared by using SbCl_5 as antimony precursor and reaction temperature of 150 °C. b) HR-TEM image of the agglomerated nanoparticles.

3.3.2 Solubility of ATO Nanoparticles

The particles can be easily redispersed at high concentration (~3-8 wt. %) in different solvents, such as water, ethanol, or THF, without the addition of any surface-stabilizing agent to form stable transparent colloidal solutions (Figure 3.3.4-a). The dispersibility of the antimony-doped nanoparticles is much better than that of the pristine SnO_2 ones. Moreover, it is worse in more-polar solvents such as water but is greatly improved by the addition of a few drops of concentrated hydrochloric acid. Such a striking difference could originate from the

different surface charge of the particles with the varying antimony content, and this highlights the significant role of electrostatic effects in the colloid's stabilization, Fig. 3.3.4.

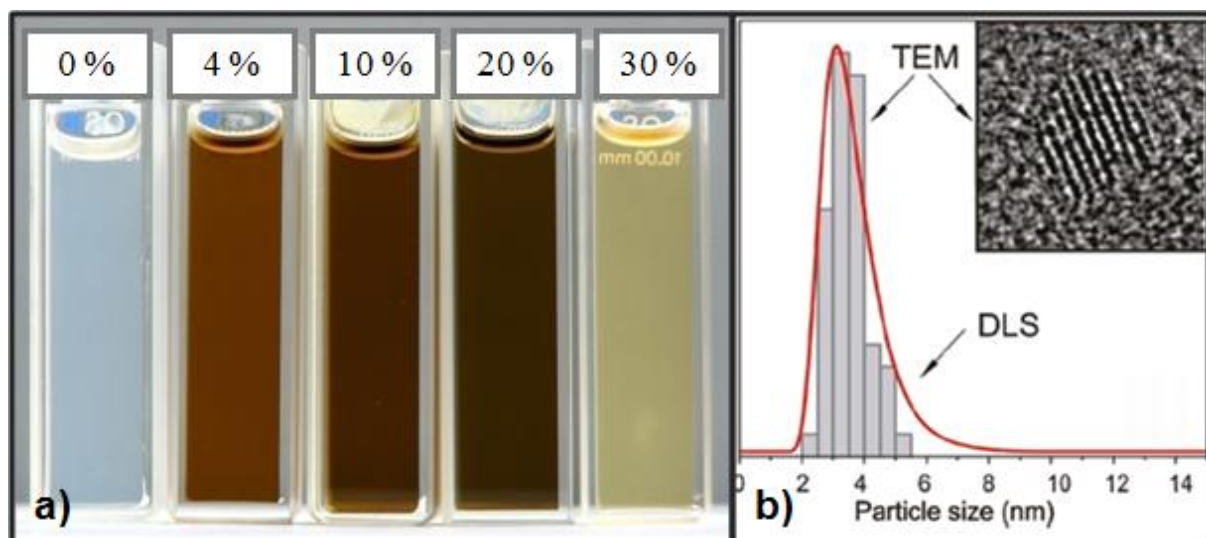


Figure 3.3.4. **a)** Colloidal dispersions of ATO nanoparticles in THF (particle concentration 5 wt%) and **b)** size distribution of the 10% ATO nanoparticles prepared using $\text{Sb}(\text{Ac})_3$ at 150°C , determined from HR-TEM images of ca. 100 nanoparticles (gray bars) and from DLS measurement (red line) of a colloidal dispersion in THF of the same nanoparticles.

The particles in the solution are practically nonagglomerated and show a narrow size distribution, as determined by DLS.

3.3.3 Structure of ATO Nanoparticles (XRD, Raman)

With regard to the properties of obtained ATO particles, the solubility limit of antimony dopant inside of the SnO_2 lattice and the influence of the dopant concentration on the structure of the formed ATO particles were of primary importance. Therefore, particles that contained 0-50 mol% antimony were prepared using $\text{Sb}(\text{ac})_3$ as the antimony source and used for investigation of the mentioned properties.

Figure 3.3.5 shows the XRD patterns of the undoped and antimony-doped ($x = 10\text{-}50\text{ mol \%}$) tin oxide synthesized at 150°C using $\text{Sb}(\text{OAc})_3$ as the antimony precursor.

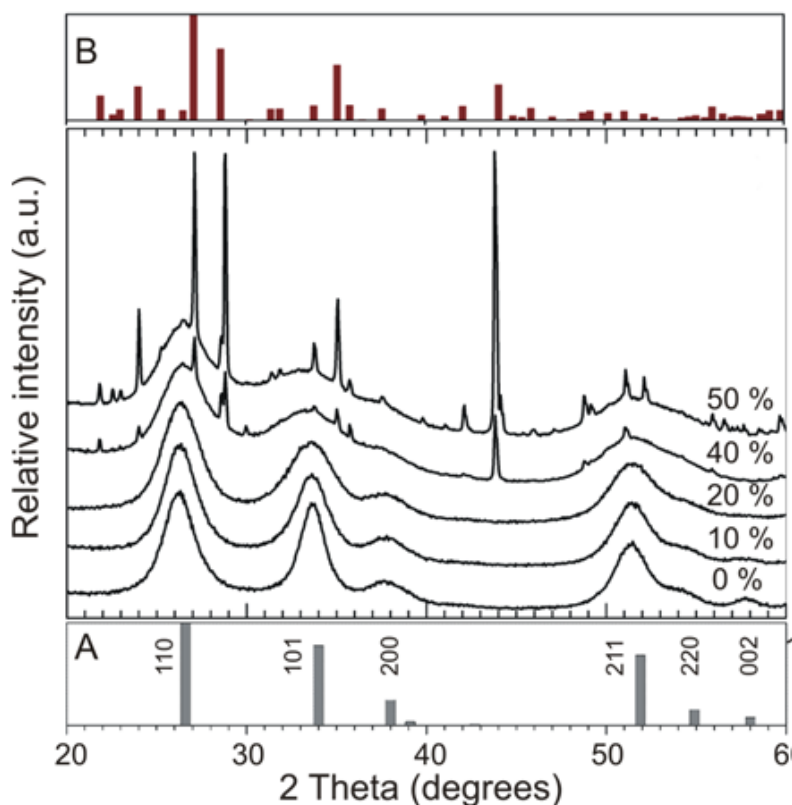


Figure 3.3.5. X-ray diffractograms of the particles synthesized at 150 °C using $\text{Sb}(\text{Ac})_3$ as the antimony source.

The XRD pattern of the undoped sample contains broad diffraction lines typical of cassiterite ($\text{P4}_2/\text{mm}$, JCPDS File Card No. 41-1445). The ATO nanoparticles with antimony content up to 30 mol % show the presence of only one crystalline phase structurally closely related to cassiterite. These results indicate that the SnO_2 lattice can accommodate up to 30 mol % Sb atoms without the significant changes in the structure. The first indication of a second crystal phase ($\text{Sb}_4\text{O}_5\text{Cl}_2$, $\text{P2}_1/\text{a}$, JCPDS File Card No. 30-0091) appears only at a very high antimony concentration of 40 mol %. [Note that, because the patterns indicate strongly preferred orientation in the 001 direction, the 002 ($28.9^\circ 2\theta$) and 003 ($43.9^\circ 2\theta$) diffraction lines appear significantly stronger than they should be, according to JCPDS File Card No. 30-0091.] In collaboration with Dr. Goran Štefanić (Ruđer Bošković Institute, Zagreb, Croatia) it was found that the solid solubility limit of Sb ions in the cassiterite lattice is ~ 38 mol %, as estimated from the dependence of the diffraction line intensities of the $\text{Sb}_4\text{O}_5\text{Cl}_2$ phase (the 100, 212, and 111 lines) on the initial content of antimony, and by extrapolation to zero

intensity (Figure A-3.1.). With increasing antimony content, peaks that correspond to the cassiterite structure become broader, as a result of the decrease in particle size from 4.3 nm for the undoped sample to 4.1 and 4.0 nm for samples with 10 and 20 mol% antimony, respectively. These results are in good agreement with the results obtained by TEM (Table 3.3.1). An increase in the antimony content shifts the 110 diffraction line toward higher angles, while the position of the 101 diffraction line remains almost unchanged (see Figure 3.3.6).

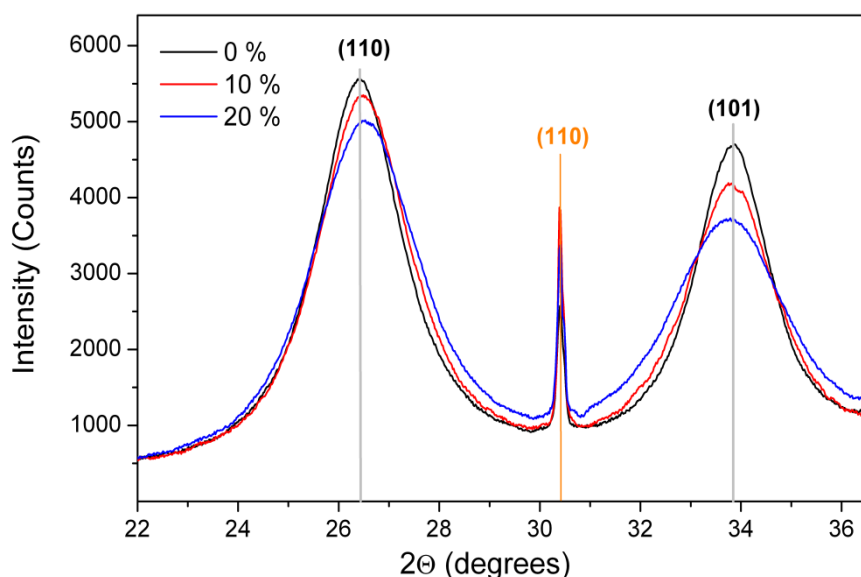


Figure 3.3.6. Portion of the diffraction patterns of the ATO samples with up to 20 mol% of antimony synthesized at 150 °C. Gray bars mark the positions of the cassiterite diffraction lines 110 and 101. Orange bar marks the position of LaB₆ diffraction line 110.

Consequently, the incorporation of Sb ions causes an asymmetric distortion of the cassiterite lattice, because of the difference in the ionic radii of the Sn⁴⁺ ion (0.69 Å in six-coordination) and Sb ions (0.76 Å and 0.61 Å in six-coordination for the Sb³⁺ and Sb⁵⁺ ions, respectively). Estimated values of the unit cell parameters of cassiterite (0% ATO) and cassiterite type solid solutions (10% ATO and 20% ATO) obtained from the Le Bail and Rietveld refinements of the XRD patterns performed by Dr. Goran Štefanić are listed in the Appendix Table A-3.1 and in the Appendix Figure A-3.2. The obtained results show that the increase in the antimony

content causes a linear decrease in parameter a and a linear increase in parameter c , Appendix Figure A-3.3.

The phase composition of the ATO particles was further studied by Raman spectroscopy, which is able to deliver structural information on amorphous and poorly crystalline samples and is very sensitive to the presence of even minor amounts of crystalline phases.⁴¹ The typical bulk vibration modes predicted by group theory for the SnO₂ rutile structure,⁴² namely, A_{1g} (630 cm⁻¹), B_{2g} (775 cm⁻¹), and E_g (477 cm⁻¹) are observed for the undoped SnO₂ sample, although with low intensity, probably because of the small particle size, Fig. 3.3.7.

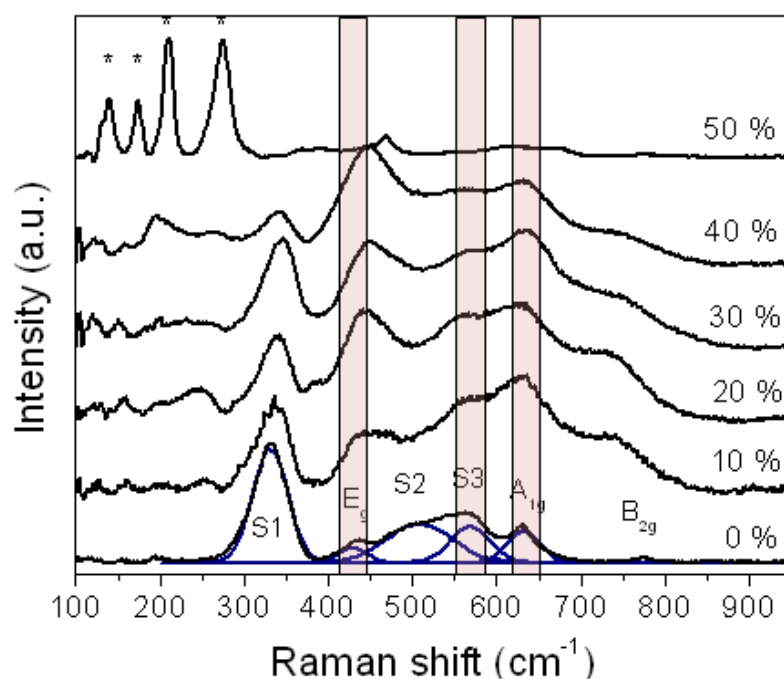


Figure 3.3.7. Raman spectra of the as-prepared ATO particles with different antimony content. The particles were synthesized at 150 °C using Sb(Ac)₃ as the antimony source.

Moreover, the spectra of the samples that contain up to 40 mol% antimony show only the bands that correspond to rutile-type SnO₂. The position of these bands shifts with the increasing antimony content, indicating the influence of the replacement of Sn ions with Sb ions within the lattice. A_{1g} and B_{2g} modes, which correspond to the vibrations perpendicular to the c -axis,⁴² decrease in intensity and shift to lower wave numbers with increasing

antimony content, while the E_g mode, which corresponds to vibration in the direction of c-axis,⁴² follows the opposite trend. This continuous change in the vibration modes of the doped oxides is in good agreement with the XRD data, which also proves the slight asymmetric distortion of the crystalline SnO_2 lattice, which is due to the incorporation of Sb ions. No bands that correspond to antimony oxides were found for the samples that contained up to 40% antimony. Strong bands of the antimony (III) oxide⁴³ were observed only for the sample that contained 50 mol% antimony. All the spectra of ATO particles feature an intense band at 333 cm^{-1} (S1) and bands between 500 and 570 cm^{-1} (S2 and S3). They were often observed for nanosized tin oxides,^{41, 44-46} being frequently assigned to the surface vibration modes of tin oxide.⁴⁷⁻⁴⁹ The intensity of these bands changes with increasing antimony content, which can be related to vibration modes of incorporated Sb atoms inside the cassiterite lattice.⁴³

3.3.4 Composition of ATO Nanoparticles

One of the most important properties of the ATO nanoparticles for this research is the electrical conductivity which is to a large extent dependent on the antimony content and its oxidation state in the tin oxide lattice. Therefore an extensive investigation of the composition of the ATO nanoparticles was performed.

The total antimony content determined by the surface sensitive XPS method is practically the same as that obtained by the bulk-sensitive energy-dispersion X-ray (EDX) spectroscopy method. The results indicate that the particle composition is homogeneous throughout the complete sample without any enrichment of the surface of the nanoparticles with Sb atoms, Table 3.3.2.

Table 3-2. Properties of ATO nanoparticles with different Sb content^a.

Sb content in precursor solution, (mol %)	Particle size, (nm)		Sb content in ATO nanoparticles, (mol %)		Molar fraction of Sb ³⁺ and Sb ⁵⁺ atoms ^c (%)		Electric conductivity, (S cm ⁻¹)
	XRD ^b	HRTEM	EDX	XPS	Sb ⁵⁺	Sb ³⁺	
0	4.3	3.7	0	0	0	0	9·10 ⁻⁷
4	-	-	3.0	4.9	58	42	1·10 ⁻⁴
10	4.1	3.6	10.0	12.0	60	40	8·10 ⁻⁶
20	3.6	3.5	19.0	19.1	60	40	6·10 ⁻⁶
30	3.0	3.0	30.0	28.9	57	43	1·10 ⁻⁶

^a The particles were prepared via the nonaqueous solvothermal reaction of SnCl₄ and Sb(Ac)₃ in benzyl alcohol at 150 °C without additional thermal treatment.

^b Determined from the broadening of the d₁₁₀ reflection, using the Scherrer formula.

^c Determined by XPS.

The oxidation state of the antimony present in ATO nanoparticles significantly influences the conductivity. While Sb⁵⁺ ions act as electron donors, forming a shallow donor level close to the conduction band of SnO₂, Sb³⁺ behaves as an electron acceptor. If both oxidation states coexist, which is often observed for ATO materials, the resistivity is given by the ratio of Sb⁵⁺ and Sb³⁺ sites,⁵⁰ which was analyzed by X-ray photoelectron spectroscopy (XPS). The overview spectra (see Figure 3.3.8-a) obtained for the ATO samples demonstrate the strong peaks that correspond to Sn¹⁴ (see Figure 3.3.8-b) and to oxygen and antimony (see Figure 3.3.8-c).

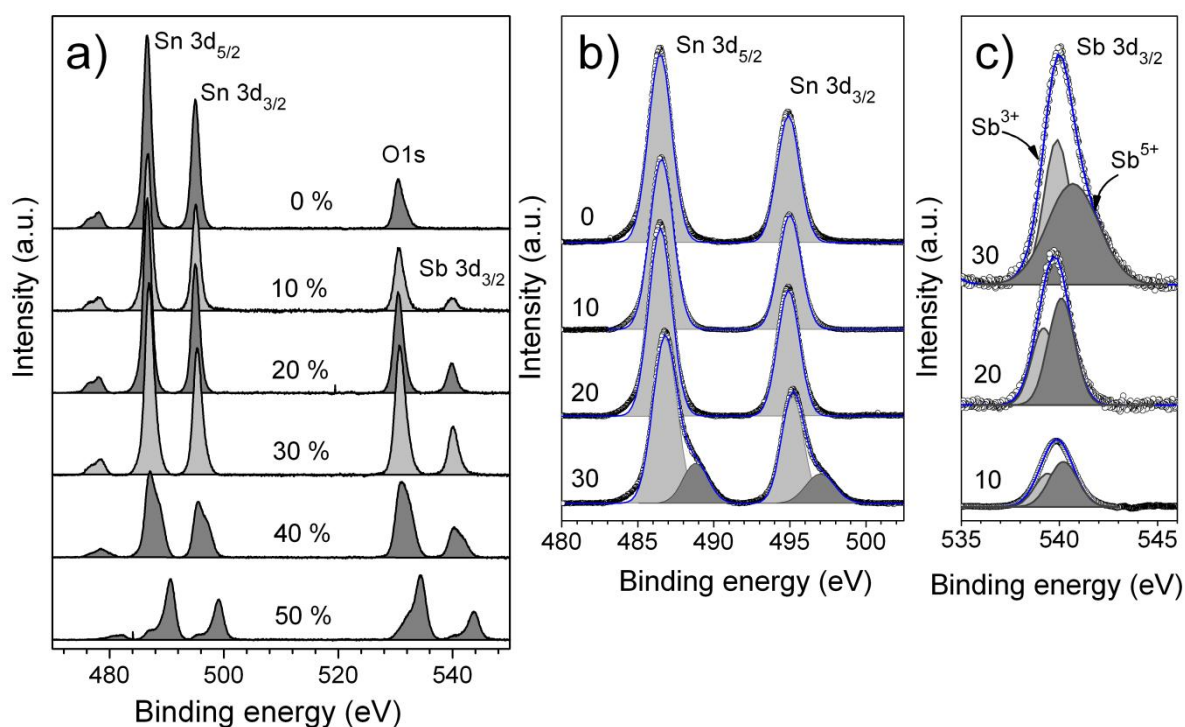


Figure 3.3.8. X-ray photoelectron spectra (XPS) of the as-prepared ATO nanoparticles with varying antimony content synthesized at 150 °C, using $\text{Sb}(\text{Ac})_3$ as an antimony source: overview spectra for (a) the energy region between 460 and 560 eV and the sections corresponding to (b) the Sn 3d doublet¹² and (c) the Sb 3d_{3/2} peaks. The solid lines correspond to the experimental spectra, and the open circles and the gray-shaded areas indicate the results of the Gaussian peak fits.

The Sb 3d_{3/2} peak fits proved that all the particles contain ca. 60% Sb^{5+} and 40% Sb^{3+} independently on the total amount of antimony. Therefore, the effective donor Sb^{5+} concentration exceeds that of the acceptor by 20% (effective n-type doping).

3.3.5 Characterization of Nanoparticles by Spatially Resolved Techniques

The necessity for investigation of the homogeneity of dopant distribution inside of the cassiterite lattice rises from the direct influence of the dopant on the conductivity of ATO nanoparticles. Even slight variations in the composition of such nanosized object alter physicochemical properties of ATO nanoparticles. The diminishing size of the ATO nanoparticles implies serious requirements on characterization techniques. Due to this the further characterization of their composition was performed through High Resolution Transmission Electron Microscopy (HR TEM) and Electron Energy Loss Spectroscopy (EELS). Such

evaluation can provide information on even small changes in composition of nanoparticles directly indicating the possible presence of the phase enrichment of the shell of nanoparticles.

In order to confirm the presence of only one phase in ATO nanoparticles a detailed analysis of HR-TEM and SAED images of pure SnO_2 and antimony doped samples was performed.

The analysis of SAED of pure SnO_2 nanoparticles shows the diffraction rings typical for cassiterite structure. The distance between the lattice fringes in 110 direction corresponds to 3.3 Å, Fig. 3.3.9.

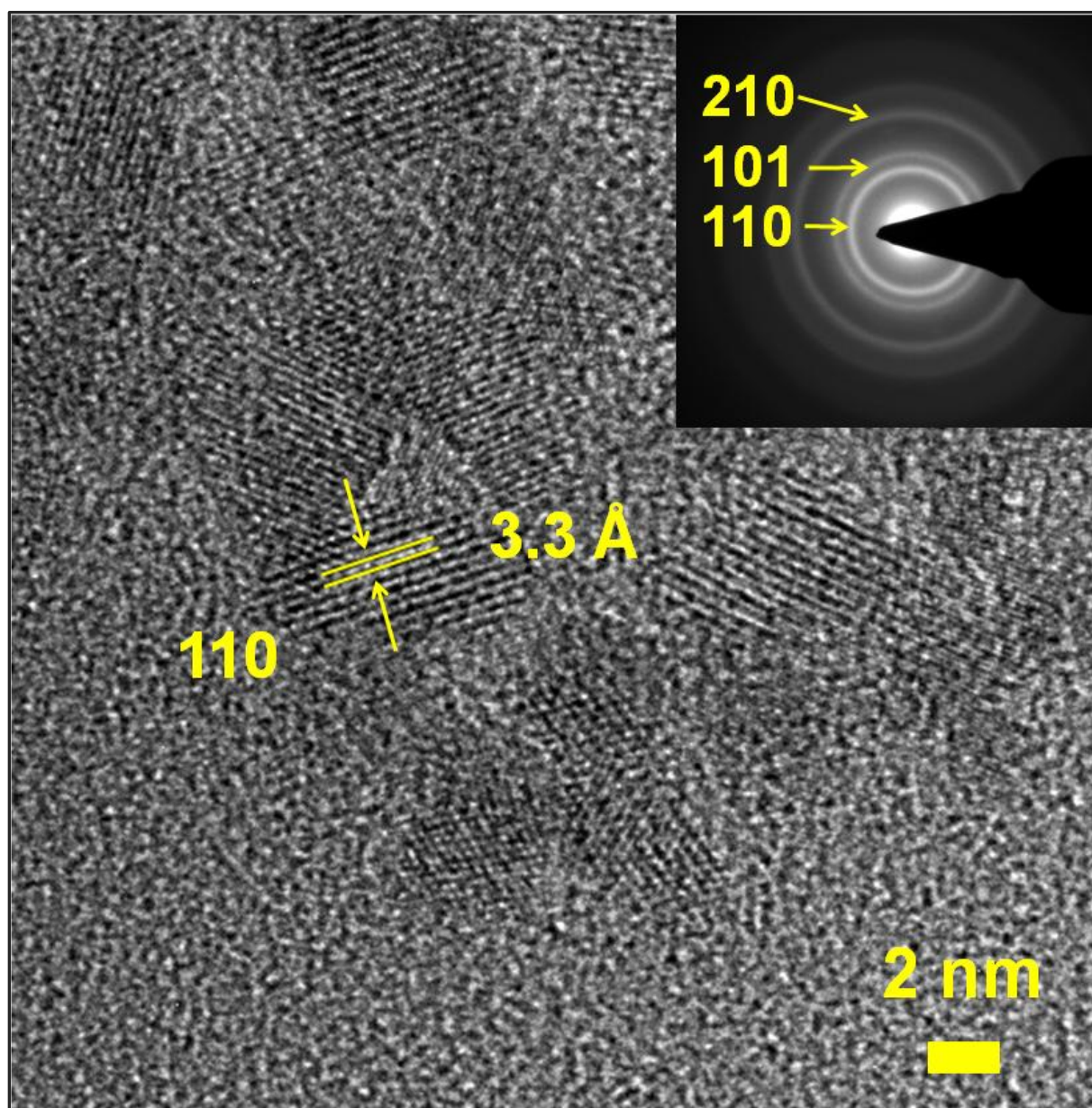


Figure 3.3.9. High resolution TEM image of SnO_2 nanoparticles. Inset shows selected area electron diffraction of pure SnO_2 nanoparticles.

The obtained lattice distance for 110 is in good agreement with the literature data and obtained XRD data. The same type of analysis on the sample which contains 20 mol% of antimony was performed, Fig. 3.3.10.

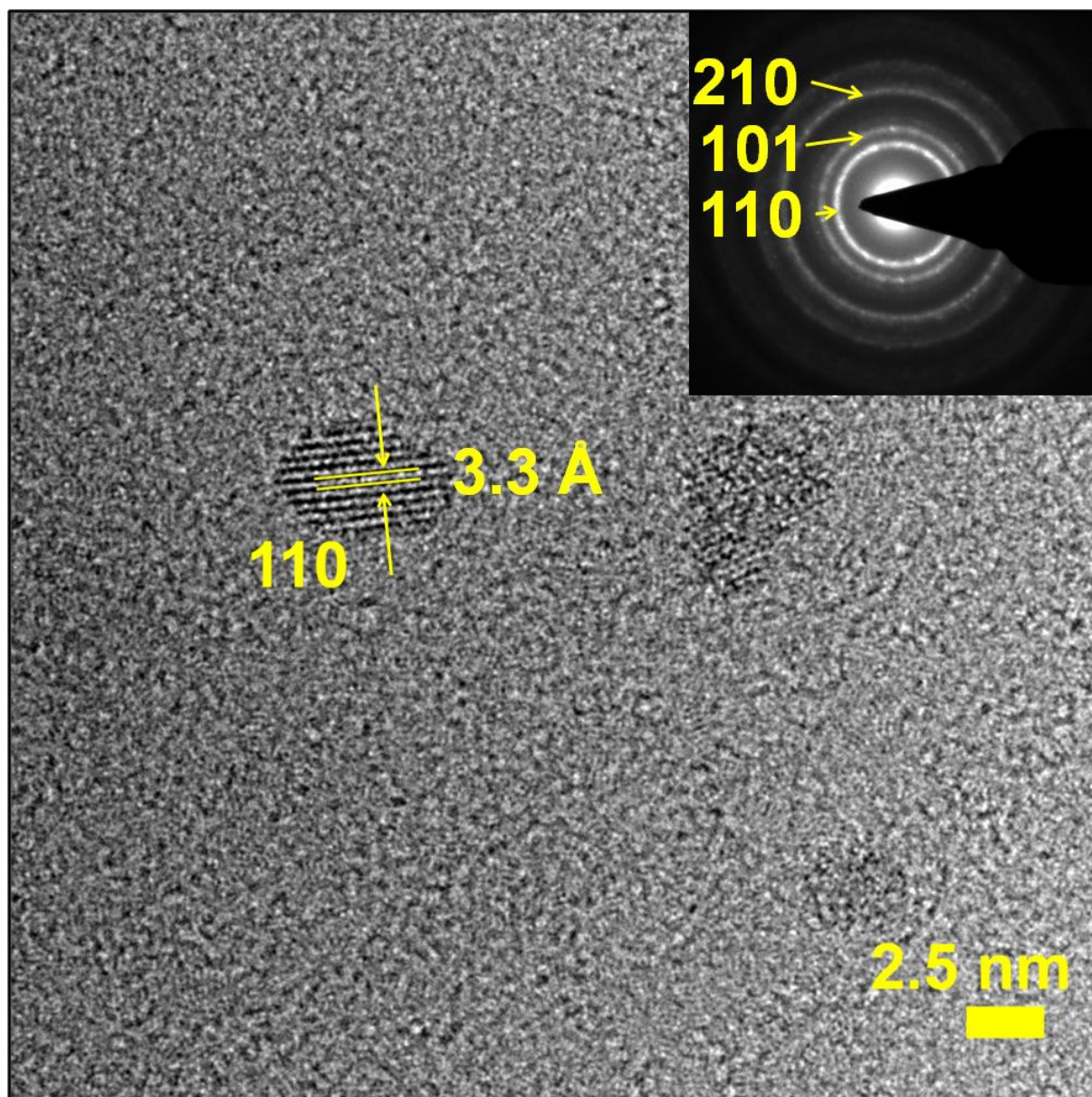


Figure 3.3.10. High resolution TEM image of ATO nanoparticles containing 20 mol% of antimony. Inset shows selected area electron diffraction (SEAD) of ATO₂₀ nanoparticles.

In the case of particles that contain 20 mol% of antimony, evaluation of electron diffraction data indicates the presence of only one phase with typical cassiterite structure, without the presence of any other phase. These data are in good agreement with results obtained through X-ray diffraction. The lattice parameters of ATO₂₀ nanoparticles for the 110 direction are

3.3 Å indicating no changes in lattice parameters in comparison to the particles of pure SnO₂. Although the evaluation of XRD data shows a minor influence of incorporation of antimony into the cassiterite lattice was observed, the observed changes are below the detection limit in TEM analysis.

Further analysis of SnO₂ and ATO nanoparticles was performed by Electron Energy Loss Spectroscopy (EELS), Fig. 3.3.11.

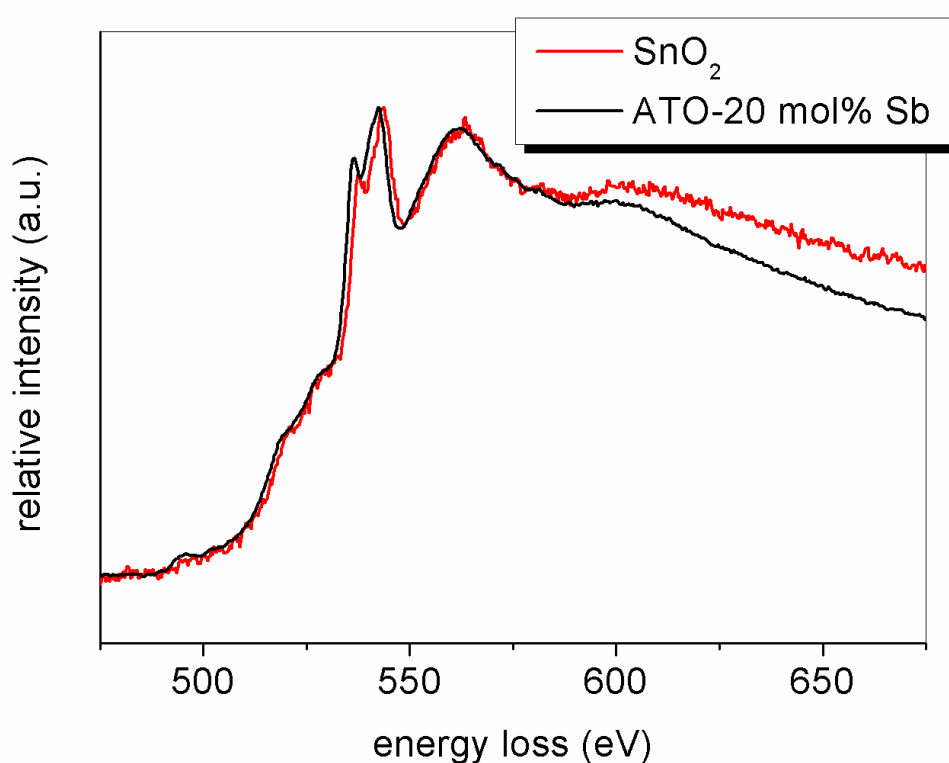


Figure 3.3.11. EELS spectra of pure SnO₂ and ATO nanoparticles containing 20 mol% of antimony.

EELS spectra of pure SnO₂ nanoparticles contain sharp peaks which start at 537 eV and correspond to the oxygen K-edge. The tin M_{4,5} edge is observed low in intensity around 492 eV and is positioned close to the oxygen edge. Spectra of ATO nanoparticles which contain 20 mol % of antimony appear similar to spectra of pure SnO₂. According to the literature the Sb M_{4,5} edge is positioned at 524 eV and is almost completely overlapping with oxygen K edge.⁵¹ However, the enrichment of the particles with antimony would lead to slight changes

in the intensities of edges, which in this case was not observed. Therefore, it is possible to assume from the obtained results that particles are completely homogeneous in composition.

3.3.6 Electrical Conductivity (Hall Effect Measurements)

The results of the electrical conductivity measurements performed on pelletized ATO nanopowders with different antimony contents are presented in Figure 3.3.12. The conductivity of the pure SnO₂ sample is very low, being only 9×10^{-7} S/cm. The conductivity dramatically increases because of the introduction of small amounts of antimony, reaching a maximum for the 4% ATO nanoparticles. The conductivity of this sample is more than 2 orders of magnitude higher compared to that of pure tin oxide nanoparticles.

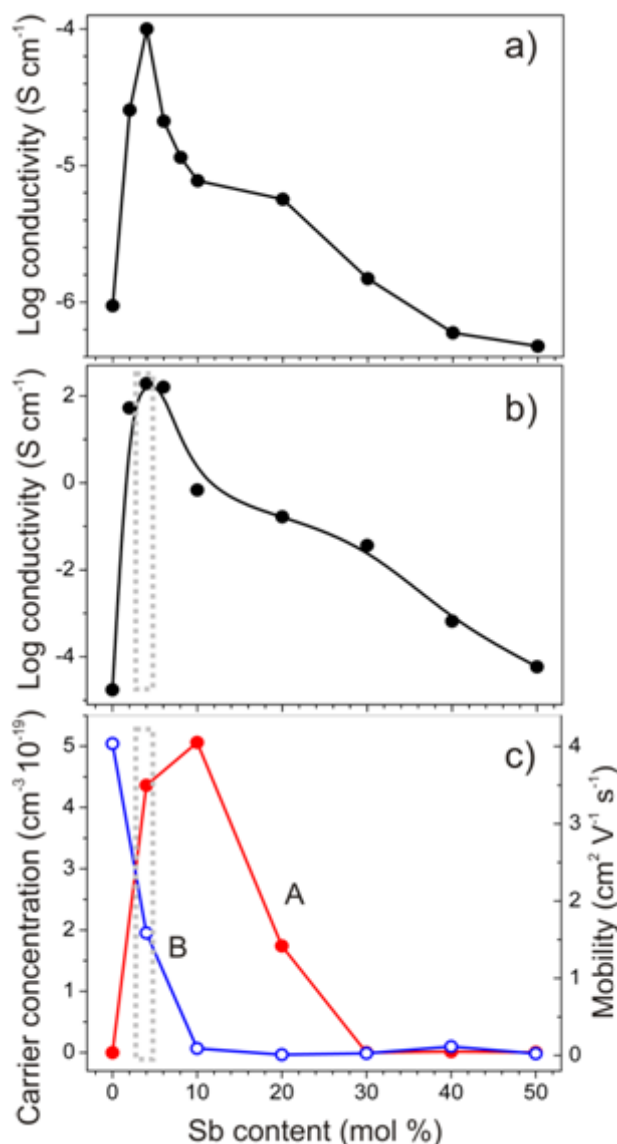


Figure 3.3.12. Conductivity (plotted in a logarithmic scale) of the pellets pressed from ATO nanoparticles using $\text{Sb}(\text{Ac})_3$ as the antimony precursor and synthesized at 150 °C. **a)** as prepared pellets, **b)** pellets after calcination in air at 500 °C, **c)** corresponding charge carrier concentrations (line A) and charge carrier mobility (line B) of the calcined pellets.

Further increase in the antimony content leads to a deterioration of the electrical conductivity. Samples containing >20 mol% antimony exhibit a conductivity comparable to or even worse than that of the undoped SnO_2 . The value of 1×10^{-4} S/cm for conductivity is the highest ever reported for nonannealed ATO particles only a few nanometers in size. Nuetz et al.²⁵ obtained a value of ca. 5×10^{-7} S/cm for pressed 6% ATO nanoparticles 4-6 nm in size. Goebbert et al. reported a conductivity on the order of 10^{-8} S/cm for ATO particles ca. 4 nm in size that were

prepared by hydrothermal treatment, but were annealed at 300 °C.²⁶ The conductivity measured for our ATO nanoparticles, which was in the order of 10^{-4} S/cm, however, is far below that obtained for dense ATO films (which have conductivities up to 1×10^3 S/cm).¹⁰ The main reason is the charge scattering at the grain-boundary contacts between the nanoparticles, which is the main scattering mechanism in nanocrystalline ATO materials.⁵² This effect becomes much stronger with decreases in particle size and is the dominating scattering mechanism in our particles, which are only 3-4 nm in size. One also must recall that the particles contain some traces of organic species (mostly benzoate groups) adsorbed on their surface (these are not completely removed after particle washing and act as an insulating shell), and that the particles were not annealed to improve the contact between them. Therefore, the apparent conductivity of the particle ensemble is much lower than the real bulk conductivity of the ATO lattice of a single particle, because of the very small particle size and the very poor contact between the particles. This observation is confirmed by the drastic increase in the pellets conductivity (by 4 orders of magnitude) after their calcination at 500 °C in air (see Figure 3.3.12.b). The thermal treatment mainly leads to particle sintering and the removal of organic impurities, providing good electrical contact between them and, to some extent, leads to an increase in the particle size. The calcined pellets exhibit a similar effect of the antimony content on the conductivity, but at a much higher conductivity level. The dependence of the charge carrier concentration on the antimony content in our ATO particles exhibits a pronounced maximum for the antimony concentration of 4%-10% (see Figure 3.3.12-c), which is attributed to the formation of a shallow donor level close to the conduction band of SnO₂.^{52, 53} For even higher antimony contents, the carrier concentration decreases, because the increased disorder raises the effective activation energy of the donor.^{52, 53} Even more strongly than the charge carrier concentration, the carrier mobility is affected by the variation of the dopant concentration, rapidly decreasing with the introduction of rather small amounts of antimony. As the XRD, Raman, and TEM experiments have shown, the particle

size decreases and the lattice disorder increases as the antimony content increases. This contributes to the increased effects of grain-boundary scattering, which is the reason of the deteriorated charge carrier mobility in doped samples.⁵² Consequently, the best performance of the sample with 4 mol% antimony is the result of the optimum combination of the high charge carrier concentration and high mobility inside the lattice.

3.4 Conclusions

Conducting ATO nanoparticles were prepared by a nonaqueous solution route, using benzyl alcohol, tin tetrachloride, and a suitable Sb(III) compound. The nonagglomerated particles, 3-4 nm in size, are easy to redisperse in a variety of solvents and form stable transparent colloidal solutions without any stabilizing agents. The increase in antimony content causes a continuous decrease in particle size and a slight asymmetric distortion of the cassiterite SnO₂ lattice. The particle composition is homogeneous throughout the entire volume, without any enrichment of the surface with Sb atoms. Introduction of an antimony dopant dramatically increases the particle conductivity, which reaches a maximum for 4% antimony, being more than 2 orders of magnitude higher than that of the pristine SnO₂ nanoparticles. The conductivity further improves to ca. 2×10^2 S/cm because of particle sintering during annealing in air at 500 °C.

The combination of exceptional virtues makes the developed ATO nanoparticles an ideal material for electrostatic applications or use as a conducting additive for both organic and inorganic composites. As such, colloidal solutions of conducting nanoparticles are of special interest for the direct printing of patterned electrodes. Above all, the reported ATO particles are attractive building blocks for assembling transparent conducting three-dimensional (3-D) architectures, which offer favorable extra properties, in comparison to those of traditional conducting layers.

3.5 Appendix

Table A-3.1. Refined values of the unit-cell parameters of cassiterite (0 % ATO) and cassiterite-type solid solutions (10 % ATO and 20 % ATO) obtained from the results of Le Bail and Rietveld refinements of XRD patterns.

Sample	Le Bail refinement (GSAS program)			
	$a / \text{\AA}$	$c / \text{\AA}$	$V / \text{\AA}^3$	R_{wp}
0 %	4.7679(2)	3.1841(2)	72.38(1)	0.033
10 %	4.7573(2)	3.1932(2)	72.27(1)	0.029
20 %	4.7510(2)	3.2024(2)	72.28(1)	0.024
Sample	Rietveld refinement (MAUD program)			
	$a / \text{\AA}$	$c / \text{\AA}$	$V / \text{\AA}^3$	R_{wp}
0 %	4.7677(2)	3.1869(2)	72.44(1)	0.036
10 %	4.7575(3)	3.1936(3)	72.28(2)	0.038
20 %	4.7517(3)	3.2026(3)	72.31(2)	0.033

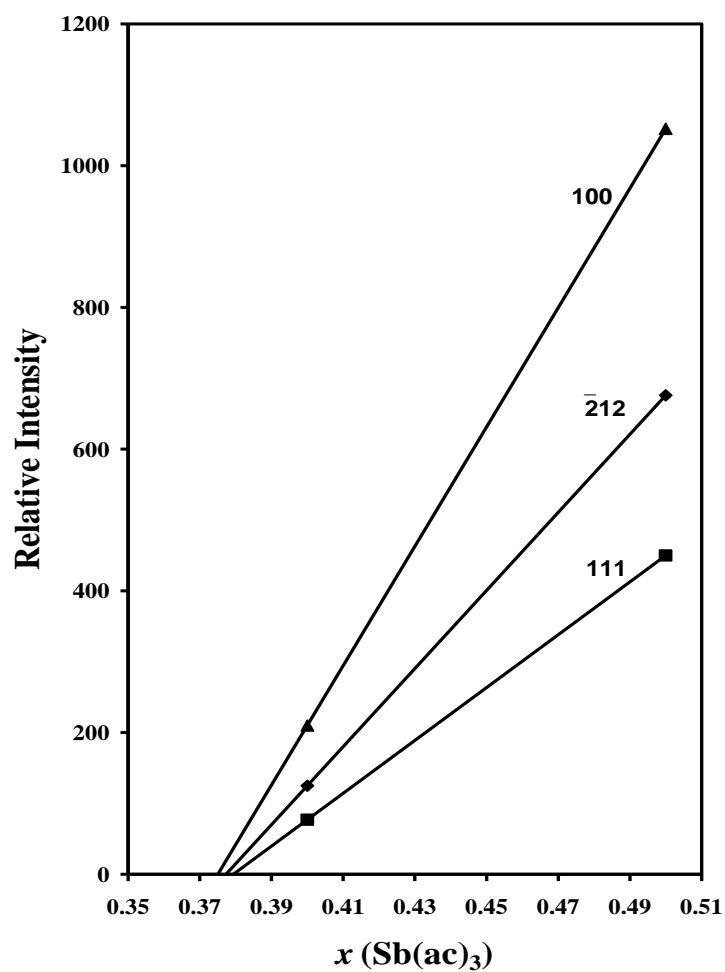


Figure A-3.1. Determination of solid solubility limits of antimony ions in cassiterite lattice from the dependence of relative intensities of prominent diffraction lines of the $\text{Sb}_4\text{O}_5\text{Cl}_2$ phase (lines 100, $\bar{2}12$ and 111) on the initial content of $\text{Sb}(\text{ac})_3$, and by extrapolation to zero intensity

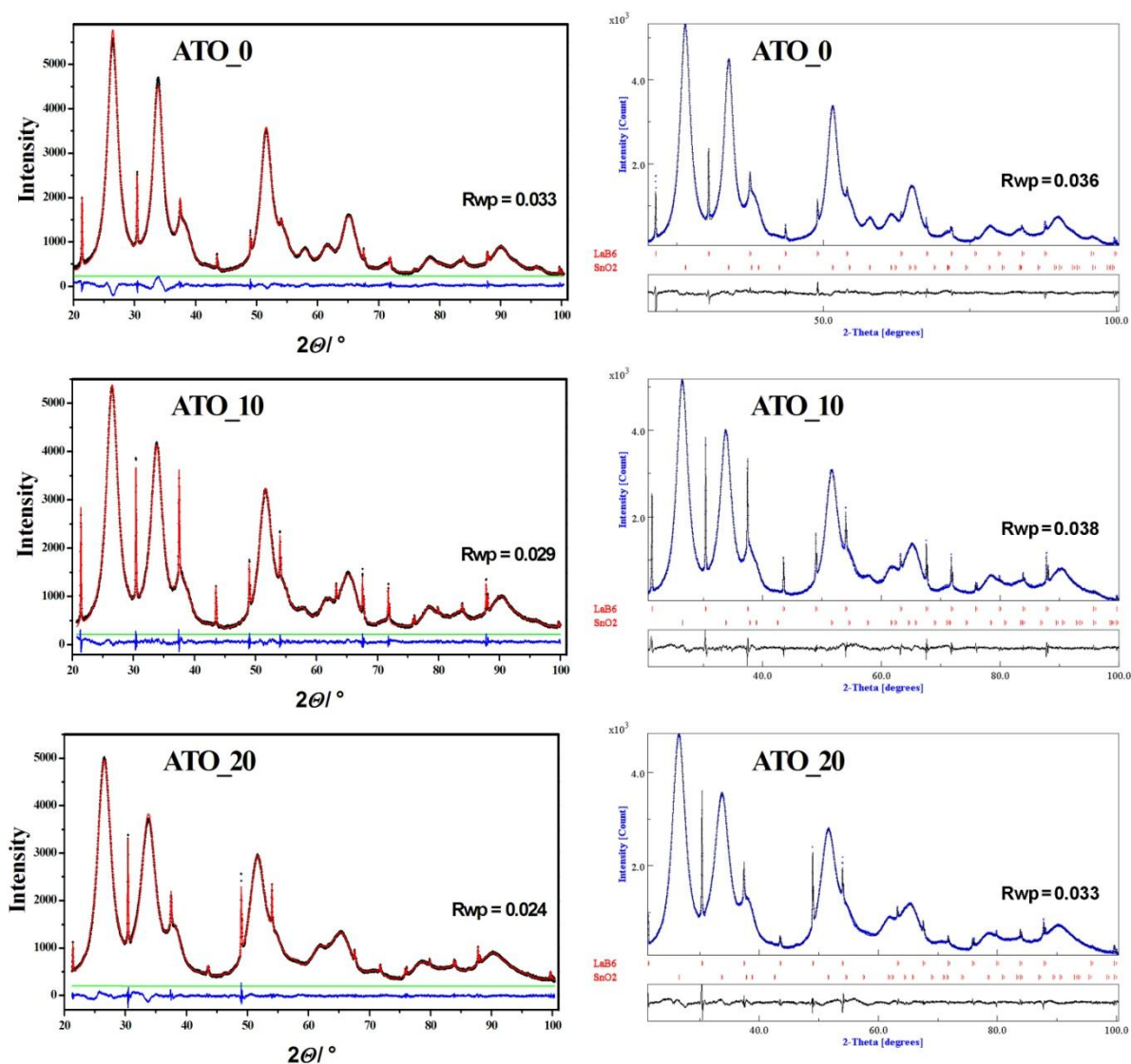


Figure A-3.2. The results of Le Bail refinements (left) and Rietveld refinements (right) on powder diffraction patterns of the ATO samples with up to 20 mol% of antimony, synthesized at 150 °C, and lanthanum hexaboride as an internal standard. The difference between the observed and calculated patterns is shown as a line in the lower field.

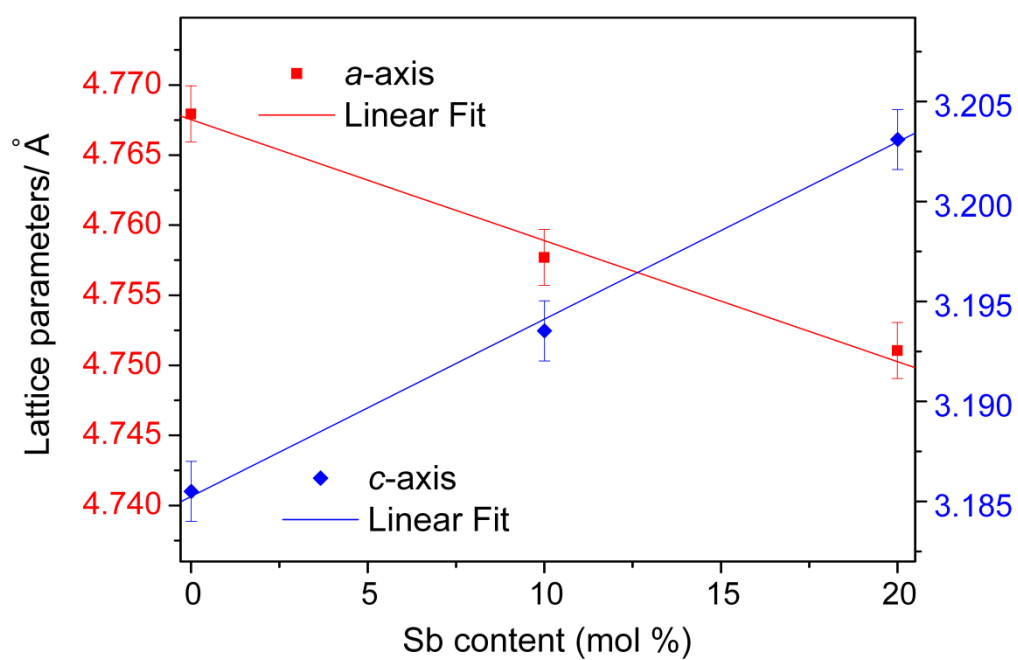


Figure A-3.3. Influence of antimony content on the parameter a (■) and c (◆) of the cassiterite type solid solutions, as determined from the results of Rietveld and Le Bail refinements of the XRD patterns.

3.6 References

1. Al-Dahoudi, N.; Aegerter, M. A., *J. Sol–Gel Sci. Technol.* **2003**, 26, 693.
2. Goebbert, C.; Nonninger, R.; Aegerter, M. A.; Schmidt, H., *Thin Solid Films* **1999**, 351, 79.
3. Hammarberg, E.; Prodi-Schwab, A.; Feldmann, C., *Thin Solid Films* **2008**, 516, 7437.
4. Sanchez, C.; Boissiere, C.; Grosso, D.; Laberty, C.; Nicole, L., *Chem. Mater.* **2008**, 20, 682.
5. Szeifert, J. M.; Fattakhova-Rohlfing, D.; Georgiadou, D.; Kalousek, V.; Rathousky, J.; Kuang, D.; Wenger, S.; Zakeeruddin, S. M.; Graetzel, M.; Bein, T., *Chem. Mater.* **2009**, 21, 1260.
6. Ba, J. H.; Polleux, J.; Antonietti, M.; Niederberger, M., *Adv. Mater.* **2005**, 17, 2509.
7. Fattakhova-Rohlfing, D.; Brezesinski, T.; Rathouský, J.; Feldhoff, A.; Oekermann, T.; Wark, M.; Smarsly, B. M., *Adv. Mater.* **2006**, 18, 2980.
8. Hou, K.; Puzzo, D.; Helander, M. G.; Lo, S. S.; Bonifacio, L. D.; Wang, W.; Lu, Z. H.; Scholes, G. D.; Ozin, G. A., *Adv. Mater.* **2009**, 21, 2492.
9. Wang, Y.; Brezesinski, T.; Antonietti, M.; Smarsly, B., *ACS Nano* **2009**, 3, 1373.
10. Chopra, K. L.; Major, S.; Pandya, D. K., *Thin Solid Films* **1983**, 102, 1.
11. Jung, D. W.; Park, D. W., *Appl. Surf. Sci.* **2009**, 255, 5409.
12. Aegerter, M. A.; Reich, A.; Ganz, D.; Gasparro, G.; Putz, J.; Krajewski, T., *J. Non-Cryst. Solids* **1997**, 218, 123.
13. Ganz, D.; Gasparro, G.; Aegerter, M. A., *J. Sol–Gel Sci. Technol.* **1998**, 13, 961.
14. Geraldo, V.; Scalvi, L. V. A.; Lisboa-Filho, P. N.; Morilla-Santos, C., *J. Phys. Chem. Solids* **2006**, 67, 1410.
15. Bernardi, M. I. B.; Soledade, L. E.; Santos, I. A.; Leite, E. R.; Longo, E.; Varela, J. A., *Thin Solid Films* **2002**, 405, 228.

16. Leite, D. R.; Mazali, I. O.; Aguiar, E. C.; Las, W. C.; Cilense, M., *J. Mater. Sci.* **2006**, 41, 6256.
17. de Melo, D. S.; Santos, M. R. C.; Santos, I. M. G.; Soledade, L. E. B.; Bernardi, M. I. B.; Longo, E.; Souza, A. G., *J. Therm. Anal. Calorim.* **2007**, 87, 697.
18. Giraldi, T. R.; Escote, M. T.; Bernardi, M. I. B.; Bouquet, V.; Leite, E. R.; Longo, E.; Varela, J. A., *J. Electroceram.* **2004**, 13, 159.
19. Dyshel, D. E.; Lobunets, T. F., *Powder Metall. Met. Ceram.* **1999**, 38, 309.
20. Hu, Y.; Hou, S. H., *Mater. Chem. Phys.* **2004**, 86, 21.
21. Grzeta, B.; Tkalec, E.; Goebbert, C.; Takeda, M.; Takahashi, M.; Nomura, K.; Jaksic, M., *J. Phys. Chem. Solids* **2002**, 63, 765.
22. Jeon, H. J.; Jeon, M. K.; Kang, M.; Lee, S. G.; Lee, Y. L.; Hong, Y. K.; Choi, B. H., *Mater. Lett.* **2005**, 59, 1801.
23. Van Bommel, M. J.; Groen, W. A.; Van Hal, H. A. M.; Keur, W. C.; Bernards, T. N. M., *J. Mater. Sci.* **1999**, 34, 4803.
24. Nutz, T.; Haase, M., *J. Phys. Chem. B* **2000**, 104, 8430.
25. Nutz, T.; zum Felde, U.; Haase, M., *J. Chem. Phys.* **1999**, 110, 12142.
26. Goebbert, C.; Aegerter, M. A.; Burgard, D.; Nass, R.; Schmidt, H., *J. Mater. Chem.* **1999**, 9, 253.
27. Niederberger, M.; Bartl, M. H.; Stucky, G. D., *J. Am. Chem. Soc.* **2002**, 124, 13642.
28. Niederberger, M.; Garnweitner, G., *Chem.-Eur. J.* **2006**, 12, 7282.
29. Pinna, N.; Niederberger, M., *Angew. Chem., Int. Ed.* **2008**, 47, 5292.
30. da Silva, R. O.; Conti, T. G.; de Moura, A. F.; Stroppa, D. G.; Freitas, L. C. G.; Ribeiro, C.; Camargo, E. R.; Elson, L.; Leite, E. R., *ChemPhysChem* **2009**, 10, 841.
31. Ba, J. H.; Fattakhova-Rohlfing, D.; Feldhoff, A.; Brezesinski, T.; Djerdj, I.; Wark, M.; Niederberger, M., *Chem. Mater.* **2006**, 18, 2848.

32. Müller, V.; Rasp, M.; Štefanić, G.; Ba, J.; Günther, S.; Rathousky, J.; Niederberger, M.; Fattakhova-Rohlfing, D., *Chem. Mater.* **2009**, 21, 5229.
33. Le Bail, A.; Duroy, H.; Fourquet, J. L., *Mater. Res. Bull.* **1988**, 23, 447.
34. Larson, A. C.; Von Dreele, R. B., General Structure Analysis System (GSAS); Report LAUR 86-748, Los Alamos National Laboratory, Los Alamos, CA. **2001**.
35. Toby, B. H., *J. Appl. Crystallogr.* **2001**, 34, 210.
36. Rietveld, H., *J. Appl. Crystallogr.* **1969**, 2, 65.
37. Lutterotti, L.; Matthies, S.; Wenk, H. R., *Proceeding of the Twelfth International Conference on Textures of Materials (ICOTOM-12)*. 1999; Vol. null, p 1599.
38. Wagner, C. D., *Auger and Photoelectron Energies and the Auger Parameter: A Data Set*. 1987.
39. Yeh, J. J.; Lindau, I., *At. Data Nucl. Data Tables* **1985**, 32, 1.
40. Terrier, C.; Chatelon, J. P.; Roger, J. A.; Berjoan, R.; Dubois, C., *J. Sol-Gel Sci. Technol.* **1997**, 10, 75.
41. Abello, L.; Bochu, B.; Gaskov, A.; Koudryavtseva, S.; Lucazeau, G.; Roumyantseva, M., *J. Solid State Chem.* **1998**, 135, 78.
42. Dieguez, A.; Romano-Rodriguez, A.; Vila, A.; Morante, J. R., *J. Appl. Phys.* **2001**, 90, 1550.
43. Kravets, V. G.; Poperenko, L. V., *J. Appl. Phys.* **2008**, 103, 083904-1.
44. Pagnier, T.; Boulova, M.; Sergent, N.; Bouvier, P.; Lucazeau, G., *J. Raman Spectrosc.* **2007**, 38, 756.
45. Sergent, N.; Epifani, M.; Comini, E.; Faglia, G.; Pagnier, T., *Sens. Actuators B* **2007**, 126, 1.
46. Ocana, M.; Serna, C. J.; Garciamos, J. V.; Matijevic, E., *Solid State Ionics* **1993**, 63–5, 170.
47. Ristic, M.; Ivanda, M.; Popovic, S.; Music, S., *J. Non-Cryst. Solids* **2002**, 303, 270.

48. Rumyantseva, M. N.; Gaskov, A. M.; Rosman, N.; Pagnier, T.; Morante, J. R., *Chem. Mater.* **2005**, 17, 893.
49. Zhou, J. X.; Zhang, M. S.; Hong, J. M.; Yin, Z., *Solid State Commun.* **2006**, 138, 242.
50. Terrier, C.; Chatelon, J. P.; Berjoan, R.; Roger, J. A., *Thin Solid Films* **1995**, 263, 37.
51. Sun, K.; Liu, J.; Browning, N. D., *J. Catal.* **2002**, 205, 266.
52. Shanthi, E.; Dutta, V.; Banerjee, A.; Chopra, K. L., *J. Appl. Phys.* **1980**, 51, 6243.
53. Shanthi, E.; Banerjee, A.; Chopra, K. L., *Thin Solid Films* **1982**, 88, 93.

4 Assembly of ATO Nanoparticles into Mesoporous Films

This chapter is based on the following publication:

Vesna Müller, Matthias Rasp, Jiri Rathousky, Benedikt Schütz, Markus Niederberger, and Dina Fattakhova-Rohlfing, “Transparent Conducting Films of Antimony-Doped Tin Oxide with Uniform Mesostructure Assembled from Preformed Nanocrystals”, *Small*, **2010**, 6, 633-637

4.1 Introduction

The recent rapid progress in nanoscience and nanotechnology has led to the development of completely new nanoscale materials. Novel morphologies of already known materials have substantially extended their application potential.¹ Transparent conducting oxides are known as thin, dense films, being indispensable for touch-panel displays, organic light emitting diodes (OLEDs), or nonsilicon solar cells.^{2, 3} However, other types of optoelectronic devices, especially those involving immobilized species or functional layers, such as biochemical sensors,⁴ supramolecular energy-conversion junctions,⁵ or redox-protein-based arrays,⁶⁻⁸ require three-dimensional (3D) conducting networks rather than flat electrode interfaces. Such 3D electrode architectures with very high interface areas are suitable as conducting hosts accommodating functional guest species, which allows for a substantially more efficient electron transfer and consequently increases the efficiency of the devices.

In 2006 Fattakhova-Rohlfing et al. reported the preparation of 3D networks of indium tin oxide (ITO) and demonstrated their potential as efficient electrode systems.⁹ Very recently, Frasca and Aksu demonstrated the expansion of the application of such ITO systems as efficient network for incorporation of small proteins.^{10, 11} The extension of such architectures to other 3D organized transparent conductors, replacing the rare and expensive indium and

providing a different surface chemistry or energy-level properties, is of great interest. One widely used system is extrinsically doped tin oxide, such as fluorine- or antimony-doped tin oxide (ATO).¹²

Very recently, two communications have been published reporting mesoporous ATO electrodes^{13, 14} and their potential was demonstrated for the fabrication of efficient electrochemiluminescence biosensors, for example.¹¹ However, the manufacture of 3D transparent electrodes remains a nontrivial task, limiting the full exploitation of their application potential. All of the reported methods are practically solely based on self-assembly of sol-gel-derived metal oxide precursors assisted by amphiphilic structure-directed agents (the so-called evaporation-induced self-assembly process).^{15, 16} As the inorganic framework formed is amorphous, they must be treated at higher temperatures to induce the crystallization essential for electron conductivity.¹⁷ Such phase transformation without mesostructural collapse was achieved for ATO films only using special amphiphilic copolymers of the poly(ethylene-co-butylene)-block-poly(ethylene oxide) (KLE) type¹⁸ with outstanding templating properties and increased thermal robustness,¹⁹ which, however, are not commercially available. Easily available and rather cheap copolymers of the Pluronic family, successfully used for the preparation of mesoporous crystalline metal oxides,^{20, 21} have failed due to the different sol-gel chemistry of tin. The formation of a crystalline mesoporous structure of tin oxide requires a special postsynthetic treatment at a carefully controlled humidity and temperature for several days (the so-called delayed humidity treatment),^{20, 21} which is rather elaborate and time consuming. Consequently, the development of a simple and generally applicable procedure for the preparation of transparent conducting 3D frameworks using easily available components is highly desirable. One passable solution might be the replacement of the amorphous metal oxide precursor with crystalline building blocks, which could form the mesoporous crystalline network at much milder conditions. The preformed nanocrystals could also bring the additional advantage of a fine adjustment of the doping level

and thus the electrical conductivity, which is often better controlled in the particle synthesis than in the sol–gel one. Nevertheless, the use of nanocrystalline building blocks for the preparation of mesoporous materials has been reported only for a few oxides,²²⁻²⁷ probably due to the fact that it is rather difficult to prepare stable and agglomeration-free nanoparticle dispersions. On the other hand, it has been shown recently that mesoporous titania prepared from preformed nanoparticles can, as a matter of fact, have superior electrochemical properties in comparison to sol–gel-derived materials.

In the previous chapter the preparation of crystalline monodisperse ATO nanoparticles of 3–4 nm in size by a nonaqueous approach was described. This approach utilizes cheap and easily available metal oxide precursors and non-toxic benzyl alcohol. The reaction is completed after heating the precursor mixture for several hours at 100–150 °C in a closed glass vessel, without the need of an autoclave.²⁸ The obtained nanocrystals can accommodate up to 38 mol% of antimony without phase separation. They exhibit a high electrical conductivity and are dispersible at high concentration in both water and a number of organic solvents. Consequently, these nanocrystals are suitable building blocks for assembly into a mesostructure. In this chapter a procedure enabling the assembly of such crystals to create mesoporous conducting films is presented. This process is directed by commercially available Pluronic copolymers as structure directing agents. The parameters influencing the self-assembly properties have been analyzed in detail, as well as the textural properties, crystallinity, and conductivity of the obtained films.

4.2 Experimental Section

4.2.1 Chemicals

Tin(IV) chloride (99 %), antimony(III) acetate (99.99 %), anhydrous benzyl alcohol (99.8 %, <0.003 % water), anhydrous toluene (≥99.7 %; <0.005 % water), anhydrous dichloromethane

(DCM) (≥ 99.5 %; < 0.005 % water), tetrahydrofuran (THF) (≥ 99.5 %), (3-aminopropyl)triethoxysilane (APTES) (99 %), ferrocenecarboxylic acid (≥ 97 %), N,N-dicyclohexylcarbodiimide (DCC) (≥ 97 %), N-(3-Dimethylaminopropyl)-N'-ethylcarbodiimide (EDC) (≥ 97 %), potassium dihydrogen phosphate (≥ 99.5 %), lithium perchlorate (≥ 95 %), disodium hydrogen phosphate (≥ 99 %) were purchased from Aldrich and used without further purification. Ruthenium dye, ruthenizer 455-PF6 was purchased from Solaronix.

4.2.2 Preparation of Mesoporous Films

Mesoporous films of ATO were prepared by the self-assembly of ATO nanoparticles using a Pluronic F127 block copolymer (Aldrich) as a structure-directing agent. The preparation of ATO nanoparticles with different Sb contents was described in the previous chapter²⁸. Briefly, for the preparation of ATO nanoparticles with 10 mol% of antimony (designated as ATO_10), tin tetrachloride (3.2 g, 12.3 mmol), and Sb(III) acetate (1.35 mmol) were dissolved in toluene (10 mL) and added to benzyl alcohol (30 mL, 291 mmol) with continuous stirring. The solution was kept in a closed glass vessel in a laboratory oven at 100 °C for 20 h. Afterwards, the particles were separated by centrifugation at 50 000 rcf for 10 min and washed sequentially in toluene and acetone. Each washing step included ultrasonication for 15 min and centrifugation. The washed particles (0.2 g) were dispersed in a solution of Pluronic F127 (0.14 g) in THF (5 mL) by stirring for 3 h at 50 °C. When necessary, a drop of concentrated HCl was added to make the solutions completely transparent. Alternatively, the particles can be used for the preparation of the mesoporous films without any washing method. The as prepared particles, after centrifugation and drying in air, contained some amount of organic residuals present on their surfaces after the synthesis. The amount of the pure ATO nanoparticles, without organic residuals, has to be determined by TGA. In a typical synthesis, 0.2 g of ATO nanoparticles were dispersed in 5 mL solution of Pluronic F127 in THF. The

amount of used Pluronic, has to be in a 1:1 weight ratio to the amount of the pure ATO nanoparticles calculated from TGA (for 0.2 g of particles). The final solutions prepared in both ways were transparent, being of yellow-to-orange color. The films were prepared by dip coating of the prepared solution on glass, Si wafers, and ITO-coated glass substrates at 23 ± 2 °C with a relative humidity of $55 \pm 5\%$ and a withdrawal rate of 1.8 mm s^{-1} and then calcination at 300 °C to 500 °C (with a ramp rate of 0.6 °C min^{-1}) for 30 min.

4.2.3 *Functionalization of Mesoporous Films*

For the electrochemical characterization, the mesoporous ATO films were deposited on a conducting ITO-coated glass substrate.

The incorporation of ferrocene moieties was performed in the following way. The surface functionalization of the ATO films was performed in a 20 mM solution of 3-aminopropyltriethoxysilane (APTES) in dichloromethane under reflux for 2 h, followed by washing with dichloromethane. For the covalent anchoring of ferrocene moieties, the APTES functionalized films were stirred for 3 h in a 0.2 mM solution of ferrocene carboxylic acid and a 2mM solution of N,N-dicyclohexylcarbodiimide in dichloromethane in reflux for 3 h and washed twice with dichloromethane.

The incorporation of ruthenium dye was performed by covalent attachment and adsorption. For adsorption the mesoporous films were left overnight in 0.3 mM aqueous solution of ruthenium dye and subsequently washed with distilled water.

For the covalent attachment of ruthenium dye the ATO surface was functionalized with APTES. Two temperatures for APTES functionalization were tested. In the first the functionalization with APTES was performed in a 20 mM solution of 3-aminopropyltriethoxysilane (APTES) in dichloromethane in reflux (40 °C) for 2 h, followed by washing with dichloromethane and ethanol. In the second the surface functionalization was

performed in a 20 mM solution of 3-aminopropyltriethoxysilane (APTES) in toluene in reflux (110 °C) for 2 h, followed by washing with dichloromethane and ethanol.

In both types of the surface functionalized films the incorporation of ruthenium dye was performed either by stirring films at room temperature overnight or at 70 °C for 3 h in 0.3 mM aqueous solution of ruthenium dye and 2 mM solution of N-(3-Dimethylaminopropyl)-N'-ethylcarbodiimide (EDC).

4.2.4 Preparation of the Phosphate Buffer

The 0.05 M phosphate buffer pH 7.4 was prepared in the way that amounts of 0.25 g of potassium dihydrogenphosphate (KH_2PO_4) and 1.51 g of disodium hydrogen phosphate (Na_2HPO_4) were dissolved in 250 ml of distilled water.

4.2.5 Characterization Techniques

Film thicknesses were determined using a profilometer Veeco Dektak 150 equipped with a diamond stylus (12.5- μm radius) in contact mode. The typical thickness of the films was 210 ± 10 nm.

Small-angle XRD measurements of the thin films on various substrates were performed on a SCINTAG XDS 2000 diffractometer with Ni-filtered $\text{CuK}\alpha$ radiation ($\lambda=1.5406$ Å), theta/theta geometry, and a scintillation detector operated at 40 kV and 30 mA.

Wide-angle XRD was carried out in reflection mode using a Bruker D8 Discover diffractometer with Ni-filtered $\text{CuK}\alpha$ radiation equipped with a Vantec-1 position sensitive detector. The crystal size, d , was estimated from the broadening of the 110 reflection in the XRD pattern using Scherrer's equation $d = K\lambda/(B \cos\theta_B)$, where B is the full width at half maximum (FWHM) of the diffraction peak, θ_B is the diffraction angle, and K is the Scherrer's constant (about 0.9).

TEM and HRTEM measurements were performed using a FEI Titan 80-300 equipped with a field emission gun operated at 300 kV. The samples were prepared by scraping the thin films off the substrate onto a Plano holey carbon-coated copper grid.

SEM images of the films on Si substrates were obtained with a JEOL JSM-6500F scanning electron microscope equipped with a field emission gun operated at 4 kV.

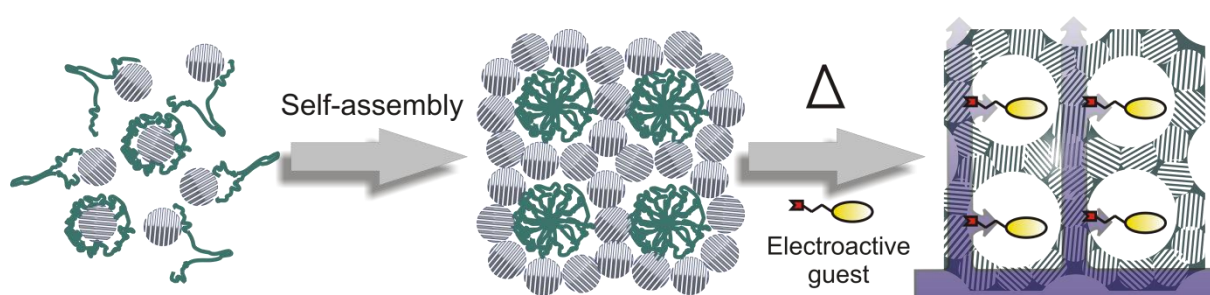
The porosity was determined in collaboration with Dr. Jiri Rathousky (Prague). The porosity of the films was determined by analysis of adsorption isotherms of Kr at the boiling point of liquid nitrogen (≈ 77 K) using an ASAP 2010 apparatus (Micromeritics).

Conductivity measurements of ATO films on glass substrates were carried out on an ECOPIA HMS 3000 apparatus using Van der Pauw geometry.

Cyclic voltammograms were obtained using a PARSTAT 2273 potentiostat (with PowerSuite 2.56 software for data collection and analysis) in a standard three electrode electrochemical cell using a Pt wire as a counter electrode. In the case of ferrocene-functionalized films an Ag wire as a quasi-reference electrode, and 0.5 M LiClO₄ in acetonitrile as an electrolyte were used. In the case of ruthenium dye an Ag/AgCl reference electrode and 0.05 M phosphate buffer as supporting electrolyte were used. Functionalized ATO films on ITO glass used as working electrodes were masked with silicone resin, leaving an exposed area of 1 cm². Cyclic voltammograms were taken in a range of scan rates from 10 to 200 mV s⁻¹. The amount of charge transferred in the oxidation and reduction of ferrocene was found by integration of the corresponding peaks in the voltammograms (represented as current–time curves) after subtraction of the background current, as approximated by a polynomial. Both cathodic and anodic branches of the voltammograms were used for flat ITO as well as mesoporous ATO electrodes and an average charge value was taken for the calculation of surface coverage.

4.3 Results and Discussion

The main task of this project was to prepare crystalline mesoporous films with commercially available polymers from the Pluronic family. In order to make this procedure of the preparation of mesoporous ATO films with commercially available polymers possible, the EISA process was modified. Instead of using amorphous metal oxide precursor the crystalline ATO nanoparticles were used as building blocks for such architecture, Scheme 4.3.1.



Scheme 4.3.1. Formation of mesoporous crystalline electrode layers (right) via self-assembly of crystalline nanoparticles (gray) directed by amphiphilic molecules (green). Violet arrows indicate the direct electron flow to each redox species immobilized in the 3D-conducting scaffold.

This type of preparation of mesoporous materials has been reported for a few oxides.²²⁻²⁷ In the previous chapter the preparation of crystalline monodisperse ATO nanoparticles through nonaqueous sol-gel procedure was described.²⁸ The ATO nanoparticles, prepared through this method, are 3-4 nm in size and completely dispersible which makes them suitable building blocks for assembly into mesostructures.

For obtaining the mesostructuring in ATO films it was found that the amount of organic residuals present on the surface of the as synthesized ATO nanoparticles is important for their assembly into mesostructure. The amount of organic residuals in the form of adsorbed benzyl alcohol and benzyl alcoholate moieties has to be taken into account prior to mixing the solution of pluronic in THF with ATO nanoparticles. The amount of added Pluronic has to be in the same weight ratios to the nanoparticles without organic moieties. The amount of the

pure nanoparticles has to be calculated according to the TGA data and the amount of added Pluronic to the nanoparticles has to be in the weight ration 1:1. However, if the as-obtained nanoparticles contain significant amounts of organic residuals (ca. 50 wt. % or more) only a thermally unstable lamellar structure was formed, even if they were mixed with Pluronic in the ratio 1:1, Fig. 4.3.1. The amount of the adsorbed organics in such nanoparticles can be significantly reduced by particle washing once with acetone, which improves the self-assembly ability of the nanoparticles into the mesoporous structures.

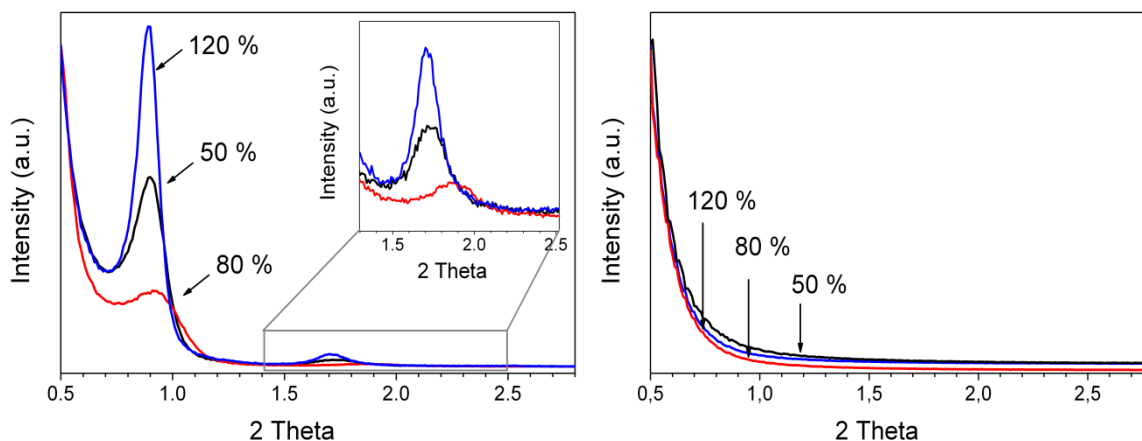


Figure 4.3.1. Small angle XRD patterns of the mesoporous films assembled from non-washed ATO₂₀ nanoparticles using Pluronic P123 as a templating agent at different Pluronic to particle ratios (assigned in labels): as prepared (left) and after calcination at 300 °C (right).

If the as-synthesized nanoparticle contained 30-40 wt. % of the organic residuals, the 1:1 mixtures with Pluronic gave the thermally stable mesostructures, Fig 4.3.2.

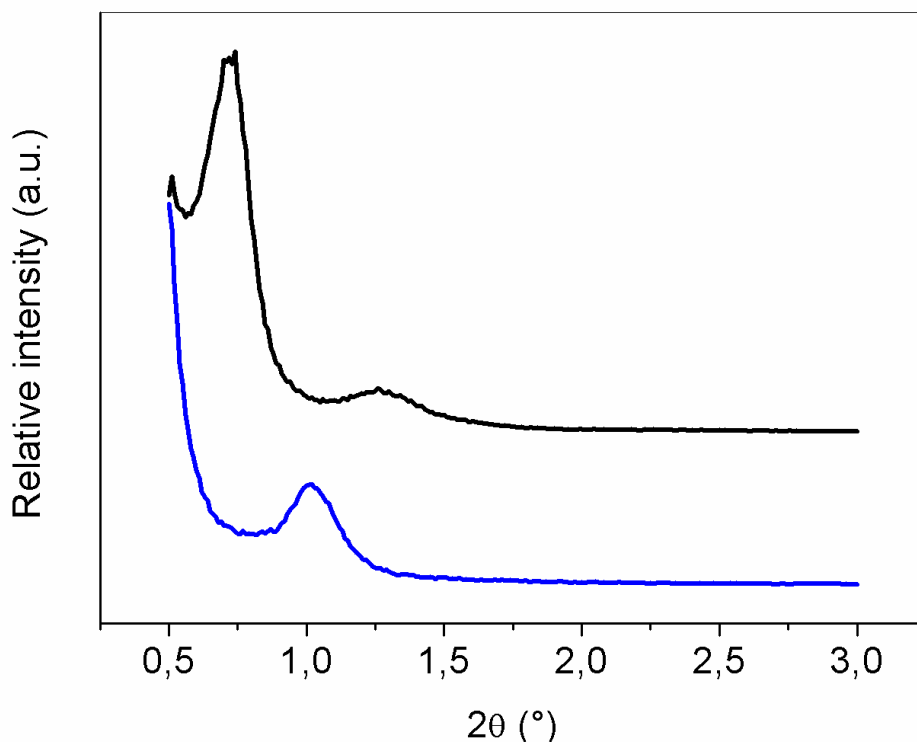


Figure 4.3.2. Small angle XRD patterns of the mesoporous films assembled by using pluronic F127 as structure directing agent and ATO₁₀ which contain 30 wt. % of organic residuals. The weight ratio between pluronic F127 and ATO nanoparticles was 1:0.7. The black line shows the XRD pattern before calcination and the blue line presents the XRD pattern after calcination at 500 °C.

The composition of nanoparticles influences the formation of mesostructure as well. Only ATO nanoparticles with a Sb content exceeding 6 % could be assembled into thermally stable periodic mesostructured films in the presence of the Pluronic copolymer. The observed influence of the composition of the particles and their surface chemistry on their self-assembly behavior suggests an important role of the coordination of the Pluronic block copolymer molecules, presumably of their hydrophilic polyethyleneoxide blocks, on the particle surface. Beside the amount of adsorbed organic moieties, the additional factor which influences the dispersibility and assembly of ATO nanoparticles is their surface charge. From zeta potential measurements it can be estimated that the point of zero charge (pzc) of the ATO particles changes linearly with Sb content, Fig. 4.3.3.

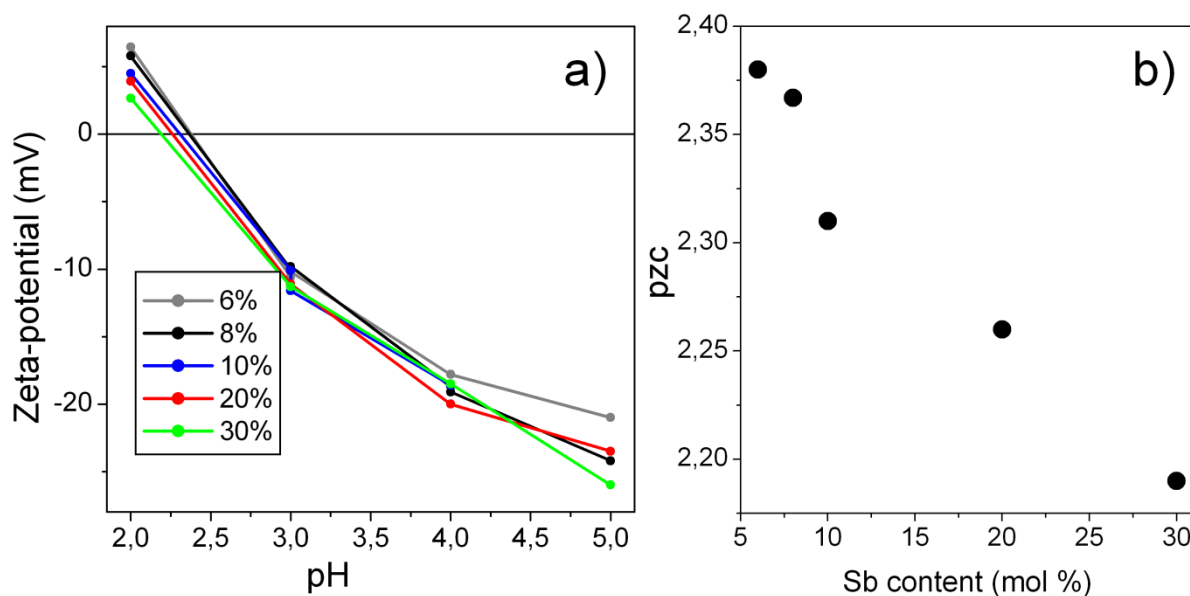


Figure 4.3.3. Zeta-potential of the aqueous colloidal dispersions of ATO nanoparticles with various Sb doping levels measured at different solution pH (a), and variation of the measured point of zero charge (pzc) with the Sb doping level (b).

This alteration of the surface charge and the replacement of the surface Sn atoms by Sb ones could be one of the reasons for the remarkably different self-assembly behavior of Sb-doped particles compared to undoped ones. The influence of the replacement of the surface Sn atoms with antimony was demonstrated before by Raman measurements.²⁸

4.3.1 Morphology of the Mesoporous Films

It was found that the obtained morphology of the films is strongly influenced by the composition of the assembled nanoparticles and the calcination temperature. ATO nanoparticles with doping levels from 6 to 30 mol% were used for the assembly into mesoporous structure. The as-prepared films were calcined at different temperatures in order to remove the organic template and to induce the sintering between the nanoparticles. The applied temperatures were varied from 300 °C up to 500 °C. According to the TGA data the combustion of Pluronic starts at 300 °C and the temperature is sufficiently high to remove all of the organics from the material (Appendix Fig. A-4.1.).

The scanning electron microscopy (SEM) images of the films prove the very good uniformity of the films and their crack-free character, Fig. 4.3.4, c) and f).

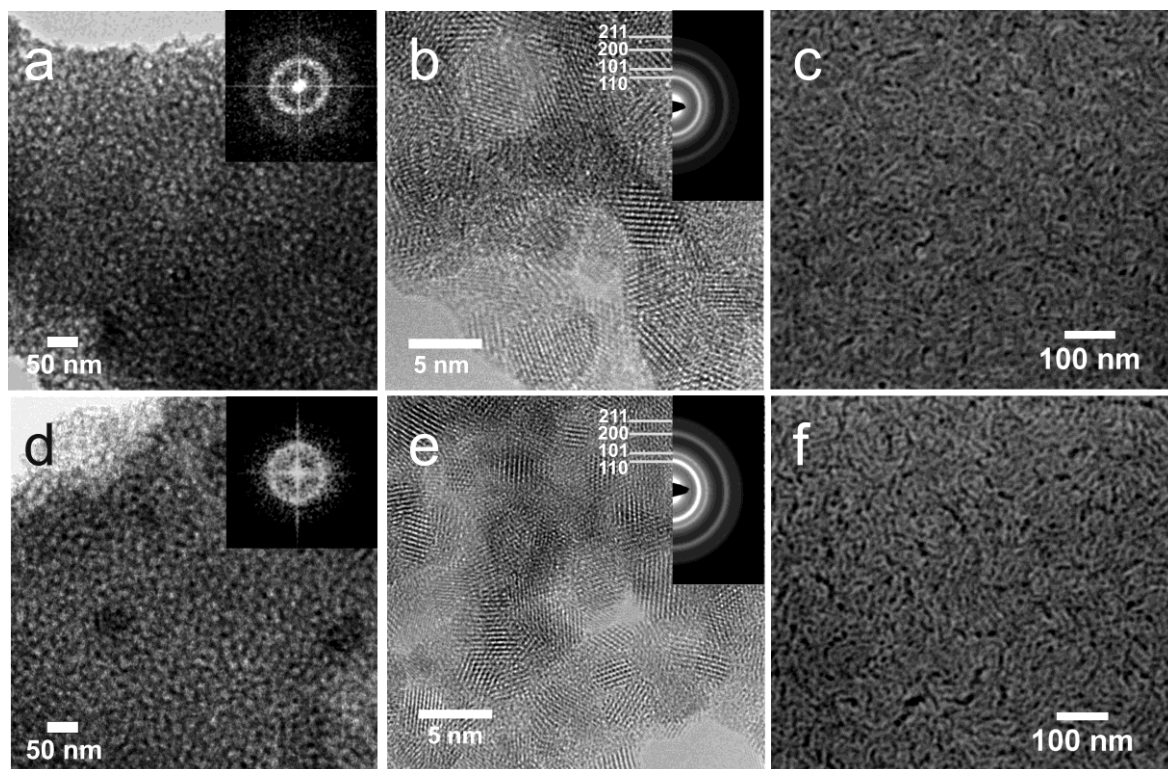


Figure 4.3.4. Mesostructure and crystallinity of the films assembled from ATO_20 nanoparticles: (a, d) TEM image, inset: the Fourier transform spectra; (b, e) high resolution TEM image, inset: corresponding SAED patterns, and (c, f) SEM image (top view). The first (a, b, c) and second (d, e, f) rows correspond to the films calcined at 400 and 500 °C, respectively.

The transmission electron microscopy (TEM) images show that the nanoparticles with different doping levels form similar films with highly porous 3D architectures, Fig. 4.3.4 a) and d). The wormhole mesostructure contains ≈ 100 -nm-large domains with some indication of pore ordering (Appendix Fig. A-4.2). The Fourier-transformation of the TEM images of the films calcined at 300–400 °C show two rings corresponding to a mesostructure periodicity of 14 ± 1 and 8 ± 0.5 nm, respectively (insets of Fig. 4.3.4 a and d).

The high-resolution TEM (HRTEM) images of the mesoporous ATO films (Fig. 4.3.4, b and e) show the completely crystalline pore walls which are composed of similarly sized nanocrystals. The HRTEM images of the calcined films (Appendix Fig. A-4.3) indicate that

the particles in the walls grow anisotropically. This leads to an increase in the particle size in one direction along the pore walls.

The d spacing of the lattice fringes and corresponding selected-area electron diffraction (SAED) patterns taken from various parts of the film indicate only a cassiterite SnO_2 phase. These results confirm that phase separation did not occur during the thermal treatment.

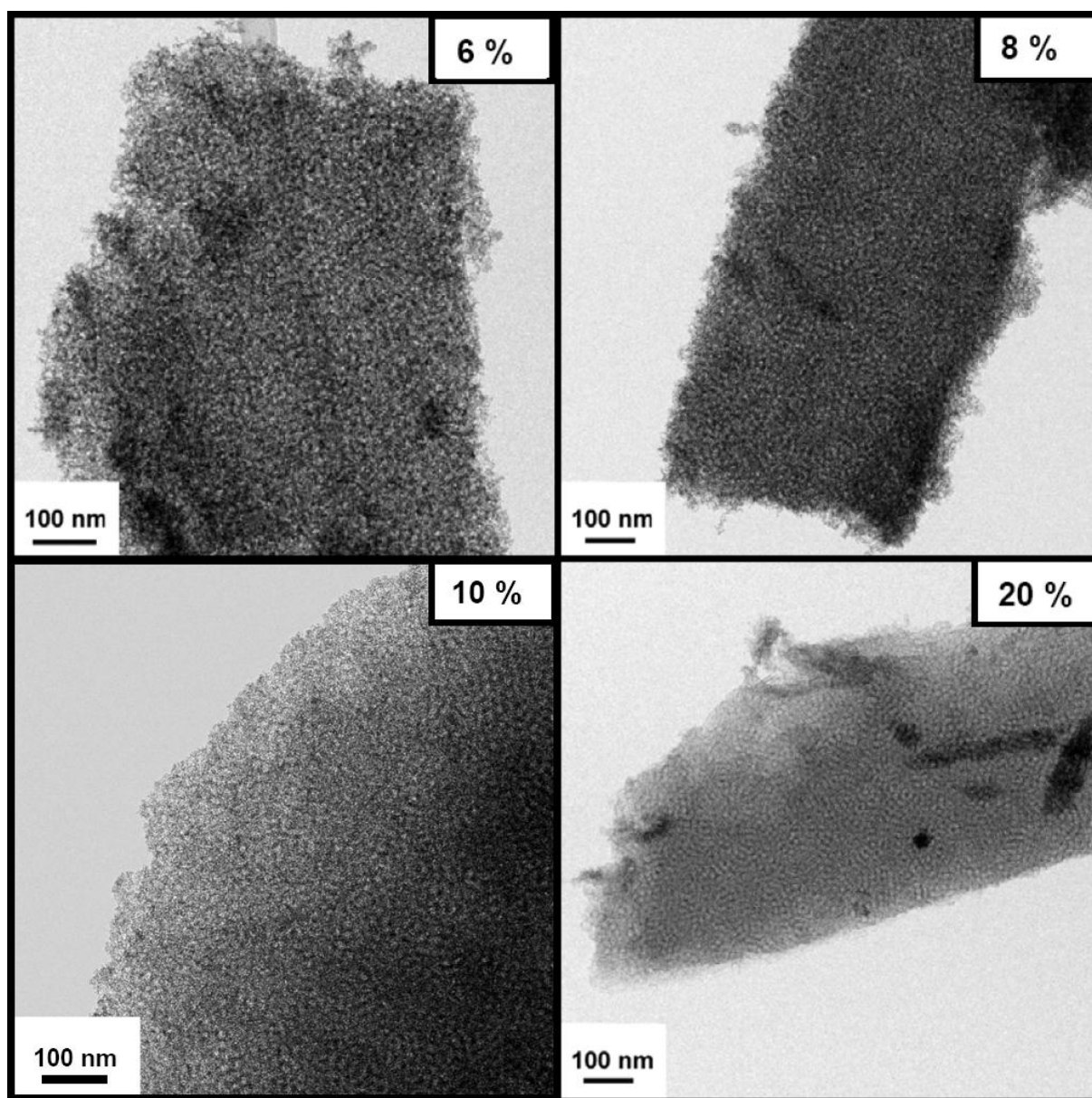


Figure 4.3.5. TEM images of the thin films calcined at 300 °C produced by self-assembly of nanoparticles with different Sb content (given in labels).

Although all films feature a good porosity the periodicity of mesostructure becomes worse when particles with lower amount of antimony are used for assembly, Fig. 4.3.5

4.3.2 Structure of ATO Films

The small-angle X-ray diffraction (SAXS) patterns are in good agreement with the electron microscopy data. SAXS measurements indicate the presence of two reflections due to the pore organization with a similar mesostructure periodicity found in TEM data, Fig. 4.3.6, a).

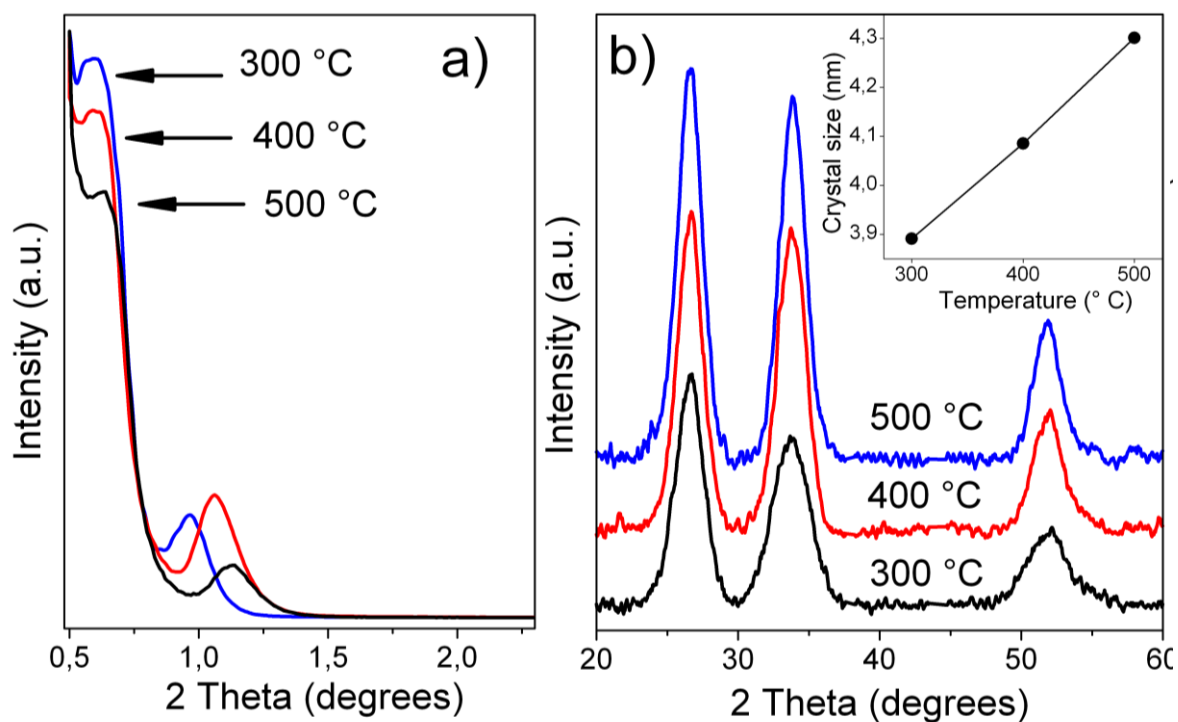


Figure 4.3.6. Characterization of the mesoporosity and crystallinity of the films assembled from ATO₂₀ nanoparticles and treated at different temperatures: (a) small angle X-ray diffraction, (b) wide angle X-ray diffraction. The inset in the Figure 2b shows dependence of the crystal size on the calcination temperature estimated from the broadening of the 110 reflection of SnO₂ using the Scherrer equation.

The first reflection, corresponding to a mesostructure d -spacing of ≈ 14 nm, slightly shifts to higher angles due to shrinkage of the mesostructure in a direction perpendicular to the substrate. This behavior is well known for crystalline mesoporous films.¹⁷ In contrast to sol-gel-derived films, the mesostructural shrinkage of the films assembled from nanoparticles is only marginal, indicating high temperature stability of the mesoporous framework. The second reflection, corresponding to a higher order of periodicity, becomes weaker with the increase in the calcination temperature due to the increasing distortion in the mesostructure

ordering. The films assembled from ATO₁₀ and ATO₂₀ nanoparticles feature similar mesostructure properties.

The size of the crystallites in the pore walls is determined from the line broadening of the wide angle X- ray scattering (WAXS) patterns (Fig. 4.3.6, b). The result indicates a slight growing of the crystallite size from 3.9 to 4.3 nm by increasing the calcination temperature from 300 to 500 °C.

The sintering of nanoparticles within the pore walls leads to a slight mesostructure shrinkage and thus to some deterioration of the periodicity of mesostructure.

4.3.3 Porosity of Mesostructured ATO Films

The porosity of films was examined in collaboration by Dr. Jiri Rathousky. The textural properties and accessibility of the internal surface of the ATO thin films were studied by krypton adsorption at ≈ 77 K. The Kr-adsorption isotherms of the films calcined from 300 to 500 °C show that all the films exhibit typical isotherms for mesoporous materials. The isotherms indicate well developed mesoporosity without any pore blocking, Fig. 4.3.7.

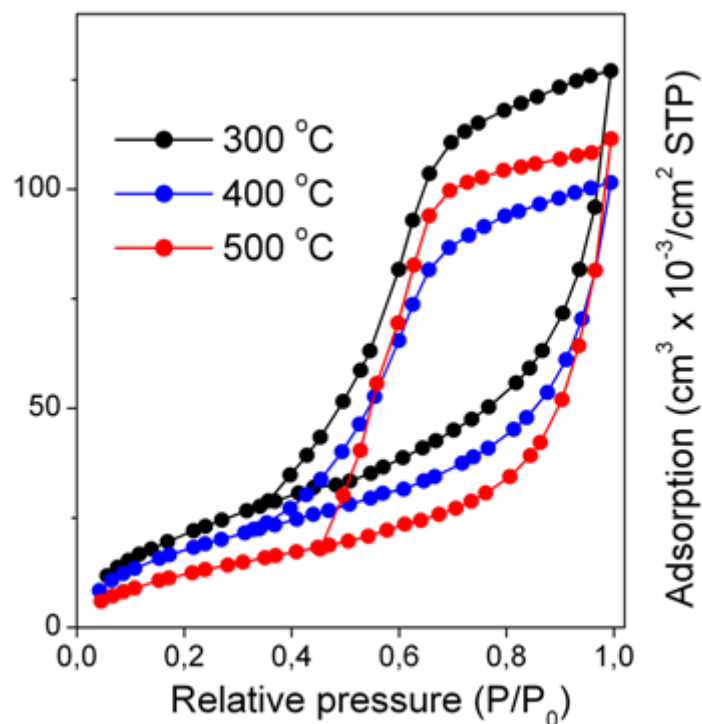


Figure 4.3.7. Kr adsorption isotherms of the films prepared from ATO_20 nanoparticles calcined at 300, 400, and 500 °C.

The increase in the calcination temperature from 300 to 500 °C does not essentially change the character of the porosity, but induces some quantitative changes in the texture characteristics. The specific surface area related to the total film volume slightly decreases with increasing calcination temperature but remains remarkably high, achieving 300, 270, and 200 cm² cm⁻² for calcination temperatures of 300, 400, and 500 °C, respectively. From the limiting adsorption at a relative pressure of ≈ 1 , the pore volume and the porosity were calculated giving 45, 30, and 55 % porosity for the mentioned calcination temperatures. Using these values for mesoporosity, the surface area expressed per gram becomes 79, 56, and 64 m² g⁻¹, respectively. These results are in good agreement with the surface area of 66 m² g⁻¹ found for pure bulk mesoporous SnO₂.²⁶ The pore width slightly increases with increasing calcination temperature from ≈ 6 nm (for 300 and 400 °C) to ≈ 8 nm (for 500 °C), as follows from the shift of the hysteresis loop towards higher relative pressures and the analysis using

the comparative-plots method. The pore size distribution becomes broader for the sample calcined at 500 °C.

A non-monotonous dependence of the porosity on calcination temperature shown by nanoparticulate ATO films was observed also for other templated materials. Thus, Sanchez et al.²⁹ described the evolution of the porosity of templated titania films. The porosity reached a local maximum at 330 °C due to pyrolysis of the template, then decreased to a minimum at 440 °C because of dominating film relaxation, and increased again at even higher temperatures due to pore coalescence via sintering, leading to densification of titania in the directions parallel to the film surface and generating porosity. As these data are in very good agreement with those in the mentioned study, the same mechanism also seems to be operative for our films. The Kr-adsorption results, in combination with the electron microscopy and X-ray diffraction data, indicate that the mesostructure assembled from the preformed nanocrystals has a high thermal stability.

4.3.4 Conductivity of ATO Films

The variation of the electrical conductivity of the mesoporous ATO films was determined with respect to the Sb-doping level in the used nanoparticles and the applied calcination temperature. The film conductivity is the highest when the film is assembled from particles containing 8–10 % of Sb, Fig. 4.3.8, Table 4.3.1.

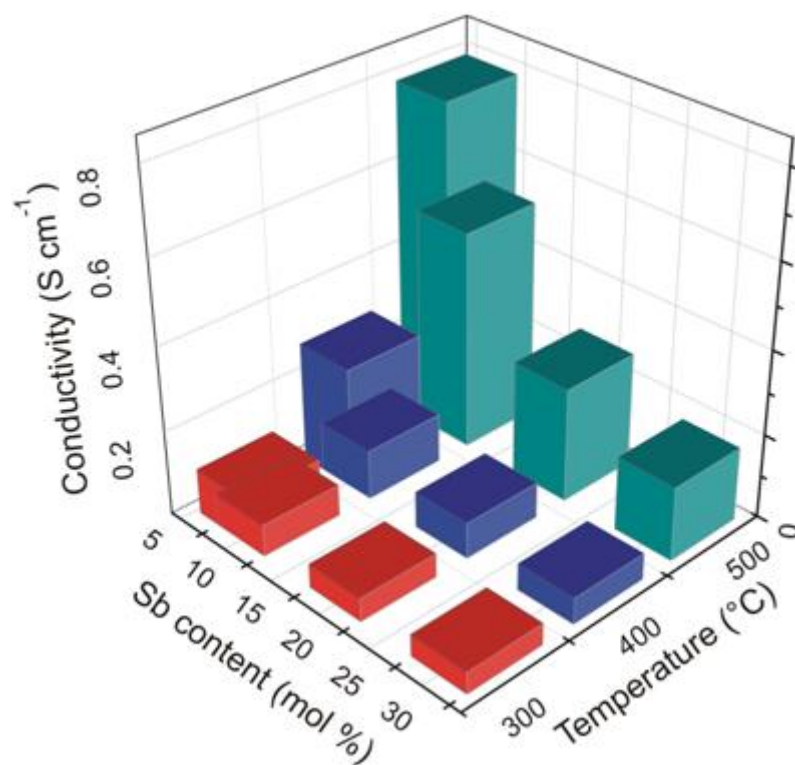


Figure 4.3.8. Dependence of the electric conductivity of the mesoporous films assembled from ATO nanocrystals with Sb content in the precursor nanoparticles and the calcination temperature of the prepared films.

Table 4.3.1. The values of electrical conductivities obtained for samples containing from 8 to 30 mol% Sb after calcination at 300, 400 and 500 °C.

Amount of Sb (mol %)	Electrical conductivity (S cm ⁻¹)		
	Samples calcined at 300 °C	Samples calcined at 400 °C	Samples calcined at 500 °C
8	0,1083	0,2872	0,7945
10	0,0749	0,1170	0,5193
20	0,0562	0,0856	0,2716
30	0,0513	0,0626	0,1760

These results are in good agreement with the conductivity of the nanoparticles themselves, which achieve a maximum at 4–10 % of Sb.²⁸ The conductivity of the films increases with increasing calcination temperature, which is due to particle sintering, a slight increase in the crystal size, and the related increase in the electron mobility. The highest conductivity of 0.8 S cm⁻¹ was obtained for the film assembled from ATO_8 nanoparticles and calcined at 500 °C. This is practically the same conductivity that was obtained for the parent ATO_8 nanoparticles in pressed pellets treated at the same temperature (1 S cm⁻¹),²⁸ being quite high for a film with a porosity of ≈ 50 %.

4.3.5 Applicability of the Mesoporous ATO Films as Nanostructured Electrodes

To test the applicability of mesoporous ATO films as electrode layers, they were deposited on flat conducting ITO substrates in order to minimize Ohmic losses. Ferrocene moieties were covalently anchored via peptide bonds to the surface of mesoporous films as standard redox probes.^{9, 13} Figure 4.3.9 shows an example of the electrode performance of the film assembled from ATO_10 nanoparticles calcined at different temperatures.

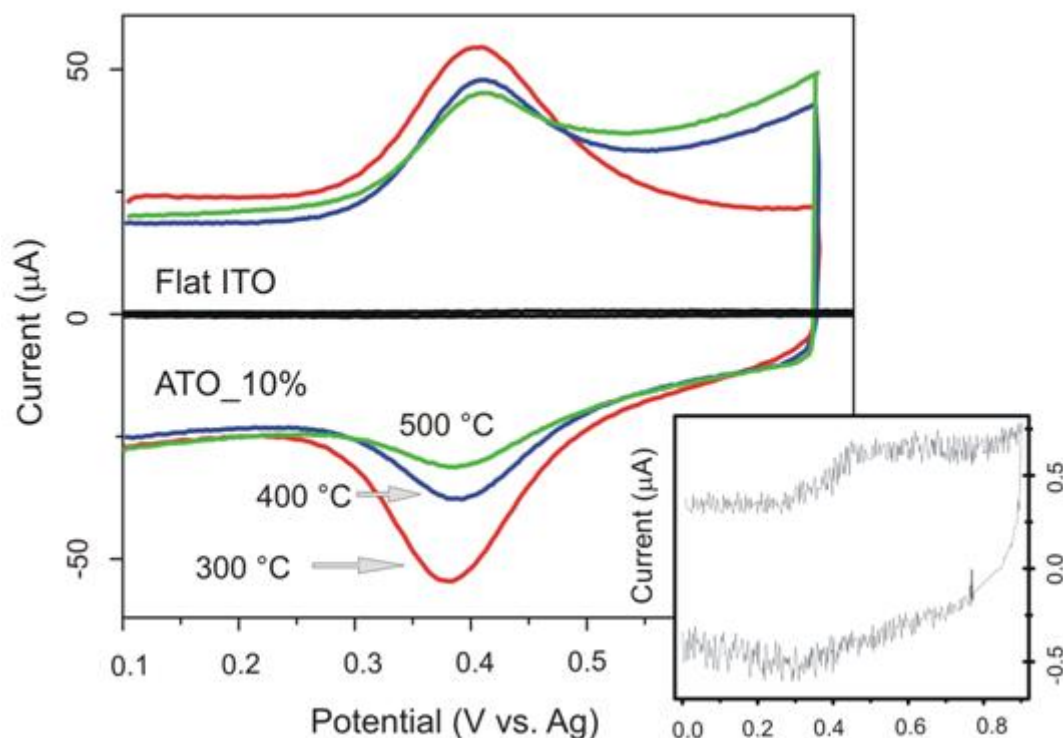


Figure 4.3.9. The cyclic voltammograms of the ferrocenecarboxylic acid covalently anchored on the mesoporous ATO_10 layers calcined at 300 °C (red), 400 °C (blue), 500 °C (green) and on a flat ITO electrode (black and inset). Scan rate is 50 mV s⁻¹.

The voltammograms of all the samples exhibit Gaussian-shaped peaks of reversible ferrocene oxidation and reduction, characteristic for modified electrodes with immobilized redox species.³⁰ Both the double-layer-charging and Faradaic currents of the ferrocene oxidation and reduction on the mesoporous electrodes drastically increase compared to those on the flat ITO electrode modified in the same way. The surface coverage of the electrochemically accessible ferrocene molecules obtained by integration of the peak area corresponds to 1.9×10^{-11} mol cm⁻² for the flat ITO electrode and 9.4×10^{-10} mol cm⁻² (50 times), 6.5×10^{-10} mol cm⁻² (35 times), and 5.5×10^{-10} mol cm⁻² (29 times) for the mesoporous ATO electrodes calcined at 300, 400, and 500 °C, respectively. The numbers in brackets indicate the corresponding increase in surface coverage compared to the flat ITO electrode. This increase in the Faradaic charge is in excellent agreement with the specific surface areas of the films obtained by Kr-adsorption measurements. Consequently, the mesoporous ATO films calcined at lower temperatures are,

as a matter of fact, suitable for application as transparent electrode layers with the very high surface area enabling direct electrochemical addressing of each redox molecule immobilized on its surface. The surface area of the mesoporous ATO layers seems to play a more important role in enhancing the charge-collection efficiency compared to their specific conductivity. This can be due to the fact that the total serial resistance of the “sandwich” electrodes composed of a porous conducting layer on a dense conducting substrate is low enough to provide efficient electron transport. The transparency of the films assembled from particles with different Sb contents is above 93 % of transmission in the visible range (Fig. 4.3.10), which makes them promising candidates for electrode layers for optoelectronic applications.

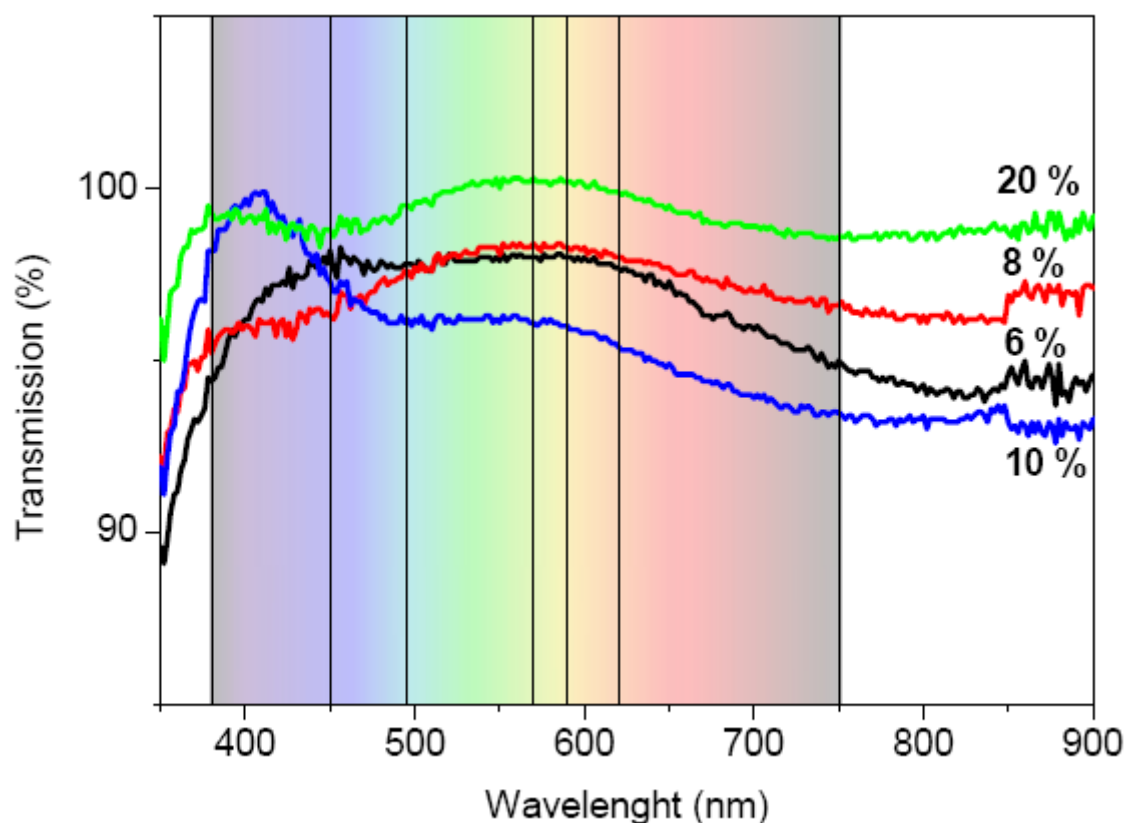


Figure 4.3.10. UV/VIS spectra of the mesoporous films assembled from ATO nanoparticles with different antimony content (given as the labels) and calcined at 400 °C. The average thickness of all films is 210 ± 10 nm.

4.3.6 Incorporation of Ruthenium Dye

One of the interesting electroactive guests which could use the full potential of 3D conductive and transparent electrodes is ruthenium dye. Ruthenium dyes were intensively studied with potential application in electrochemiluminescence devices for detection of amines.^{13, 31-34} The reaction is based on electro-oxidation of amines followed by their deprotonation which as a consequence gives excited species of amines, Figure 4.3.11. These amino excited species interact and excite the ruthenium dye, whereas they are transferred into oxidized products. The transformation of ruthenium dye into initial state is followed by the release of visible light (fluorescence).³³

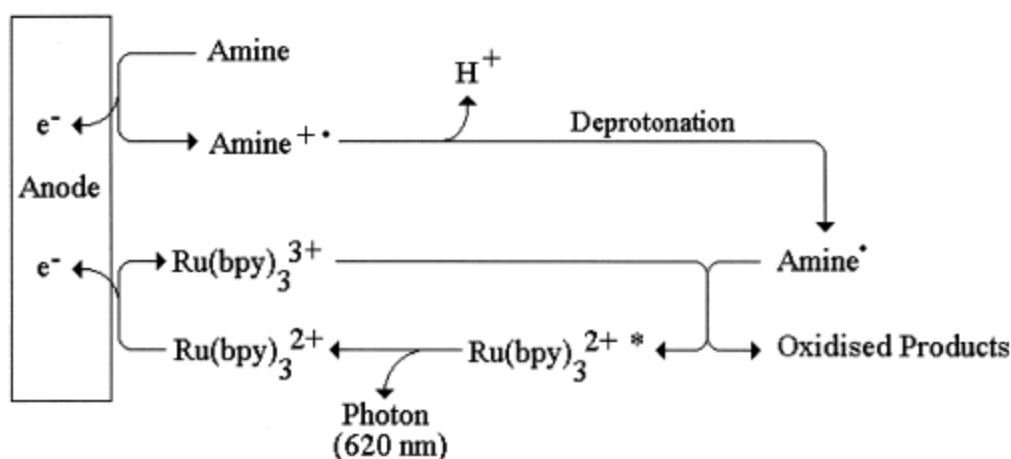


Figure 4.3.11. Proposed mechanism for the electrogenerate chemiluminescence (ECL) of $\text{Ru}(\text{bpy})_3^{2+}$ with an alkylamine. The figure is adopted from the reference [33].

In order to investigate the possibility of using mesoporous films as a platform for electroluminescence devices, two types of incorporation of ruthenium dye were explored. In the first case the dye was adsorbed in the mesoporous films, while in the second the dye was covalently attached in the same way as for previously described ferrocene carboxylic acid. The UV-VIS measurements of ATO films with incorporated ruthenium dye indicate its presence inside of the ATO films for both types of incorporation, Fig. 4.3.12.

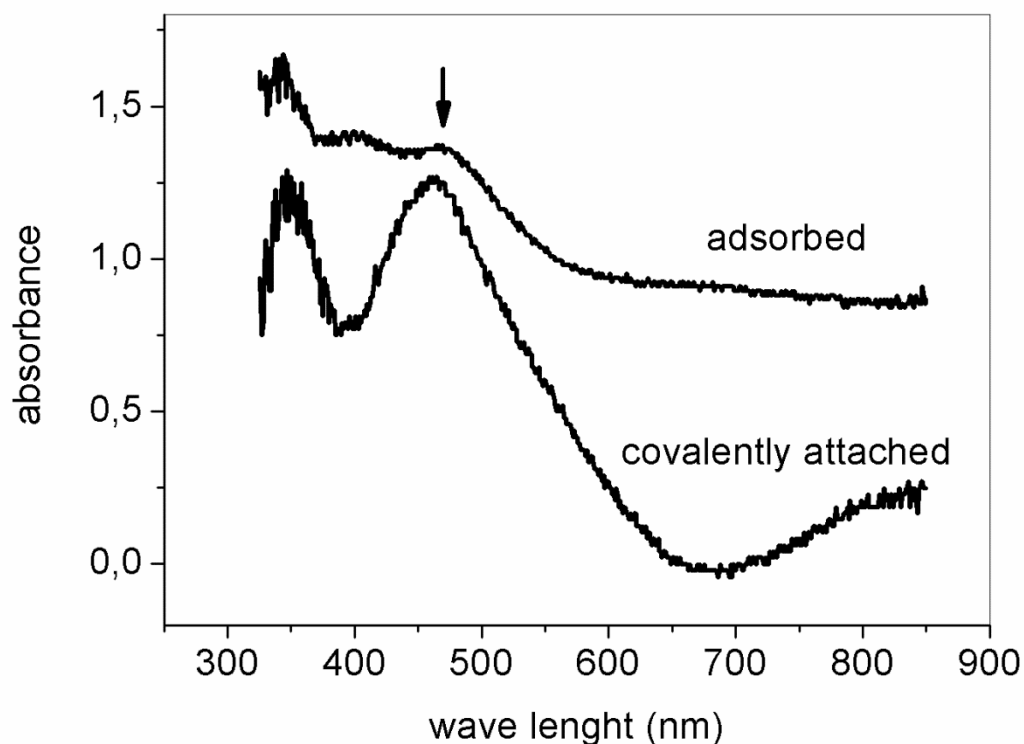


Figure 4.3.12. UV-VIS spectra of ruthenium dye adsorbed and covalently attached in ATO_10 mesoporous films. Spectra of the adsorbed sample is shifted for factor 0.85 in contrast to the sample with covalently attached. For the background subtraction a pure mesoporous film of ATO_10 was measured under the same condition and the spectra of the ATO_10 film was subtracted from ATO_10 modified films.

Both spectra contain peaks at 463 nm typical for ruthenium dye. However, the covalent attachment leads to a much stronger intensity confirming a better incorporation of the dye. I worked on optimization of the protocol for covalent attachment of the ruthenium dye by a variation of conditions of both reaction steps, namely the surface functionalization with APTES and the covalent binding of the dye. The varied parameters included the solvent and the reaction temperature, Table 4.3.2.

Table 4.3.2. List of samples according to the variation in the temperature for surface functionalization and the applied temperature for attachment of the dye

Sample	Surface functionalization with APTES	Applied temperature for attachment of the dye
1.	Dichlorometane (40 °C)	Room temperature
2.	Dichlorometane (40 °C)	70 °C
3.	Toluene (110 °C)	Room temperature
4.	Toluene (110 °C)	70 °C

From the UV-VIS results it can be seen that the surface functionalization of ATO films with APTES performed in toluene provides a higher loading of the ruthenium dye in comparison with the same attachment was performed in dichloromethane, Fig. 4.3.13.

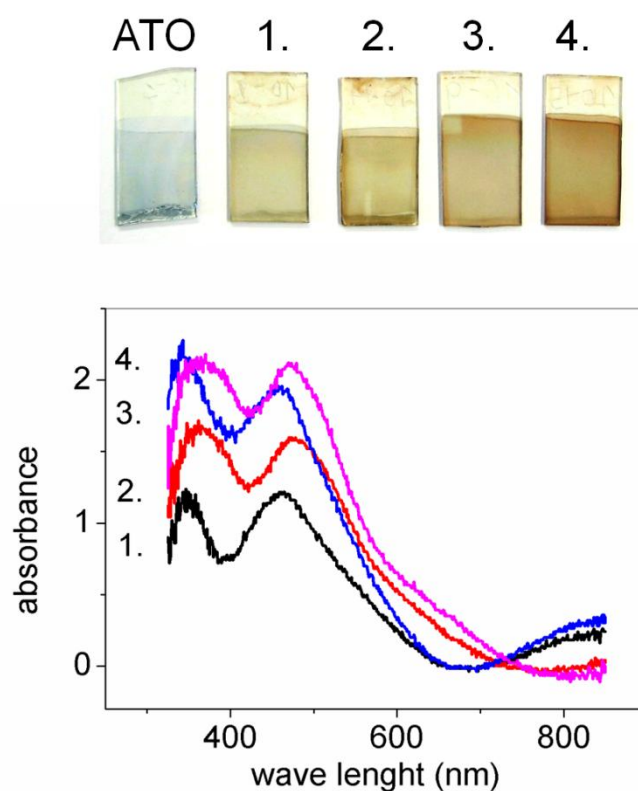


Figure 4.3.13. UV-VIS spectra of covalently attached ruthenium dye in mesoporous ATO₁₀ films and the images of the respective films. 1. Surface functionalization with APTES was performed in dichloromethane at 40 °C and the attachment of the dye at room temperature. 2. Surface functionalization with APTES was performed in dichloromethane at 40 °C and the attachment of the dye at 70 °C. 3. Surface functionalization with APTES was performed in toluene at 110 °C and the attachment of the dye at room temperature. 4. Surface functionalization with APTES was performed in toluene at 110 °C and the attachment of the dye at 70 °C. For the subtraction of the background the UV-VIS spectra of non-functionalized ATO sample presented in the figure above was used.

Covalent attachment of ruthenium dye via amide bond formation with the amino group of APTES functionalized ATO surface is strongly influenced by the temperature. The increase of temperature to 70 °C leads to a higher incorporation of ruthenium dye in comparison to the same synthesis procedure performed at room temperature. However, the dye incorporated in this way shows a slight shift of the peak in UV-VIS spectra from 463 nm to 474 nm. Considering that the colour in complex compounds comes from the transition between filled and unfilled *d*-orbitals with energies that depend on the ligands bonded to the metal ion, a slight distortion of the ligand field might induce a shift in the absorption of UV-VIS peaks.³⁵ Obviously an increase in temperature to 70 °C induces a higher incorporation of the dye. However, the increase in the temperature influences a non-preferable orientation of the dye which as a consequence might have the distortion of the ligands' bonds in octahedral coordination. This type of behaviour may explain the shift in the peak from 463 to 474 nm in UV-VIS absorption spectra.

4.3.7 Cyclic Voltammetry of Ruthenium Dye

Ruthenium Dye in Solution

In the first set of experiments, the voltammetric behaviour of the non-grafted ruthenium dye in solution was tested. The mesoporous ATO films and the flat ITO glass were used as the electrodes. Cyclic voltammograms of ruthenium dye in solution (0.3 mM, supporting electrolyte: 0.05 M phosphate buffer) are presented in Fig. 4.3.14. Cyclic voltammograms show a quasi-reversible pair of peaks both on flat ITO and mesoporous ATO working electrodes.

The formal potential, calculated as $E_{1/2} = (E_{pa} + E_{pc})/2$, is 1.15 V vs. Ag/AgCl reference electrode. The ATO electrode shows strong increase in charging current in comparison to the flat electrode as a result of a significantly increased surface area. For both types of electrodes

the peak current is low, although the active surface area of mesoporous ATO is in several times higher (20 – 50 times) than that of flat ITO.

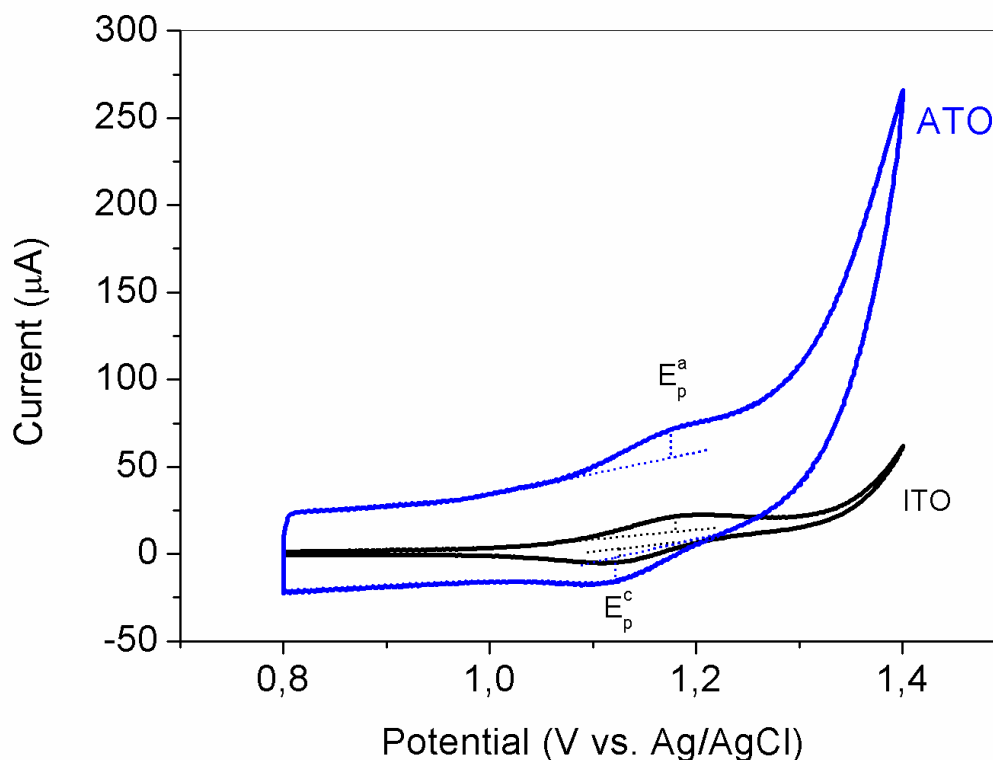


Figure 4.3.14. Cyclic voltammograms of ruthenium dye in solution (0.03 mM in 0.05 M phosphate buffer) recorded at scan rate of 50 mV/s. Black line represents the voltammogram when flat ITO was used as working electrode, whereas the blue line presents the voltammogram when mesoporous ATO was used as working electrode.

The electrochemiluminescence of the ruthenium dye in solution was tested in the presence of tripropylamine (TPA). After addition of TPA the cyclic voltammogram of the dye in solution shows different behaviour. Instead of the quasireversible pair of peaks only one oxidation peak is observed, which is positioned at 1.3 V (Fig. 4.3.15a), which is accompanied by a luminescence at the working electrode (Fig. 4.3.15b).

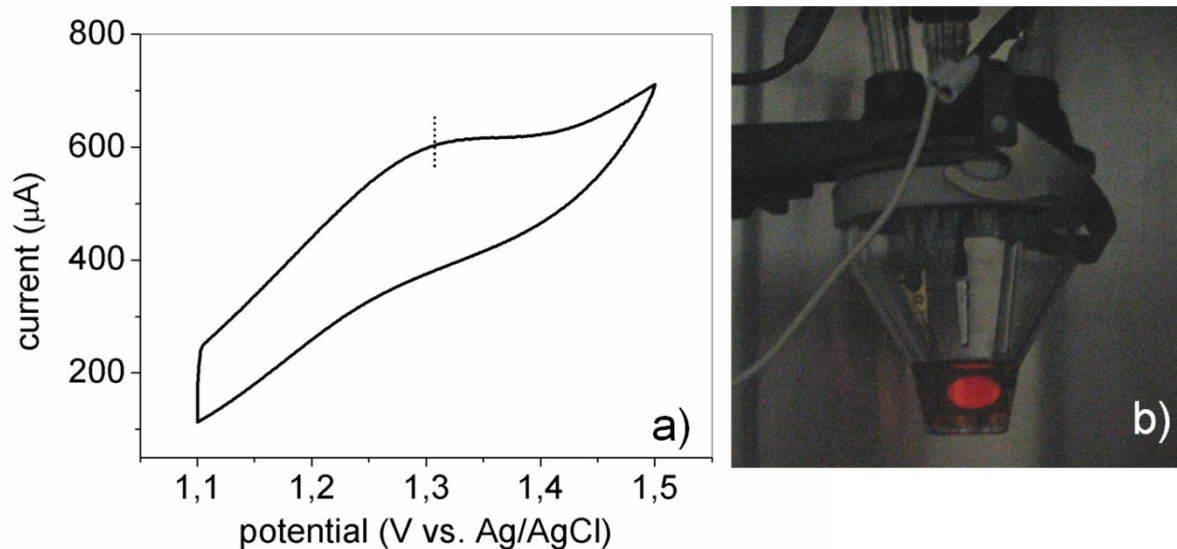


Figure 4.3.15. a) Cyclic voltammogram of 0.3 mM solution of ruthenium dye, 0.1 M TPA in 0.05 M phosphate buffer as supporting electrolyte with mesoporous ATO electrode as working electrode. The voltammogram was recorded at a scan rate of 50 mV/s. b) Observed fluorescence on working electrode.

Covalently Immobilized Ruthenium Dye

After the covalent attachment of ruthenium dye according to the procedure described above its electrochemical activity is preserved, as can be seen from the cyclic voltammogram in Fig. 4.3.16a. However, the redox current of incorporated ruthenium dye (calculated after the baseline subtraction) is very low. Moreover, the formal potential of covalently attached ruthenium dye (0.9 V vs. Ag/AgCl) is shifted to lower potentials compared to that in solution. The peaks have a Gaussian shape with a small peak separation of 20 mV at a scan rate of 50 mV/s.

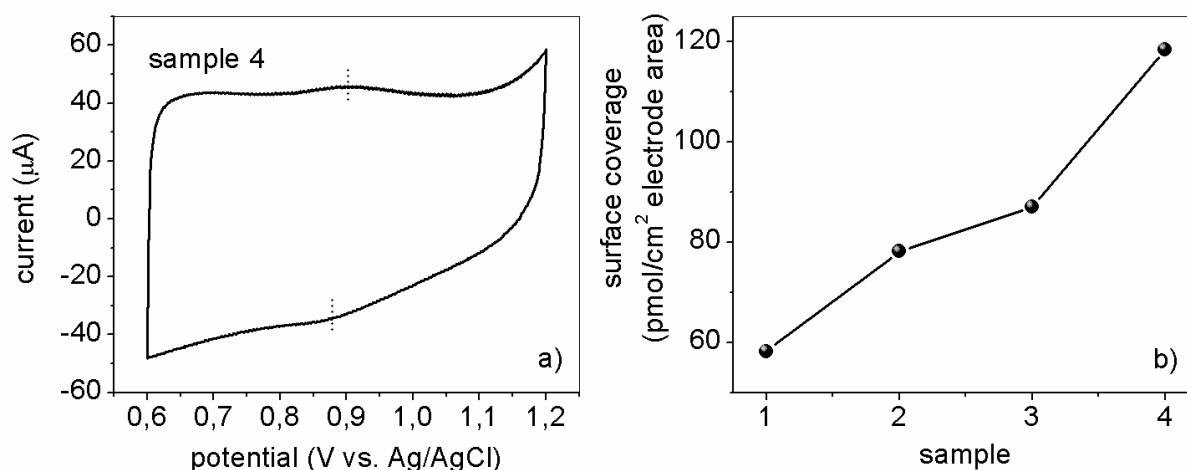


Figure 4.3.16. **a)** Cyclic voltammogram of the sample 4 obtained at 50 mV/s. Surface functionalization with APTES was performed in toluene, the attachment of Ru dye was performed at 70 °C. **b)** Surface coverage with ruthenium dye of ATO electrodes performed by modified attachment procedures.

The loading of ruthenium dye in mesoporous ATO films can be improved by the optimization of attachment procedure, but still the obtained values for surface coverage are very low. The electrochemiluminescent properties of the ruthenium dye immobilized in the mesoporous ATO was tested in the same system as the dye in solution described above. However, the light intensity of the immobilized dye is incomparably lower, probably due to the low loading of the dye.

4.4 Conclusions

Transparent conducting layers of antimony-doped tin oxide with a uniform mesoporosity and crystalline framework can be easily manufactured by the directed assembly of preformed ATO nanocrystals using commercially available and cheap polymers of the Pluronic family. The crystallinity of the nanoparticles serving as building blocks, enables fully crystalline inorganic frameworks with sufficient electrical conductivity to be obtained already at temperatures as low as 300 °C without any need for elaborate post synthetic treatment. Another attractive feature of this approach is the high thermal stability of the obtained mesostructure, exhibiting practically no shrinkage due to the temperature treatment, which is

a typical disadvantage of amorphous sol–gel-derived precursors. The use of preformed nanocrystals, whose preparation can be controlled with high precision, ensures a high reproducibility.

Owing to the open and accessible character of the porosity, the high surface area, and the uniform pore size, the mesoporous frameworks obtained are promising host materials for the accommodation of functional redox moieties. The high potential of the obtained mesoporous layers as nanostructured transparent electrodes with high surface areas was demonstrated with an example of ferrocene molecules, which were covalently immobilized in the conducting matrix, showing the significantly enhanced electrochemical response proportional to the electrode surface area.

The mesoporous ATO matrix was also tested as a platform for the covalent grafting of ruthenium dye aimed for the use in electroluminescence devices. However, the obtained low loadings of the dye resulted in a non sufficient amount of electrochemiluminescence response.

4.5 Appendix

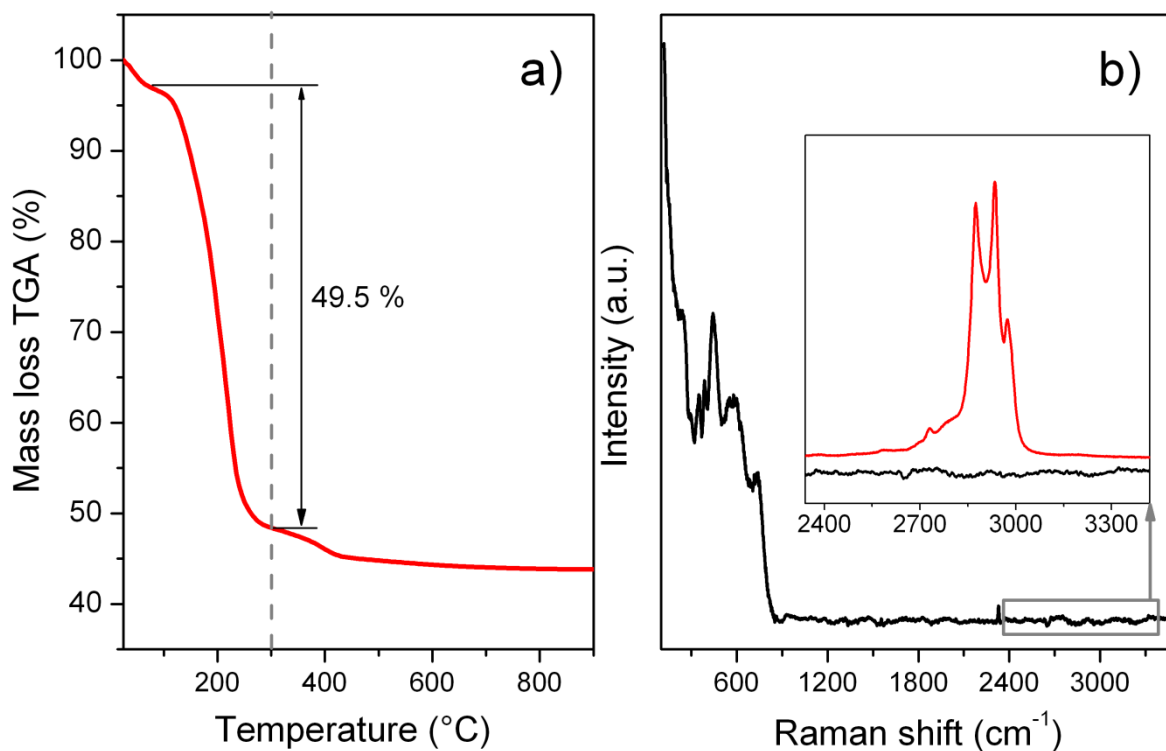


Figure A-4.1. Thermogravimetry data of the as prepared mesoporous film assembled from ATO₂₀ nanoparticles using Pluronic F127 as a templating agent at 1:1 weight ratio. A mass loss due to the Pluronic combustion takes place below 300 °C, which was selected as the lower temperature for the film's calcination and the template removal (a). Raman spectra of the film after calcination at 300 °C (b). An inset shows a range corresponding to the valence vibrations of C-H groups in the Pluronic copolymer before (red) and after calcination at 300 °C (black).

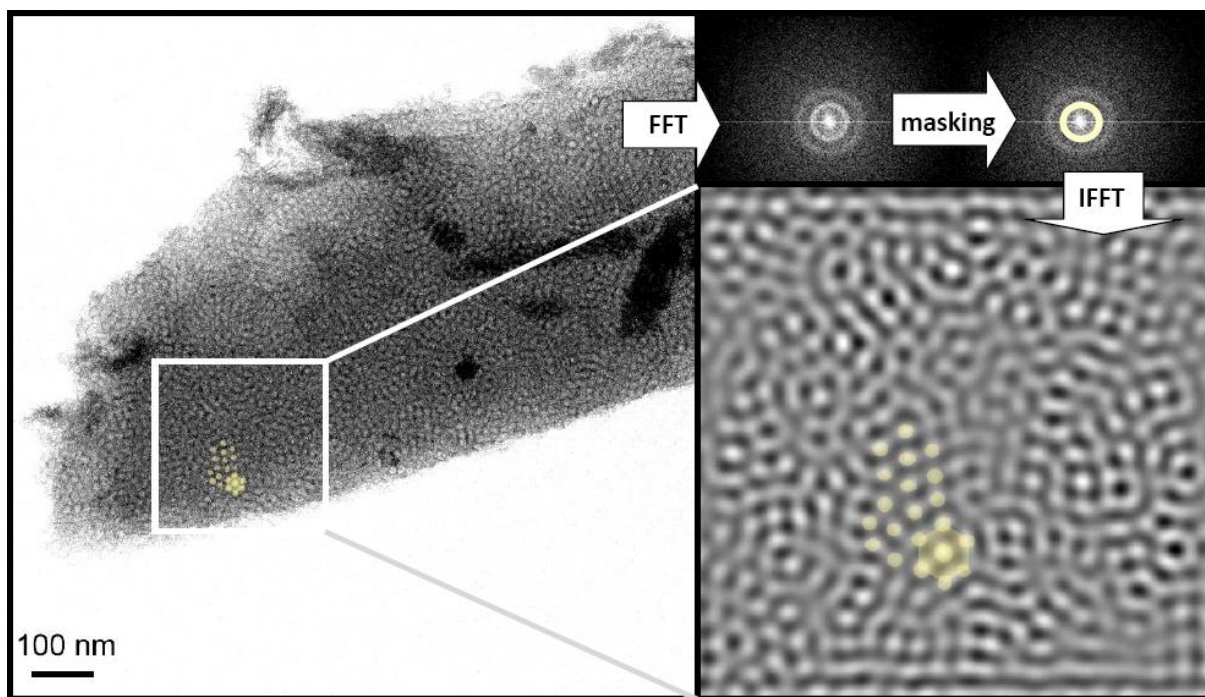


Figure A-4.2. TEM image of the film assembled from the ATO_20 nanoparticles and calcined at 300 °C. The domains with the periodicity of 14 ± 1 nm (marked in yellow) are apparent in the morphology (left) and in the inverse fast Fourier transformed (IFFT) images of the films.

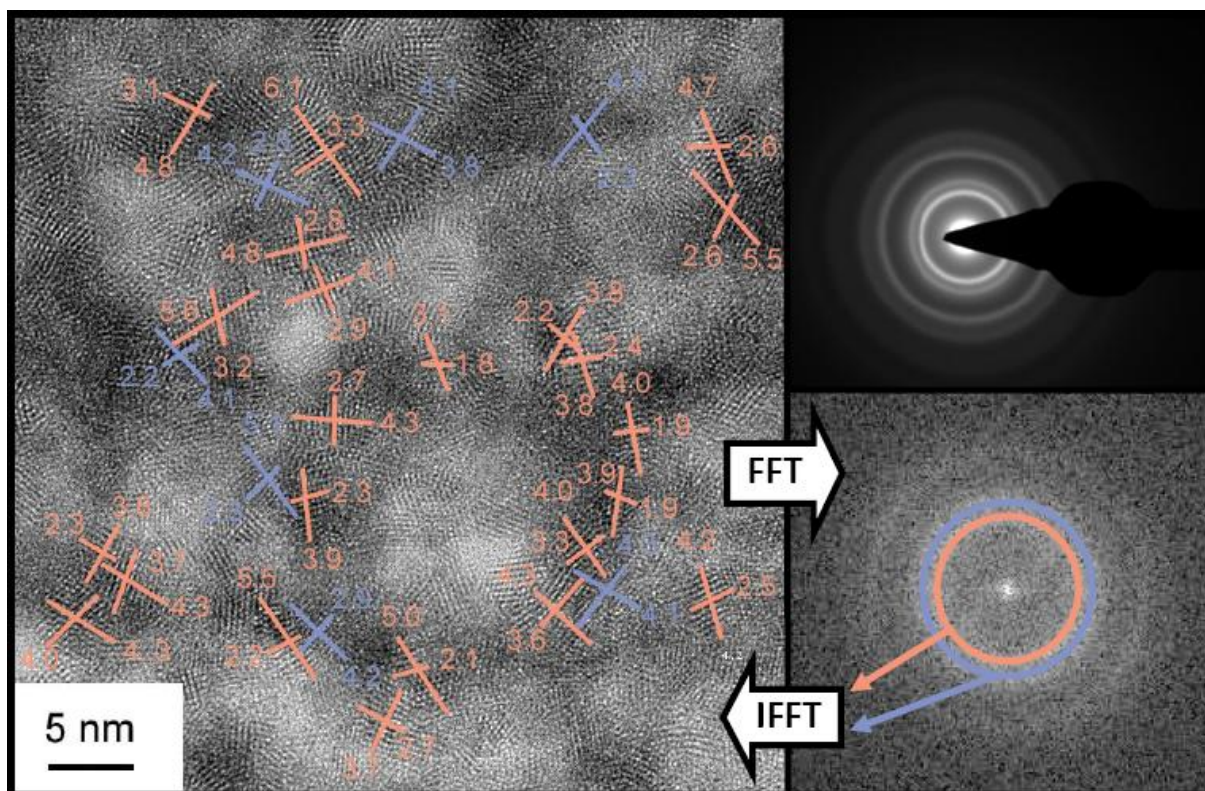


Figure A-4.3. Crystal size of the ATO₂₀ nanoparticles assembled to a mesoporous film and calcined at 400 C. The crystal size was determined for different crystal planes (indicated on the images) found after FFT filtering of the corresponding HR-TEM images. The numbers indicate the corresponding particle size in nm.

4.6 References

1. Hornyak, G. L.; Tibbals, H. F.; Dutta, J.; Moore, J. J., *Introduction to Nanoscience and Technology*. CRC Press, Boca Raton: 2009.
2. Chopra, K. L.; Major, S.; Pandya, D. K., *Thin Solid Films* **1983**, 102, 1.
3. Granqvist, C. G., *Sol. Energy Mater. Sol. Cells* **2007**, 91, 1529.
4. Franke, M. E.; Koplin, T. J.; Simon, U., *Small* **2006**, 2, 36.
5. Briseno, A. L.; Yang, P., *Nat. Mater.* **2009**, 8, 7.
6. Astuti, Y.; Topoglidis, E.; Briscoe, P. B.; Fantuzzi, A.; Gilardi, G.; Durrant, J. R., *J. Am. Chem. Soc.* **2004**, 126, 8001.
7. Topoglidis, E.; Astuti, Y.; Duriaux, F.; Grätzel, M.; Durrant, J. R., *Langmuir* **2003**, 19, 6894.
8. Vargo, M. L.; Gulka, C. P.; Gerig, J. K.; Manieri, C. M.; Dattelbaum, J. D.; Marks, C. B.; Lawrence, N. T.; Trawick, M. L.; Leopold, M. C., *Langmuir* **2010**, 26, 560.
9. Fattakhova-Rohlfing, D.; Brezesinski, T.; Rathouský, J.; Feldhoff, A.; Oekermann, T.; Wark, M.; Smarsly, B. M., *Adv. Mater.* **2006**, 18, 2980.
10. Frasca, S.; von Graberg, T.; Feng, J.-J.; Thomas, A.; Smarsly, B. M.; Weidinger, I. M.; Scheller, F. W.; Hildebrandt, P.; Wollenberger, U., *ChemCatChem* **2010**, 2, 839.
11. Aksu, Y.; Frasca, S.; Wollenberger, U.; Driess, M.; Thomas, A., *Chem. Mater.* **2011**, 23, 1798.
12. Batzill, M.; Diebold, U., *Progr. Surf. Sci.* **2005**, 79, 47.
13. Hou, K.; Puzzo, D.; Helander, M. G.; Lo, S. S.; Bonifacio, L. D.; Wang, W.; Lu, Z. H.; Scholes, G. D.; Ozin, G. A., *Adv. Mater.* **2009**, 21, 2492.
14. Wang, Y.; Brezesinski, T.; Antonietti, M.; Smarsly, B., *ACS Nano* **2009**, 3, 1373.
15. Smarsly, B. M.; Fattakhova-Rohlfing, D., in *Solution Processing of Inorganic materials*. John Wiley & Sons: New Jersey, 2009.

16. Sanchez, C.; Boissiere, C.; Grosso, D.; Laberty, C.; Nicole, L., *Chem. Mater.* **2008**, 20, 682.
17. Grosso, D.; Boissiere, C.; Smarsly, B.; Brezesinski, T.; Pinna, N.; Albouy, P. A.; Amenitsch, H.; Antonietti, M.; Sanchez, C., *Nat. Mater.* **2004**, 3, (11), 787.
18. Brezesinski, T.; Fischer, A.; Iimura, K. i.; Sanchez, C.; Grosso, D.; Antonietti, M.; Smarsly, B. M., *Adv. Funct. Mater.* **2006**, 16, 1433.
19. Thomas, A.; Schlaad, H.; Smarsly, B.; Antonietti, M., *Langmuir* **2003**, 19, 4455.
20. Yang, P.; Zhao, D.; Margolese, D. I.; Chmelka, B. F.; Stucky, G. D., *Chem. Mater.* **1999**, 11, 2813.
21. Yang, P.; Zhao, D.; Margolese, D. I.; Chmelka, B. F.; Stucky, G. D., *Nature* **1998**, 396, 152.
22. Wong, M. S.; Jeng, E. S.; Ying, J. Y., Supramolecular Templating of Thermally Stable Crystalline Mesoporous Metal Oxides Using Nanoparticulate Precursors. *Nano Letters* **2001**, 1, (11), 637-642.
23. Bosc, F.; Ayral, A.; Albouy, P.-A.; Datas, L.; Guizard, C., *Chem. Mater.* **2004**, 16, 2208.
24. Corma, A.; Atienzar, P.; Garcia, H.; Chane-Ching, J.-Y., *Nat. Mater.* **2004**, 3, 394.
25. Deshpande, A. S.; Pinna, N.; Smarsly, B.; Antonietti, M.; Niederberger, M., *Small* **2005**, 1, 313.
26. Ba, J. H.; Polleux, J.; Antonietti, M.; Niederberger, M., *Adv. Mater.* **2005**, 17, 2509.
27. Brezesinski, T.; Wang, J.; Polleux, J.; Dunn, B.; Tolbert, S. H., *J. Am. Chem. Soc.* **2009**, 131, 1802.
28. Müller, V.; Rasp, M.; Štefanić, G.; Ba, J.; Günther, S.; Rathousky, J.; Niederberger, M.; Fattakhova-Rohlfing, D., *Chem. Mater.* **2009**, 21, 5229.
29. Bass, J. D.; Grosso, D.; Boissiere, C. d.; Sanchez, C. m., *J. Am. Chem. Soc.* **2008**, 130, 7882.

30. Bard, A. J.; Faulkner, L. R., *Electrochemical Methods, Fundamentals and Applications*. John Wiley & Sons, Inc.: New York, 2001.
31. Dennany, L.; O'Reilly, E. J.; Keyes, T. E.; Forster, R. J., *Electrochem. Commun.* **2006**, 8, 1588.
32. Miao, W., *Chem. Rev.* **2008**, 108, 2506.
33. Knight, A. W., *Trends Anal. Chem.* **1999**, 18, 47.
34. Bertoncello, P.; Forster, R. J., *Biosens. Bioelectron.* **2009**, 24, 3191.
35. Skoog, D. A.; Holler, F. J.; Crouch, S. R., *Principles of Instrumental Analysis*. Thomson Brooks/Cole: 2007.

5 Surface Functionalization of Mesoporous Antimony Doped Tin Oxide

This chapter is based on the following publication:

Vesna Müller, Frederik Haase, Jiri Rathousky and Dina Fattakhova-Rohlfing,

“Surface functionalization of mesoporous antimony doped tin oxide by metalorganic reaction”, Materials Chemistry and Physics, **2012**, 137, 207-212

5.1 Introduction

Grafting of organic moieties in the pores of nanoporous metal oxides is a very important step in the preparation of functional materials for applications in catalysis, separation, energy conversion and drug delivery. Organic groups can have different functions depending on the intended application, for example serve as anchoring sites for an attachment of desired moieties, surface modifiers and catalysis or polymerization sites. Therefore, various strategies have been developed for the functionalization of porous materials.¹ The developed strategies are mostly based on the surface hydroxide groups of metal oxides, which react with easily hydrolysable compounds such as metal (typically silicon) chlorides, alkoxides, hydrides or allyls as coupling agents with formation of metal-oxide bridges.²⁻⁴

This is one of the most common approaches for grafting various organic moieties in the pores of silica⁵ and metal oxides.^{6, 7} However, not all the functional groups can be introduced by this method, as the corresponding silicon compounds bearing the desired functionalities are often unavailable or difficult to prepare. Moreover, extensive polymerization and cross-linking of the reactive silicon groups in the pores leading to the pore blocking, or non-homogeneous distribution of the grafted groups at the pore openings and inside the pores are the other frequent problems of the silanization grafting route.⁸

As an alternative approach, a metalorganic functionalization of porous metal oxides was developed, which in many cases offers a much easier and simpler route to grafting of various functional groups and was intensively studied in our group.⁹⁻¹¹

As due to a different reaction mechanism the presence of the surface hydroxide groups is not required, hydrophobic metal oxides and non-oxide materials can be successfully functionalized. An additional feature of metalorganic approach unachievable by the silanization route is the direct attachment of the organic moieties to the metal atoms. This can be of special interest in applications involving electron transfer between the grafted organic groups and the semiconducting or conducting metal oxides, where such a direct connection of a functional group to the metal atom of the oxide is often desirable.¹⁰⁻¹²

The metalorganic approach has been successfully performed for the grafting organic functionalities on the surface of mesoporous silica,¹¹⁻¹³ amide-modified Au nanoparticles and Ge nanowires,^{14, 15} amorphous carbon substrates¹⁶ or group III-V semiconductors.^{17, 18}

As the suitability of this approach for chemical functionalization of porous semiconducting or conducting metal oxides has not been investigated yet, this communication is aimed at the functionalization of the surface of mesoporous antimony-doped tin oxide (ATO) by the Grignard reactions. ATO belongs to transparent conducting oxides,¹⁹⁻²¹ and its mesoporous form is attractive as nanoporous conducting electrodes with a large surface area, able to accommodate large amounts of the functional redox guests.^{6, 22} The efficient heterogeneous charge transfer requires an intimate coupling between the redox groups and the electrode, which can be achieved by the successful grafting of organic functions on the ATO surface.

In this work multiple bonded systems and aromatic groups were introduced into the mesoporous ATO by the Grignard reaction. The chosen Grignard reagents served as model compounds bearing double bonds (vinyl and allyl) and an aromatic system (phenyl). The incorporation of double bonded systems offers the possibility for a further attachment of functional molecules¹⁰ and a use of conjugated chain system as a charge linker¹ between an

electroactive moiety and the surface of oxide. Addition to this surface functionalization with organosilane molecules was explored and used later on for the anchoring of electroactive species.

5.2 Experimental Section

5.2.1 Chemicals

Tin(IV) chloride (99 %), antimony(III) acetate (99.99 %), anhydrous benzyl alcohol (99.8 %, <0.003 % water), anhydrous toluene (≥ 99.7 %; <0.005 % water), anhydrous dichloromethane (DCM) (≥ 99.5 %; <0.005 % water), anhydrous diethylether (DE) (≥ 99.7 %) and tetrahydrofuran (THF) (≥ 99.5 %), absolute ethanol (99.9 %), (3-aminopropyl)triethoxysilane (APTES) (99 %), phenylmagnesium bromide (1.0 M in THF), vinylmagnesium bromide (1.0 M in THF), allylmagnesium bromide (1.0 M in DE) were purchased from Aldrich and used without further purification.

5.2.2 Synthesis of ATO Nanoparticles and Mesoporous Powders

The ATO nanoparticles, which were used as building block for the assembly into mesoporous nanostructure, were synthesized according the previously established procedure.²² In short, the preparation of the nanoparticles with 10 mol % of antimony tin(VI) chloride (3.2 g, 12.3 mmol), and Sb(III) acetate (0.41 g, 1.35 mmol) were dissolved in toluene (10 mL) and added to benzyl alcohol (30 mL, 291 mmol) under continuous stirring. The solution was kept in a closed glass vessel in a laboratory oven at 100 °C for 20 h. Afterwards, the particles were separated by centrifugation at 50 000 rcf for 20 min and dried in air. The amount of organic residuals left from the synthesis was evaluated through TG analysis and was found to be 30 wt %. The preparation of solutions, which were used for assembly of mesoporous structured

and ATO powders, was described in previous chapter.²² Briefly, the as prepared nanoparticles (0.4 g) containing 10 mol% Sb were dispersed in a solution of Pluronic F127 (0.28 g) in THF (6 ml) by stirring for 2 h at room temperature. The final solution was transparent, orange-brownish in colour and in that way used for the preparation of mesoporous powders. The mesoporous powders were prepared by drop casting of the mentioned solutions in porcelains crucibles. The dried residuals were transferred into an oven and calcined at 500 °C (with a ramp rate of 0.6 °C min⁻¹) for 30 min in order to remove the organic template. The mesoporous ATO powders are assigned as mATO.

5.2.3 Surface Functionalization of Mesoporous ATO with APTES

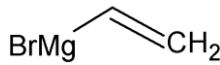
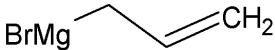
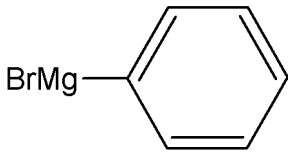
The mATO films or powders were transferred into Schlenk bottles and dried for 90 minutes at 110 °C in vacuum. Afterwards, 20 mM solution of APTES in either dried toluene or dried dichloromethane was added and all was refluxed for 2 h. In the case of the solution of toluene the reflux temperature was set to 110 °C whereas in the case of DCM it was 40 °C. Subsequently, in both cases, films or powders were washed once with DCM and once with ethanol and dried over night at 60 °C.

5.2.4 Surface Functionalization of Mesoporous ATO with Grignard Reagents

The mATO (0.5 g) was dried for 12 h in the oven at 60 °C in air and then for 90 minutes at 120 °C in Schlenk bottles under vacuum. The dried material was cooled to room temperature. The specific metal-organic compound (10 mmol; 1 M solution in THF or DE) was added drop wise to the mATO-10 powder in Schlenk bottles. The resulting suspension was stirred for 4 h at room temperature, quenched with ethanol, and filtered. The remaining powder was washed with 100 mL of water, centrifuged and washed again with 100 mL of ethanol followed by centrifugation. The resulting powder was dried at 60 °C in air overnight followed by a 24 h

Soxhlet extraction using dichloromethane. The names of the respective Grignard compounds used for modification are listed in Table 5.2.1.

Table 5.2.1. Grignard compounds used for the modification of the mesoporous ATO.

Functional group	Solvent	Sample name
	THF	Vinyl-ATO
	THF	Allyl-ATO
	THF	Phenyl-ATO

5.2.5 Characterization Techniques

Scanning transmission electron microscopy in high-angle annular dark-field mode (STEM-HAADF) were performed using a FEI Titan 80-300 system that was equipped with a field-emission gun operated at 300 kV. The mesoporous ATO particles were prepared by evaporating a drop of a diluted suspension of particles in ethanol on a Plano carbon-coated copper grid.

Small-angle XRD measurements of the mesoporous powders were performed on a SCINTAG XDS 2000 diffractometer with Ni-filtered $\text{CuK}\alpha$ radiation ($\lambda=1.5406 \text{ \AA}$), theta/theta geometry, and a scintillation detector operated at 40 kV and 30 mA.

The TGA analysis was performed on a Netzsch Model STA 4400 C TG/DSC instrument by heating a 10 mg sample at a heating rate of 10 K/min in a stream of synthetic air (25 mL/min). Nitrogen sorption measurements on the mesoporous ATO powders were obtained using a Quantachrome Instrument NOVA 4000e Surface Area & Pore Size Analyzer at 77 K. Surface area calculations were made using the Brunauer-Emmett-Teller (BET) equation in the range

from $p/p_0 = 0.05 - 0.3$. The pore-size distribution was determined using a DFT-method (NLDFT adsorption branch, cylindrical pores, N_2 on silica). The reason for applying this method instead of BJH, which is common for most of the oxides, is a smaller error resulting from the calculation. Although the NLDFT does not have a model for the tin oxide, it provides more precise results in our case, in comparison to BJH, even when silica as a model is used. The reason for this is that the BJH method does not provide accurate results in the case of small pores and usually the average error is in the range of 10-20 %.

The IR spectra were measured on a Bruker Equinox 55 in transmission mode. The samples for IR measurements were mixed with KBr at a 1:100 ratio and pressed into pellets. The obtained spectra are background subtracted. For recording the background a pure KBr pallet was prepared and measured under the same conditions as the pellet with sample.

Raman spectra were recorded with a LabRAM HR UV-VIS (Horiba Jobin Yvon) Raman microscope (Olympus BX41) coupled with a Symphony CCD detection system, using a HeNe laser at a wavelength of 632.8 nm.

5.2.6 Calculation Methods

The Amount of Attached Organic Groups

The surface functionalization density was calculated from TGA data. The minor loss of 1.5 % in mATO is attributed to the combustion of organic residuals which remained from the synthesis procedure. The true mass loss was calculated by subtracting the mass loss of the parent non functionalized mATO from the corresponding mass loss of the functionalized sample. Using this value the amount of organic group per gram of mATO was calculated. This can be achieved by dividing the mass loss by the amount of mATO in one gram of the sample.

$$\frac{\text{mol (functional group)}}{\text{g (ATO)}} = \frac{\text{mass los of functional group (per g of sample)}}{(\text{molar weight of functional group}) \left(1 - \frac{\text{percent of tatal mass loss}}{100}\right)} \quad (\text{eq. 5.2.1})$$

5.3 Results and Discussion

5.3.1 Mesoporous ATO Powders

The mesoporous ATO systems prepared by the assembly of ATO nanoparticles so far have been studied as mesoporous films.⁶ On the basis of previous results, the mesoporous powders were prepared from the solutions which were used for coating substrates, by casting them in air. After the heat treatment at 500 °C, used to remove the organic template, the mesostructuring of the prepared powders was investigated by a small angle X-ray scattering (SAXS) and the data were compared with the data for mesoporous films, Fig. 5.3.1.

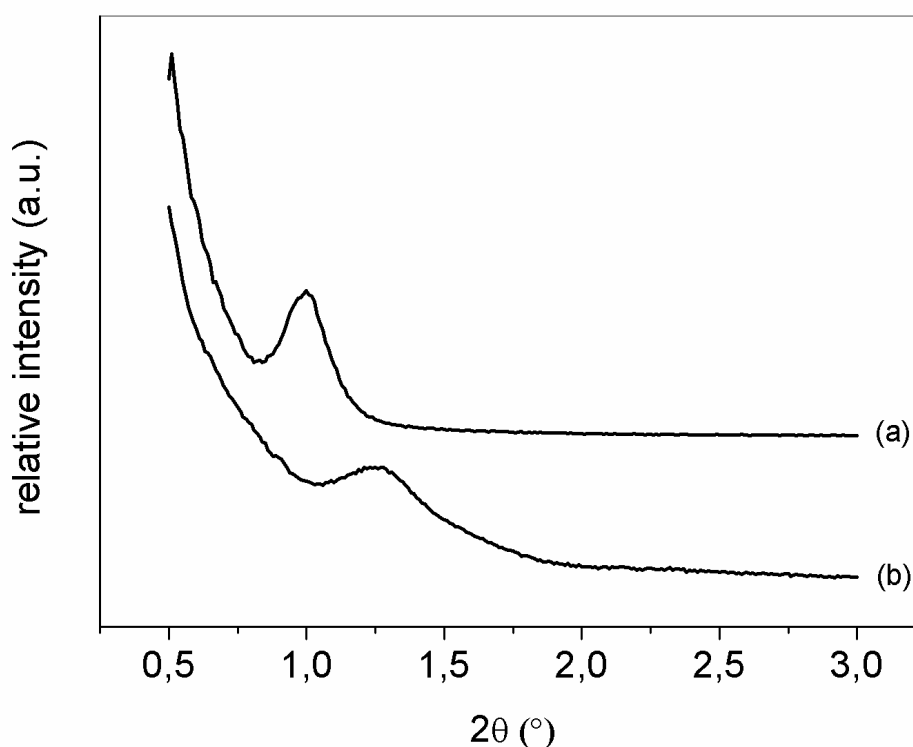


Figure 5.3.1. Small angle X-ray scattering data of (a) mesoporous ATO film and (b) mesoporous ATO powder.

The presence of periodic mesostructured domains in porous ATO powders was confirmed via X-Ray diffraction, nitrogen sorption measurements and in Scanning Transmission Electron Microscopy (STEM). Compared to mesoporous ATO films which show a sharp peak

positioned around $1.0^\circ 2\theta$ in XRD pattern, the mesoporous ATO powder shows a similarly broad smaller peak shifted towards higher 2θ values. This indicates that the pore shrinkage during the combustion of the mesostructuring template is much more pronounced than in the case of films. The calculated d spacing for mesoporous powder was found to be 7.2 nm in comparison to the mesoporous films where it is 9 nm. This significant change in d spacing may be due to the fact that during the calcinations procedure, in the case of the powder, the shrinkage is happening in all three dimensions whereas, in the case of films it is happening only in the direction perpendicular to the plane of the films. STEM images of mesoporous powders indicate a good periodicity of the pore ordering, Fig. 5.3.2

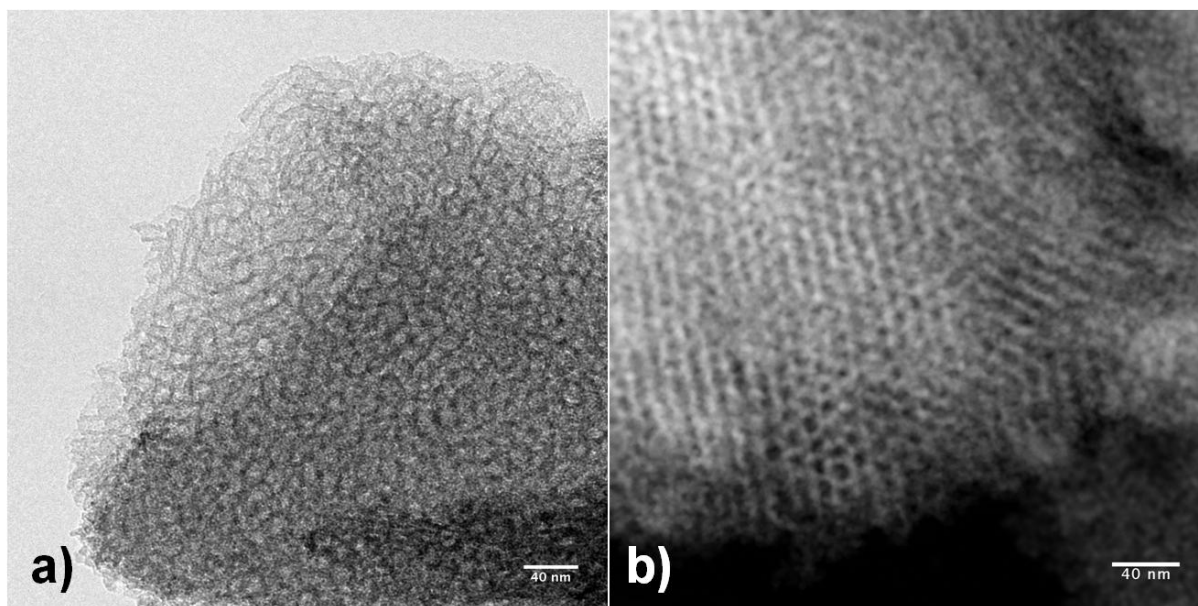


Figure 5.3.2. a) TEM image of mesoporous ATO film and b) STEM image of mesoporous ATO powder

5.3.2 Surface Functionalization with APTES

The presence of the attached APTES molecules on the mesoporous ATO powders was confirmed by IR spectroscopy, Fig. 5.3.3.

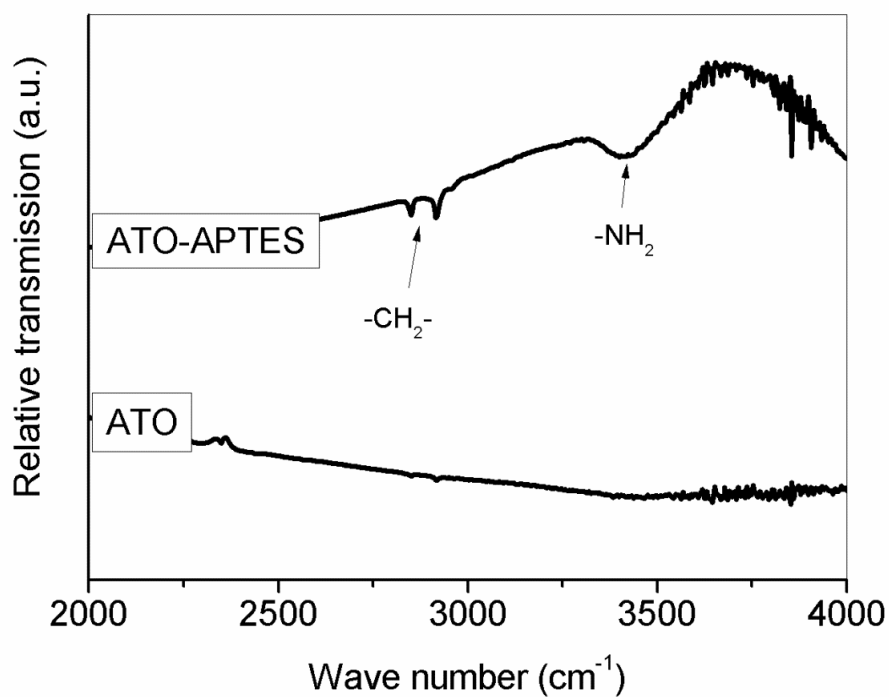


Figure 5.3.3. IR spectra of the mesoporous ATO powder assigned in the graph as ATO and IR spectra of the APTES functionalized mesoporous ATO assigned in the graph as APTES-ATO.

The APTES functionalized mesoporous ATO powder shows vibrations of -CH₂- and -NH₂ in IR spectra which are in the pristine mesoporous ATO powder absent.

The presence of the functional groups attached to the pore walls of ATO was additionally shown by nitrogen sorption measurements, Fig. 5.3.4.

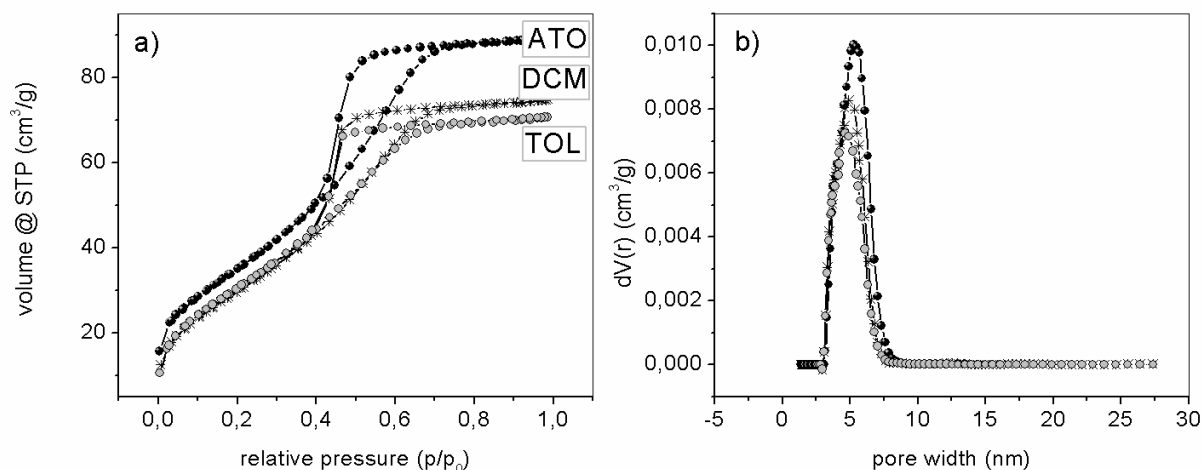


Figure 5.3.4. a) Nitrogen sorption isotherms and b) pore size distribution of pristine ATO powder (ATO), APTES functionalized powder in dichloromethane (DCM) and APTES functionalized powder in toluene (TOL). Evaluation of the pore size is performed via NLDFT fitting, silica model, adsorption branch.

Both non-functionalized and APTES functionalized samples show the type IV isotherms typical for the mesoporous materials. The total pore filling takes place at lower relative pressures for APTES modified samples in comparison to non modified ones as a result of the reduction of the pore size after attachment of the functional groups. The change in pore size between pristine mesoporous ATO and functionalized powders is obtained through the evaluation of sorption data. The APTES functionalized sample in toluene shows slightly lower BET area and larger pore size reduction in comparison to the APTES functionalized sample in dichloromethane. These results indicate a higher degree of surface functionalization of ATO when reaction is performed at higher temperature i.e. in toluene in comparison to lower temperature in dichloromethane. Nevertheless, all samples show a decrease in BET surface area, pore volume and pore size after the incorporation of APTES molecules on the inner surface of the pores (Table 2). This suggests a successful surface functionalization of the pore walls in mesoporous powders.

Table 5.3.1 The BET surface area and obtained pore sizes for non-functionalized ATO (mATO), APTES-functionalized ATO in dichloromethane (DCM) and APTES-functionalized ATO in toluene (TOL).

Sample	BET surface (m ² /g)	Pore size (nm)
mATO	130.3	5.68
DCM	119.5	5.1
TOL	114.1	4.9

5.3.3 Surface Coverage with APTES Molecules

The functionalization density was determined by thermogravimetric analysis (Fig. 5.3.5).

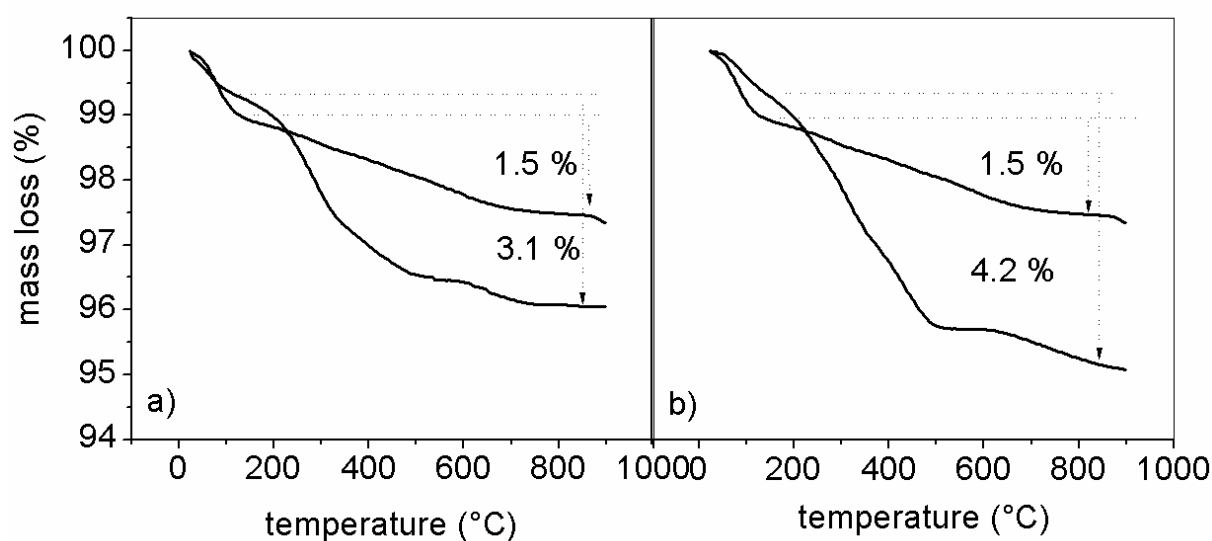


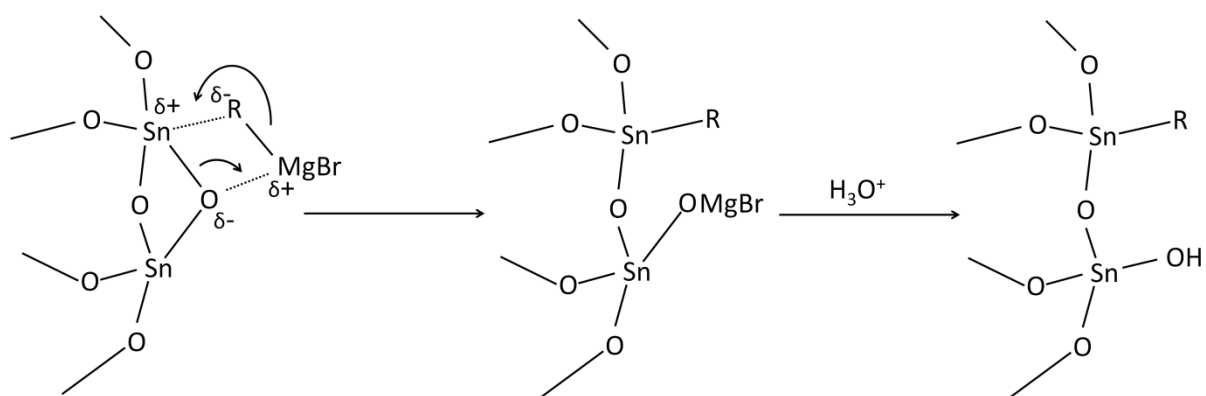
Figure 5.3.5. TGA data of APTES-functionalized sample in **a)** dichloromethane and **b)** toluene.

The non-functionalized mesoporous ATO powder shows only a minor mass loss of 1.5 % (Fig. 5.3.5) (beyond that below 200 °C associated with volatile molecules), which was attributed to dehydroxylation. In the case of APTES surface functionalized sample in toluene, the total mass loss of 4.2 % (or additional 2.7 %) corresponds to 0.47 mmol g⁻¹ of the aminopropyl residues ($M = 58.104 \text{ g mol}^{-1}$, $m = 27.1 \text{ mg/g}$ of ATO) bound to the ATO

surface. When the same reaction of the surface functionalization with APTES is performed in DCM a slightly different result is obtained (Fig. 5.3.4-a). The amount of incorporated aminopropyl residues bound to the ATO surface is smaller, namely 0.28 mmol g^{-1} (16.5 mg/g of ATO). Apparently the difference in the reflux temperature results in a lower amount of attached APTES.

5.3.4 Surface Functionalization with Grignard Reagents

Due to the lack of the available literature on metalorganic reaction of the tin oxide, the proposed reaction mechanisms are extrapolated from the available literature on silica materials. The grafting of organic groups on the surface of dehydrated metal oxides (silica) using Grignard reaction is expected to follow the general scheme proposed by Lim et al.²³ The proposed mechanism can be easily adapted for grafting of the organic groups on the surface of tin oxide using Grignard reagents typically presented as R-MgBr (or R-MgX), Scheme 5.3.1. During the reaction of the Grignard reagents with the surface of silica, the magnesium atom is expected to form a complex with bridging oxygen from the surface of SiO_2 and to increase electrophilicity of the silicon atoms on the surface,^{23, 24} Simultaneously, the organic part of the Grignard reagent (R) acts as a nucleophile. An addition of the nucleophile (organic part of the Grignard reagent) to the silicon atom forms a starting product of the Grignard reaction. Hydrolysis of the Mg-O bond forms a final product i.e. hydroxylic group. In comparison to silica materials, the tin atoms have a higher partial positive charge and consequently exhibit a higher reactivity in the nucleophilic substitution reaction.²⁵



Scheme 5.3.1. Proposed mechanism of the Grignard reaction on tin oxide surface

For testing the possibility of surface functionalization of mesoporous conducting ATO materials via metalorganic reactions we introduced several types of non-saturated moieties containing multiple bonds and aromatic groups (Table 5.2.1). such as vinyl, allyl and phenyl groups. These moieties were selected as the model representatives of the conjugated systems and as practically important functionalities which can be used as anchor sites for further surface reactions (e.g. electrophilic addition).

The parent ATO material features a uniform open mesoporosity with a reasonable degree of the pore ordering, as follows from the presence of the reflection at small angles in the XRD pattern corresponding to the mesostructure periodicity of 7.2 nm (Fig. 5.3.1) and N_2 sorption isotherms (Fig. 5.3.4). For organic functionalization, the mesoporous ATO was stirred at room temperature with the corresponding Grignard reagent and washed afterwards using Soxhlet extraction with dichloromethane for 24 hours to ensure that any physisorbed organics were removed. The mesoporous ATO material features the same porous characteristics also after reaction with the Grignard reagents (Fig. 5.3.6), indicating stability and integrity of the mesoporous ATO framework in this type of reactions.

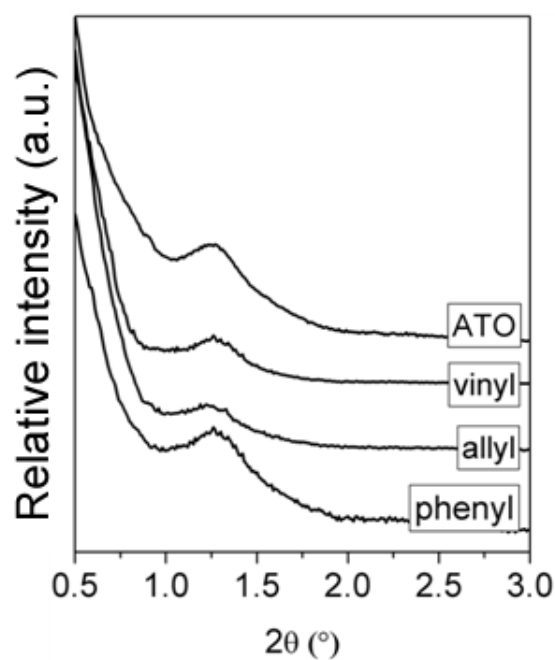


Figure 5.3.6. XRD patterns of the non-modified mesoporous ATO and mesoporous ATO functionalized with vinyl-, allyl- and phenyl-groups.

The homogeneity of the pore functionalization was investigated by nitrogen sorption measurements. Both pristine and surface functionalized samples show the type IV isotherms typical for the mesoporous materials (Fig. 5.3.7, a), indicating that the mesoporous character of the ATO is preserved after the Grignard reaction.

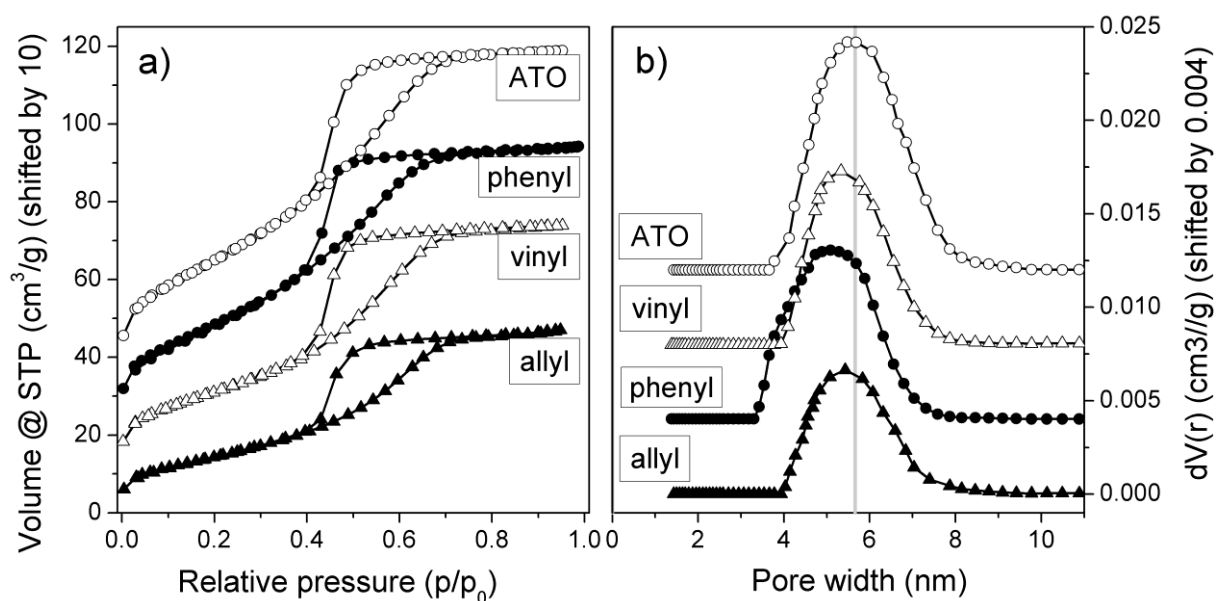


Figure 5.3.7. a) Nitrogen sorption isotherms and b) pore size distribution for the mesoporous ATO non modified and functionalized with vinyl, allyl, butyn and phenyl groups. The curves in a) and b) are shifted by 10 cm³/g and 0.004 cm³/g, respectively (from bottom to top), for the sake of comparison. The sorption plots with the original scale are shown in Figure A-5.1. (Appendix).

The introduction of the organic moieties however leads to a decrease in the BET surface area and of the pore size (Table 5.3.2). The total pore filling takes place at lower relative pressures for organically modified samples in comparison to non modified ones as a result of the reduction of the pore size after the attachment of the functional groups (Fig. 5.3.7-b and Table 5.3.2). Preservation of the character of porosity together with the reduction in the pore size gives an indication of a successful incorporation of organic moieties on the pore walls without pore blocking.

Table 5.3.2. BET area and pore diameter of non functionalized and functionalized samples.

Samples	BET (m ² /g)	Pore diameter (nm)*
ATO	130.3	5.68
Vinyl-ATO	77.4	5.48
Allyl-ATO	61.3	5.48
Phenyl-ATO	104.7	5.09

* Obtained through NLDFT calculation on adsorption branch using silica model.

5.3.5 Surface Coverage Obtained by Metalorganic Reactions

The total amount of the incorporated organic groups was evaluated from the thermogravimetric data (TGA). TGA curves of the ATO samples after the Grignard functionalization show significant mass losses compared to the pristine ATO due to removal of the grafted organic moieties, Fig. 5.3.8.

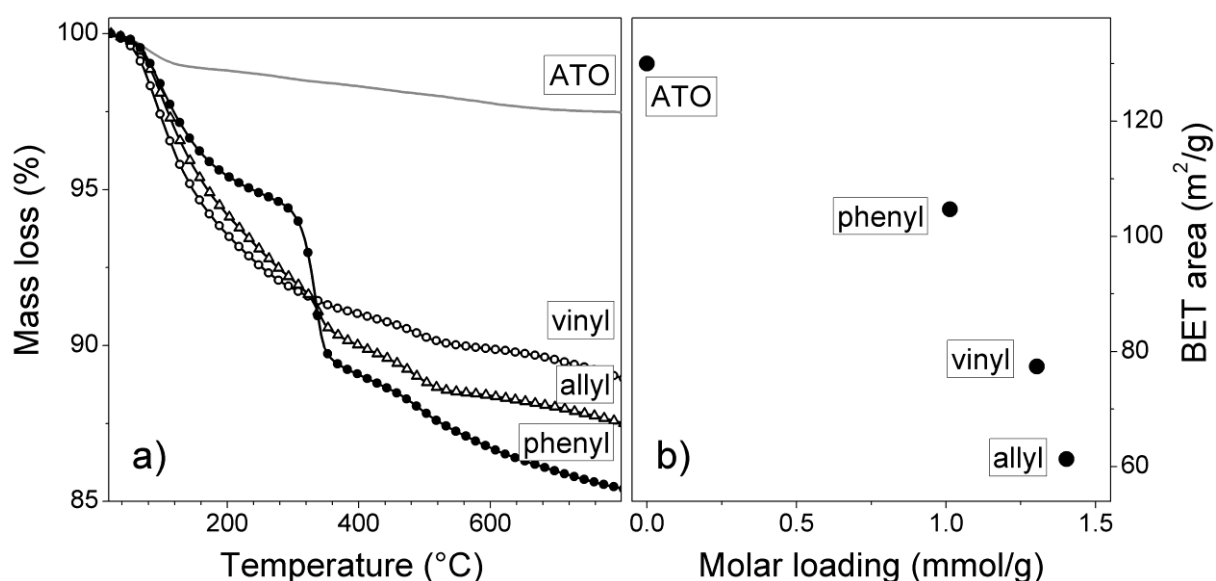


Figure 5.3.8. The TGA data of the mesoporous ATO: non-functionalized (grey line) and functionalized with vinyl (open black circles), allyl (open black triangles) and phenyl groups (filled black circles) (a). The influence of molar loading of the organic moieties on the BET area of the respective samples (b).

The strong mass loss around 100 °C corresponds to the removal of the water adsorbed on the surface of the ATO powder. The mass losses at the temperatures from 200 to 550 °C (the range corresponding to the thermal decomposition of organic moieties, Table A-5.1) were used for estimation of the loading of the respective functional groups (Table 5.3.3). As can be seen from the obtained data, the highest loadings are obtained for the smaller vinyl and allyl groups, which could be due to their lower bulkiness compared to the phenyl group.

Table 5.3.3. Calculated amounts of the attached organic according the TGA data.

Samples	Mass loading organic/ATO [mg/g]	Molar loading organic/ATO [mmol/g]	Surface coverage ^b [$\mu\text{mol} / \text{m}^2$]
Vinyl-ATO	35.2	1.3	10.0
Allyl-ATO	56.6	1.4	10.7
Phenyl-ATO	78.0	1.0	7.8

The increase in the molar loading is accompanied by the decrease in the BET surface area of the corresponding mesoporous ATO materials (Fig. 5.3.8, b). The observed dependence provides a strong indication that the organic groups are indeed incorporated in the pores; moreover, a homogeneous distribution of the grafted species on the available surface of the mesoporous materials can be assumed. This conclusion is supported by the observed decrease in the average pore size after organic functionalization and decrease in BET surface area, which is in good agreement with the predicted pore size for monolayer coverage of the pore walls with organic moieties.

Combination the molar loading and the BET surface area obtained from TGA and N_2 sorption measurements, respectively, enables us to calculate the surface coverage of the organic groups on the ATO surface, which is ca. $8 - 10 \mu\text{mol}/\text{m}^2$ or $5 - 6 \text{ molecules}/\text{nm}^2$ for the vinyl, allyl and phenyl groups (Table 5.3.3). Taking into account that the maximum theoretical amount of the available metal sites for the Grignard reaction is ca. $9.4 \mu\text{mol}/\text{m}^2$ or $15.7 \text{ atoms}/\text{nm}^2$ on the ATO surface estimated for the most often available 110 face of cassiterite,²⁶ the obtained values corresponds to ca. 50 – 60 % of the maximum monolayer surface coverage. These values are far higher than the surface coverage reported for the tin oxide functionalized using allyl route,¹ which makes the metal organic approach very promising for the post-synthesis functionalization of porous tin oxide materials.

5.3.6 Confirmation of the Presence of Organic Groups by Vibrational Spectroscopy Measurements

The presence of the organic groups on the surface of mesoporous ATO powders was confirmed via infrared spectroscopy measurements (Fig. 5.3.9, a). The characteristic deformation and wagging vibrations of CH₂ groups can be found at 1450 and 1430 cm⁻¹ respectively, whereas the C=C deformation can be found at 1640 cm⁻¹. The IR measurements indicate the constant increase in absorption of the respective groups by increasing the number of C-H bonds in organic moieties. The organic groups we found stable against prolonged Soxhlet extraction, which indicates the stability of their grafting on the surface of the mesoporous ATO.

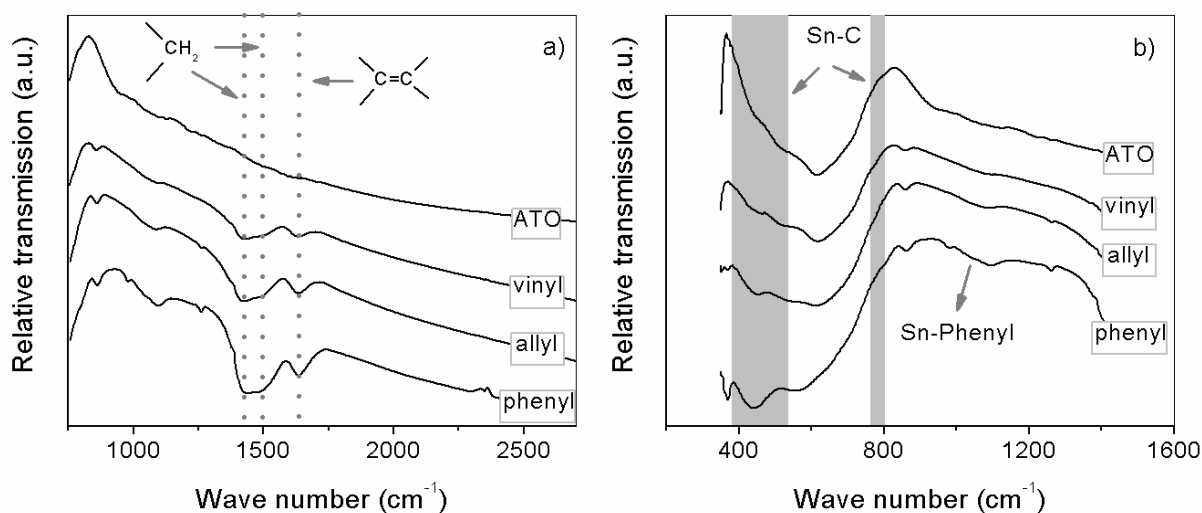


Figure 5.3.9. a) IR spectra of the mesoporous ATO samples: non modified and functionalized with vinyl-, allyl- and phenyl-groups. b) Low IR wave number region of the non modified and the surface functionalized samples. Grey lines present the region of appearance Sn-C bonds.

The possible formation of the Sn-C in the presented ATO samples is difficult to confirm. The vibrations of Sn-C bonds in the IR are very low in intensity and occur at low energy (Fig. 5.3.9, b) causing overlap with vibrations of the cassiterite structure.

High conductivity of the ATO system prevents investigation of the sample by solid state NMR that could provide the information about the formation of Sn-C bond. Therefore, the

Grignard functionalization on undoped mesoporous tin oxide powder as model compound (synthesized in the same way and designated as Ph-SnO₂) was performed. As the information concerning the chemical shifts of organyl tin oxides is absent in literature, we have prepared a reference compound containing a covalent Sn-C bond (designed as Ph-Sn(OH)₃ by hydrolysis and subsequent condensation of PhSnCl₃. ¹³C MAS NMR spectrum of the reference Ph-Sn(OH)₃ compound shows two peaks in the aromatic carbon region (Figure A-5.2. in Appendix). Although the spectrum of Ph-SnO₂ is much noisier due to significantly lower concentration of phenyl groups in the surface-functionalized material, the peaks of aromatic carbons located at the same positions can be clearly recognized. The similarity of the features of NMR spectra of both compounds gives an indication of the direct attachment of the ligands to the surface tin atoms. Therefore, the direct attachment of the Phenyl, Allyl and Vinyl compounds on metal atoms from the mesoporous ATO surface can be assumed also.

5.4 Conclusions

The use of APTES functionalization and metal organic reactions for the surface functionalization of mesoporous ATO samples was investigated. Surface functionalization with APTES proved to be an easy method for the implementation of organic moieties. This method provides high surface loadings with organic groups. It was found that the functionalization density is dependent on the synthesis reaction conditions (reflux). This type of surface functionalization provides terminal amine groups which can serve as anchor groups for the subsequent attachment of the desired species. In the case when organosilanes bearing desired functional groups are not available, organometallic reactions can become an alternative. Thus, different Grignard reagents were reacted with the internal surface of the ATO materials. The presence of organic species inside of mesoporous ATO was confirmed by IR. Nitrogen sorption measurements indicate a decrease in pore size and BET surface area

after functionalization with the respective groups, implying the the presence of the organic molecules inside of the pores of ATO. Small angle X-ray scattering showed that the integrity of the structure was preserved during the metalorganic reactions. TGA data show that through this method a high amount of surface functionalization can be achieved. The percentage of the surface coverage slightly decreased with the increase of the size of the organic group. This effect can be explained by steric interactions between the large organic moieties that could act as blocking groups for further reaction. Nevertheless, large quantities of organic groups were incorporated in all reactions. The Grignard reactions provide the possibility to incorporate various organic molecules and groups which are not available in traditional silane compounds.

5.5 Appendix

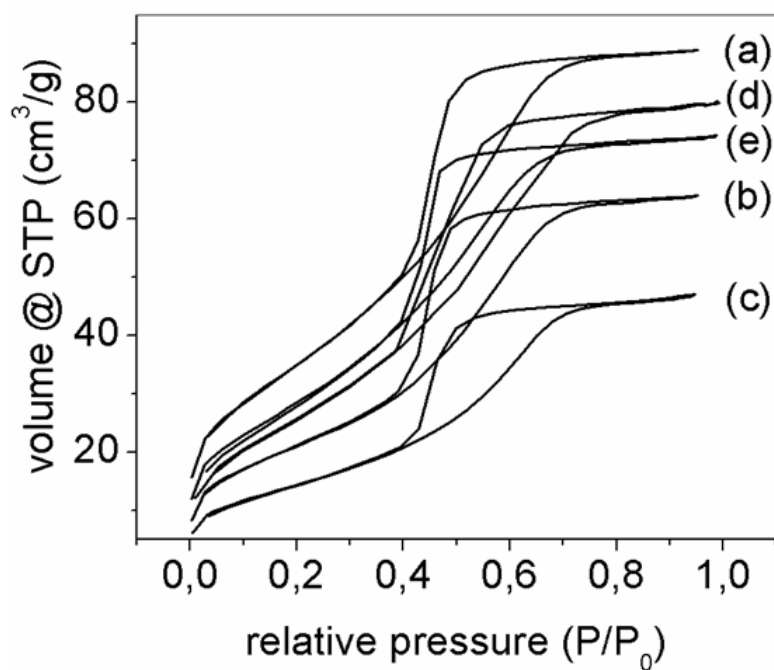


Figure A-5.1. Nitrogen sorption isotherms and of (a) pristine ATO, (b) vinyl, (c) allyl, (d) butyne and (e) phenyl modified ATO.

Table A-5.1. Mass losses of the attached groups obtained from TGA measurements and molar weights of the attached groups.

Attached group	Obtained mass loss (%)	Molar weight of the functional group (g/mol)
Vinyl	4.79	27
Allyl	7.05	41
Phenyl	9.82	77

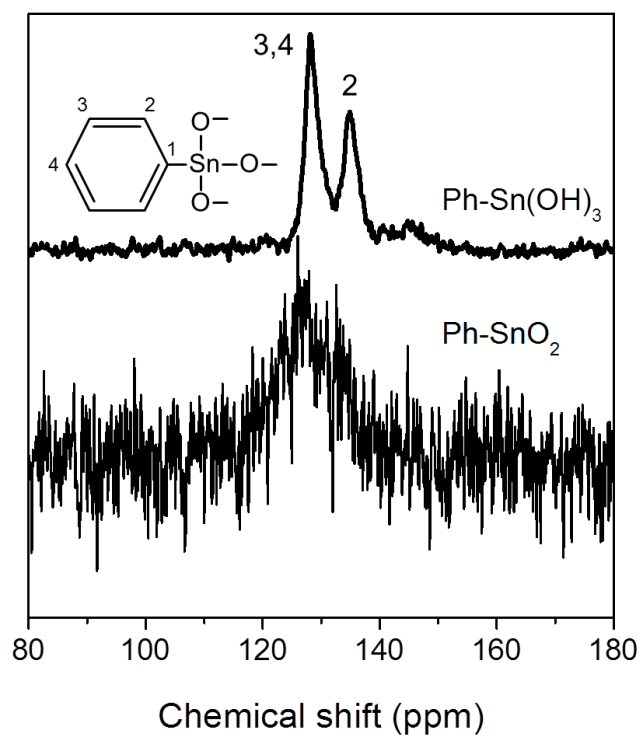


Figure A-5.2. ^{13}C MAS NMR spectra of the reference compound prepared by hydrolysis and condensation of PhSnCl_3 (top) and of the mesoporous SnO_2 powder treated with PhMgBr (bottom).

5.6 References

1. Vilaça, G.; Jousseume, B.; Mahieux, C.; Belin, C.; Cachet, H.; Bernard, M. C.; Vivier, V.; Toupance, T., *Adv. Mater.* **2006**, 18, 1073.
2. Shimada, T.; Aoki, K.; Shinoda, Y.; Nakamura, T.; Tokunaga, N.; Inagaki, S.; Hayashi, T., *J. Am. Chem. Soc.* **2003**, 125, 4688.
3. Vallant, T.; Kattner, J.; Brunner, H.; Mayer, U.; Hoffmann, H., *Langmuir* **1999**, 15, 5339.
4. Fadeev, A. Y.; McCarthy, T. J., *J. Am. Chem. Soc.* **1999**, 121, 12184.
5. Bruhwiler, D., *Nanoscale* **2010**, 2, 887.
6. Müller, V.; Rasp, M.; Rathouský, J.; Schütz, B.; Niederberger, M.; Fattakhova-Rohlfing, D., *Small* **2010**, 6, 633.
7. Hou, K.; Puzzo, D.; Helander, M. G.; Lo, S. S.; Bonifacio, L. D.; Wang, W.; Lu, Z. H.; Scholes, G. D.; Ozin, G. A., *Adv. Mater.* **2009**, 21, 2492.
8. Schlossbauer, A.; Schaffert, D.; Kecht, J.; Wagner, E.; Bein, T., *J. Am. Chem. Soc.* **2008**, 130, 12558.
9. Fattakhova-Rohlfing, D.; Wark, M.; Rathousky, J., *Stud. Surf. Sci. Cat.* **2007**, 165, 573.
10. Angloher, S.; Kecht, J.; Bein, T., *Chem. Mater.* **2007**, 19, 3568.
11. Angloher, S.; Kecht, J.; Bein, T., *Chem. Mater.* **2007**, 19, 5797.
12. Angloher, S.; Bein, T., *J. Mater. Chem.* **2006**, 16, 3629.
13. Yamamoto, K.; Tatsumi, T., *Microporous and Mesoporous Mater.* **2001**, 44-45, 459.
14. Thode, C. J.; Williams, M. E., *Langmuir* **2008**, 24, 5988.
15. Wang, D.; Chang, Y.-L.; Liu, Z.; Dai, H., *J. Amer. Chem. Soc.* **2005**, 127, 11871.
16. Lockett, M. R.; Smith, L. M., *Langmuir* **2009**, 25, 3340.
17. Mukherjee, J.; Peczonczyk, S.; Maldonado, S., *Langmuir* **2010**, 26, 10890.

18. Bansal, A.; Li, X.; Yi, S. I.; Weinberg, W. H.; Lewis, N. S., *J. Phys. Chem. B* **2001**, 105, 10266.
19. Chopra, K. L.; Major, S.; Pandya, D. K., *Thin Solid Films* **1983**, 102, 1.
20. Granqvist, C. G., *Sol. Energy Mater. Sol. Cells* **2007**, 91, 1529.
21. Batzill, M.; Diebold, U., *Progr. Surf. Sci.* **2005**, 79, 47.
22. Müller, V.; Rasp, M.; Štefanić, G.; Ba, J.; Günther, S.; Rathousky, J.; Niederberger, M.; Fattakhova-Rohlfing, D., *Chem. Mater.* **2009**, 21, 5229.
23. Lim, J. E.; Shim, C. B.; Kim, J. M.; Lee, B. Y.; Yie, J. E., *Angew. Chem. Int. Ed.* **2004**, 43, 3839.
24. Pine, S. H., *Organic Chemistry*. 5th ed.; McGraw-Hill: New York, 1987.
25. V. Müller, F. Haase, J. Rathousky, D. Fattakhova-Rohlfing, *Mat. Chem. Phys.* **2012**, 137, 207
26. Kodakari, N.; Katada, N.; Niwa, M., *Chem. Vap. Depos.* **1991**, 3, 59.

6 Incorporation of Cytochrome C in Transparent Conducting Electrode Networks

6.1 Introduction

The implementation of evolution-optimized natural systems in man-made electronic circuits opens new perspectives for the development of efficient bioelectronic devices for sensing, diagnostics, catalysis or energy conversion.¹⁻³ The use of biological functional units as principal components of such electronic devices faces, however, serious challenges. One of the key issues is the immobilization of biomolecules in electrodes without any destruction of their biological functionality, which is essential for an efficient electric communication. The structure and the morphology of the electrodes are also of vital importance for the total device efficiency. The electrode systems have to establish an optimum of electronic communication with the biomolecules and ensure their long-term stability, to enable the highest possible loading of the biomolecules without kinetic restrictions due to slow diffusion or slow charge transport, and to provide an optimal chemical surrounding for the biomolecules.

Porous conducting electrodes provide a large conducting interface and high biomolecule loading due to their large surface area. They make it possible to increase biomolecule stability due to the “encapsulation” of biomolecules in the pores or to tune their chemical surrounding by a chemical modification of the pore interior.⁴⁻⁶ The advantages of such systems as current collectors for highly efficient enzyme-based biosensors were demonstrated for porous metal or carbon electrodes.^{7, 8} These materials however are not transparent, which limits their application in optoelectronic biodevices. On the other hand, many transparent porous materials such as metal oxides have a very low electrical conductivity, which is detrimental for a direct electrical communication with the biomolecules. The only class of materials which combines both high electrical conductivity and transparency, the so called transparent conducting oxides (TCO), have been much less investigated for this purpose because of the

experimental difficulties of their fabrication with a defined porous morphology, which has been mastered only very recently.⁹⁻¹² Wollenberger et al.^{9, 10} have demonstrated that mesoporous indium tin oxide (ITO) electrodes can be used as efficient platforms for the incorporation of small proteins, enabling very high protein loading and at the same time a direct electron transfer. These remain so far the only examples of a successful use of porous TCOs as an electrode matrix for the encapsulation of biomolecules. The other types of porous TCO materials were not investigated yet for this purpose, although their differences in surface properties, morphology and conductivity can provide additional possibilities for a tailored design of bioelectronic devices. Besides the types of the electrodes, the way of immobilization of biomolecules in porous conducting oxide matrices has practically not been investigated. Covalent immobilization, which can substantially increase the binding stability of the biomolecules, was intensively explored only for insulating porous silica materials.¹³

In this chapter the suitability of transparent conducting porous ATO frameworks for the incorporation of redox biomolecules by either non-covalent or covalent binding is explored. The protein cytochrome c is selected as a model biomolecule, whose grafting on various electrode systems was already studied, such as on porous silica and zeolites,^{14, 15} metal oxides,^{9, 10, 16-22} carbon²³⁻²⁶ and gold electrodes.^{1, 27-31} Cytochrome c is able to exchange electrons directly with the electrode, which provides the opportunity to investigate the efficiency of electron transfer and to determine its electrochemically active loading. Previously we have shown that the mesoporous ATO films can be used as a high surface area conducting electrode (Chapter 4).¹¹ Therefore, such matrix could be suitable for the incorporation of the cytochrome at high loading, leading to a greatly enhanced direct heterogeneous electron transfer. In the following section it will be demonstrated the possibility of covalent grafting of the cytochrome c in the porous electrode matrix, leading to a greatly enhanced binding stability and a lower susceptibility to the environment.

6.2 Experimental Part

6.2.1 Chemicals

Tin(IV) chloride (99 %), antimony(III) acetate (99.99 %), anhydrous benzyl alcohol (99.8 %, <0.003 % water), anhydrous toluene (≥ 99.7 %; <0.005 % water), anhydrous dichloromethane (DCM) (≥ 99.5 %; <0.005 % water) and tetrahydrofuran (THF) (≥ 99.5 %), (3-aminopropyl)triethoxysilane (APTES) (99 %), (3-mercaptopropyl)triethoxysilane (MPTES) (95 %), N-(3-Dimethylaminopropyl)-N'-ethylcarbodiimide (EDC) (≥ 97 %), N-hydroxysulfosuccinimide sodium salt (≥ 98.5 %), lithium perchlorate (≥ 95 %), potassium nitrate (≥ 99 %), potassium chloride (≥ 99.5 %), potassium dihydrogen phosphate (≥ 99.5 %), disodium hydrogen phosphate (≥ 99 %) and hydrogen peroxide (30 wt.% in water) were purchased from Aldrich and used without further purification. Cytochrome c from bovine heart (95 %; $M \approx 13000$) was purchased from Fluka and used without further purification.

6.2.2 Synthesis of ATO Nanoparticles

The ATO nanoparticles, which were used as building blocks and assembled into mesoporous nanostructures, were synthesized according to the previously established procedure (Chapter 3).³² Briefly, for the synthesis of ATO nanoparticles with 10 mol % of antimony, tin(VI) chloride (3.2 g, 12.3 mmol), and Sb(III) acetate (0.41 g, 1.35 mmol) were dissolved in toluene (10 mL) and added to benzyl alcohol (30 mL, 291 mmol) under continuous stirring. This solution was kept in a closed glass vessel in a laboratory oven at 100 °C for 20 h. Afterwards, the particles were separated by centrifugation at 50 000 rcf for 20 min and dried in air. The amount of organic residuals in the dried particles was evaluated by TG analysis.

6.2.3 Preparation of Solutions for Mesoporous Films and Mesoporous Powders

The above solutions, which were used for the coating of the glass substrates in the procedure for the preparation of the mesoporous ATO films, were used for the preparation of the mesoporous powders as well. The preparation of these solutions was performed according to the previously established procedure.¹¹ Shortly, the dried nanoparticles (0.4 g, which contained 0.12 g of organic residuals and, 0.28 g of pure ATO particles according to TGA measurements) were dispersed in a solution of Pluronic F127 (0.28 g) in THF (6 ml) by stirring for 2 h at room temperature. The final solutions are transparent and orange-brownish in color.

The films were prepared by dip coating of the above solution on ITO-coated glass substrates at 23 ± 2 °C with a relative humidity of 55 ± 5 % and a withdrawal rate of 1.8 mm s^{-1} followed by calcination of the coated substrates at 500 °C (with a ramp rate of 0.6 °C min^{-1}) for 30 min in air. The mesoporous powders were prepared by casting the same solutions in porcelain crucibles, drying them in air and calcining them according to the procedure above.

6.2.4 Incorporation of Cytochrome C in Mesoporous ATO

For the adsorption of cytochrome c, the mesoporous ATO films (mATO) were immersed overnight in a 50 μM aqueous solution of cytochrome c at 4 °C (6 ITO glasses coated with mesoporous ATO films with 1 cm^2 of the exposed area and roughness factor of 200 and area of $64 \text{ m}^2/\text{g}$ in 60 ml of the cytochrome c solution), subsequently intensively washed with distilled water and stored in the fridge till the measurements were performed.

The covalent attachment of the cytochrome c to the porous ATO was performed in two steps. In the first step the mesoporous material was functionalized with APTES, and in the second step cytochrome c was grafted to the amino groups of the APTES via formation of amide bonds with carboxylic groups from the protein. For the functionalization with APTES, the

ATO films or powders were transferred into Schlenk bottles and dried for 90 minutes at 110 °C in vacuum. Afterwards, 20 mM solution of APTES in dried toluene or dried dichloromethane was added to the powders and all was refluxed for 2 h. In the case of the toluene solution the reflux temperature was set to 110 °C whereas in the case of DCM it was 40 °C. Subsequently, in both cases, films or powders were washed once with DCM and once with ethanol.

The amount of cytochrome c which can be covalently incorporated into porous ATO is strongly influenced by the degree of the functionalization of mATO with APTES, which depends on the reaction conditions and the macroscopic form of the mATO. For the powders the highest cytochrome loading is obtained when the first functionalization step with APTES is performed in toluene as a result of the higher temperature. However, for the films this reaction leads to the polymerization of APTES inside the pores leading to a pore blocking, which might be attributed to the different character of diffusion in powders and films.³³ Therefore, the functionalization of powder ATO material with APTES was performed in toluene, while for the films this reaction was performed in DCM. For the covalent anchorage of cytochrome c, the APTES functionalized films or powders were transferred in a 50 µM aqueous solution of cytochrome c and stirred for 30 minutes (0,1 g of the mesoporous powder with BET area 130 m²/g in 60 ml of the cytochrome c solution). Subsequently, 10.9 µL (6×10^{-5} mol) of N-(3-dimethylaminopropyl)-N'-ethylcarbodiimide (EDC) and 13.2 mg (6×10^{-5} mol) of N-hydroxysulfosuccinimide sodium salt were added in order to form the amide bonds between the protein and APTES. The amount of added EDC and N-hydroxysulfosuccinimide sodium salt was calculated based on the total amount of available carboxylic groups on the protein.³⁴ The solution was stirred at 4 °C over night; afterwards films or powders were washed with water and stored in the fridge in the flask filled with nitrogen (without a buffer) till the measurements were performed.

6.2.5 Preparation of the Phosphate Buffer

The 0.05M phosphate buffer of pH 7.4 was prepared by dissolving 0.25 g of potassium dihydrogenphosphate (KH_2PO_4) and 1.51 g of disodium hydrogenphosphate (Na_2HPO_4) were dissolved in 250 ml of distilled water.

6.2.6 Characterization Techniques

Small-angle XRD measurements of the thin films on various substrates and mesoporous powders were performed on a SCINTAG XDS 2000 diffractometer with Ni-filtered CuK_α radiation ($\lambda=1.5406 \text{ \AA}$), theta/theta geometry, and a scintillation detector operated at 40 kV and 30 mA.

Nitrogen sorption measurements on the mesoporous ATO powders were obtained using a Quantachrome Instrument NOVA 4000e Surface Area & Pore Size Analyzer at 77 K. Surface area calculations were made using the Brunauer-Emmett-Teller (BET) equation in the range from $p/p_0 = 0.05 - 0.25$. The pore-size distribution was determined using a DFT-method (NLDFT adsorption branch, cylindrical pores, N_2 on silica). The reason for applying this method instead of BJH, which is common for most of the oxides, is the fact that it provides a smaller error for small pore size systems in comparison to BJH. Although an NLDFT model for the tin oxide is not available, it provides more precise results in our case, in comparison to BJH, even if silica is used as a model.

The porosity of the films was determined by analysis of adsorption isotherms of Kr at the boiling point of liquid nitrogen ($\approx 77 \text{ K}$) using ASAP 2010 apparatus (Micromeritics).

The IR spectra were measured on a Bruker Equinox 55 in transmission mode. The samples for IR measurements were mixed with KBr in the ratio of 1:100 and pressed into pellets. The obtained spectra are background subtracted. For the background a pure pellet of KBr was prepared and measured in the same way as KBr pellets with the sample.

Absorption spectra of the cytochrome c functionalized films were recorded on a Hitachi U-3501 UV–vis spectrophotometer. Bare mesoporous ATO electrodes, of the same thickness as the investigated ATO electrodes containing cytochrome c, were used for background subtraction. The spectroscopic determination of the surface coverage was based on the extinction coefficient (ϵ) of cytochrome c of $106100 \text{ M}^{-1} \text{ cm}^{-1}$ of the Soret band (410 nm).³⁵ Cyclic voltammograms were obtained using a PARSTAT 2273 potentiostat (with PowerSuite 2.56 software for data collection and analysis) in a standard three electrode electrochemical cell using a Pt wire as counter electrode, an Ag/AgCl/sat. KCl electrode as reference electrode, whereas cytochrome c modified mesoporous ATO films served as working electrode. The supporting electrolyte was 0.05M phosphate buffer. Prior to the measurements the cytochrome c functionalized ATO films on ITO glass were masked with adhesive glass fiber tape leaving an exposed area of 1 cm^2 . Cyclic voltammograms were taken in a range of scan rates from 10 mV s^{-1} to 1 V s^{-1} . The amount of transferred charges during oxidation and reduction of cytochrome c was evaluated by integration of the corresponding peaks in the respective voltammograms (represented as current–time curves) after subtraction of the background current, as approximated by a polynomial. Both cathodic and anodic branches of the voltammograms were used for flat ITO as well as mesoporous ATO electrodes and an average charge value was taken for the calculation of surface coverage.

6.2.7 Calculation Methods

The kinetics of the electron transfer were analyzed using the model of Laviron.³⁶ The electron transfer rate constant is calculated from the potential peak difference for the oxidation and reduction processes ΔE_p at different scan rates (for $\Delta E_p \geq 0.06 \text{ V}$) using the equation:

$$\log k = \alpha \log(1 - \alpha) + (1 - \alpha) \log \alpha - \log(RT/nFv) - \alpha(1 - \alpha)nF\Delta E_p/2.3RT$$

(eq. 6.2.1)

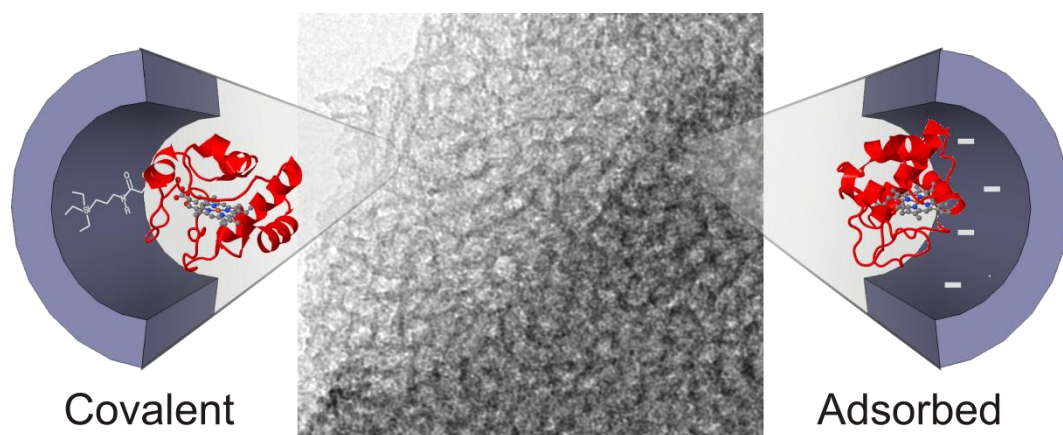
where α is the transfer coefficient, R the gas constant, T the absolute temperature, F the Faraday constant, n the number of electrons, ΔE_p the peak separation and ν the respective scan rate. The transfer coefficients α were calculated from the slope of the linear part of the trumpet plot of the peak potentials vs. the logarithm of the scan rate according to the equations: cathodic slope = $-2.3RT/\alpha nF$, anodic slope = $2.3RT/(1 - \alpha)nF$, where R is the gas constant, T the absolute temperature, n the number of electrons and F the Faraday constant.

6.2.8 Leaching Stability

In order to test the leaching stability of cytochrome c incorporated by different procedures, the films with incorporated cytochrome were characterized by cyclic voltammetry, then immersed in a salt solution with higher ionic strength for 3 hours, intensively washed with distilled water and left in 0.05 M phosphate buffer for 2 h prior to the repetition of cyclic voltammetry measurements.

6.3 Results and Discussion

The cytochrome c was incorporated in the porous matrix of conducting ATO electrodes by either adsorption or covalent grafting (Scheme 6.3.1).



Scheme 6.3.1. Incorporation of cytochrome c in the pores of mesoporous ATO framework via covalent and non-covalent (adsorption) grafting.

The benefit of the use of the mesoporous ATO for the incorporation of small biomolecules, , in comparison to the known mesoporous silica materials, zeolite or other types of oxides, is the fact that the good conductivity of the mesoporous ATO framework provides a three-dimensional conducting network. At the same time the transparency of ATO gives the possibility of using such bio-inorganic hybrid materials for applications in bio-optoelectronic devices (for instance thin films of DNA-CTMA has been successfully used in applications as organic light emitting diodes). The advantage of the incorporation of cytochrome c into the ATO framework by adsorption is its simplicity, which enables the immobilization of the proteins on the electrode surface without any additional protein treatment. However, the adsorbed molecules usually have a rather low leaching stability in the electrolytes, and therefore an insufficient long-term stability of the electrode systems results. This problem can be overcome by the covalent binding of the proteins to the electrode surface, which is stable and much less susceptible to the influence of the environment. For the covalent immobilization, an amide chemistry approach was used. Although not orientation-specific, it enables the grafting of proteins to the amino-functionalized substrates via the formation of amide bonds with glutamic or aspartic acid residues usually present on the protein surface. The amide bond is formed in mild conditions and is therefore very frequently used for the

immobilization of proteins on various substrates. However, the approach becomes more challenging when applied to porous substrates. The basic issues are as follows: (i) is the protein incorporated within the pores, or is it only attached to the external surface of the porous material; (ii) is the protein homogeneously distributed within the porous framework, or is it mostly located near the pore openings due to diffusion and kinetic restrictions; (iii) does the protein keep its integrity and activity after incorporation into the porous matrix; (iv) does the chemical surrounding of the pores influence the specific activity of the protein; (v) and does the redox protein also show its electrochemical activity inside the porous electrode matrix. Moreover, the efficiency of covalent immobilization strongly depends on the efficiency of surface functionalization with organic moieties acting as anchor groups (the amino groups in case of amide bonding).

In order to estimate the efficiency of the two-step covalent immobilization of cytochrome c inside the mesoporous ATO, the prepared material was characterized both after functionalization of the pores with amino groups and after covalent attachment of the protein. The non-electrochemical characterization was performed mostly with mesoporous ATO powders, while for the electrochemical characterization the ATO was deposited as a thin film on the electrode surface.

6.3.1 Influence of the Incorporation of Cytochrome C on the ATO Mesostructure

Previously it was shown that the ATO powders have, in comparison to the films, an inferior periodicity of the pore arrangement and a smaller pore size due to an isotropic shrinkage during calcinations (Chapter 4). Therefore, the properties of powders are not identical with those of the films, but they are more convenient for the quantitative characterization.

The XRD patterns of the mesoporous ATO show a reflection at small angles typical for a regular arrangement of the pores. This signal is present also after both functionalization steps,

indicating that the porous matrix remains intact after the introduction of the protein (Fig. 6.3.1).

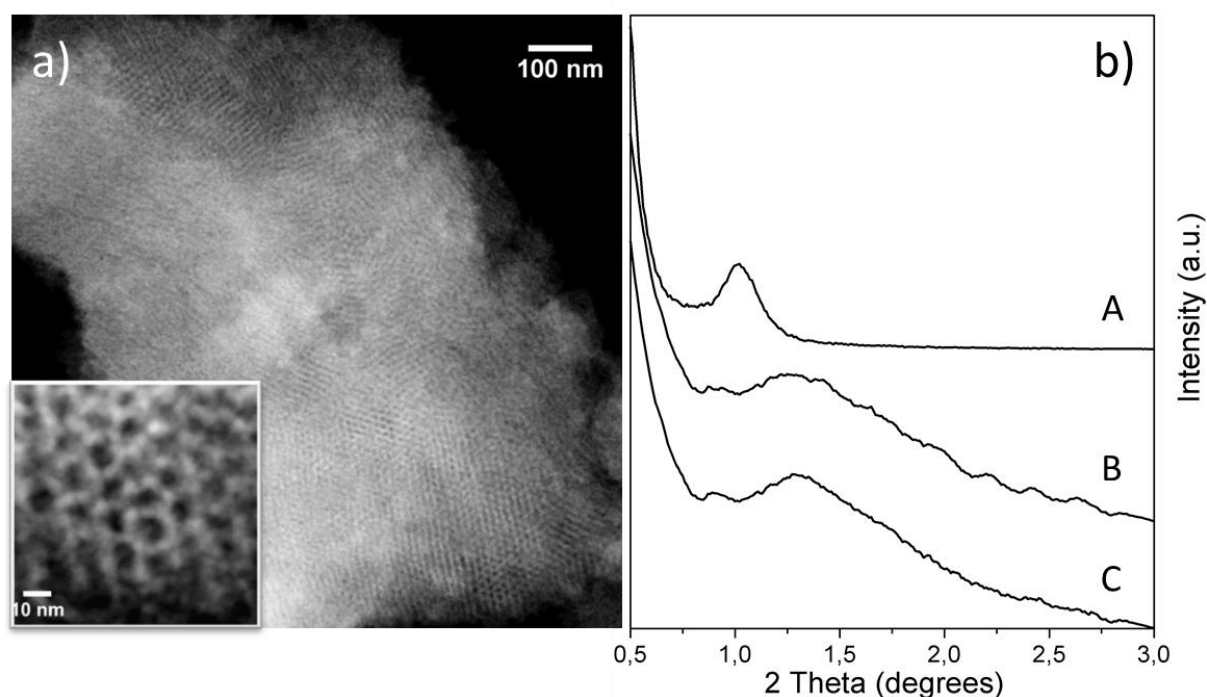


Figure 6.3.1. Morphology characteristics of mesoporous ATO: **a)** STEM-HAADF image of mesoporous ATO powder (two different magnifications are shown); **b)** small angle XRD patterns of mesoporous ATO film (A) and mesoporous ATO powder (B) calcined at 500 °C, and mesoporous ATO powder after incorporation of cytochrome c (C).

6.3.2 Influence of the Incorporation of Cytochrome C on Pore Size of ATO

The presence of the regular porous ATO architecture after each functionalization step is shown also by nitrogen sorption measurements, which demonstrate type IV isotherms typical for mesoporous materials (Fig. 6.3.2).

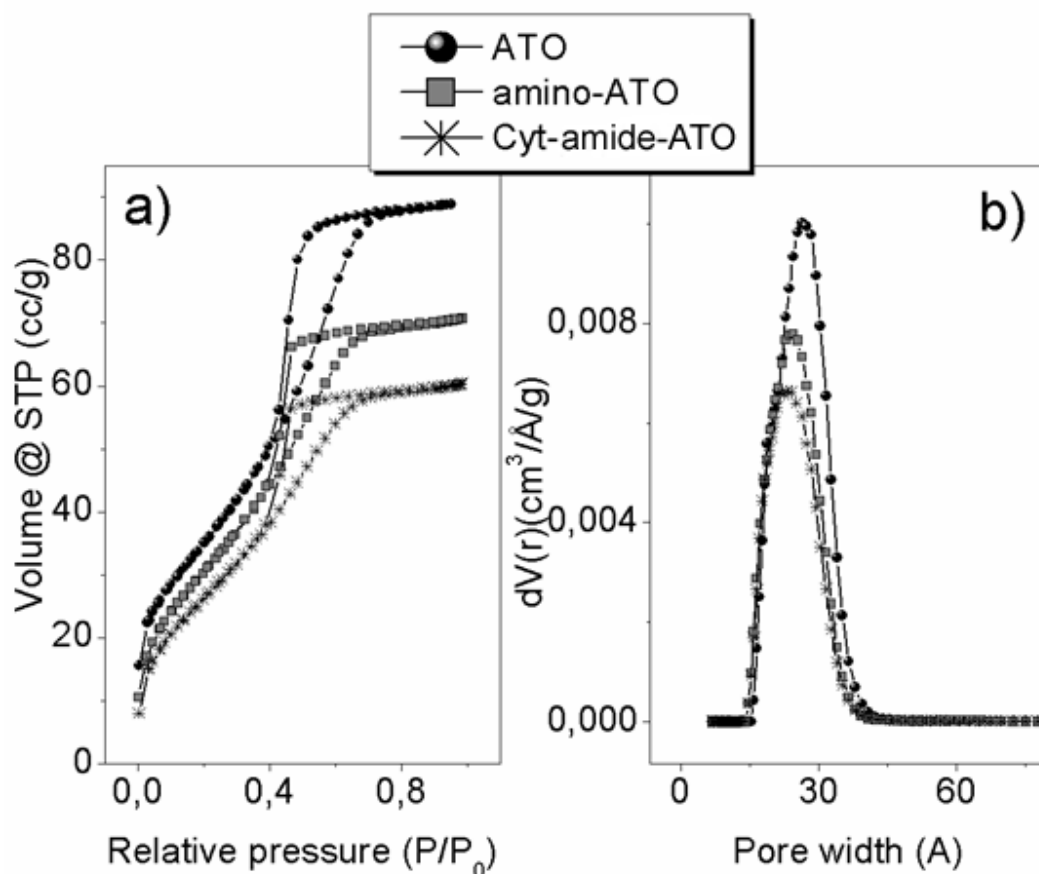


Figure 6.3.2. a) Nitrogen sorption isotherms, b) pore size distribution for as prepared mesoporous ATO powder, the ATO functionalized with APTES in toluene (amino-ATO) and final ATO with covalently incorporated cytochrome c (Cyt-amide-ATO) (powder samples).

The surface area, pore volume and pore size all decrease when comparing parent ATO materials (ATO) with the amino functionalized sample (amino-ATO) to the cytochrome incorporated sample (Cyt-amide-ATO), keeping however the same character of porosity (Fig. 6.3.2 and Table 6.3.1).

Table 6.3.1. Nitrogen sorption data for the pristine mesoporous ATO, the APTES functionalized ATO (amino-ATO) and mesoporous ATO with covalently attached cytochrome c (Cyt-amide-ATO) (powder samples).

Sample name	BET surface (m ² /g)	Pore size* (nm)	Pore volume* (cm ³ /g)
ATO	128.3	5.3	0.132
amino-ATO	114.1	4.9	0.105
Cyt-amide-ATO	98.9	4.4	0.090

These results indicate that cytochrome c is successfully incorporated into the entire pore volume without any blocking of the pores.

6.3.3 Amount of Incorporated Cytochrome C

The amount of incorporated molecules was determined by thermogravimetric analysis (TGA, Fig. 6.3.3).

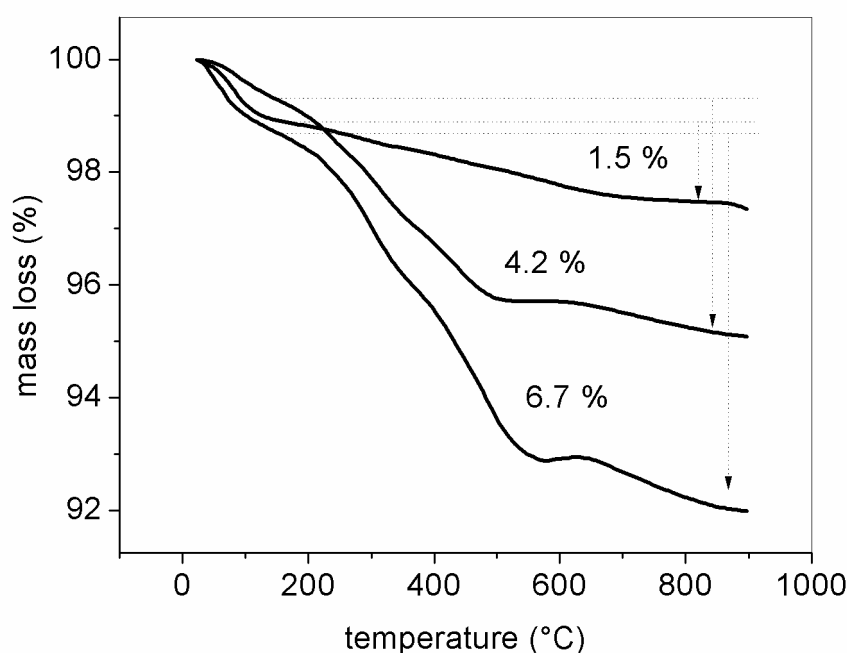


Figure 6.3.3. Thermal gravimetric analysis (from top to the bottom) for pristine as-prepared mesoporous ATO powder, the ATO functionalized with APTES in toluene (amino-ATO) and final ATO with covalently incorporated cytochrome c (Cyt-amide-ATO) (powder samples).

The non-functionalized mesoporous ATO powder shows only a minor mass loss of 1.5 %. The amino functionalized samples show a mass loss of 4.2 % corresponding to 0.47 mmol g^{-1} of the amino-propyl residues bound to the ATO surface. The total mass loss increases to 6.7 % after covalent immobilization of cytochrome, corresponding to $2.3 \text{ } \mu\text{mol/g}$ of bound protein. Although this value seems to be much lower compared to that of mesoporous silica (for example, $41.5 \text{ } \mu\text{mol/g}$ for cytochrome c adsorbed on silica SBA-15⁵), the much higher density of ATO (6.9 g/cm^3 vs. 2.5 g/cm^3 for silica) and its lower BET surface area ($128 \text{ m}^2/\text{g}$

vs. $910 \text{ m}^2/\text{g}$), respectively, should be taken into account. Considering those factors, the obtained surface coverage of $18 \text{ nmol}/\text{m}^2$ is comparable to ca. $45 \text{ nmol}/\text{m}^2$ for cytochrome c adsorbed on silica SBA 15.⁵

6.3.4 Spectroscopic Characterization of Incorporated Cytochrome C

The integrity of cytochrome c in the mesoporous ATO matrix after covalent immobilization is indicated by IR and UV-Vis spectroscopy (Fig. 6.3.4).

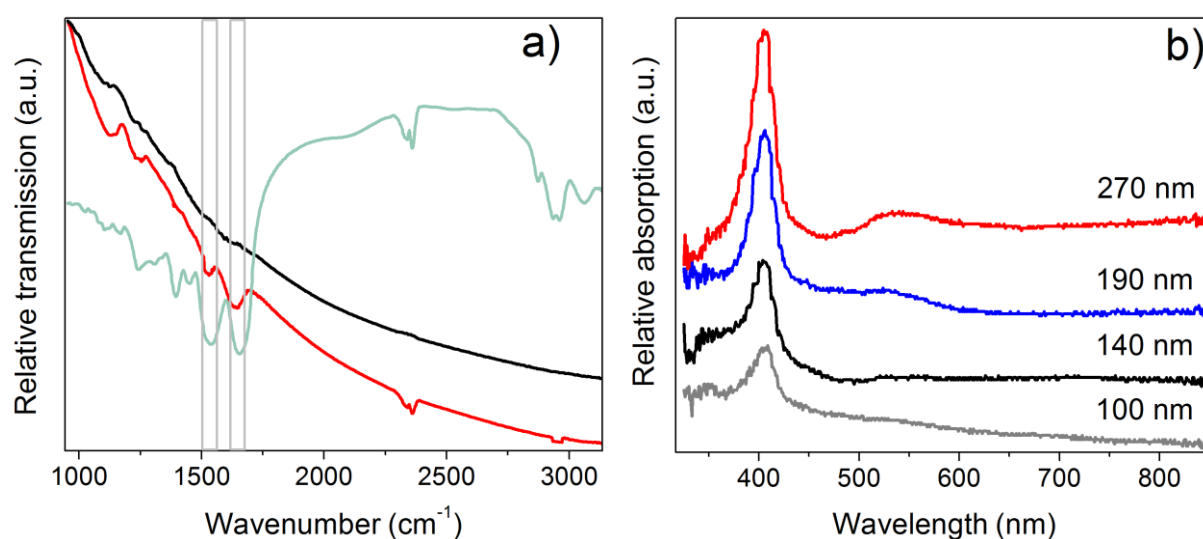


Figure 6.3.4. Spectroscopic characterization of cytochrome c covalently immobilized on the mesoporous ATO: (a) IR spectra of mesoporous ATO powder (black line), powder with incorporated cytochrome c (red line) and pristine cytochrome c (green line). The amide band I due to C=O stretching vibrations is found at $1700\text{--}1600 \text{ cm}^{-1}$ whereas the amide II band due to a combination of C-N stretching and N-H bending occurs at $1600\text{--}1500 \text{ cm}^{-1}$, and (b) UV-VIS spectra of the ATO films of different thickness containing covalently attached cytochrome c. The spectra were measured versus the parent non-functionalized ATO films of the same thickness subtracted as the background. For comparison, the UV-VIS spectrum of the pristine ATO film with a thickness of 190 nm is shown in Figure A.6.2.

The IR spectra of cytochrome covalently incorporated in ATO show the presence of characteristic amide I and II bands at ca. 1650 and 1533 cm^{-1} , respectively, which are also present in the spectrum of pristine cytochrome c and which are related to the secondary structure of proteins.²⁷ Most of the vibrations obtained for pure cytochrome are found in the ATO sample with incorporated cytochrome, however with lower intensity, while none of them is present in the spectrum of the parent mesoporous ATO. The UV-Vis spectra (Fig.

6.3.4-b) of covalently immobilized cytochrome show a Soret band (409 nm) and weaker Q bands (365 nm and 528 nm) characteristic for pristine cytochrome c.^{5, 20, 27, 37, 38} The UV-Vis spectra of the adsorbed cytochrome show the same shape without any shift in the position of the bands (Fig. 6.3.5).

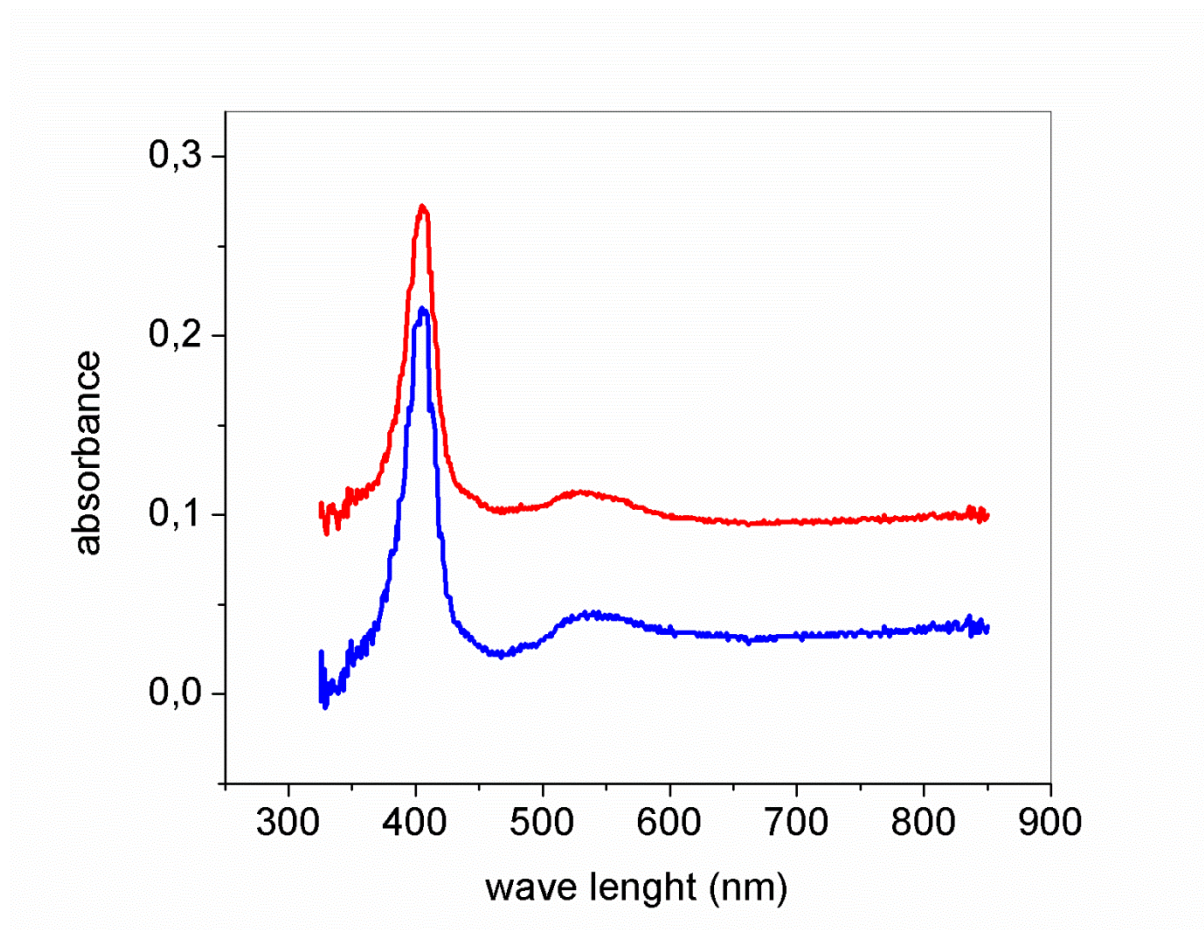


Figure 6.3.5. Comparison of the UV-VIS spectra for adsorbed (blue line) and covalently attached (red line) cytochrome c on the ATO films with the thickness 380 nm. Both spectra show the typical absorption peaks for cytochrome c at 409 nm (Soret band), 365 and 528 nm (Q bands) without visible shift in peak positions. The spectra were measured versus the parent non-functionalized ATO films of the same thickness subtracted as the background. The red curve is shifted by 0.1 along the Y-axis in comparison to the blue curve.

The amount of incorporated protein increases with increasing the film thickness (Fig. 6.3.4-b and A.6.3). This indicates that the pores of mesoporous ATO film are open and interconnected allowing a successful insertion of functional moieties from the top surface deeper into the porous layer.

6.3.5 Electrochemical Activity of Incorporated Cytochrome C

The electrochemical activity of the cytochrome incorporated into the conducting ATO matrix both covalently and non-covalently was investigated by cyclic voltammetry (Fig. 6.3.6 and Fig. A.6.4).

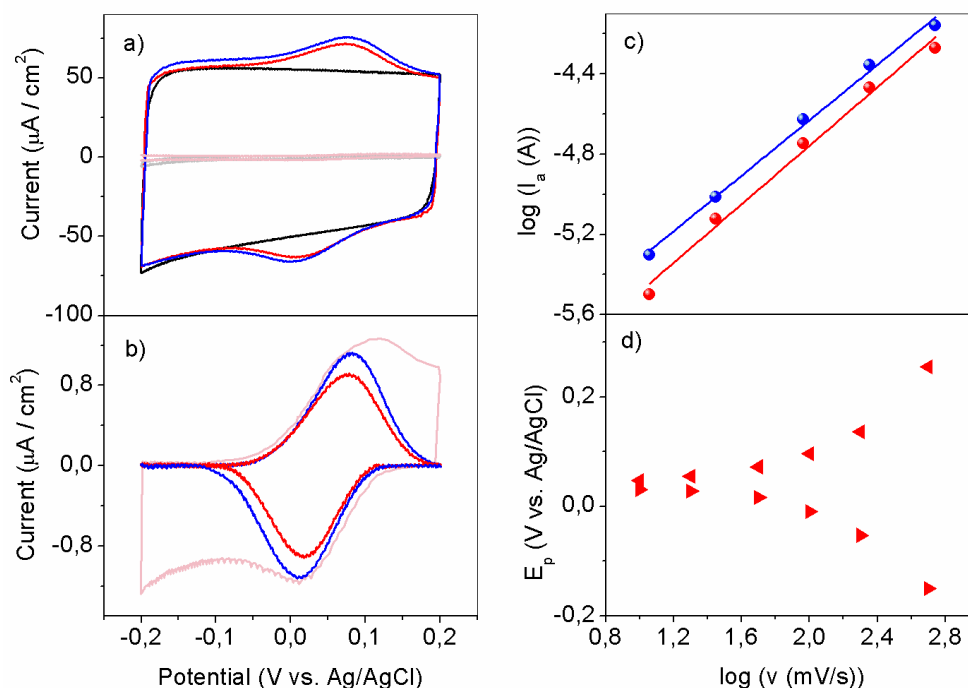


Figure 6.3.6. **a)** Cyclic voltammograms of the parent mesoporous ATO electrode (black line) and after incorporation of cytochrome c via adsorption (blue line) and via covalent grafting (red line). The grey line shows a cyclic voltammogram of a 50 μM cytochrome c solution on a flat ITO electrode. **b)** Cathodic and anodic peak currents obtained after subtraction of baseline current for cytochrome c incorporated in mesoporous ATO electrodes via adsorption (blue line) and via covalent attachment (red line). The currents of the cathodic and the anodic peak for covalently attached and adsorbed cytochrome c were divided by factor 20 for better comparison of the voltammogram shapes and the redox potentials with the cytochrome c solution on a flat ITO (grey line—the same as the grey line in the Figure 3a). **c)** Anodic peak current at different scan rates (in log-log scale) for cytochrome c incorporated in mesoporous ATO electrodes via adsorption (blue circles) and via covalent attachment (red squares). **d)** Difference in anodic and cathodic peak potentials ΔE_p at different scan rates (in logarithmic scale). Electrolyte: 0.05 M phosphate buffer solution. The voltammograms were recorded at scan rate 50 mV/s.

For both types of electrodes a couple of well-defined redox peaks are observed which are characteristic for the heme $\text{Fe}^{\text{III}}/\text{Fe}^{\text{II}}$ redox couple in cytochrome c molecules,^{23, 39, 40} indicating that the cytochrome has been successfully incorporated in the pores of mesoporous ATO by both methods. The formal potential value is 0.038 ± 0.005 V and 0.043 ± 0.005 V for

covalently attached and adsorbed cytochrome, respectively, which is close to the value of native cytochrome in solution (0.061 ± 0.005 V) and to the values found by other authors.^{27, 39, 41, 42} The redox peaks for both adsorbed and covalently attached cytochrome show a Gaussian shape and a linear dependence of the peak current on the scan rate in log-log coordinates typical for surface immobilized species (Fig. 6.3.6-c). This behavior is different from the cytochrome adsorbed in other types of porous electrodes. Thus, Frasca et al. demonstrated that the cytochrome adsorbed in mesoporous ITO shows a diffusion controlled behavior indicating that cytochrome is freely ‘swimming’ inside the pores.¹⁰ These results indicate that even the adsorbed cytochrome is strongly bonded to the ATO surface by electrostatic interactions. These results are in good agreement with the results reported in the literature for other metal oxides showing that the electrostatic interaction of cytochrome c with the pore walls of ATO is strong enough to provide a good attachment of the protein.^{17-19, 24, 43}

Analysis of electron transfer kinetics gives the transfer coefficient values α of 0.5 for both covalently attached and adsorbed cytochrome, similar to the other reported results for cytochrome immobilized on negatively charged electrodes.^{21, 25, 44} The electron transfer rate constant k_s equals 1.2 s^{-1} for covalently attached protein (Fig. 6.3.6-c). The adsorbed cytochrome shows slower electrode kinetics, the charge transfer constant being 0.53 s^{-1} . The calculated charge transfer rate constants are lower than those observed for cytochrome on metal electrodes (the typical reported values are around 10 s^{-1}),^{14, 16, 28} but are similar to the heterogeneous charge transfer constants observed by different groups for cytochrome immobilized on metal oxide electrodes.^{10, 17, 22, 26, 27, 38, 45}

6.3.6 Surface Coverage with Cytochrome C

The loading of cytochrome c, obtained from cyclic voltammetry data, is proportional to the thickness of the films (Fig. 6.3.7 and Fig. A6.3). The peak current as well as the

electrochemically accessible loading obtained by integration of voltammetric curves depends practically linearly on the thickness of porous ATO electrodes used for immobilization, in a good agreement with the results of UV/Vis measurements on the same films (Fig. 6.3.4 and Fig A6.3)

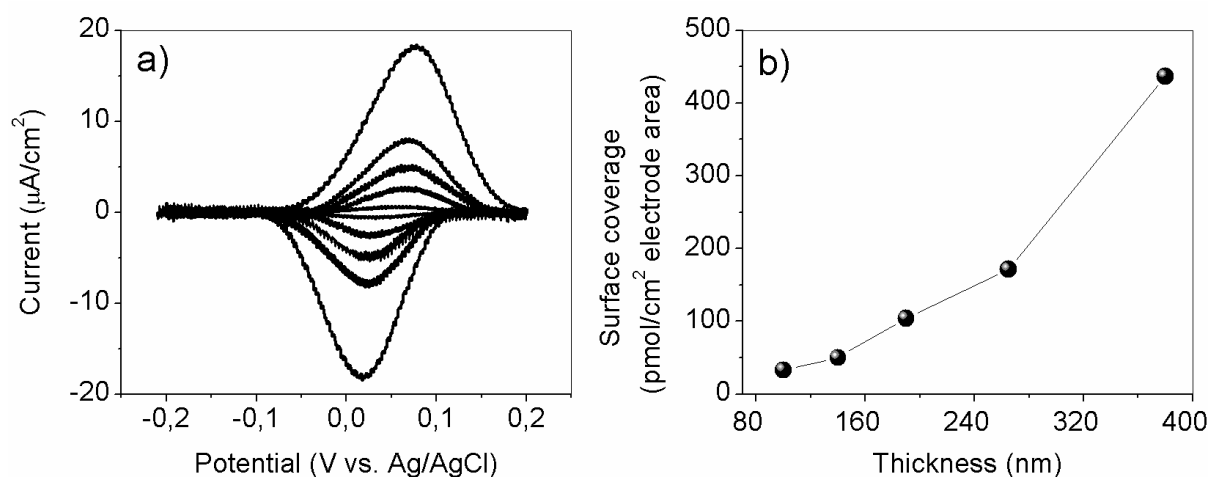


Figure 6.3.7. a) Voltammograms of covalently attached cytochrome (after the baseline subtraction) for the films with different thickness. The film thickness is given in (b); b) Electrochemically accessible surface coverage for films with different thickness. Scan rate 50 mV/s.

This increase in peak current and consequently in surface coverage indicates that pores in the films are open and interconnected allowing the incorporation of cytochrome within the entire film volume. The highest surface coverage obtained for covalently grafted cytochrome is ca. 440 pmol/cm² of electrode area (for the film of 380 nm in thickness). Even higher loadings can be achieved for the adsorbed cytochrome, reaching ca. 600 pmol/cm² for the film of the same thickness. The somewhat lower loading in the case of covalent immobilization can be attributed to a non-quantitative yield of the amide bonding, as well as to some decrease in the pore diameter after amino-functionalization of the pores. The obtained loadings are anyway much higher than reported for the cytochrome immobilized on the flat electrode surface (typically 20 pmol/cm² for a flat ITO)¹⁴ due to the very high surface area of the porous electrodes. However, it should be pointed out that the mentioned values correspond to the electrochemically active cytochrome c. Recently, even higher loadings were reported only for

the cytochrome adsorbed on mesoporous amorphous tin-rich indium oxide films which is explained by their much larger thickness,⁹ and for cytochrome multilayers.³¹ Moreover, the surface coverage presented by Aksu et al. was obtained by evaluation of spectroscopic measurements. In Table 6.3.2 the values of the electrochemical surface coverage, Γ_{el} , and the spectroscopic surface coverage, Γ_s , are compared.

Table 6.3.2. The values of the surface coverage with cytochrome c on differently thick films obtained by spectroscopic measurements (Γ_s) and electrochemical measurements (Γ_{el})

Thickness of the films (nm)	Type of cytochrome bonding	Γ_s (pmol/cm ²)	Γ_{el} (pmol/cm ²)
100	covalent	106	33
140	covalent	132	50
190	covalent	202	104
270	covalent	245	171
370	covalent	414	440
370	adsorbed	490	600

The values of the surface coverage obtained through spectroscopic measurements differentiate in some amount from the values of the cyclic voltammetry measurements but indicate the same trend, increase in surface coverage with increasing the film thickness, Table 6.3.2. Scaling of the absolute electrochemical loading to the real surface area of the films (expressed as the specific surface area) gives the surface coverage of 22 pmol/cm² and 30 pmol/cm² for covalently grafted and adsorbed protein, respectively, which is close to the calculated theoretical monolayer of the cytochrome c.¹⁹

6.3.7 Leaching of Cytochrome C

As can be seen from the electrochemical data, both adsorbed and covalently bound cytochrome c is strongly attached at high loading to the porous ATO surface, showing a direct heterogeneous electron transfer. The strong attachment in case of adsorption can be attributed mostly to the presence of strong electrostatic interaction between the protein and the surface of ATO. At neutral pH the cytochrome c is strongly positively charged (its isoelectric point is at pH 10), which ensures its appropriate binding and possibly orientation on the negatively charged surfaces. On the other hand, the ATO nanoparticles used as building blocks for the film fabrication are negatively charged as shown previously, the charge becoming more negative with the increasing antimony content.¹¹ The negative charge of the tin oxide surface and its strong Coulomb interactions with cytochrome c was reported also by other authors.^{17-19, 43} Therefore, the negatively charged ATO framework provides a good platform for the immobilization of positively charged proteins. However, the adsorbed cytochrome c shows a tendency toward desorption upon multiple cycling measurements in 0.05 M phosphate buffer. (Fig. 6.3.8). While the covalently attached cytochrome c shows a decrease of 7 % in peak current, the peak current of the adsorbed cytochrome c decreases by 57 % after 100 cycles.

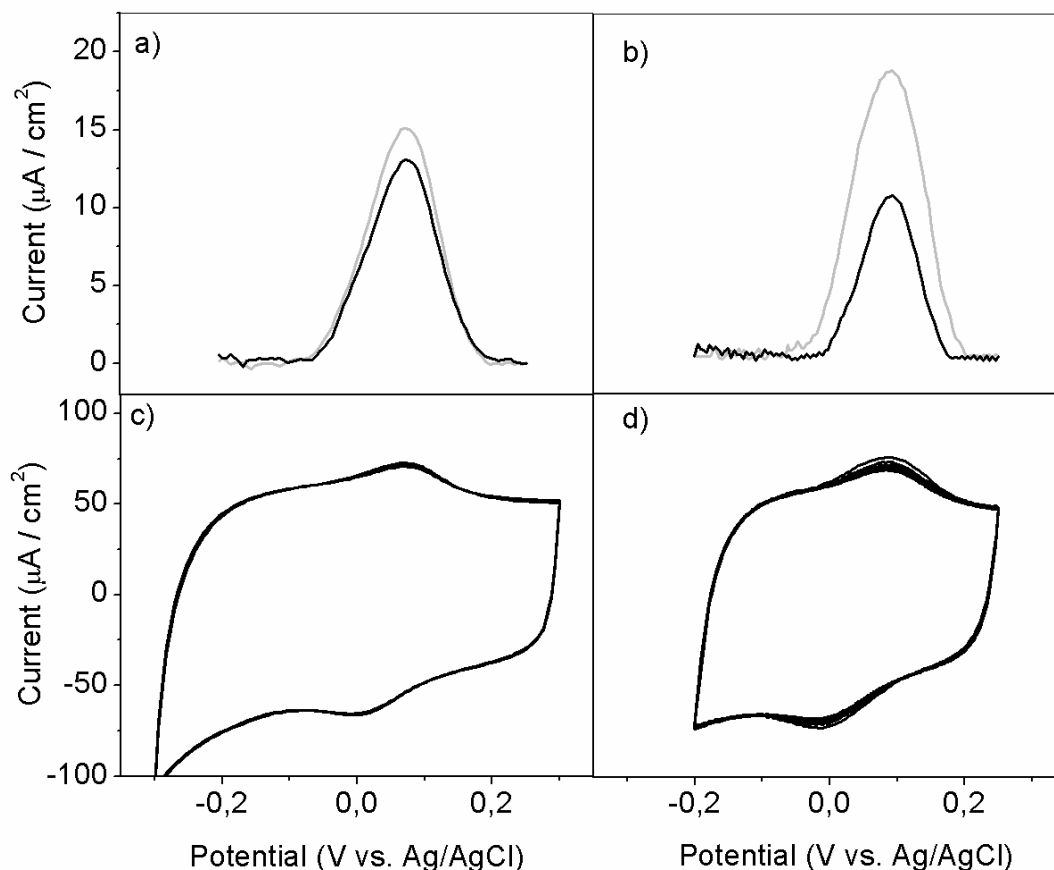


Figure 6.3.8. Multi-cycle voltammograms (anodic peaks after background subtraction) of covalently attached (a) and adsorbed (b) cytochrome c after the first cycle (gray lines) and after 100 cycles (black lines). (c) and (d) show full multicycle voltammograms of the covalently attached (c) and adsorbed cytochrome c (d), respectively. The voltammograms were obtained in 0.05 M phosphate buffer as supporting electrolyte and at a scan rate of 50 mV/s.

Moreover, the difference in the immobilization stability between the adsorbed and covalently bound protein becomes much more evident when the ionic strength of the electrolyte solution becomes higher.

In order to test the leaching stability of cytochrome c incorporated by the different procedures, the cytochrome c-containing films were immersed in a 0.2 M KCl solution for 3 hours, as described in the experimental section. The redox peak of the covalently attached cytochrome c decreases by 22 % after the leaching procedure, whereas in the case of the adsorbed cytochrome c, it decreases by 85 % (practically vanishes), as it was demonstrated also by other authors for adsorbed cytochrome c (Fig.6.3.9).^{14, 29, 46}

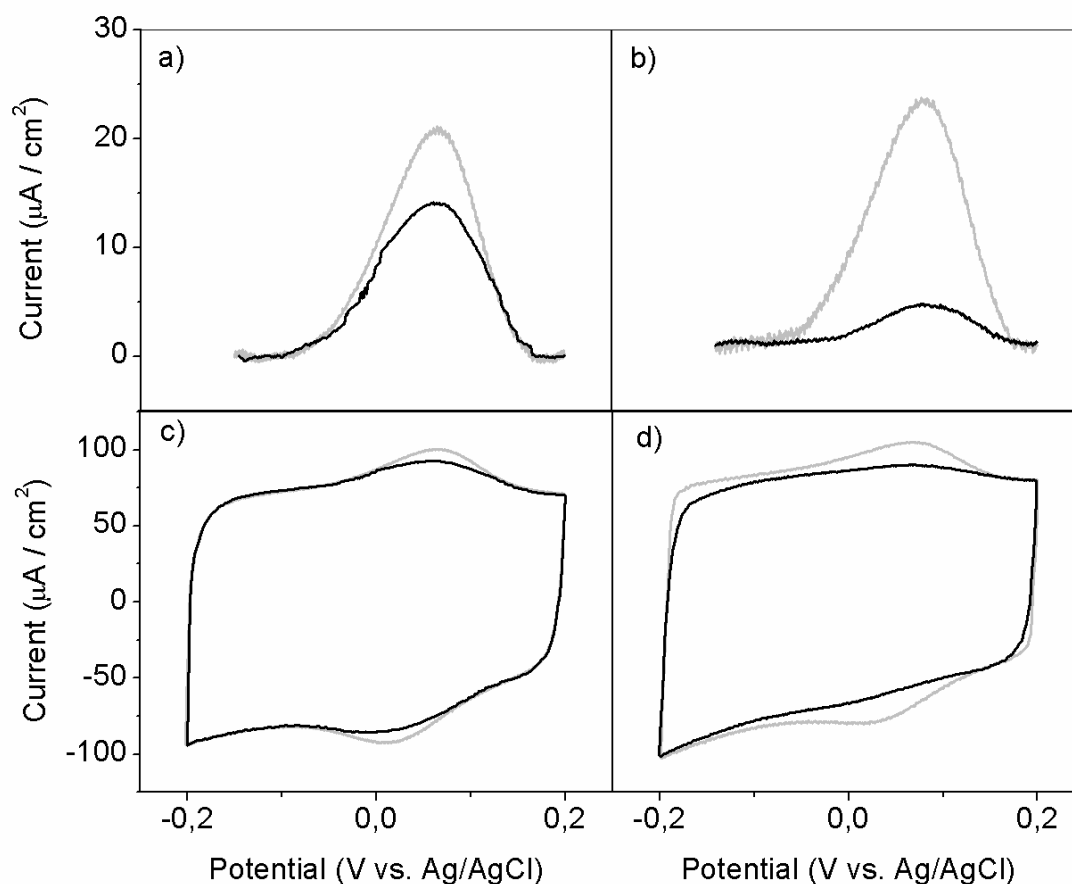


Figure 6.3.9. (a) Cyclic voltammograms of covalently attached cytochrome c before (gray line) and after (black line) desorption in a high ionic strength electrolyte (anodic peaks after background subtraction). (b) The same for the adsorbed cytochrome c. Full cyclic voltammograms for (c) covalently attached and (d) adsorbed cytochrome c. In all graphs the gray lines present the voltammogram before treatment in high ionic strength solution, whereas the black line presents the voltammogram obtained after treatment in high ionic strength solution. Scan rate in the measurement was 50 mV/s.

These results are expected considering that the amide bonds are not sensitive to the ionic strength of the solution. However, a slight decrease in redox peak current for the covalently immobilized cytochrome indicates that a certain amount of the protein is immobilized electrostatically due to its interaction either with the bare ATO surface, or with the amino groups after surface functionalization. It is difficult to obtain direct spectroscopic proof for the formation of the amide bonds between the protein and the amino-groups on the electrode surface, since they are indistinguishable from the peptide bonds of the protein itself. As an additional confirmation that the protein is indeed covalently attached after the performed procedure and not only adsorbed on the surface, the leaching stability of cytochrome adsorbed

on APTES modified films without the addition of an activator for an amide bond formation was tested. The redox signal of cytochrome in such films vanishes completely after the leaching test, indicating that all cytochrome was detached from the surface. Such an obvious difference in the leaching stability of the protein immobilized by two different procedures, additionally supported by the spectroscopic measurements and the difference in electrochemical performance (formal potential values and electrode kinetics), gives a strong indication of covalent bond formation.

6.3.8 Electrocatalytic Activity of Cytochrome C

Besides the difference in immobilization stability, the cytochrome c grafted via covalent and non-covalent bonds shows different electrocatalytic activity towards hydrogen peroxide, which reflects the difference in protein conformation inside the pores. The native cytochrome c, as present in the buffer solution, does not feature enzymatic peroxidase activity since the six-coordinated heme iron in the native protein is not available for interaction with peroxide.⁴⁷⁻⁴⁹ However, the availability of the reaction center to hydrogen peroxide (pseudo peroxidase electrocatalytic activity) can be induced by very slight changes in the protein conformation,⁵⁰ as also demonstrated for the denatured cytochrome c in solution in the presence of 0.05 M guanidine hydrochloride (shoulder pointed with arrows in Fig. 6.3.10). However, additionally it was found that the adsorbed cytochrome c shows electrocatalytic activity in the presence of hydrogen peroxide, whereas the covalently bound cytochrome c does not show this activity, Fig. 6.3.10-c and d.

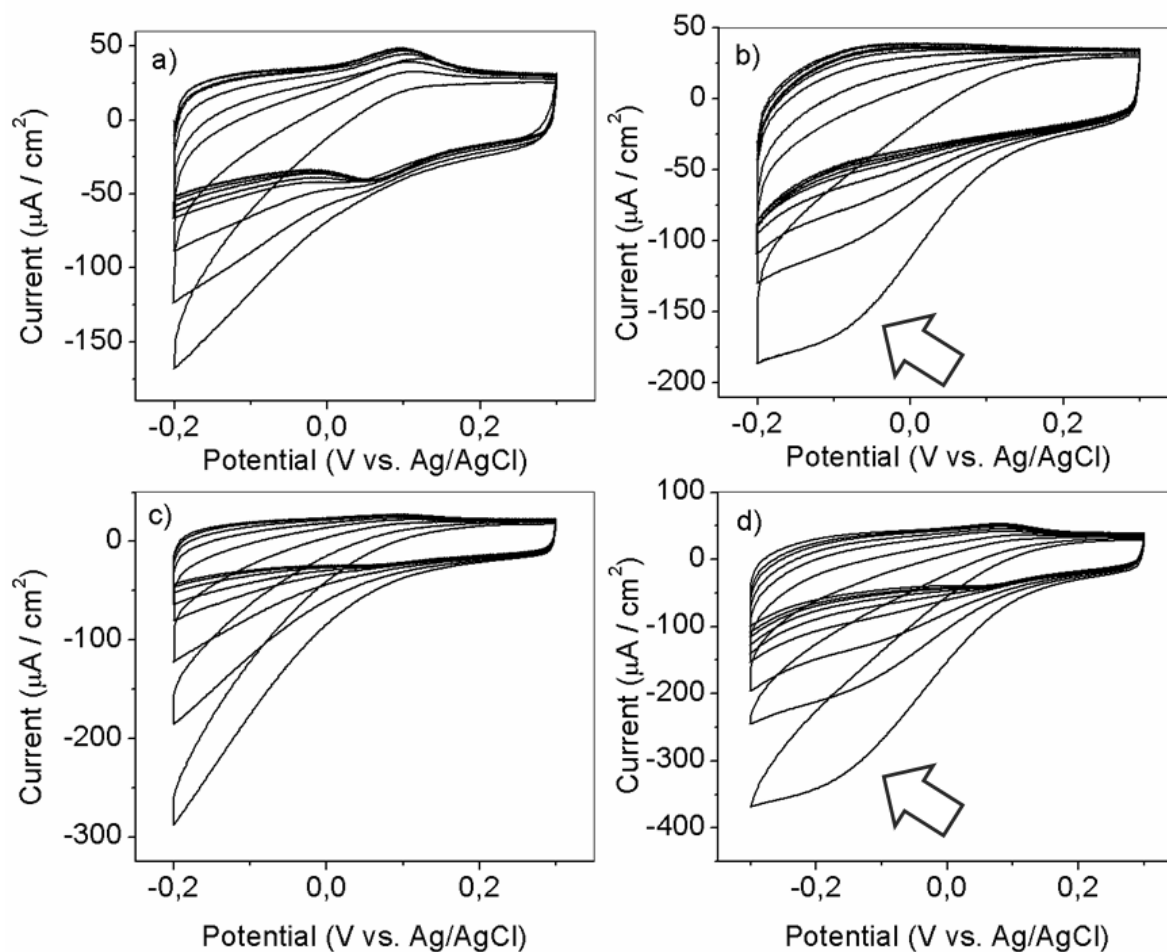


Figure 6.3.10. Catalytic activity of cytochrome c in the presence of H_2O_2 (in each graph from the top to the bottom): 0 mM, 0.02 mM, 0.04 mM, 0.08 mM, 0.16 mM, 0.32 mM, 0.64 mM, 1.2 mM. **(a)** Catalytic activity of the native cytochrome c present in 0.05 M phosphate buffer solution, and **(b)** of the solution of denatured cytochrome c which contains 0.05 M guanidine hydrochloride. In both cases the mesoporous ATO electrode served as working electrode. **(c)** Catalytic activity of the covalently attached cytochrome c on the mesoporous ATO electrode and **(d)** adsorbed cytochrome c on mesoporous ATO electrode. The native cytochrome c in a phosphate buffer solution does not show any electrocatalytic activity towards hydrogen peroxide (a). However, after denaturing the cytochrome c in the presence of 0.05 M guanidine hydrochloride and by addition of the peroxide subsequently significant increase in cathodic current was observed indicating catalytic activity of the denatured protein (b). All voltammograms were recorded at scan rate of 30 mV/s.

These results indicate that the adsorption of cytochrome c by electrostatic interactions of the protein chain with the pore walls induces a change in the conformation of the protein, which results in an appearance of this catalytic activity. These results are in good agreement with catalytic activity obtained by other authors where cytochrome c was adsorbed by electrostatic interactions. The difference in electrocatalytic activity of the protein immobilized in different ways can be caused by different degrees of interaction of the protein with the electrode surface. The positive charge of the cytochrome c is located mostly in the vicinity of the heme

due to protonated lysine moieties surrounding the redox center and playing an important role in the electron transfer.^{51, 52} It is therefore possible that the strong electrostatic interaction of this part of the protein with the negatively charged ATO causes slight changes in the conformation of the heme pocket, making it more accessible for the hydrogen peroxide molecules. On the other hand, the interaction of the protein with the electrode in case of covalent bonding is less direct since the protein is attached by a long-chain linker to the electrode surface, and the native conformation of the protein is possibly more preserved. The direct electrical communication of the protein with the electrode is obviously possible in both cases as can be observed from the voltammetric response, but the possible difference in the conformation of protein grafted by different approaches can explain the observed slight differences in the formal potential and in the rate transfer constants. The possibility to vary electrocatalytic activity of cytochrome c by changing its interaction with the electrode surface can bring an additional means to tune the performance of protein-containing electrode layers in the desirable applications. Moreover, the use of such hybrid transparent electrode systems can be advantageous in analytical spectroscopic devices.

6.4 Conclusions

Mesoporous films of antimony doped tin oxide (ATO) were shown to be a suitable electrode matrix for the incorporation of small redox proteins such as cytochrome c with a very high loading using different grafting approaches. Due to the negative charge of the ATO framework, the positively charged cytochrome is sufficiently attached to the pore surface via electrostatic interactions that it demonstrates a surface-immobilized electrochemical behavior. This feature of the ATO framework makes it very attractive for the immobilization of other positively charged biomolecules. It was shown for the first time that the cytochrome c can also be covalently incorporated in the porous electrode matrix. The covalent bonding of the

cytochrome c significantly enhances the binding stability and makes it much less susceptible to the influence of the environment such as the ionic strength of the electrolyte. Both adsorbed and covalently bound cytochrome c molecules keep their integrity after their incorporation in the pores and show a direct reversible heterogeneous electron transfer. The amount of electrochemically addressable cytochrome is very high for both types of immobilization and is proportional to the specific surface area, reaching up to 440 and 600 pmol/cm² of electrode area for covalently attached and adsorbed protein, respectively. Besides the difference in the binding stability, the way of immobilization influences the electrocatalytic activity of cytochrome towards hydrogen peroxide. This reflects the slight difference in protein conformation inside the pores, which can be attributed to different interactions with the electrode surface. The strong electrostatic interaction of the protein with the negatively charged ATO may cause slight changes in the conformation of the heme pocket, while the interaction of the protein with the electrode in case of covalent bonding is less direct since the protein is attached by a long-chain linker to the electrode surface, and the native conformation of the protein appears to be more preserved.

The demonstrated ability of coupling functional biomolecules such as redox proteins with transparent porous electrode substrates with a high conducting surface area promises to open new opportunities toward integrating natural biological functions with the capabilities of modern microelectronics. Such hybrid materials are expected to enable both fundamental studies of protein functions and sophisticated applications in bioanalytical devices that combine optical and electrochemical detections, health care or environmental monitoring and transparency of the electrode can be advantageous in analytical spectroscopic devices.

6.5 Appendix

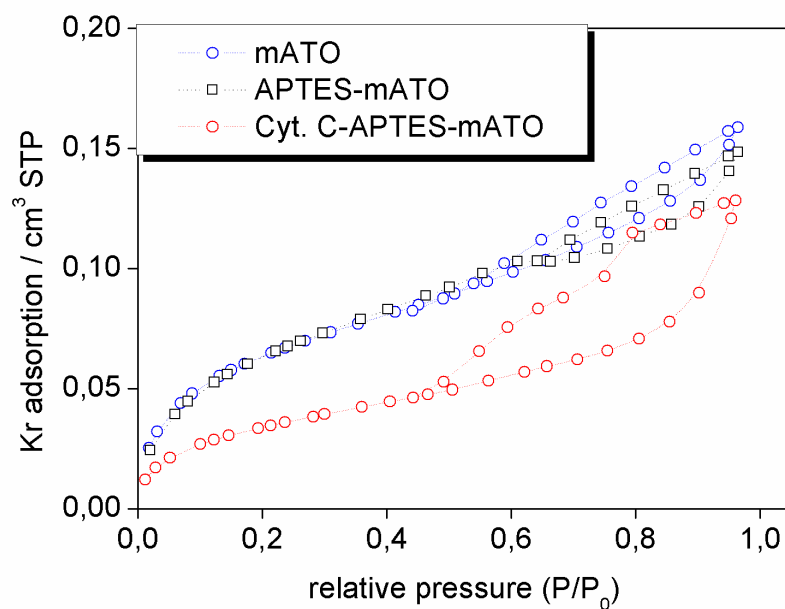


Figure A-6.1. Krypton adsorption isotherms on mesoporous ATO film (mATO), ATO film functionalized with APTES (APTES-mATO) and mesoporous film with incorporated cytochrome c (Cyt. C-APTES-mATO).

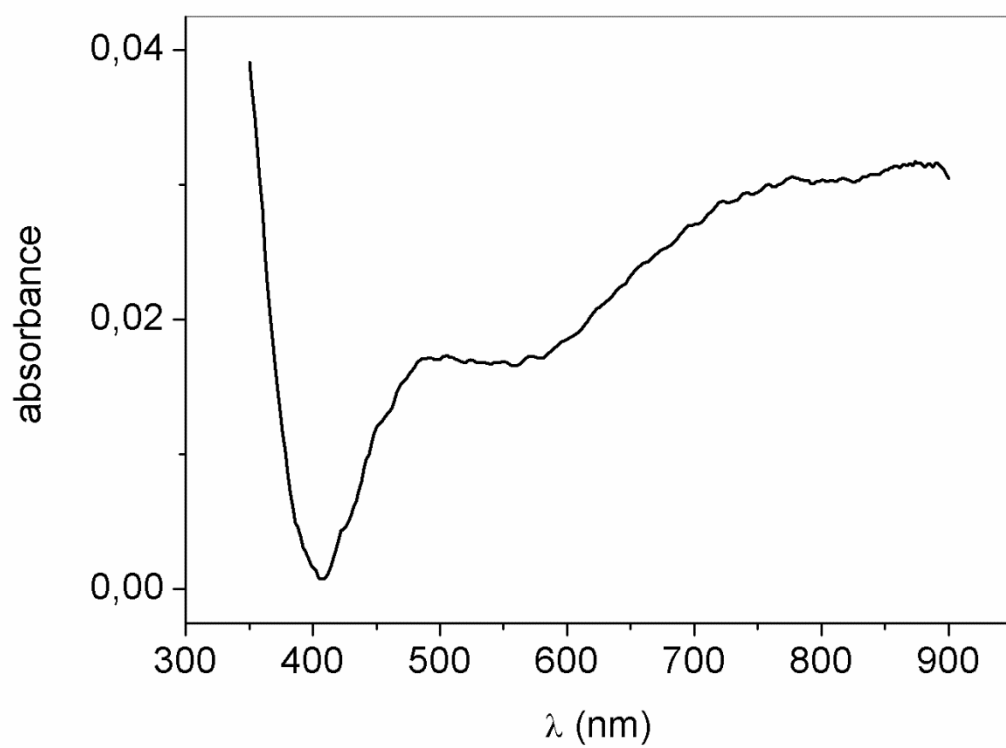


Figure A-6.2. The UV-Vis spectra of the pure ATO film.

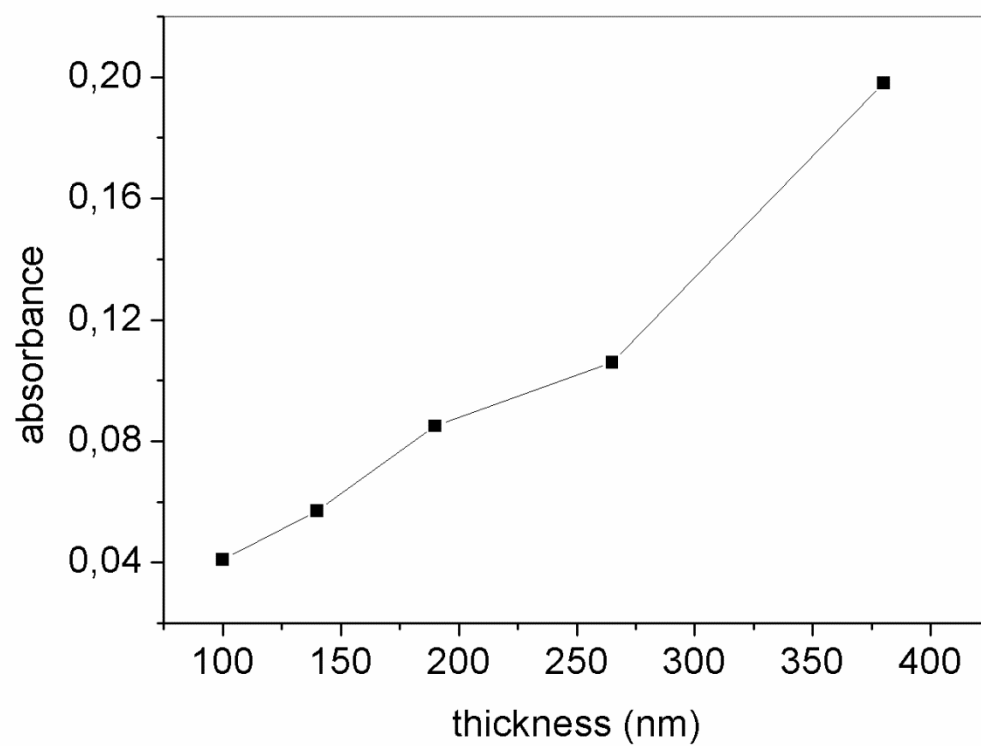


Figure A-6.3. Increase in intensity of the Soret band (409 nm) of covalently attached cytochrome c obtained from UV-Vis measurements in films with different thicknesses.

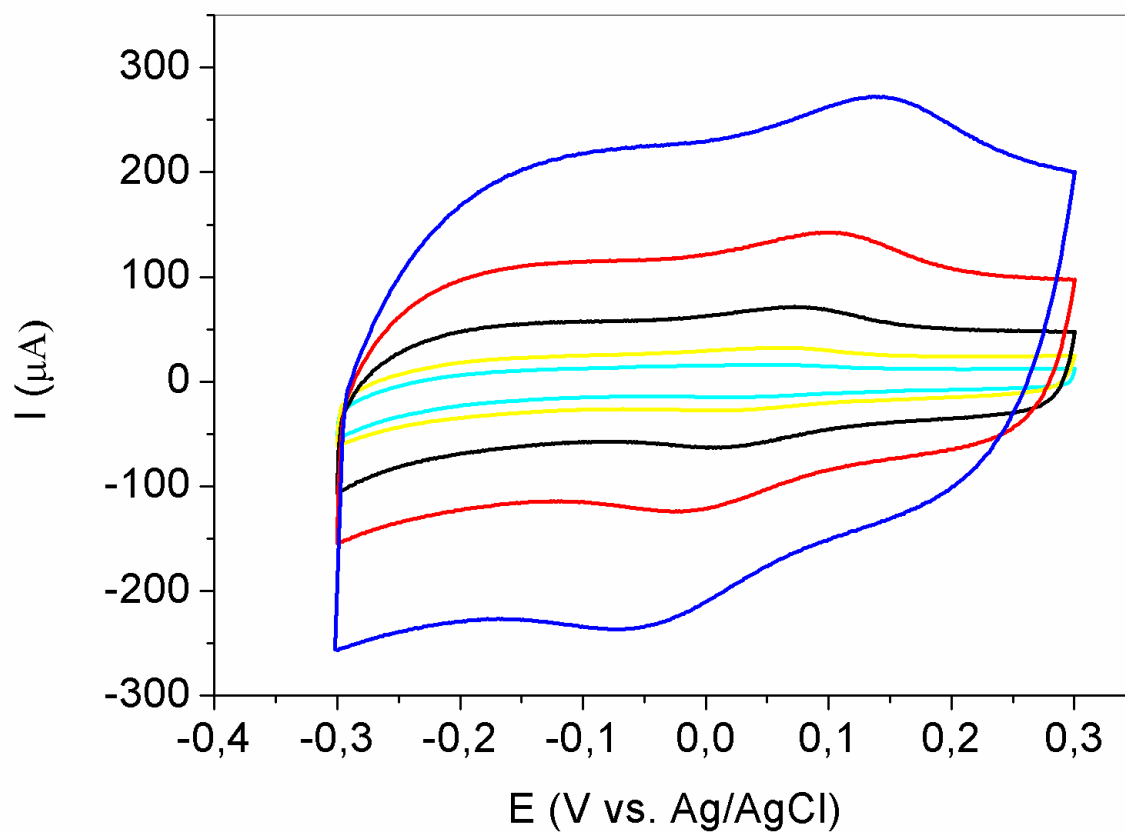


Figure A-6.4. Cyclic voltammograms of cytochrome c covalently attached to mesoporous ATO film, obtained at 50, 100, 200, 500 and 1000 mV/s (from bottom to top).

6.6 References

1. Bonanni, B.; Andolfi, L.; Bizzarri, A. R.; Cannistraro, S., *J. Phys. Chem. B* **2007**, 111, 5062.
2. Das, R.; Kiley, P. J.; Segal, M.; Norville, J.; Yu, A. A.; Wang, L.; Trammell, S. A.; Reddick, L. E.; Kumar, R.; Stellacci, F.; Lebedev, N.; Schnur, J.; Bruce, B. D.; Zhang, S.; Baldo, M., *Nano Lett.* **2004**, 4, 1079.
3. Mallouk, T. E.; Yang, P., *J. Am. Chem. Soc.* **2009**, 131, 7937.
4. Klibanov, A. M., *Science* **1983**, 219, 722.
5. Vinu, A.; Murugesan, V.; Tangermann, O.; Hartmann, M., *Chem. Mater.* **2004**, 16, 3056.
6. Hartmann, M.; Jung, D., *J. Mater. Chem.* **2010**, 20, 844.
7. Walcarius, A.; Kuhn, A., *TrAC Trends Anal. Chem.* **2008**, 27, 593.
8. Szamocki, R.; Reculosa, S.; Ravaine, S.; Bartlett, P. N.; Kuhn, A.; Hempelmann, R., *Angew. Chem. Int. Ed.* **2006**, 45, 1317.
9. Aksu, Y.; Frasca, S.; Wollenberger, U.; Driess, M.; Thomas, A., *Chem. Mater.* **2011**, 23, 1798.
10. Frasca, S.; von Graberg, T.; Feng, J.-J.; Thomas, A.; Smarsly, B. M.; Weidinger, I. M.; Scheller, F. W.; Hildebrandt, P.; Wollenberger, U., *ChemCatChem* **2010**, 2, 839.
11. Müller, V.; Rasp, M.; Rathouský, J.; Schütz, B.; Niederberger, M.; Fattakhova-Rohlfing, D., *Small* **2010**, 6, 633.
12. Hou, K.; Puzzo, D.; Helander, M. G.; Lo, S. S.; Bonifacio, L. D.; Wang, W.; Lu, Z. H.; Scholes, G. D.; Ozin, G. A., *Adv. Mater.* **2009**, 21, 2492.
13. Yiu, H. H. P.; Wright, P. A., *J. Mater. Chem.* **2005**, 15, 3690.
14. Guo, K.; Hu, Y.; Zhang, Y.; Liu, B.; Magner, E., *Langmuir* **2010**, 26, 9076.
15. Davis, M. E., *Nature* **2002**, 417, 813.

16. El Kasmi, A.; Leopold, M. C.; Galligan, R.; Robertson, R. T.; Saavedra, S. S.; El Kacemi, K.; Bowden, E. F., *Electrochem. Commun.* **2002**, 4, 177.
17. Topoglidis, E.; Astuti, Y.; Duriaux, F.; Grätzel, M.; Durrant, J. R., *Langmuir* **2003**, 19, 6894.
18. Topoglidis, E.; Campbell, C. J.; Cass, A. E. G.; Durrant, J. R., *Langmuir* **2001**, 17, 7899.
19. Willit, J. L.; Bowden, E. F., *J. Phys. Chem.* **1990**, 94, 8241.
20. Renault, C.; Balland, V.; Martinez-Ferrero, E.; Nicole, L.; Sanchez, C.; Limoges, B., *Chem. Comm.* **2009**, 7494.
21. Rui, Q.; Komori, K.; Tian, Y.; Liu, H.; Luo, Y.; Sakai, Y., *Anal. Chim. Acta* **2010**, 670, 57.
22. Li, Q.; Luo, G.; Feng, J., *Electroanal.* **2001**, 13, 359.
23. Yin, Y.; Wu, P.; Lü, Y.; Du, P.; Shi, Y.; Cai, C., *J. Solid State Electrochem.* **2007**, 11, 390.
24. Wang, J.; Li, M.; Shi, Z.; Li, N.; Gu, Z., *Anal. Chem.* **2002**, 74, 1993.
25. Zhang, L., *Biosens. Bioelectr.* **2008**, 23, 1610.
26. Alwarappan, S.; Joshi, R. K.; Ram, M. K.; Kumar, A., *App. Phys. Lett.* **2010**, 96, 263702.
27. Liu, H.; Tian, Y.; Deng, Z., *Langmuir* **2007**, 23, 9487.
28. Zhu, A.; Tian, Y.; Liu, H.; Luo, Y., *Biomater.* **2009**, 30, 3183.
29. Avila, A.; Gregory, B. W.; Niki, K.; Cotton, T. M., *J. Phys. Chem. B* **2000**, 104, 2759.
30. Albery, W. J.; Eddowes, M. J.; Hill, H. A. O.; Hillman, A. R., *J. Amer. Chem. Soc.* **1981**, 103, 3904.
31. Ju, H.; Liu, S.; Ge, B.; Lisdat, F.; Scheller, F. W., *Electroanal.* **2002**, 14, 141.
32. Müller, V.; Rasp, M.; Štefanić, G.; Ba, J.; Günther, S.; Rathousky, J.; Niederberger, M.; Fattakhova-Rohlfing, D., *Chem. Mater.* **2009**, 21, 5229.

33. Fattakhova-Rohlfing, D.; Wark, M.; Rathousky, J., *Stud. Surf. Sci. Cat.* **2007**, 165, 573.
34. Nakashima, T.; Higa, H.; Matsubara, H.; Benson, A. M.; Yasunobu, K. T., *J. Biol. Chem.* **1966**, 241, 1166.
35. Collinson, M.; Bowden, E. F., *Anal. Chem.* **1992**, 64, 1470.
36. Laviron, E., *J. Electroanal. Chem.* **1979**, 101, 19.
37. Zhang, X.; Wang, J.; Wu, W.; Qian, S.; Man, Y., *Electrochem. Comm.* **2007**, 9, 2098.
38. Zhao, J.; Zhu, W.; Liu, T.; Yang, J.; Li, G., *Anal. Bioanal. Chem.* **2010**, 397, 695.
39. Eddowes, M. J.; Hill, H. A. O., *J. Amer. Chem. Soc.* **1979**, 101, 4461.
40. Stellwagen, E., *Nature* **1978**, 275, 73.
41. Yeh, P.; Kuwana, T., *Chem. Lett.* **1977**, 1145.
42. Eddowes, M. J.; Hill, H. A. O., *J. Chem. Soc. Chem. Comm.* **1977**, 771b.
43. Willit, J. L.; Bowden, E. F., *J. Electroanal. Chem. Interf. Electrochem.* **1987**, 221, 265.
44. Topoglidis, E.; Palomares, E.; Astuti, Y.; Green, A.; Campbell, C.; Durrant, J. R., *Electroanal.* **2005**, 17, 1035.
45. Dai, Z.; Liu, S.; Ju, H., *Electrochim. Acta* **2004**, 49, 2139.
46. McKenzie, K. J.; Marken, F., *Langmuir* **2003**, 19, 4327.
47. Casalini, S.; Battistuzzi, G.; Borsari, M.; Bortolotti, C. A.; Di Rocco, G.; Ranieri, A.; Sola, M., *J. Phys. Chem. B* **2010**, 114, 1698.
48. Deere, J.; Magner, E.; Wall, J. G.; Hodnett, B. K., *Biotech. Progr.* **2003**, 19, 1238.
49. Diederix, R. E. M.; Ubbink, M.; Canters, G. W., *Biochem.* **2002**, 41, 13067.
50. Casalini, S.; Battistuzzi, G.; Borsari, M.; Ranieri, A.; Sola, M., *J. Amer. Chem. Soc.* **2008**, 130, 15099.
51. Mirkin, N.; Jaconic, J.; Stojanoff, V.; Moreno, A., *Proteins* **2008**, 70, 83.

52. Molina-Heredia, F. P.; Wastl, J.; Navarro, J. A.; Bendall, D. S.; Hervas, M.; Howe, C. J.; De la Rosa, M. A., *Nature* **2003**, 424, 33.

7 General Conclusions

In the present work the main aim was to prepare transparent conducting films of antimony doped tin (ATO) oxide which can be used as nanostructure electrodes. For this purpose a new pathway for the preparation of the transparent conducting mesoporous ATO films was developed. The obtained films were investigated as nanostructured electrodes with a high surface area allowing a high surface coverage with electro-active molecules.

Considering that for obtaining a completely crystalline mesoporous ATO framework via sol-gel procedure by using commercially available block co-polymers as templates an elaborated post synthetic treatment is needed, the EISA process for the preparation of these mesoporous ATO films was modified. In the modified EISA procedure, ATO nanoparticles were used as building blocks for the mesoporous structure while the conductivity of the films was tuned by the composition of the nanoparticles.

The ATO nanoparticles were prepared via a nonaqueous solution route, using benzyl alcohol, tin tetrachloride, and a suitable Sb(III) compound. ATO nanoparticles with different amounts of antimony were prepared. The amount of Sb was varied from 0 (pure SnO_2) to 50 mol %. The obtained ATO nanoparticles were completely crystalline, 3-4 nm in size and easily redispersible in a variety of solvents. It was found that the cassiterite SnO_2 lattice can accommodate up to 38 mol % of Sb. The particle composition is homogeneous throughout the entire volume, without enrichment of the surface with Sb. The influence of the amount of the incorporated Sb on the electrical conductivity of the ATO nanoparticles with different composition was studied. Small dopant concentrations of antimony in SnO_2 already dramatically increase the electrical conductivity of the nanoparticles. The highest conductivity was obtained for ATO nanoparticles containing 4 mol % of Sb. This increased the conductivity by two orders of magnitude compare to the pure SnO_2 nanoparticles. Additional annealing

resulted in sintering of the nanoparticles, leading to a further improvement of the conductivity.

The ATO nanoparticles with different antimony dopant concentrations were investigated for the preparation of mesoporous films. ATO nanoparticles with a composition from 6 to 30 mol % Sb were successfully used for the fabrication of mesoporous ATO films with the respective composition by using commercially available polymers from the Pluronic family as template for the mesostructure. The complete crystallinity of the nanoparticles made it possible to obtain a fully crystalline mesoporous inorganic framework by annealing the as-prepared films at a temperature as low as 300 °C without any need for further elaborated post-synthetic treatment of the films.

The electrical conductivity of the films follows the same behavior as the electrical conductivity of the nanoparticles, i.e., the highest electrical conductivity of the films was obtained when the particles with the lowest amount of antimony were used as building blocks for the mesostructure. Additionally, the annealing procedure of the films, which is needed for the removal of the organic template and sintering of the inorganic framework, influences the electrical conductivity. The electrical conductivity increases with increasing the annealing temperature from 300 °C to 500 °C. Interestingly, the obtained films show high thermal stability exhibiting practically no shrinkage during the temperature treatment which is a common issue with amorphous sol-gel derived films.

The obtained mesoporous ATO films possess an open and accessible porosity, high surface area, and uniform pore size. The high potential of the obtained mesoporous layers as nanostructured transparent electrodes with high surface areas was demonstrated with ferrocene molecules, which were covalently immobilized in the conducting matrix, showing the significantly enhanced electrochemical response that is proportional to the electrode surface area.

Additionally, alternative the surface functionalization methods for the mesoporous ATO films were investigated. Two types of surface functionalization were performed: surface functionalization with APTES molecules and surface functionalization with Grignard reagents.

The surface functionalization with APTES proved to be an easy method for the implementation of organic moieties and providing high surface loadings with organic groups. The surface functionalization of the mesoporous ATO films with APTES molecules additionally offers free amine groups which can serve as linker in the subsequent anchoring of the desired electro-active species. However, organosilanes can be limiting in the available combination of functional groups. Therefore Grignard surface reactions were investigated for the implementation of organic groups that contain multiply bonded systems and groups that are not available in common silane compounds.

In the light of the above results, considering that high surface functionalization of the ATO with organic moieties can be achieved, the mesoporous ATO framework was further investigated as a matrix for the incorporation of the small redox protein cytochrome c. For this purpose two approaches for the incorporation of the cytochrome c were chosen. First, the cytochrome c was anchored by adsorption as a result of the electrostatic interactions between the positively charged protein and negatively charged ATO network. In the second approach the covalent attachment of the cytochrome c via amide bond formation with the APTES functionalized ATO surface was investigated. For both cases it was shown that a high surface coverage of the ATO films with cytochrome c can be achieved. However, the covalent bonding of the cytochrome c indicated a significant enhancement of the binding stability of the protein. Both types of attachment allow for a direct reversible electron transfer between the ATO electrode and the protein. The amount of the electrochemically addressable protein is proportional to the surface area of the films. Nevertheless, the type of immobilization of the protein shows an influence on its electrochemical response. This behaviour was observed in

the case of the pseudo peroxidase activity of the cytochrome c. This type of activity of the cytochrome c can be attributed to the different interactions of the adsorbed and covalently attached protein with the electrode surface.

The demonstrated possibility of coupling functional biomolecules with transparent porous electrode substrates that offer a high conducting surface area allows the integration of natural biological functions within modern microelectronic devices.

8 Curriculum vitae

PERSONAL DATA

Vesna Müller, born Ličina

Date of birth: 02.12.1978

Place of birth: Zagreb, Croatia

Marital status: married

Citizenship: Croatian

EDUCATION

September 2008 – June 2011 PhD project, LMU, München, Department of Chemistry, Division of Physical Chemistry, Group of Prof. Bein

1997 – 2005 Faculty of Science, University of Zagreb, Department of Chemistry, Diploma in Chemistry (grade: excellent)
Diploma thesis in Solid State Chemistry: Study on electrical properties of iron bismuth phosphate glasses investigated by impedance spectroscopy

1993 – 1997 High school, Zagreb, graduation grade: excellent

PROFESSIONAL CAREER

July 2011-June 2012 Post Doc, Uni Erlangen-Nuremberg, Chair for Surface Science and Corrosion (LKO)

September 2008 – May 2011 PhD student, LMU, München, Department of Chemistry, Division of Physical Chemistry, Group of Prof. Bein

2006-2008 Associate, Faculty of science, University of Zagreb, Department of Chemistry

2005-2008 Research assistant, Ruđer Bošković Institute

PROFESSIONAL ORGANISATIONS MEMBERSHIP

- The Croatian Chemical Society
- The Croatian Society for Electron Microscopy
- The Croatian Crystallographic Association

FOREIGN LANGUAGES

- English: fluent
 - German: basic in writing, fluent in speaking
 - Italian: basic
 - French: basic
-

9 Publications and Presentations

9.1 Publications

1. **V. Müller**, F. Haase, J. Rathousky, D. Fattakhova-Rohlfing: *Surface functionalization of mesoporous antimony doped tin oxide by metalorganic reaction*, Mater. Chem. Phys., **137** (2012) 207-212
2. V. Skoromets, F. Kadlec, C. Kadlec, H. Nemec, I. Rychetsky, G. Panaitov, **V. Müller**, D. Fattakhova-Rohlfing, P. Moch, P. Kuzel, *Tuning of dielectric properties of SrTiO₃ in the terahertz range*, Phys. Rev. B, **84**, (2011) 174121-10
3. D. I. Fried, A. Ivanova, **V. Müller**, J. Rathousky, B. M. Smarsly, D. Fattakhova-Rohlfing: *A facile synthesis of mesoporous crystalline tin dioxide films involving a base-triggered formation of sol-gel building blocks*, Nanoscale **3**, (2011) 1234-1239
4. **V. Müller**, M. Rasp, G. Stefanic, S. Günther, J. Rathousky, M. Niederger, D. Fattakhova-Rohlfing: *Antimony doped tin oxide nanoparticles and their assembly in mesoporous films*, Physica Status Solidi C, **8** [6], (2011) 1759-1763
5. **V. Müller**, M. Rasp, B. Schütz, J. Rathousky, M. Niederberger, D. Fattakhova-Rohlfing: *Transparent Conducting Films of Antimony-Doped Tin Oxide with Uniform Mesosstructure Assembled from Pre-formed Nanocrystals*, Small **6**, (2010) 633-637
6. **V. Müller**, M. Rasp, G. Stefanic, J. Ba, S. Günther, J. Rathousky, M. Niederberger, D. Fattakhova-Rohlfing: *Highly Conducting Nanosized Monodispersed Antimony-Doped Tin Oxide Particels via Nonaquous Sol-Gel Procedure*, Chem. Mater. **21** (2009) 5229-5236
7. **V. Licina**, A. Gajovic, A. Mogus-Milankovic, I. Djerdj, N. Tomašić, D. Su: *Correlation Between the Microstructure and Electrical Properties of ZrTiO₄ Ceramics*, J. Am. Ceram.Soc., **91** [1] (2008) 178-186
8. **V. Licina**, A. Mogus-Milankovic, S. T. Reis, D. E. Day: *Electronic Conductivity in Zinc Iron Phosphate Glasses*, J. Non-Cryst. Solids, **353** (2007) 4395-4399
9. A. Mogus-Milankovic, **V. Licina**, S. T. Reis, D. E. Day: *Electronic Relaxation in Zinc Iron Phosphate Glasses*, J. Non-Cryst. Solids, **353** (2007) 2659-2666
10. S. T. Reis, A. Mogus-Milankovic, **V. Licina**, Y. Jinbo, M. Karabulut, D. E. Day, R. K. Brow: *Iron Redox Equilibrium, Structure and Properties of Zinc Iron Phosphate Glasses*, J. Non-Cryst. Solids, **353** (2007) 151-158

11. A. Mogus-Milankovic, A. Santic, V. Licina, D. E. Day: *Dielectric Behavior and Impedance Spectroscopy of Bismuth Iron Phosphate Glasses*, J. Non-Cryst. Solids, 351 (2005) 3235-3245.

9.2 Poster Presentations

1. Conducting Antimony Doped Tin Oxide Nanoparticles, 3rd International Symposium on Transparent Conducting Materials (TCM 2010), Crete, Greece, 17-21 October 2010
2. Highly conducting antimony doped tin oxide nanoparticles, 22. Deutsche Zeolith-Tagung, Munich, Germany, 3-5 March 2010
3. Investigation of Highly Conducting Crystalline Nanoparticles of Antimony Doped Tin Oxide (ATO); From Synthesis to Applications, International Symposium on Advanced Electron Microscopy for Catalysis and Energy Storage Materials, Berlin, Germany, 17-20 January 2010
4. Influence of ZnO on Crystallization and Electrical Conductivity of Zinc Iron Phosphate Glasses, ACerS 2008 Glass & Optical Materials Division Meeting, Tucson, Arizona, 18-21 May 2008.
5. Effect of crystallization on the electrical properties of iron phosphate glasses, VII. Croatian Meeting of Young Chemical Engineers, Zagreb, Croatia, 21-22 February 2008.
6. Effect of structural changes on the electron conductivity of zinc iron phosphate glasses, XX. Croatian Meeting of Chemists and Chemical Engineers, Zagreb, Croatia, 26 February-01 March, 2007.
7. Influence of crystallization on the electrical conductivity in zinc iron phosphate glasses, 4th Conference of the International Dielectric Society & 9th International Conference on Dielectric & Related Phenomena, Poznan, Poland, 3-7 September 2006.
8. Effect of melting temperature on electrical properties of zinc iron phosphate glasses, VI. Croatian Meeting of Young Chemical Engineers, Zagreb, Croatia, 23-24 February 2006.
9. Impedance spectroscopy of $\text{Bi}_2\text{O}_3\text{-Fe}_2\text{O}_3\text{-P}_2\text{O}_5$ glasses, Autumn School on Materials Science and Electron Microscopy 2005: "Microscopy of Tomorrow's Industrial Materials", Berlin, Germany, 3-8 October 2005.

9.3 Oral Presentations

1. Transparent Conducting Mesoporous Films of Antimony-doped Tin Oxide Assembled from Pre-formed Nanocrystals, 3rd International Symposium on Transparent Conducting Materials (TCM 2010), Crete, Greece, 17-21 October 2010
2. Transparent Conducting Films of Antimony Doped Tin Oxide: From Nanoparticle Synthesis to Their Assembly Into Mesostructures, **Invited talk**, University of Erlangen-Nuremberg, Chair for Surface Science and Corrosion (LKO), 27 May 2010.
3. Mesoporous antimony doped tin oxide films: from nanoparticle synthesis to their assembly into mesostructures, 7th International Conference on Porous Semiconductors-Science and Technology (PSST 2010), Valencia, Spain, 14-19 March 2010
4. Transparent Conducting Films of Antimony-doped Tin Oxide with Uniform Mesostructure Assembled from Pre-formed Nanocrystals, 22. Deutsche Zeolith-Tagung, Munich, Germany, 3-5 March 2010
5. Influence of crystallization on the electrical conductivity in zinc iron phosphate glasses, 10th International Conference and Exhibition of the European Ceramic Society, Berlin, Germany, 17-21 June 2007
6. Influence of crystallization on the electrical conductivity of iron phosphate glasses, 16th Croatian-Slovenian Crystallographic Meeting, Petrcane, Croatia, 13-17 June 2007. (oral presentation)
7. Microstructure and electrical properties of ZrTiO_4 ceramics, 2nd Croatian Congress on Microscopy with International Participation, Topusko, Croatia, 18-21 May 2006.
8. Impedance spectroscopy of $\text{Bi}_2\text{O}_3\text{-Fe}_2\text{O}_3\text{-P}_2\text{O}_5$ glasses, Autumn School on Materials Science and Electron Microscopy 2005: "Microscopy of Tomorrow's Industrial Materials", Berlin, Germany, 3-8 October 2005.
9. Electrical properties of bismuth iron phosphate glasses, Training course on molecular design and computer assisted combinatorial chemistry, Trieste, Italy, 04-07 July, 2005.
10. Study on electrical properties of $\text{Bi}_2\text{O}_3\text{-Fe}_2\text{O}_3\text{-P}_2\text{O}_5$ glasses investigated by impedance spectroscopy, XIX. Croatian Meeting of Chemists and Chemical Engineers, Opatija, Croatia, 24-27 April, 2005.